Karlsruhe Institute of Technology

Robert Schittny

Cloaking in Heat Conduction and Light Diffusion

2015
Dissertation

CLOAKING IN HEAT CONDUCTION AND LIGHT DIFFUSION

Zur Erlangung des akademischen Grades eines
DOKTORS DER NATURWISSENSCHAFTEN
von der Fakultät für Physik des
Karlsruher Instituts für Technologie (KIT)

genehmigte

DISSERTATION

von

Dipl.-Phys. Robert Johannes Schittny
geboren in Aachen

Tag der mündlichen Prüfung: 06.11.2015
Referent: Prof. Dr. Martin Wegener
Korreferent: Prof. Dr. Carsten Rockstuhl

CONTENTS

I THERMAL CLOAKING 9

PUBLICATIONS

PARTS OF THIS THESIS HAVE ALREADY BEEN PUBLISHED . . .
. . . in scientific journals:

- R. Schittny, M. Kadic, S. Guenneau, and M. Wegener, "Experiments on transformation thermodynamics: Molding the flow of heat", *Phys. Rev. Lett.* **110**, 195901 (2013)
- R. Schittny and M. Wegener, "Physikalische Tarnkappen", *Spektrum der Wissenschaft* **1**, 80 (2014)
- R. Schittny, M. Kadic, T. Bückmann, and M. Wegener, "Invisibility cloaking in a diffusive light scattering medium", *Science* **345**, 427 (2014)
- R. Schittny, T. Bückmann, and M. Wegener, "Im Nebel perfekt getarnt", *Physik in unserer Zeit* **45**, 214 (2014)
- R. Schittny, A. Niemeyer, M. Kadic, T. Bückmann, A. Naber, and M. Wegener, "Transient behavior of invisibility cloaks for diffusive light propagation", *Optica* **2**, 84 (2015)
- R. Schittny, A. Niemeyer, M. Kadic, T. Bückmann, A. Naber, and M. Wegener, "Diffuse-light all-solid-state invisibility cloak", *Opt. Lett.* **40**, 4202 (2015)

. . . at scientific conferences (only own presentations):

- R. Schittny, M. Kadic, S. Guenneau, and M. Wegener, "Experiments on transformation thermodynamics: Molding the flow of heat" (invited talk), META'13, Sharjah, United Arab Emirates, March 2013
- R. Schittny, M. Kadic, T. Bückmann, and M. Wegener, "3D optical invisibility cloak in the diffusive-light limit", CLEO 2014, San José, CA, USA, June 2014

- R. Schittny, M. Kadic, T. Bückmann, and M. Wegener, "Invisibility cloak in the diffusive-light limit" (invited talk), SPIE Optics + Photonics, San Diego, CA, USA, August 2014
- R. Schittny, A. Niemeyer, M. Kadic, T. Bückmann, A. Naber, and M. Wegener, "Condensed-matter invisibility cloak for diffusive light", CLEO 2015, San José, CA, USA, May 2015
- R. Schittny, A. Niemeyer, M. Kadic, T. Bückmann, A. Naber, and M. Wegener, "Invisibility cloaking in diffuse light" (invited talk), Korea-France Symposium 2015, IPCMS Strasbourg, France, May 2015

ADDITIONAL RELATED WORK HAS ALREADY BEEN PUBLISHED . . .
. . . in scientific journals:

- A. Martin, M. Kadic, R. Schittny, T. Bückmann, and M. Wegener, "Phonon band structures of three-dimensional pentamode metamaterials", *Phys. Rev. B* **86**, 155116 (2012)
- R. Schittny, T. Bückmann, M. Kadic, and M. Wegener, "Elastic measurements on macroscopic three-dimensional pentamode metamaterials", *Appl. Phys. Lett.* **103**, 231905 (2013)
- M. Kadic, T. Bückmann, R. Schittny, and M. Wegener, "On anisotropic versions of three-dimensional pentamode metamaterials", *New J. Phys.* **15**, 023029 (2013)
- T. Frenzel, J. D. Brehm, T. Bückmann, R. Schittny, M. Kadic, and M. Wegener, "Three-dimensional labyrinthine acoustic metamaterials", *Appl. Phys. Lett.* **103**, 061907 (2013)
- M. Kadic, T. Bückmann, R. Schittny, and M. Wegener, "Metamaterials beyond electromagnetism", *Rep. Prog. Phys.* **76**, 126501 (2013)
- T. Bückmann, R. Schittny, M. Thiel, M. Kadic, G. W. Milton, and M. Wegener, "On three-dimensional dilational elastic metamaterials", *New. J. Phys.* **16**, 033032 (2014)
- T. Bückmann, M. Thiel, M. Kadic, R. Schittny, and M. Wegener, "An elasto-mechanical unfeelability cloak made of pentamode metamaterials", *Nat. Commun.* **5**, 4130 (2014)

- M. Kadic, T. Bückmann, R. Schittny, P. Gumbsch, and M. Wegener, "Pentamode metamaterials with independently tailored bulk modulus and mass density", *Phys. Rev. Appl.* **2**, 054007 (2014)
- T. Bückmann, M. Kadic, R. Schittny, and M. Wegener, "Mechanical cloak design by direct lattice transformation", *Proc. Natl. Acad. Sci. USA* **112**, 4930 (2015)
- M. Kadic, R. Schittny, T. Bückmann, C. Kern, and M. Wegener, "Hall-effect sign inversion in a realizable 3D metamaterial", *Phys. Rev. X* **5**, 021030 (2015)
- T. Bückmann, M. Kadic, R. Schittny, and M. Wegener, "Mechanical metamaterials with anisotropic and negative effective mass-density tensor made from one constituent material", *Phys. Status Solidi B* **252**, 1671 (2015)
- M. Kadic, T. Bückmann, R. Schittny, and M. Wegener, "Experiments on cloaking in optics, thermodynamics, and mechanics", *Phil. Trans. R. Soc. A* **373**, 20140357 (2015)

... at scientific conferences (only own presentations):

- R. Schittny, M. Kadic, T. Bückmann, and M. Wegener, "Anisotropic versions of pentamode structures: Towards transformation elastodynamics", META'13, Sharjah, United Arab Emirates, March 2013

Chapter 1

1 INTRODUCTION

The idea of invisibility, that is, of being concealed from the visual perception of others, is a dream that is probably as old as mankind. Consequently, invisibility and mystic items that grant invisibility are recurring motifs in mythology, fiction, and science fiction all over the world. For example, in classical Greek mythology, a "cap of invisibility" (also called "cap of Hades") grants its wearer invisibility. In the Welsh tale *Culhwch and Olwen* dating back to the 11th century, a similar "mantle of invisibility" is described which is also listed in the *Thirteen Treasures of the Island of Britain* in medieval Welsh folklore. And in the German *Nibelungenlied* (written down at the beginning of the 13th century), Siegfried overcomes the dwarf Alberich, guardian of the treasure of the Nibelungen, and obtains from him a "cloak of concealment" (German: Tarnkappe[1]) that makes its wearer invisible. Modern counterparts are Harry Potter's invisibility cloak or the "One Ring" from Tolkien's *Lord of the Rings*, and invisibility devices are a rather common feature in science fiction stories and movies. All of these occurrences are unified either by their magical nature or by being based on miraculous technology beyond anything known today. And indeed, a decade ago, nobody in this world would have known how to design or even build an invisibility cloak.

This situation changed in 2006, when John Pendry and coworkes showed how the freedom of designing the permittivity and permeability of optical metamaterials[2] can be combined with a design recipe based on spatial transformations to steer light on arbitrary curved paths [1]. Today, this technique is called *transformation optics*, and Pendry illustrated it with the theoretical

---

[1] Tarn*kappe* refers to a mantle or cloak in the Nibelungenlied, but is often wrongly pictured as a cap or helmet.

[2] Metamaterials are artifical materials with properties defined by their designed structure rather than their constituents, providing properties beyond their constituents and even beyond what is found in nature.

design of an invisibility cloak: The effects of a purely mathematical spatial transformation that maps a point onto a finite sphere are recreated by a real metamaterial distribution in which the speed of light is modified such that light slows down when approaching the sphere and speeds up when traveling around the sphere. In other words, the cloak smoothly guides all incident light around this sphere as if nothing at all was there, rendering the sphere invisible. This process is possible because Maxwell's equations are *form-invariant* under spatial transformations [1, 2]. This means that applying a spatial transformation affects only the material parameters but not the general form of the equations.

Interestingly, Pendry and coworkers did not call their article "Designing an Invisibility Cloak" or something along these lines, but chose the rather unagitated title "Controlling Electromagnetic Fields". They chose well, however, since an object which we would intuitively associate with the phrase "invsibility cloak", that is, a device that makes macroscopic objects disappear in free space for all visible light and from all directions, is contradicting the laws of physics, even with transformation optics available: Broadband cloaking is impossible simply because relativity forbids any energy transport faster than the vacuum speed of light. Furthermore, macroscopic cloaking is made impossible by the finite absorption that inevitably comes along with the resonant metamaterials necessary even for cloaking within only a small frequency range [3]. So, unfortunately, mankind's dream of invisibility will for now remain a dream.

Despite this fundamental limitation, the initial theoretical work by John Pendry [1] (and also by Ulf Leonhardt on "Optical Conformal Mapping" [4]) ignited a plethora of research on transformation optics and invisibility cloaking [5–13] which also quickly spilled to areas of physics beyond electromagnetism (then called simply *transformation physics*). Examples are acoustics [14–16], elastomechanics [17–23], electric conduction [24–26], or magnetostatics [27–29]. Importantly, the fundamental restriction to narrowband and microscopic structures that relativity imposes on free-space cloaks based on transformation optics is not relevant anymore in most of these areas. For example, the energy-transport velocity in acoustics is of course also limited by the speed of light. But since acoustic waves propagate so much slower than light in any way, this limit plays practically no role in the design of an acoustic cloak. The same holds true for elastic waves, water waves, but also for non-wave phenomena such as heat conduction, electric conduction, or particle diffusion. There, "perfect" cloaking is indeed possible.

But, in agreement with the title of Pendry's initial paper, research on transformation physics and cloaking is actually not too much concerned with realizing mankind's dream of practical invisibility. It rather seeks to find ways of controlling arbitrary physical energy flows in a well-defined and precise manner. Invisibility cloaks and their counterparts in other fields of physics are just particularly demanding benchmark examples in this quest.

The main goal of this thesis is to realize such cloaking devices for heat conduction and light diffusion. These two phenomena—although completely different at first glance—have almost identical underlying differential equations and can thus be treated with similar tools at least in theory.

The results to be presented for transient cloaking in heat conduction are based on the theoretical work of Sebastien Guenneau and coworkers, who showed that the time-dependent heat-conduction equation is form-invariant under spatial transformations [30]. Together with large contrasts in the heat conductivity attainable from natural materials, heat conduction is a perfect candidate to adapt the methods of transformation optics for.

In contrast, the work on cloaking for light diffusion is based on the concept of neutral inclusions [31–34], which can be seen as heavily simplified versions of transformation-physics-based structures: For a constant gradient of the relevant physical observable (the photon density in light diffusion or the temperature in heat conduction), simple core-shell structures with homogeneous and isotropic material parameters can be made undetectable with respect to their homogeneous surrounding. While slightly less versatile and flexible, core-shell cloaks are a simple yet effective alternative to cloaks based on transformation physics.

Outline of this thesis

This thesis is divided into two major parts. Part I deals with cloaking in heat conduction, comprising chapters 2 and 3. I will begin with a general description of the fundamentals of transformation physics in chapter 2, starting with a very intuitive explanation not involving any mathematics. I will then present a mathematical description only as detailed as it is relevant for the topics covered in this thesis. In chapter 3, I will present the design, realization, and characterization of a passive thermal cloak based on transformation physics that makes a thermally isolated region in a thin copper plate invisible to heat flowing transiently through the plate.

Part II of this thesis comprises chapters 4 to 10 and deals with optical cloaking in light-diffusive media where randomly distributed scattering centers make light propagate on random, zig-zag-like paths. In chapter 4, I will describe how relativity prevents the dream of broadband and macroscopic invisibility cloaking to come true. I will then argue why one can overcome this barrier by utilizing diffuse light propagation. In chapter 5, I will give a theoretical overview of light transport in turbid media and how the light-diffusion equation can be derived and solved. Two key numerical methods for modeling diffusive light transport, namely finite-element calculations with COMSOL Multiphysics and Monte-Carlo-based photon raytracing will be presented in chapter 6. In chapter 7, I will describe how we realized and characterized various diffusive media in the context of this thesis. The majority of the experimental results on diffusive-light cloaking is then presented in chapter 8. I will describe the concept, design, and realization of core-shell cloaks for static light diffusion and will show experimental as well as accompanying numerical results for these simple yet impressive structures. Afterwards, I will show in chapter 9 that even though they work beautifully for static illumination, our core-shell cloaks fail once the illumination conditions become truly transient. I will furthermore show that this failure is a universal characteristic of any cloak for diffuse light. Finally, chapter 10 will describe inverted versions of our core-shell cloaks in an attempt to effectively demonstrate invisibility not only in transmission but also in reflection.

I will conclude this work in chapter 11 by summarizing and discussing the presented results, followed by a brief outlook on future challenges and prospects.

Part I

THERMAL CLOAKING

Chapter 2

2 FUNDAMENTALS OF TRANSFORMATION PHYSICS

Picture of a distorted city used later for intuitively explaining transformation physics

The scope of this thesis is the realization of cloaking devices for transport of heat and diffuse light. In this first chapter, I will describe the principles of transformation physics as the most prominent basis for such cloaks. Later in this work, we will make use of transformation physics for designing a cloak for transient heat flow.

2.1 An intuitive view on transformation physics

The ultimate goal of transformation physics [35] is to gain complete control over physical energy flows. Such an energy flow can be a wave such as light, sound, or vibrational waves or any current carrying energy, such as electric, particle, or heat current. Controlling an energy flow means, for example, to steer, accelerate, divide or stop it at will. One particularly fascinating as well as demanding example of controlling an energy flow is (optical) invisibility cloaking: a device (which I from now on will simply call a *cloak*) is constructed such that it completely suppresses an object's influence on the flow of light in the surrounding medium. Precisely, the cloak guides any incoming light around the object. It does this guiding in such a way that the light emerges behind as if the object had never been there in the first place, rendering it invisible from the outside world.

Invisibility cloaking as well as the control of energy flows in general poses a so-called *inverse problem*: one searches a structure that gives rise to a specific desired energy flow. While the solution of the corresponding *forward problem* (to calculate the energy flow created by a known structure) is generally rather straightforward, inverse problems are usually difficult or even impossible to solve. For the case of invisibility cloaking, which, as an idea, is probably as old as mankind itself, not a single solution existed for the longest time.

However, in 2006, John Pendry and Ulf Leonhardt simultaneously published a recipe [1, 4] that solves this inverse problem of invisibility cloaking. This recipe is now called transformation optics (or transformation physics, for the more general case of an arbitrary energy flow). Although the original publications are quite mathematical, the underlying principles can be understood easily.

Let's for a moment replace any specific energy flow (and with it all equations needed to describe it) by the abstract concept of cars driving (with constant speed) on a rectangular grid of streets in a city[1] as shown in Figure 2.1. We now take aerial photographs of this city and distort them in an image manipulation software like Photoshop, for example such that a circular hole opens up in the center (see Figure 2.2). This is done by applying a spatial (coordinate) transformation[2] to the image pixels, in our case the

---

[1] We used this cars metaphor to explain invisibility cloaking for the first time in Ref. [36]. Here, I loosely adapted the line of argumentation.

[2] These transformations are often referred to as "coordinate transformations" in the literature. Unlike usual coordinate transformations which serve to describe the exact same

Figure 2.1: For an intuitive understanding of invisibility cloaking, physical energy flows (e.g., light, sound or heat) can be considered as cars driving with constant speed on a city's rectangular grid of streets. Reproduced from Ref. 36.

linear transformation (in polar coordinates)

$$\begin{aligned} r &\to r'(r,\varphi) = R_1 + \frac{R_2 - R_1}{R_2} r \qquad (0 < r < R_2) \\ \varphi &\to \varphi'(r,\varphi) = \varphi \, , \end{aligned} \tag{2.1}$$

which "squeezes" all points inside a circle with radius R_2 into the region between R_1 and R_2 while leaving the surrounding outside R_2 untouched [1]. The result in Figure 2.2 looks quite odd: the streets bend around the hole and some seem stretched, others compressed. Applying the transformation to a whole movie, we would also see the cars driving faster on the stretched streets and slower on the compressed streets. Most importantly, in the distorted version of our city, no car will ever reach the center, while there will be no change visible from outside of the transformed area: Cars will still enter and emerge from the city just as before. This means that anything in the white hole in the center is hidden or *cloaked* from detection by the outside world.

---

physical situation merely in a different coordinate system, they rather describe a fictitious deformation of space here. I will thus call them "spatial transformations" in this work.

Figure 2.2: After a (fictitious) distortion of the street grid, the cars avoid the circular hole in the city center by driving with varying speeds on curved paths. From the outside, however, no change is visible. Thus, the hole is concealed or *cloaked*. Transformation physics means to map all effects of such a fictitious spatial transformation (the distribution of the cars' speeds and directions) onto a real material distribution. Reproduced from Ref. 36.

So far, this idea of a cloaked hole in a distorted city is nothing but a nice trick to play on the computer and has nothing to do with reality: We cannot simply transform the space around us. So how can we then translate this principle to the real world? Conceptually, this step is intriguingly simple: we only need to impose speed limits in a real city that exactly match the virtual car speeds we observed before. Assuming that the cars always take the shortest possible route to reach their destination (just as for example light does according to Fermat's principle), they would automatically follow exactly the same curved paths[3] as prescribed by the curved streets in Figure 2.2.

In short, by mapping the fictitious spatial transformation onto real parameters (the speed limits), we translate its fictitious effects to real effects. In our

---

[3] To be precise, at this point we conceptually need to replace the *discrete* model of a street grid by a *homogeneous* model (for example an open area), as the street grid would not allow for the cars to follow curved paths. Another way to think of this transition is to imagine infinitesimally small city blocks which would allow for arbitrary routes for the cars to follow.

example case of distorting a street grid, we thereby create an undetectable hole in the city center. Reverting our abstract concept of cars to real energy flows, we can now understand the fundamental concept of transformation physics: we fictitiously distort space with a spatial transformation and then map all the resulting effects onto a material-parameter distribution that can be realized by a specific structure. This structure will then mold the flow of light, sound, heat, or any other energy flow in exactly the way prescribed by the transformation.

So how exactly can we map a spatial transformation onto material parameters? To explain this mapping, we need to take a look at transformation physics that is a bit more mathematical.

2.2 MATHEMATICAL FORMULATION

To explain some mathematical details of transformation physics, let's consider the example of a generalized Laplace equation:

$$\vec{\nabla}\cdot\left(p\vec{\nabla}V(\vec{r})\right) = 0\,. \tag{2.2}$$

Here, $V(\vec{r})$ represents a physical potential and p a homogeneous scalar material parameter. Many static physical phenomena can be described with this equation by just exchanging V and p with the corresponding quantities. Examples are given in Table 2.1. Upon applying a general spatial transformation $\vec{r} \rightarrow \vec{r}\,' = f(\vec{r})$, we can use the operator identiy [37]

$$\vec{\nabla}\cdot\vec{\nabla} = \det\left(\overleftrightarrow{J}(\vec{r})\right)\vec{\nabla}'\cdot\left(\overleftrightarrow{J}(\vec{r})\,\overleftrightarrow{J}^{\mathrm{T}}(\vec{r})\frac{1}{\det\overleftrightarrow{J}(\vec{r})}\vec{\nabla}'\right), \tag{2.3}$$

where $\overleftrightarrow{J}(\vec{r})$ is the Jacobian of the transformation ($J_{ij} = \partial r'_i/\partial r_j$). The Laplace equation then retains its general form and we get

$$\vec{\nabla}'\cdot\left(\overleftrightarrow{p}'(\vec{r})\;\vec{\nabla}'V(\vec{r})\right) = 0\,, \tag{2.4}$$

where all effects of the transformation are absorbed in the transformed material parameter

$$p \rightarrow \overleftrightarrow{p}'(\vec{r}) = \overleftrightarrow{J}(\vec{r})\;p\;\overleftrightarrow{J}^{\mathrm{T}}(\vec{r})\frac{1}{\det\overleftrightarrow{J}(\vec{r})}\,. \tag{2.5}$$

Table 2.1: Differential equations derived from conservation laws in electromagnetism and thermodynamics (considering the static case and isotropic materials). All equations are mathematically equivalent; with the electric permittivity ε and the electrostatic potential $\Phi(\vec{r})$, the magnetic permeability μ and the magnetostatic potential $\Psi(\vec{r})$, the particle diffusivity D and the particle concentration $n(\vec{r})$, the heat conductivity κ and the temperature $T(\vec{r})$, and the electric conductivity σ and the electrostatic potential $\Phi(\vec{r})$. Adapted from [35]

ELECTROMAGNETISM	THERMODYNAMICS
electrostatics $\vec{\nabla} \cdot \big(\varepsilon \vec{\nabla} \Phi(\vec{r})\big) = 0$	particle diffusion $\vec{\nabla} \cdot \big(D \vec{\nabla} n(\vec{r})\big) = 0$
magnetostatics $\vec{\nabla} \cdot \big(\mu \vec{\nabla} \Psi(\vec{r})\big) = 0$	heat conduction $\vec{\nabla} \cdot \big(\kappa \vec{\nabla} T(\vec{r})\big) = 0$
	electric conduction $\vec{\nabla} \cdot \big(\sigma \vec{\nabla} \Phi(\vec{r})\big) = 0$

(Note that the first term $\det \overleftrightarrow{J}(\vec{r})$ from the right-hand side of Equation 2.3 does not appear here due to the lack of a second term in Equation 2.2.) This *form-invariance* of the differential equation underlying a physical phenomenon is the most important prerequisite for transformation physics. If the equation is *not* form-invariant, the effects of a spatial transformation cannot be implemented by a material-parameter distribution. Beyond the phenomena described by the Laplace equation shown above, this form-invariance holds for many time-dependent differential equations as well. Examples are Maxwell's equations for propagation of light [1] or the time-dependent heat-conduction equation [30] (see chapter 3). However, we will later also encounter equations that are not form-invariant and thus prevent us from applying the principles of transformation physics (see chapter 9).

By absorbing the effects of the transformation, the material parameter from above transformed from a homogeneous isotropic scalar p to an inhomogeneous and anisotropic tensor $\overleftrightarrow{p}'(\vec{r})$. This change is also intuitively clear from the distorted street grid in Figure 2.2, where a car's speed is dependent on its position as well as on its direction: Cars driving radially towards the hole in the city center are slower, cars driving azimuthally around the hole faster than in the surrounding. The resulting tensors have been calculated for various examples of spatial transformations [38]. The transformations are generally not unique one can achieve the same result with different transformations. This flexibility in the choice of transformation helps to attain material-parameter distributions that are also experimentally feasible.

Realizing such inhomogeneous as well as anisotropic material parameters with a specific structure poses yet another inverse problem that is not easy to solve. Fortunately, the available literature on metamaterials[4] provides a huge library of material realizations to choose from [38–41]. This abundance of choices greatly simplifies the realization of structures designed by transformation physics.

There has been a tremendous interest in invisibility cloaking based on transformation physics in the scientific community over the last years. Besides works published on optical cloaks [5, 6, 10], significant progress has been made on cloaking of acoustic waves [14, 15, 42–44], elasto-mechanical waves [17–22, 45, 46], water waves [43, 47], and static electric currents [24, 25, 48]. Another intensely investigated topic is the cloaking of heat flow. In the next chapter, I will discuss the techniques involved and present our experimental realization of a thermal cloak for transient heat flux.

2.3 REDUCED PARAMETER CONTRAST WITH THE CARPET CLOAK

Transformations such as Equation 2.1 that map a point onto a circle or sphere lead to infinitely high contrasts in the necessary material parameters: It takes no time for any energy flow to cross a singular point, and thus it has to take no time either to cross the finite-sized circle resulting from the spatial transformation. This problem can be softened a bit by starting from a small circle instead of a point [49], which removes the singularity which otherwise arises, but even then the required contrasts are huge and the structures are still highly anisotropic. This is a problem especially for optics, where, on the one hand, naturally attainable contrasts in the refractive index are rather small and, on the other hand, resonant structures that allow for larger contrasts introduce significant amounts of absorption [3]. As we shall see in section 4.1, transformation optics is further stymied by the fundamental upper speed limit (the vacuum speed of light) that relativity sets for any energy transport. This so-called *relativity problem* prevents broadband and macroscopic free-space cloaks in optics altogether.

---

[4] Metamaterials are artificial materials with properties defined by their structure rather than their constituents. They can attain material parameters with values beyond the

Figure 2.3: Illustration of a carpet cloak using the same cars methaphor as before. (a) The red line resembles a surface cutting the street grid at an angle of 45°. Incoming cars are "reflected" by this surface. (b) A deformed reflecting surface can be cloaked by a conformal transformation above it. The speed of the cars is adapted (via compression and elongation of the streets) to compensate for the change in the distance they travel due to the deformed reflecting surface. The conformal transformation also preserves right angles between the streets, resulting in locally isotropic material parameters.

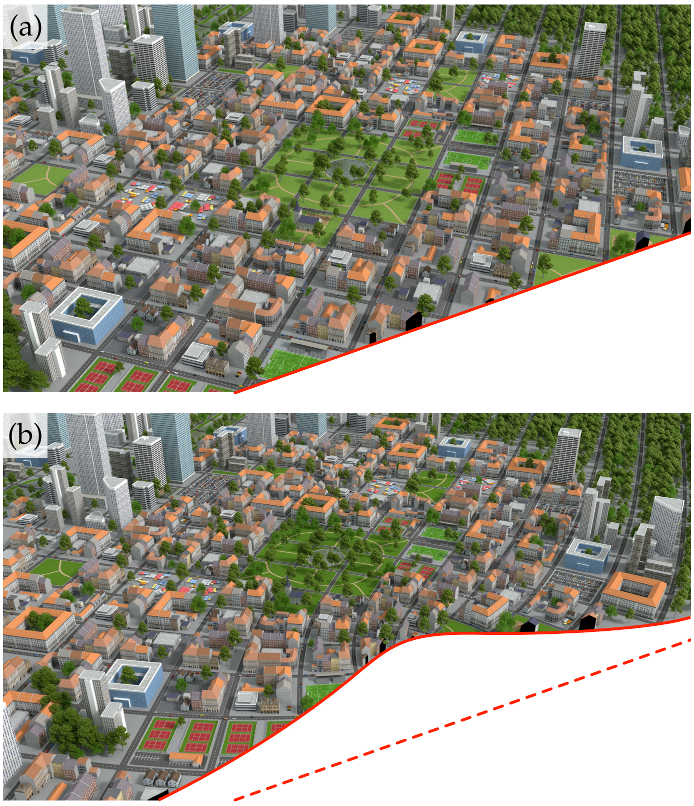

In 2008, Jensen Li and John Pendry introduced a new strategy to get around such material contrasts and anisotropies [11]. They proposed the so-called *carpet cloak* based on a half-space geometry (as opposed to free-space cloaks) with a reflecting boundary such as a mirror. An object hidden under the boundary (creating a bump in the mirror that would distort its reflections) can be cloaked by adding a suitable metamaterial distribution on top of the deformed boundary. In other words, a carpet cloak makes a curved reflective line (or plane) appear as a straight reflective line. Figure 2.3 illustrates this concept in the context of our deformed street grids. The crucial aspect to note is that the deformation is a *conformal map*, leading to low contrasts in the material parameters (the streets are compressed or stressed only moderately) as well as preserved angles and thus locally isotropic parameters (the deformed streets still cross at an angle of 90°). For optics, this means that a carpet cloak can be realized by a relatively

---

constituent parameters and even beyond what can be found in nature.

Figure 2.4: Illustration of a transformation-physics-based concentrator, again in the picture of cars driving on a street grid. The compressed central part of the street grid results in a higher density of cars. This compressed region is compensated for by a stretched region around it.

simple refractive-index distribution with values attainable from non-resonant materials (for example polymers). This distribution bends incoming light so that it always hits the reflecting surface under an angle of 45° and also makes up for any change in the light's propagation length. A number of beautiful realizations of optical carpet cloaks have been published, with operational wavelengths reaching up to the long-wavelength part of the visible [12, 13, 50, 51]. Furthermore, carpet cloaks have been successfully realized in acoustics [16, 52].

2.4 TRANSFORMATION PHYSICS BEYOND CLOAKING

Transformation physics can of course also be used for purposes different than invisibility cloaking. One example is a *concentrator* which—in a way opposite to a cloak—spatially concentrates a certain observable. Figure 2.4 depicts an illustration of such a concentrator, again using the picture of cars driving on a street grid. Concentrators have for example been published on in electromagnetism [53, 54], heat conduction [55, 56], and electric conduction [57].

But also other devices such as field rotators [58, 59] or bent waveguides [60, 61] have been investigated in the context of transformation physics. Conceptually, any objective is reasonable as long as one can come up with a corresponding spatial transformation.

2.5 Cloaking beyond transformation physics

Transformation physics is probably the most general and most versatile method of molding physical energy flows in a controlled way, but it is not the only one. In the context of cloaking, a technique usually called *scattering cancellation*, often achieved by topological optimization, provides another way of suppressing an object's interaction with an energy flow. One example is a macroscopic acoustic cloak that uniaxially reduces an object's scattering cross-section by 90 % for its operation wavelength [62]. A similar cloak has recently been investigated theoretically in microwave optics [63]

For the special case of *static* or *quasi-static* cloaking, the concept of *neutral inclusions* provides another simple yet effective alternative to transformation physics. For a constant gradient $\vec{\nabla} V(\vec{r})$ of the generalized potential introduced in the mathematical formulation of transformation physics above, simple core-shell structures can be made undetectable with respect to their homogeneous surroundings. Compared to transformation physics, they come with the big advantage of having homogeneous and isotropic material parameters as well as being structurally less complex. Interestingly, neutral inclusions have been discussed theoretically 50 years before the introduction of transformation optics in 2006 [31, 32]. They have been used for cloaking in optics (for subwavelength particles where electromagnetic waves can be considered quasi-static) [34], static mechanical deformations [64], static electric conduction [24, 26, 65], magnetostatics [27–29], and also heat conduction [66–69].

Neutral inclusions and core-shell cloaking are also the basis for our experiments on diffusive-light cloaking. A detailed description of these concepts will thus be given in Part II of this thesis.

A recent review article [70] provides a good overview on *optical* cloaking also beyond transformation optics. It also takes a look on *active* cloaking where some kind of energy source is included in the cloak, an approach that is not covered in this thesis. Such active cloaks could at least partially overcome some of the fundamental limitations passive cloaks have to face.

Chapter 3

3 A PASSIVE THERMAL CLOAK

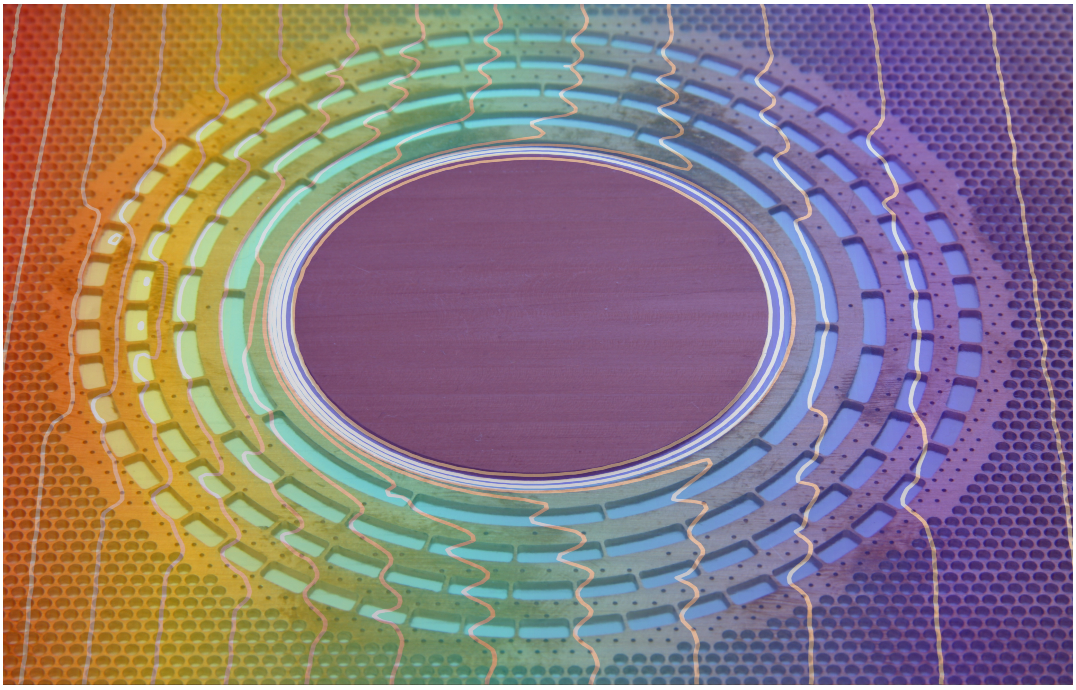

Photograph of a thermal cloak with a measurement result overlayed on a false-color scale

The time-dependent heat-conduction equation is form-invariant under spatial transformations, making it possible to create cloaking devices for the flow of heat. Here, I will describe a recipe to design such a cloak, building upon existing theoretical work. This design features a macroscopic composite metamaterial structure to realize inhomogeneous and anisotropic heat conductivities. Excellent cloaking of transient heat flow is demonstrated. The main findings of this chapter have already been published in Ref. 71.

3.1 FORM-INVARIANCE OF THE HEAT-CONDUCTION EQUATION

In 2012, Guenneau and co-workers—adapting tools of transformation optics—showed mathematically that the time-dependent heat-conduction equation,

$$\vec{\nabla} \cdot \left(\kappa \vec{\nabla} T(\vec{r}, t)\right) - c\rho \frac{\partial T(\vec{r}, t)}{\partial t} = 0 \,, \tag{3.1}$$

is form-invariant under spatial transformations [30]. Here, $T(\vec{r}, t)$ is the temperature in K, κ the heat conductivity in $\mathrm{W/(K\,m)}$, c the specific heat capacity in $\mathrm{J/(kg\,K)}$, and ρ the density in $\mathrm{kg/m^3}$. All three material parameters κ, c, and ρ are considered to be spatially homogeneous. Considering transformation optics as the original example of transformation physics, the form-invariance of the heat-conduction equation is not immediately obvious because a *parabolic* differential equation as the one above is clearly different from the *hyperbolic* differential equations governing wave propagation. In consequence, phenomena like reflections, geometric shadows, scattering, or interference that are common for all kinds of wave propagation are completely absent in heat conduction.

For the case of *static* electric conduction (which, for metals, is proportional to heat conduction according to the Wiedemann-Franz law), the so-called non-uniqueness of the Calderón tomography problem [72] was proved theoretically already in 1984 [73]: it is impossible to determine the exact conductivity distribution of a certain region by measuring the resistance between pairs of points outside that region.[1] This non-uniqueness is nothing else than what we today call cloaking (or more generally transformation physics) and corresponding (static) experiments have been published both for electric [24, 57] and for heat conduction [75].

Just as the general concept of transformation physics, transformation thermodynamics[2] is easy to understand in an intuitive way. Consider a homogeneous grid of resistors as shown in panel (a) of Figure 3.1. The resistors can be seen as *Ohmic* or *thermal*, again according to the Wiedemann-Franz law. We assume that all resistors are equal and that the resistance

---

[1] The Calderón tomography problem received new attention lately after further theoretical studies by Greenleaf and co-workers [74].

[2] The term *transformation thermodynamics* was coined in the first publication on controlling heat flux with the tools of transformation optics [30]. I will use this term with the same context in mind, even though thermodynamics might not always be associated with mere heat conduction.

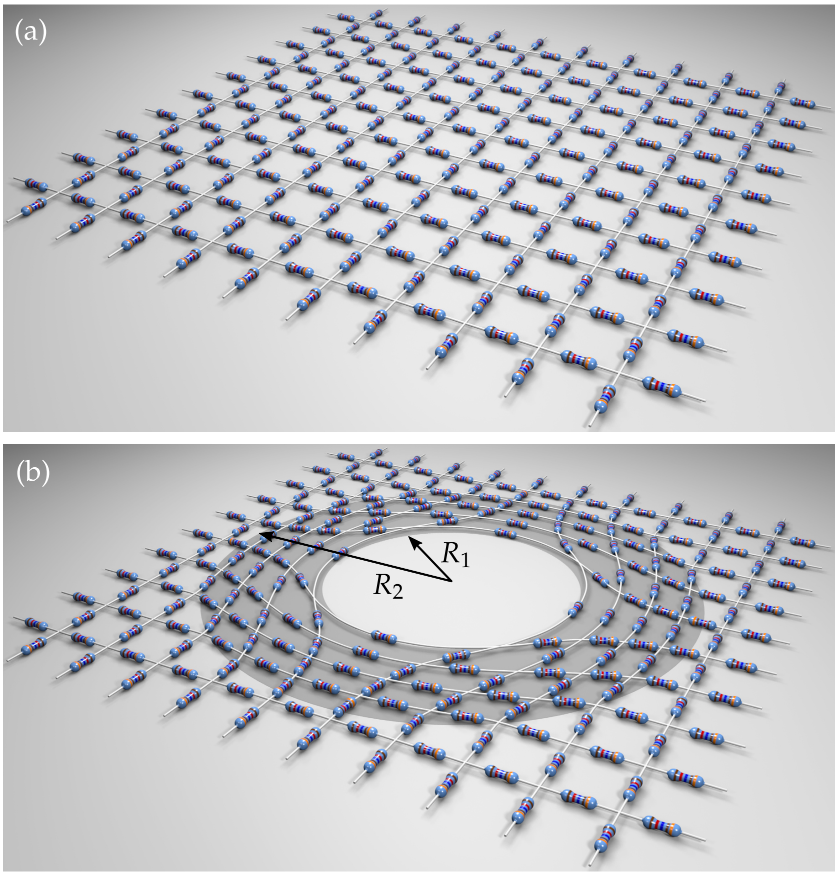

Figure 3.1: A square lattice of electric or thermal resistors (a) is deformed by a spatial transformation (see Equation 2.1) between R_1 and R_2, leading to the rearranged anisotropic and inhomogeneous resistor distribution in (b) that opens up an empty space in the center. Assuming that only the distribution of resistors is modified, both cases are indistinguishable from the outside. This is the essential idea of *transformation thermodynamics*. Reproduced from Ref. 71.

of the wires connecting them can be neglected. If we deform this resistor network with the spatial transformation we used before (Equation 2.1), the result is merely a rearranged version of the resistors while their connections remain unchanged (see panel (b) of Figure 3.1). Thus, any conductivity measurement between two points in the network will yield the same result as in the untransformed case. The central hole opened by the transformation is fully cloaked.

This very simple image of resistor networks gets a lot more complex once we think about homogeneous materials instead of a discrete grid.[3] Nonetheless, important qualitative features of the transformed material properties are already visible from the rearranged distribution of resistors in Figure 3.1 (b). Along the radial direction towards the center of the hole, many resistors are connected *serially*, leading to a high effective resistance or low effective conductivity. In contrast, many resistors are connected *parallelly* in the azimuthal direction (around the hole). Thus, a thermal (electric) cloak has to have a heat conductivity (electric conductivity) that is low in the radial and high in the azimuthal direction. Intuitively, the low radial conductivity prevents heat (electric current) from entering the cloaked hole while the high azimuthal conductivity compensates for the geometric detour around the hole. We have already encountered this kind of anisotropy in chapter 2 in our more general view on transformation physics.

In the following sections, I will explain how to realize such anisotropic heat conductivities in a thermal cloak.

3.2 Design recipe for a transient thermal cloak

Applying the transformation given in Equation 2.1 to the time-dependent heat-conduction equation (3.1), we obtain the following transformed equation [30]:

$$\vec{\nabla}' \cdot \left(\kappa \overleftrightarrow{J}(\vec{r})\, \overleftrightarrow{J}^{\mathrm{T}}(\vec{r}) \frac{1}{\det \overleftrightarrow{J}(\vec{r})} \vec{\nabla}' T(\vec{r},t) \right) - \frac{c\rho}{\det \overleftrightarrow{J}(\vec{r})} \frac{\partial T(\vec{r},t)}{\partial t} = 0 \,, \tag{3.2}$$

where $\vec{\nabla}'$ indicates spatial derivatives with respect to the transformed coordinate system. Although the effects of the transformation can easily be cast into the material parameters κ and $c\rho$, the problem of *singularities*, which I have already addressed briefly in chapter 2, remains: Because the spatial transformation maps a single virtual point onto a finite area in reality, the azimuthal heat conductivity has to be infinitely large at the cloak's inner boundary ($r = R_1$), whereas both the radial heat conductivity and the (scalar) specific heat capacity become strictly zero at this boundary. Physically, this means that heat takes an infinite amount of time to cross the central region ($r < R_1$) radially, but no time at all to go around this region azimuthally.

---

[3] The direct transformation of a discrete lattice is also a tool to design cloaks that has emerged recently [76]. Compared to transformation physics, it gets rid of the second inverse problem of mapping a material-property distribution onto a microstructure.

Obviously, an infinitely large heat conductivity is impossible to realize. Also a heat conductivity of exactly zero seems to be out of experimental reach.[4] Furthermore, controlling both the heat conductivity κ and the specific heat $c\rho$ independently from each other (as the equation above demands), is experimentally challenging at best. To provide a more feasible approach, Guenneau and co-workers also proposed a solution based on a *reduced* heat-conduction equation, where most of the aforementioned problems vanish. Following the derivation in Ref. 30, we obtain the radial component κ_r and the azimuthal component κ_θ of the reduced anisotropic heat conductivity tensor $\overleftrightarrow{\kappa}$:

$$\begin{aligned}\kappa_r(r,\varphi) &= \kappa_0 \left(\frac{R_2}{R_2 - R_1}\right)^2 \left(\frac{r - R_1}{r}\right)^2 \leq \kappa_0 \\ \kappa_\theta(r,\varphi) &= \kappa_0 \left(\frac{R_2}{R_2 - R_1}\right)^2 > \kappa_0 \,.\end{aligned} \tag{3.3}$$

Here, κ_0 is the conductivity of the background medium. We note that for this reduced set of parameters, the azimuthal component of the heat conductivity is constant throughout the cloak, while the radial component smoothly varies from zero (for $r = R_1$) to the background heat conductivity κ_0 (for $r = R_2$). Furthermore, the product $c\rho$ of density and specific heat capacity is assumed to be spatially constant everywhere.

While the parameters above have the obvious advantage of avoiding singularities, Guenneau and co-workers noted that the overall effective heat conductivity of the cloak now differs from that of the surrounding. They compared this difference to an impedance mismatch in optics, which would give rise to reflections at the cloak's boundary. As there are no waves in heat conduction, *impedance* itself is a meaningless term here. Still, mismatched effective heat conductivities would lead to impaired cloaking performance. In our experimental realization, however, we were able to avoid this mismatch by carefully adjusting the surrounding accordingly, as will become apparant later in this chapter.

THE NEXT STEP on our journey to a thermal cloak was to realize the anisotropic heat conductivity given in Equation 3.3. Generally, anisotropic material properties can be achieved by laminate structures made up of at least two different constituents [38, 39]. An example of a simple laminate

---

[4] Vacuum does has $\kappa_{\text{vac}} = 0$ when only heat conduction is concerned, but is cumbersome to integrate in user-friendly experimental setups.

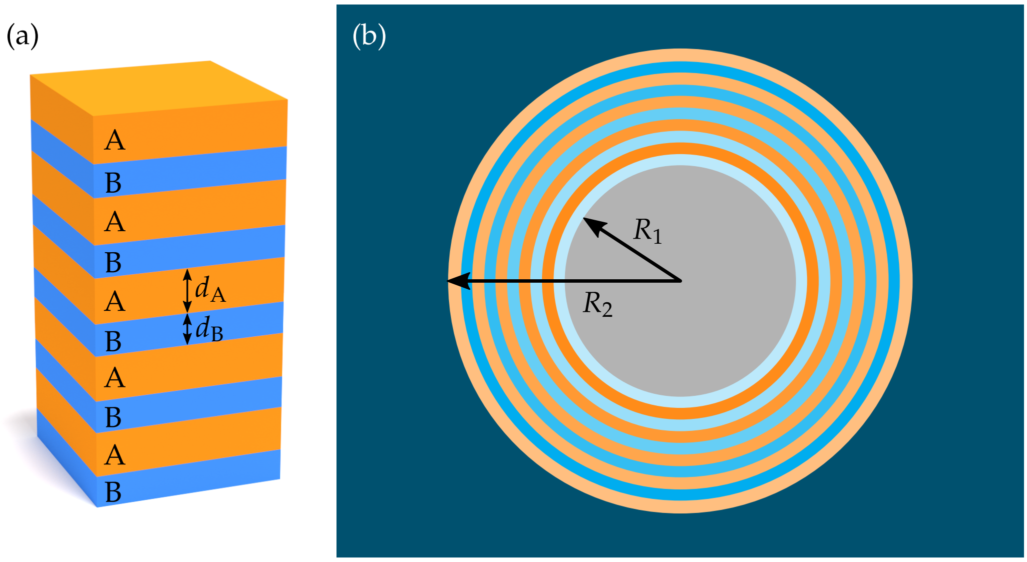

Figure 3.2: (a) Scheme of an anisotropic metamaterial made up of a laminate stack of two different constituents A and B. (b) Realization of a thermal cloak with a laminate ring structure that creates anisotropic heat flow. Radially, heat is repeatedly blocked by the blue rings with low heat conductivities, which isolates the gray central region. In contrast, the orange rings have a high heat conductivity to allow for fast azimuthal heat propagation, compensating for the detour around the cloaked region. As indicated by the changing color saturation, the heat conductivity varies slightly for each ring according to equations 3.3 and 3.4. Numerical values are found in Table 3.1.

is shown in Figure 3.2 (a). A large contrast in the constituent parameters means a large possible anisotropy in the resulting effective parameters. In our case, we first discretized the cloak area ($R_1 \leq r \leq R_2$) into 5 equally thick rings and thereby approximated the smoothly varying functions κ_r and κ_θ by sets of *piecewise homogeneous* (but still anisotropic) functions. Each of these 5 anisotropic rings we then approximated by one pair of isotropic rings described by the following homogenization formulae[5] given in Ref. [30]:

$$\frac{d_\mathrm{A} + d_\mathrm{B}}{\kappa_r} = \frac{d_\mathrm{A}}{\kappa_\mathrm{A}} + \frac{d_\mathrm{B}}{\kappa_\mathrm{B}} \,, \quad \kappa_\theta = \frac{d_\mathrm{A}\kappa_\mathrm{A} + d_\mathrm{B}\kappa_\mathrm{B}}{d_\mathrm{A} + d_\mathrm{B}} \,, \quad c\rho = \frac{d_\mathrm{A} c_\mathrm{A} \rho_\mathrm{A} + d_\mathrm{B} c_\mathrm{B} \rho_\mathrm{B}}{d_\mathrm{A} + d_\mathrm{B}} \,. \tag{3.4}$$

In our design, the layer thicknesses d_A and d_B were the same. This left us with a cloak made up of 10 rings with alternatingly high and low heat

---

[5] The given formulae are strictly valid for planar laminates as in Figure 3.2 (a) only. However, for not too small radii, utilizing them for our ring structure is a good approximation.

Table 3.1: Material parameters for the discretized thermal cloak. The index i runs over all rings starting from the center.

i	f_i	$c_i\rho_i$ MJ/(K m^3)	κ_i W/(K m)	κ_r W/(K m)	κ_θ W/(K m)
1	0.0000	1.42	0.15	0.30	197.08
2	1.0000	3.43	394.00		
3	0.0097	1.49	3.97	7.86	197.08
4	0.9903	3.50	390.18		
5	0.0282	1.71	11.26	21.87	197.08
6	0.9718	3.61	382.89		
7	0.0479	1.90	19.02	36.20	197.08
8	0.9521	3.73	375.13		
9	0.0667	2.08	26.42	49.30	197.08
10	0.9333	3.83	367.73		

conductivity as shown in Figure 3.2 (b) (we chose $R_2 = 2R_1$). It is easy to understand how such a laminate structure creates an effectively anisotropic heat conductivity: following the radial direction towards the cloak's centre, heat flow is repeatedly "blocked" by the blue rings with low heat conductivities. In contrast, along the azimuthal direction around the centre, heat can easily follow the continuous orange rings of high heat conductivity. This is exactly what we wanted: the heat is slowed down when flowing towards the protected central area but speeds up around that area to compensate for the geometrical detour it has to take.

FINALLY, WE HAD TO IMPLEMENT OUR DESIGN by an actual realizable structure. Instead of finding 11 different materials (one for each ring plus one for the surrounding) with just the right heat conductivity, we chose to make each ring a composite of two materials, in our case copper and the silicone polydimethylsiloxane (PDMS). Their heat conductivities are $\kappa_{\mathrm{Cu}} = 394\,\mathrm{W/(Km)}$ and $\kappa_{\mathrm{PDMS}} = 0.15\,\mathrm{W/(Km)}$, with a contrast between them of more than three orders of magnitude. By drilling holes into a copper plate and filling them with PDMS, the desired heat conductivity for each ring was obtained via the metal filling fraction f_i: $\kappa_i = f_i\,\kappa_{\mathrm{Cu}} + (1 - f_i)\,\kappa_{\mathrm{PDMS}}$. The product $c\rho$, which should be constant according to the reduced

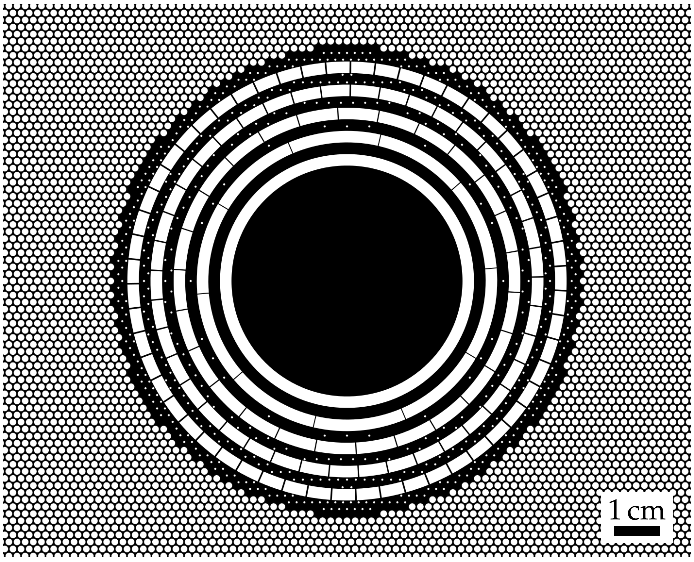

Figure 3.3: Blueprint of our thermal cloak implementing the design shown in Figure 3.2 (b). The black regions are copper, the white ones are PDMS, with heat conductivities of $\kappa_{\mathrm{Cu}} = 394.0\,\mathrm{W/(K\,m)}$ and $\kappa_{\mathrm{PDMS}} = 0.15\,\mathrm{W/(K\,m)}$, respectively. Each ring's heat conductivity is tailored via the metal filling fraction f_i (also see Table 3.1). Reproduced from Ref. 71

heat-conduction equation, could not be controlled independently with our approach. However, as the bulk values of copper ($c\rho = 3.4\,\mathrm{MJ/(Km^3)}$) and PDMS ($c\rho = 1.4\,\mathrm{MJ/(Km^3)}$) are not too different, the local specific heat didn't vary too much either in the cloak area. The numerical values of f_i, κ_i, $c_i\rho_i$, and the resulting radial and azimuthal heat conductivities are summarized in Table 3.1. To compensate for the non-constant product $c\rho$ and for the aforementioned heat-conductivity mismatch between the cloak and the surrounding, we chose the background heat conductivity to be $\kappa_0 = 85\,\mathrm{W/(Km)}$, based on a numerical optimzation of the cloaking performance.[6] (From Equation 3.4 alone, assuming $R_2 = 2R_1$ and the bulk heat conductivities of copper and PDMS as given above, we initially got $\kappa_0 = 49.27\,\mathrm{W/(K\,m)}$.)

Furthermore, we chose the dimensions of the cloak to be $R_1 = 2.5\,\mathrm{cm}$ and $R_2 = 5\,\mathrm{cm}$, embedded in a homogeneous surrounding plate $15\,\mathrm{cm} \times 10.7\,\mathrm{cm} \times 0.2\,\mathrm{cm}$ in size. The plate's thickness of 2 mm was chosen such that the heat conduction in its volume material dominated over (convective and radiative) losses occuring at its surfaces, while keeping its total heat capacity small compared to that of the temperature baths used in the experiment. Filling the holes in the copper plate with solid PDMS also helped to contain convective losses compared to having only air in the holes.

---

[6] We performed numerical calculations with COMSOL Multiphysics. Details of the numerical implementation are described in section 3.3.

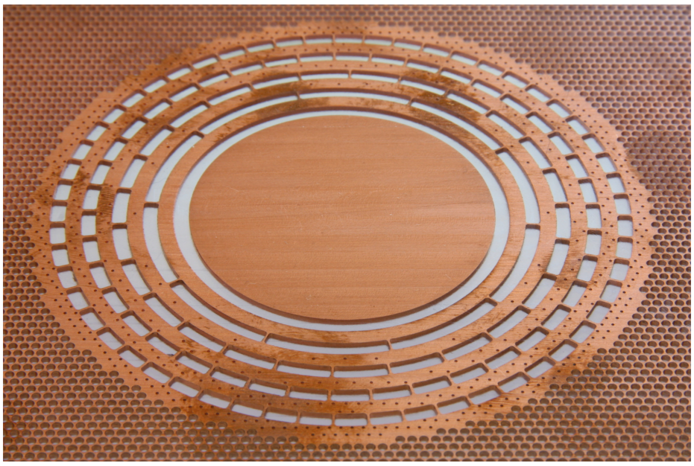

Figure 3.4: Photograph of the fabricated thermal cloak, comprising a composite of copper and the silicone PDMS. Note that the central part is held in place only by the first pure-PDMS ring. Reproduced from Ref. 71

Figure 3.3 shows the blueprint of our cloak. Black regions are solid copper, white regions are drilled holes filled with PDMS. For the high-conductivity rings, holes with a diameter of 0.5 mm were drilled in a hexagonal lattice to achieve the desired metal filling fraction. For the very low filling fractions of the low-conductivity rings, however, we used tiny metal bridges instead of holes. This effectively makes heat conduction in these rings anisotropic. However, we could not detect any negative effects of this anisotropy in our experiments.

To compensate for all simplifications we made and for unavoidable experimental imperfections (like, for example, convective and radiative heat losses), we experimentally optimized the surrounding's metal filling fraction by adjusting the lattice constant of the hexagonal lattice of 1.5 mm holes drilled into the copper plate. In the end, we chose a lattice constant of 1.76 mm, corresponding to a metal filling fraction of $f_0 = 0.342$.

After CNC-machining the pattern into the copper plate, the plate's sides were bent to a 90° angle and the plate was inserted upside-down into a Teflon cast with liquid PDMS of the right volume to fill all the holes. The bent sides later provided contact to the heat baths, see Figure 3.5. After polymerization of the PDMS, the cast was removed and a thin PDMS layer with a thickness of about 100 µm remained on both sides of the plate. Figure 3.4 shows a photograph of the fabricated sample. Besides the cloak, we also built a reference sample consisting of the central massive copper disc embedded in the same perforated surrounding as for the cloak, but isolated only by the first pure-PDMS ring in order to maximize its heat-flow disturbance. We call this sample the "obstacle".

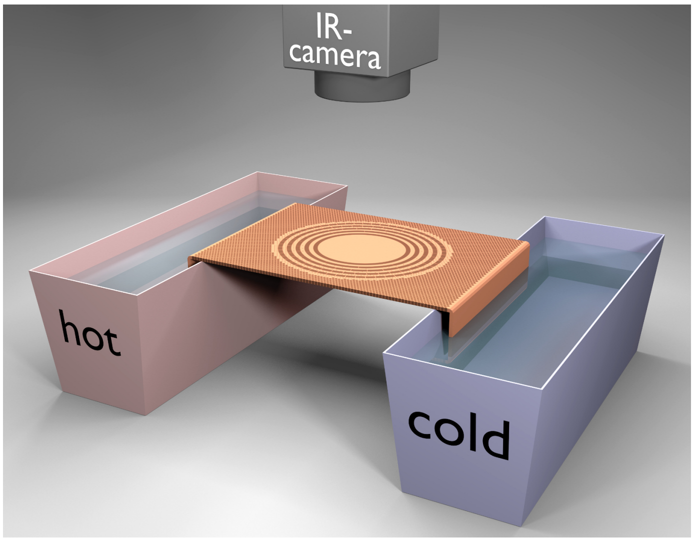

Figure 3.5: Experimental setup for the cloak characterization. Two water tanks, filled with boiling and room-temperature water, respectively, act as heat baths for the sample ends. The thin PDMS layer on the sample surface results in a homogeneous emissivity everywhere and enables temperature-profile monitoring with an infrared heat camera. Reproduced from Ref. 71

3.3 Experimental and numerical results

To characterize and evaluate our thermal cloak, we needed to expose the samples to a transient heat flow and monitor their temperature distribution over time. The experimental setup for this characterization is illustrated in Figure 3.5.

At the start of each measurement, that is, at $t = 0$, we immersed the sample sides into two tanks filled with boiling and room-temperature water, respectively. The water in each tank had a heat capacity more than 30 times higher than that of the whole sample. We could thus regard the tanks as heat baths with a constant temperature for the duration of our experiments. Since the complete sample was at room temperature at $t = 0$, the immersion in the hot bath resulted in a sudden increase in temperature on one side of the sample, thus initiating heat flow along the sample with a very steep leading edge. I will elaborate a bit more on the criteria for a truly transient experiment later in this chapter.

We measured the transient heat flow through the sample by monitoring the spatial temperature distribution over time with an infrared heat camera[7]. Here, a homogeneous emissivity close to 100 % of the sample surface was necessary across the detection spectrum of the heat camera (usually 7–14 µm). A low emissivity corresponds to a high reflectivity (true for blank

---

[7] FLIR Systems A320

copper surfaces, for example) and would have caused reflections of the environment, whereas an inhomogeneous emissivity would have resulted in wrong temperature measurements. Fortunately, the thin PDMS layer remaining on the sample surface after production provided a homogeneous coating with a high emissivity on the whole sample, thereby removing any unwanted reflections or inhomogeneities. The absolute temperature values shown below were derived from the camera data assuming an emissivity of 90 %.

EXPERIMENTAL RESULTS A thermal cloak serves two purposes: first, it protects the cloaked region from heating up; second, it molds the flow of heat in such a way that the presence of the cloak cannot be detected from the outside. The measured temperature profiles shown in the first column of Figure 3.6 (a) prove that our cloak meets both those demands. The isolated central region is kept significantly cooler over time than its immediate surrounding and thus protected from the transient heat flow. (It is not isolated *perfectly* though due to the small but finite heat conductivity of the innermost ring.) Furthermore, the iso-temperature lines shown in white in Figure 3.6 remain almost perfectly straight before and behind the cloak. This compares to the behavior of a homogeneous plate, where the absence of any vertical heat flow leads to vertically straight iso-temperature lines. Thus, our cloak makes the downstream heat flow look exactly like that of a homogeneous plate. Let's compare this performance to the obstacle case shown in the second column of Figure 3.6 (a), where the central region is isolated by just one ring of solid PDMS. Here, we note that the single ring of PDMS protects the center from heating up just as well, with no significant difference to the cloak. In sharp contrast to the cloak, however, the iso-temperature lines are far from being straight vertical lines here. Their curvature indicates inhomogeneous heat flux (which is perpendicular to the isolines) through the plate caused by the object in the center, which can thus be detected from the outside.

Due to the different nature of the heat-conduction equation and the wave equation, the differences between cloak and obstacle are not as pronounced here as in similar experiments in wave-based systems. There, a merely isolated object would lead to strong scattering, reflection and shadowing of the incoming waves (see Refs. 5 and 20 for experimental examples in microwave optics and mechanics, respectively). In heat conduction, all these effects are absent, which also makes it more difficult to properly judge the

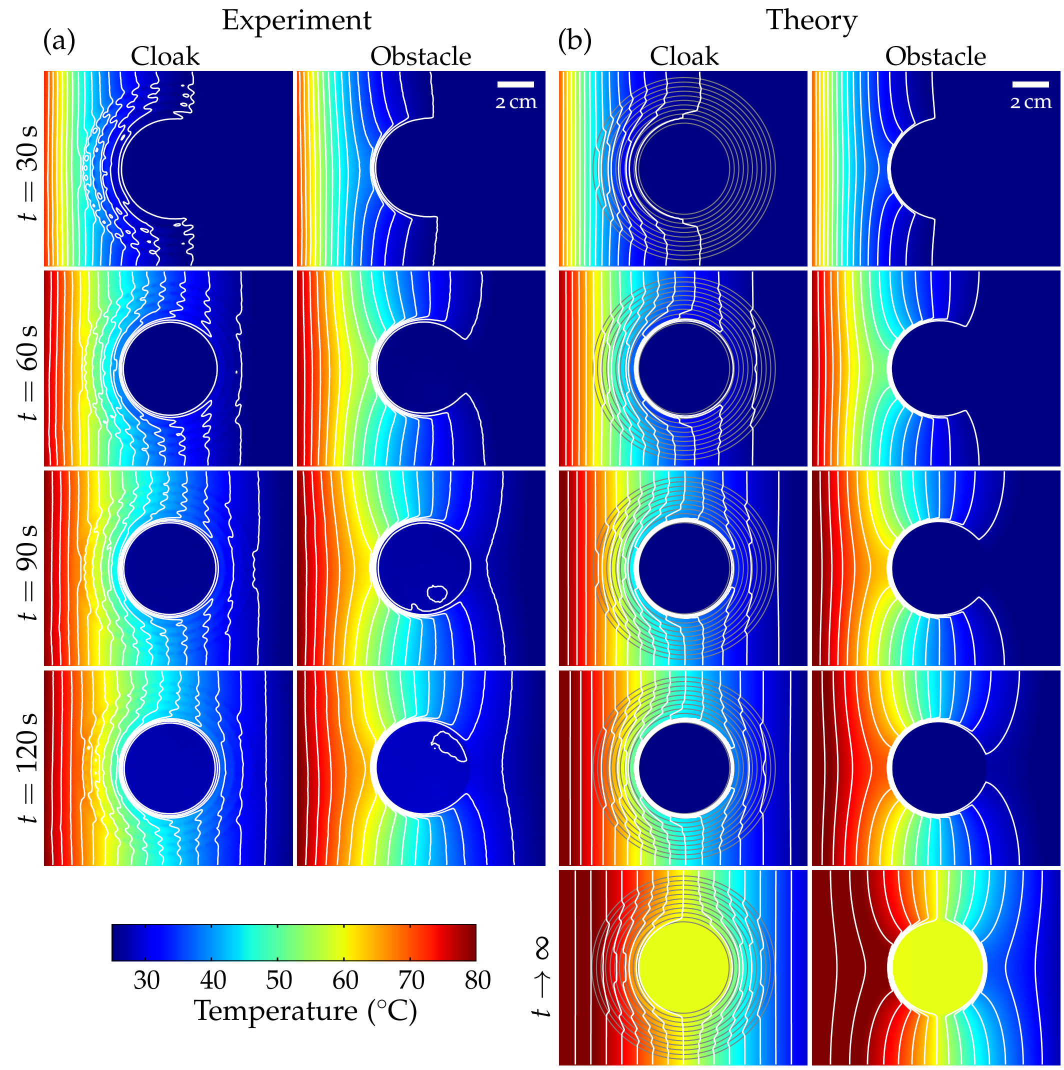

Figure 3.6: (a) Spatial false-color temperature profiles for the cloak and obstacle sample measured at different times after exposure to the heat baths at $t = 0$. Iso-temperature lines are superimposed in white with a temperature spacing of 3 K. Both cloak and obstacle succeed in transiently protecting the center from heating, but only the cloak makes the heat flow look like that of a homogeneous plate, as indicated by the straight vertical isolines outside of the cloak area. (b) Corresponding calculated temperature profiles are in good agreement with the experimental results. The cloak's rings are indicated by the gray circles. The quasi-static case displayed in the last row shows that heat protection works only transiently for both cloak and obstacle. Due to the finite heat conductivity of the isolating innermost ring, the center will eventually heat up over time.

performance of a transformation-thermodynamics device. Obviously, the iso-temperature lines are crucial to do so, as they make even small spatial temperature variations visible and also indicate the direction of heat flux.

NUMERICAL RESULTS Figure 3.6 (b) shows results of numerical calculations corresponding to the experiments shown in panel (a). We implemented the numerical model in COMSOL Multiphysics with the "Heat transfer in solids" module. For the sake of faster calculations, we did not recreate the complete microstructure (with the many small holes in cloak and surrounding) but used effective parameters according to Equation 3.4 for each ring and the surrounding. Generally, the numerical results agree very well with the experiments, even though they miss some of the small features visible in the experimentally obtained iso-temperature lines, which are due to the small holes and metal bridges in the samples. The slightly higher temperatures (or slightly more red colors in our false-color representation) seen at later times at the high-temperature ends of the numerical results indicate that the thermal isolation of the heat baths was not perfect in the experiments, leading to a cooling of the hot bath over time. The contact to the temperature baths was modeled by pure-copper regions (corresponding to the bent sample ends, compare Figure 3.5) set to fixed temperatures of $T_{\text{hot}} = 95\,^{\circ}\text{C}$ and $T_{\text{cold}} = 22\,^{\circ}\text{C}$, respectively.

The last row of Figure 3.6 (b) shows results for the quasi-static limit of transient heat conduction, where $t \to \infty$. This case is obviously not easily reachable in the experiments, as a long waiting time will lead to significant errors due to the non-ideal heat baths. Here, the implications of the good but not perfect isolation of the central region becomes apparent: if one only waits long enough, the cloaked region will eventually heat up. Protection from heat thus only works on rather short time scales. Despite this imperfection, the cloak succeeds in making the temperature distribution look like nothing was there also in the quasi-static case.

3.4 TIME CONSTANTS AND TRULY TRANSIENT HEAT FLOW

From the heat-conduction equation (3.1) and its transformed version (3.2), it is clear that transformation thermo*statics* is inherently easier to realize than transformation thermo*dynamics*: If $\partial/\partial t \approx 0$, the product $c\rho$ of density and specific heat capacity vanishes from the equations and the only parameter left is the heat conductivity κ. Thus, a thermo*static* cloak can have any distribution of $c\rho$; it will never influence the cloaking performance.

But how can we be certain we are in the truly transient regime when testing a cloak designed for this case? First hints may be obtained by inspecting the iso-temperature lines of a spatial temperature distribution. In the static limit, the spatial temperature distribution between two fixed values (prescribed by the heat baths in our case) is linear, resulting in a constant temperature gradient and equally-spaced isotemperature lines (see last row of Figure 3.6). While there is still heat flowing from one bath to the other, the temperature distribution does not change over time. In contrast, unevenly-spaced isolines (as in the first row of Figure 3.6) correspond to a nonlinear temperature gradient and suggest a non-static temperature distribution.

To quantify the time frame of transient heat flow, let's first consider the simplified case of a material (initially at T_0) that occupies the half-space $x \geq 0$. At $t = 0$, the surface $x = 0$ is suddenly heated to $T_1 > T_0$. The time-dependent temperature profile $T(x,t)$ has been derived analytically in the literature [77, ch. 12]:

$$\begin{aligned} \frac{T(x,t) - T_0}{T_1 - T_0} &= 1 - \frac{2}{\sqrt{\pi}} \int\limits_0^{x/\sqrt{4Dt}} \exp\left(-\eta^2\right) \mathrm{d}\eta \\ &= 1 - \operatorname{erf}\left(\frac{x}{\sqrt{4Dt}}\right) , \end{aligned} \tag{3.5}$$

with the heat diffusivity $D = \kappa/(c\rho)$. The error function $\operatorname{erf}(\chi)$ becomes 0.99 for an argument of $\chi \approx 2$, which leads to the *thermal penetration length* defined as $l_\mathrm{p} = 4\sqrt{Dt}$. This means that for distances $x > l_\mathrm{p}$, the relative temperature change is less than 1 %. We can thus define a thermal time constant τ_th indicating the time heat needs to penetrate a certain distance L into the material as

$$\tau_\mathrm{th} = \frac{L^2}{16D} . \tag{3.6}$$

For $L = 15\,\mathrm{cm}$, $\kappa = 85\,\mathrm{W/(K\,m)}$, $\rho = 2682.7\,\mathrm{kg/m^3}$, and $c = 1228.4\,\mathrm{J/(kg\,K)}$ (corresponding to a homogeneous copper-PDMS composite like the surrounding of our samples), we obtain $\tau_\mathrm{th} = 30.3\,\mathrm{s}$. Although our samples are different from the idealized half-space geometry considered here, the solution given in Equation 3.5 and thus also the time constant τ_th should be a good approximation for early times.

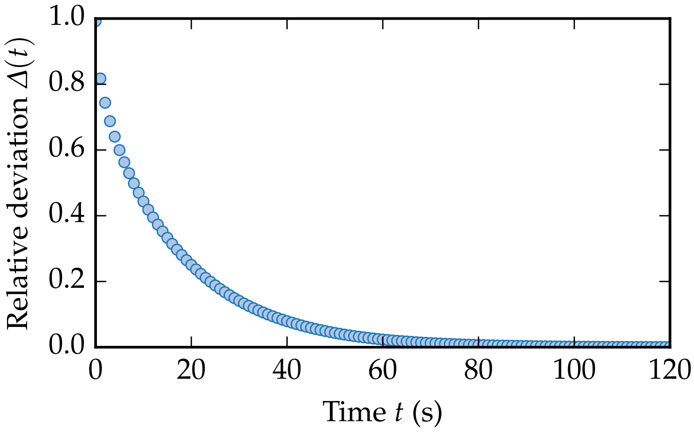

Figure 3.7: A plate that is suddenly heated to T_1 on one side while the other side is fixed at T_0 approaches a steady state over time. The blue dots show the relative deviation from this steady state for parameters as given above. After about 60 s, almost no change in temperature is occuring anymore and the system reaches a quasi-static state. This means that the later parts of our experiments on thermal cloaking (see Figure 3.6) cannot be considered truly dynamic. Parameters are: plate length $L = 15\,\mathrm{cm}$, heat conductivity $\kappa = 85\,\mathrm{W/(K\,m)}$, density $\rho = 2682.7\,\mathrm{kg/m^3}$, and specific heat capacity $c = 1228.4\,\mathrm{J/(kg\,K)}$.

A scenario slightly closer to our experiments is to compare the transient temperature profile of a plate with fixed temperatures T_0 and T_1 at the sides to its static limit. We did a corresponding COMSOL Multiphysics simulation and calculated the time-dependent relative deviation of the temperature distribution $T(t)$ from the static distribution $\tilde{T}$ via

$$\Delta(t) = \frac{\sqrt{\sum_i (\tilde{T}_i - T_i(t))^2}}{\sqrt{\sum_i \tilde{T}_i^2}}\,, \tag{3.7}$$

with the index i running over all spatial positions of the discretized simulation results. Figure 3.7 shows $\Delta(t)$ for the same parameters L, κ, ρ, and c as used above. At a time of $t \approx 36\,\mathrm{s}$, the relative deviation is as small as 10 %, meaning that 90 % of the transient change in temperature has already happened.

So what does this mean for our experiments shown in Figure 3.6? Both the iso-temperature lines and the calculated time constants suggest that the experiment was truly transient for roughly the first minute. In contrast, the last snapshot shown (2 minutes after exposing the sample to the heat baths) is already quite close to the quasi-static limit, with the result for $t = 90\,\text{s}$ lying somewhere in between.

In optics, transient photon flow can be realized easily using pulsed laser light, as we shall see later in our experiments on transient diffusive-light cloaking described in chapter 9. Creating truly transient heat flow, however, is generally much more demanding. Most importantly, open boundaries for heat are necessary for "heat pulses" but cannot be realized with heat baths prescribing fixed temperatures (and thus fixed boundaries). Furthermore, fixing the temperature at a sample boundary automatically straightens the iso-temperature lines in the vicinity of that boundary, making it more difficult to judge whether straight isolines originate from good cloaking or merely from a nearby boundary. Moving the boundary further away from the cloak would improve this situation but even further complicate realization of a nonlinear temperature gradient across the cloak. Eventually, compromises have to be accepted when designing a thermal cloak.

3.5 SUMMARY AND DISCUSSION

In this chapter, I motivated the form-invariance of the time-dependent heat-conduction equation in an intuitive way and described the design, fabrication, and characterization of a thermal cloak that protects a region from transient heat flow and hides it from external detection. Experimental and numerical results agree well and show good cloaking performance. However, our cloak is of course not perfect. We saw that the cloak doesn't protect the center better than a mere isolation and it does so only for some time: the center does eventually heat up, albeit more slowly than its surrounding. Reducing the heat conductivity of the innermost isolating ring would improve the isolation and thus the heat protection, but the qualitative behavior of the cloak would not change. Even vacuum (with $\kappa_{\text{vac}} = 0$) could not solve the problem because heat would still be transferred to the center via radiation. Perfect isolation in heat conduction seems to be out of reach. This is mainly due to the lack of an absorption mechanism, as heat is already at the "end of the food chain" of energy forms. In contrast, even a thin layer of metal can block all incident light in optics.

We studied thermal cloaking in relatively thin two-dimensional plate geometries. Three-dimensional transformation-thermodynamics structures are conceptually feasible but would obviously impose bigger fabricational challenges when creating the desired three-dimensional anisotropies. Also, characterization would be more difficult as there is no easy way to "look" into a three-dimensional heat-conducting solid the way we monitored our samples with an infrared heat camera. Attempts have been made, though, to exploit the symmetry of a spherical cloak and use a half-space geometry to realize three-dimensional cloaking [68].

The theoretical discussion of transformation thermodynamics [30], early work on thermal metamaterials [75], and our own experiments shown above [71] have sparked interest in the scientific community, leading to numerous recent publications. Most notable are experiments on static cloaks featuring a core-shell geometry that allows for very thin cloaks [67, 68] instead of a transformation-physics design,[8],[9] concentrators that focus heat into a region instead of routing it around [55, 78], and devices that work for multiple physical energy flows at the same time. Examples of the latter are simultaneous cloaking of heat and electric current [79, 80], or, more excitingly,[10] simultaneous cloaking for electric conduction and concentration of heat flux [81]. Related work has also been published on the manipulation of static eletrical conduction [24, 25, 82], which is governed by the same differential equation as static heat conduction (also see Table 2.1).

Transformation thermodynamics (or more generally the specific manipulation of heat flow) became a quite active scientific field, and new publications are popping up every month. Still, applications seem to be rather limited so far. This is mainly due to the compromise one has to live with in terms of isolation, which makes it hard to compete with conventional methods of heat management. The cloaking effect (that is, unchanged iso-temperature lines compared to a homogeneous reference) is not an exceptional advantage in itself, especially as sharp contrasts quickly smear out over time and space in heat conduction. Still, thermal cloaking is a beautiful demonstration how of physical energy flows can be manipulated and certainly has brought the field of transformation physics further.

---

[8] We utilized the same core-shell concept in our work on diffusive-light cloaking described in Part II.

[9] Both these publications also claim transient cloaking. We shall, however, see later that core-shell cloaks inherently fail under transient conditions (see chapter 9). Refs. 67 and 68 once more show how quickly one approaches a quasi-static regime in heat conduction that might be mistaken for a transient one.

[10] Creating a "multi-cloak" for heat conduction and electric conduction is conceptually easy: Due to the Wiedemann-Franz law, electric and thermal conductivities are proportional to each other in many metals and when choosing the right materials, a thermal cloak automatically works for electric conduction and vice versa.

Part II

DIFFUSIVE-LIGHT CLOAKING

Chapter 4

4 THE RELATIVITY PROBLEM OF INVISIBILITY CLOAKING

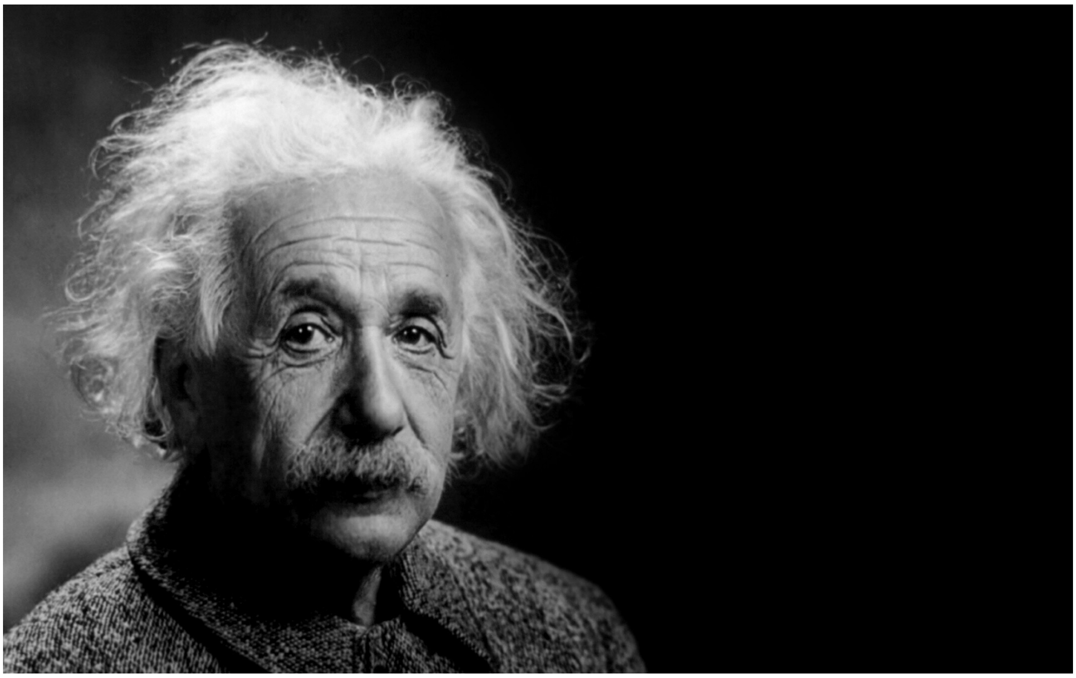

"Ideal" invisibility cloaking requires energy to be transported faster than the vacuum speed of light and thus is not compatible with the laws of physics. Here, I will elaborate on where this requirement comes from for any free-space cloak in optics and why this so-called relativity problem becomes irrelevant for light that propagates diffusively.

4.1 FUNDAMENTAL LIMITS OF OPTICAL CLOAKING

Only shortly after Pendry's and Leonhardt's theoretical description of transformation optics, a first experimental realization was published by D. Smith's group [5]. It used concentric arrays of split-ring resonators in a two-dimensional waveguide geometry to guide microwaves around a cylindrical scatterer. However, this cloak was somewhat limited in that it worked only for one particular polarization and only in a very narrow frequency range. Furthermore, the object hidden by the cloak was barely larger than the wavelength. In contrast, an *ideal* invisibility cloak should work not only in three dimensions and for all possible polarizations, but also over the entire frequency range of interest while being truly macroscopic, that is, much larger than the wavelength of the used light. As it turns out, the shortcomings of this first invisibility cloak do not merely stem from fabricational difficulties or a lack of suitable materials. They rather demonstrate a most fundamental limitation that makes broadband and macroscopic optical free-space cloaks impossible.

So why are these two aspects—broadband operation and macroscopic size—impossible to realize in optics? Obviously, light that impinges on a cloaking device as described above takes a detour around the object to be hidden, thus travelling a longer distance than it would without the cloak (again, the cars in Figure 2.2 demonstrate this aspect nicely). To make up for this detour, a propagation speed higher than in the surrounding medium is needed. If the surrounding medium is vacuum or air, that means a speed higher than the vacuum speed of light, c_0. This race against the speed of light is not a problem in principle. Indeed, phase as well as group velocities higher than the speed of light are perfectly compatible with Maxwell's equations and have been achieved experimentally [83]. Once we demand broadband, dispersion-free operation, though, phase and energy velocity become strictly the same. We all know that energy velocities higher than c_0 are fundamentally forbidden by Einstein's theory of relativity. A truly broadband cloak would thus violate relativity.

But even if we lower our expectations and decide to be satisfied with a macroscopic cloak for a single wavelength, things do not get much better. The resonant structures that give rise to the necessary superluminal phase and group velocities of light necessarily would be highly dispersive, and with dispersion always come finite losses.[1] While these losses might be

---

[1] Dispersion and loss are intimately connected via the Kramers-Kronig relations [84].

tolerable for a cloak with dimensions on the order of the light's wavelength, estimations have shown that a cloak much larger than that would effectively absorb almost all incident light and thus become useless [3].

In contrast to optics, the relativity problem plays hardly any role for cloaking beyond optics such as described in Part I of this thesis. This is because most other energy flows inherently propagate so much slower than light that the vacuum speed of light is way out of reach in any way.

Apparently, transformation optics cannot give us invisibility cloaks as envisioned by mankind for millenia. More pertinently, ideal passive free-space invisibility cloaking seems to be generally incompatible with the laws of physics. It is of course possible to "accept" the relativity problem and content oneself with narrowband, non-macroscopic cloaking devices or with otherwise limited structures such as carpet cloaks, which by themselves already are astounding pieces of science put into practice and shall not at all be discredited here. However, also in optics, there is a way to avoid the relativity problem altogether.

4.2 OVERCOMING THE RELATIVITY PROBLEM WITH DIFFUSE LIGHT

For probably most people, the term *light propagation* evokes associations with the straight, ray-like nature of light that we experience in our everyday life. We (most of the time) see light that traveled on straight paths, or, equivalently, we see straight, geometric shadows, and we cannot look around corners. However, for example in dense fog, clouds, a glass of milk, paper or also human tissue or bone, light does *not* follow such straight paths but is rather performing random walks between scattering centers that are randomly distributed in such *turbid* media. Under certain conditions, light propagation is then described by a diffusion equation—just like heat propagating in a metal or like particles diffusing in a liquid—rather than by Maxwell's equations for continua.

In this work, I will call a medium *turbid* when light interacts with it mainly by scattering and absorption. I will call it *diffusive* or *diffuse*, when light propagates in it according to the diffusion equation. With this definition, all diffusive media are turbid, but not all turbid media need to be diffusive.

As it turns out, the relativity problem effectively vanishes for diffusive media. The random, zig-zag-like path every photon takes in such a medium results in a huge detour compared to propagation without scattering. And while the velocity of an individual photon is not affected by this detour, the overall effective speed of the transport of energy can be reduced significantly.[2]

With the energy transport effectively slowed down with respect to the speed of light in the background medium, speeding it up again inside a cloak poses no fundamental problem. All that needs to be done is to control the amount of scattering via the concentration of scattering particles. The energy velocity is of course still limited by the vacuum speed of light, but the scattering still opens up a window that we can use to realize macroscopic and broadband free-space cloaks, something that is impossible for ballistic light propagation.

In the following chapters, I will first give an overview of light-diffusion theory and experimental and numerical methods, before introducing the concept of core-shell cloaking for diffuse light and experimental realizations thereof.

---

[2] Assigning a *velocity* to the energy transport is actually not very meaningful anymore for highly scattering media. The meaningful quantity for such a process is rather the *diffusivity* D (given in $\mathrm{m}^2\,\mathrm{s}^{-1}$).

5

Chapter 5

THEORY OF DIFFUSIVE LIGHT TRANSPORT

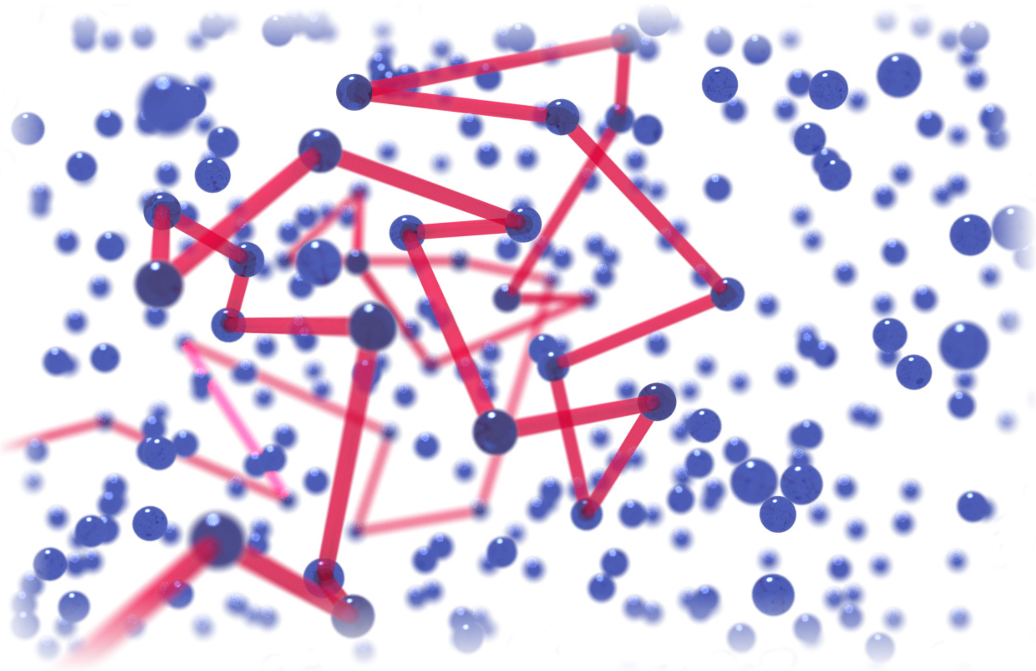

Artist's view of a medium with randomly arranged scatterers, where light propagates diffusively

In disordered media where light propagates diffusively, the limitations that prevent optical free-space cloaking become irrelevant. In this chapter, I will give an overview of the theory of light diffusion, starting from basic scattering and absorption properties of turbid media and ending with the diffusion equation and its solutions. This theory forms the basis for the later design and realization of diffusive-light cloaks. The derivations closely follow Ref. 85*, where further details can be found.*

5.1 SCATTERING AND ABSORPTION PROPERTIES OF TURBID MEDIA

A turbid medium can be described as a dielectric background medium with refractive index n in which dielectric scattering particles with a different refractive index are suspended. In the following, it is assumed that light interacts with such a medium by two effects only: absorption and elastic scattering. This is a crude simplification that naively ignores much of the complexity of light-matter interaction, but it comes with the big advantage of a rather simple mathematical formulation and still yields solutions that are applicable to many realistic media.

SCATTERING PROPERTIES The interaction of light and matter through elastic scattering is characterized by the scattering coefficient μ_s and by the scattering phase function $p(\hat{s}, \hat{s}')$.

The *scattering coefficient* μ_s is defined as the ratio of the scattered power per unit volume and the incident power per unit area. In general, scattering originates from the refractive-index contrast between the background medium and the particles therein as well as from fluctuations in the background medium alone. However, the latter are usually negligible for media exhibiting multiple scattering and shall be ignored henceforth. We will furthermore assume only elastic scattering without any energy exchange between the scattered light and the scattering center. In this case, μ_s can be expressed by the particles' scattering cross section $C_\mathrm{s,p}$ (given in mm^2) and their number density N_p (given in mm^{-3}):

$$\mu_\mathrm{s} = N_\mathrm{p} C_\mathrm{s,p} \qquad [\mu_\mathrm{s}] = \mathrm{mm}^{-1}\ . \tag{5.1}$$

The *scattering phase function* $p(\hat{s}, \hat{s}')$ (or just scattering function) is the probability that a photon traveling along the direction $\hat{s}$ is scattered into the unit solid angle around the direction $\hat{s}'$ and thus describes the angular dependence of the scattering. In this work, we assume isotropic scatterers such as spherical particles or randomly oriented non-spherical particles. Then, the scattering function depends only on the angle θ between $\hat{s}$ and $\hat{s}'$ and becomes $p(\hat{s}, \hat{s}') = p(\theta)$. The scattering function is assumed to be normalized according to

$$\int_{4\pi} p(\hat{s}, \hat{s}')\,\mathrm{d}\Omega' = 2\pi \int_{0}^{\pi} p(\theta)\sin(\theta)\,\mathrm{d}\theta = 1\ . \tag{5.2}$$

If every photon undergoes multiple scattering events before it is detected or absorbed (as it is true for diffusive media), the scattering function may be characterized by just one parameter, the *asymmetry factor*[1] g, which is defined as the average of the scattering angle's cosine:

$$g = \langle \cos(\theta) \rangle = 2\pi \int_0^\pi \cos(\theta) p(\theta) \sin(\theta)\, \mathrm{d}\theta \,. \tag{5.3}$$

The asymmetry factor can take values between -1 and 1 and heavily depends on the diameter d of the scattering particles compared to the light's wavelength λ. For particles much bigger than the wavelength ($d \gg \lambda$), scattering is mainly geometric and forward scattering dominates, which results in g being close to 1 (pure *backward* scattering would mean $g = -1$). In contrast, particles much smaller than the wavelength ($d \ll \lambda$) exhibit Rayleigh scattering [86] with $g \approx 0$. (The scattering function for Rayleigh scatterers is not isotropic, but symmetric with respect to $\theta = \pi/2$. This shows that $g = 0$ can be obtained even for anisotropic scattering functions). In between those two extremes, scattering is described by Mie theory [87] with more complex scattering functions and $|g|$ ranging between 0 and 1.

The beauty of the construction above is that—at least for media dominated by multiple scattering—the scattering properties are fully characterized by only two scalar parameters, μ_s and g.

ABSORPTION PROPERTIES In analogy to the scattering coefficient, the *absorption coefficient* μ_a is defined as the ratio of the light power absorbed per unit volume and the incident power per unit area.

In general, absorption in a turbid medium is caused by the light's interaction with the atoms and molecules of the background medium (described by the medium absorption coefficient $\mu_\mathrm{a,m}$) as well as with the scattering particles (described by the particle absorption coefficient $\mu_\mathrm{a,p}$). Which of the two dominates depends on the specific medium. Absorption by molecules in the background medium is governed by their absorption cross section $C_\mathrm{a,m}$ and their number density N_m. As long as the scattering particles are separated from each other by a mean distance such that the absorption of each particle is not influenced by its neighbor particles, the particles' absorption cross section $C_\mathrm{a,p}$ and their number density N_p likewise characterize the

---

[1] The asymmetry factor is sometimes also called *anisotropy factor*. However, g can be zero even for anisotropic scattering phase functions, making *asymmetry factor* a more reasonable choice of name.

absorption due to the particles and the overall absorption coefficient is given by

$$\mu_\mathrm{a} = \mu_\mathrm{a,m} + \mu_\mathrm{a,p} = N_\mathrm{m} C_\mathrm{a,m} + N_\mathrm{p} C_\mathrm{a,p} \qquad [\mu_\mathrm{a}] = \mathrm{mm}^{-1} \, . \tag{5.4}$$

We consider the absorption of photons to be ultimate, that is, the re-emission of absorbed photons, possibly at another wavelength, is ignored. Also, nonlinear processes such as two-photon absorption are not considered.

THE LAMBERT-BEER LAW Combining scattering and absorption, one can define the extinction coefficient μ_ex which defines the overall attenuation of light (traveling in one direction) due to light-matter interaction:

$$\mu_\mathrm{ex} = \mu_\mathrm{s} + \mu_\mathrm{a} \, . \tag{5.5}$$

The variation of the power $P(/z)$ of a light beam traveling along z is then

$$\mathrm{d}P(z) = -\mu_\mathrm{ex}(z) P(z) \, \mathrm{d}z \, , \tag{5.6}$$

and hence the beam's power is changing with z according to the Lambert-Beer law:

$$P(z) = P_0 \exp\left(- \int_0^z \mu_\mathrm{ex}(z') \, \mathrm{d}z' \right) \, , \tag{5.7}$$

which for a homogeneous medium (with $\mu_\mathrm{ex}(z) = \text{const.}$) simplifies to

$$P(z) = P_0 \exp\left(-\mu_\mathrm{ex} z\right) \, . \tag{5.8}$$

As $P(z)$ is the part of the light beam that is *not* scattered or absorbed, it is usually called the *ballistic* component of the beam. By measuring only the ballistic portion of light traveling through a turbid medium, one thus gains direct access to its extinction coefficient, a method that we will use later for the experimental characterization of diffusive media (see chapter 7).

5.2 STATISTICAL MEANING OF THE OPTICAL PROPERTIES OF TURBID MEDIA

From the scattering and absorption properties discussed above, statistical results in the form of probability distributions for the propagation of photons in turbid media can be derived.

As outlined before, the scattering function only depends on the scattering angle θ for isotropic particles. Then, the probability functions f_θ and f_φ for the angles θ and φ that define the scattering direction $\hat{s}'$ are simply given by

$$f_\theta = 2\pi\, p(\theta) \sin(\theta) \tag{5.9}$$

and

$$f_\varphi = \frac{1}{2\pi} \, . \tag{5.10}$$

The Lambert-Beer law (Equation 5.7) can be used to obtain the probability distribution f_z for the path length a photon statistically travels before being absorbed or scattered by the medium. The probability that a photon emitted at $z = 0$ will be scattered or absorbed between z and $z + \mathrm{d}z$ is given by the power $\mu_{\mathrm{ex}} P(z)\,\mathrm{d}z$ that is extracted in the volume element between z and $z + \mathrm{d}z$ divided by the incident power P_0. Inserting the Lambert-Beer law for $P(z)$, we obtain

$$f_z = \mu_{\mathrm{ex}} \exp\left(- \int_0^z \mu_{\mathrm{ex}}(z')\,\mathrm{d}z' \right) , \tag{5.11}$$

which for a homogeneous medium becomes

$$f_z = \mu_{\mathrm{ex}} \exp\left(-\mu_{\mathrm{ex}} z\right) . \tag{5.12}$$

f_z can then be used to obtain the mean free path l_{ex} that a photon statistically travels before it is scattered or absorbed. For a homogeneous, infinitely extended medium, we get

$$l_{\mathrm{ex}} = \int_0^\infty z f_z \,\mathrm{d}z = \frac{1}{\mu_{\mathrm{ex}}} \, . \tag{5.13}$$

Analogously, we can define the *scattering mean free path* $l_{\mathrm{s}} = 1/\mu_{\mathrm{s}}$ for an absorption-free medium (which is the path a photon statistically travels between two scattering events) and the *absorption length* $l_{\mathrm{a}} = 1/\mu_{\mathrm{a}}$ for a scattering-free medium (the path a photon statistically travels before being absorbed).

For absorption-free turbid media, the propagation of photons can be seen as a random walk of each photon, which changes its direction with each scattering event and ends only when the photon exits the medium. The probability functions f_θ, f_φ, and f_z describe the rules of this random walk and thus can be used as the foundation of Monte-Carlo-based raytracing of photons in turbid media. See section 6.2 for a detailed description of this method.

Reduced scattering coefficient and transport mean free path

With the theory of random walks, it has been shown that for a photon in an infinite and absorption-free medium emitted at $z = 0$ along the positive z-axis, the expectation value for the coordinates (x_k, y_k, z_k) at which the kth scattering event occurs is

$$\langle x_k \rangle = \langle y_k \rangle = 0 \,, \quad \langle z_k \rangle = \frac{1}{\mu_\mathrm{s}} \sum_{i=0}^{k-1} g^i = \frac{1}{\mu_\mathrm{s}} \frac{1-g^k}{1-g} \,. \tag{5.14}$$

With $-1 \leq g \leq 1$, we obtain for large values of k:

$$\lim_{k \to \infty} \langle z_k \rangle = \frac{1}{\mu_\mathrm{s}} \frac{1}{1-g} \,. \tag{5.15}$$

This equation means that $1/(\mu_\mathrm{s}(1-g))$ is the average distance a photon travels before it “forgets” its initial traveling direction. We can therefore define the *reduced scattering coefficient* μ_t and the *transport mean free path* l_t:

$$\mu_\mathrm{t} = \mu_\mathrm{s}(1-g) \,, \qquad l_\mathrm{t} = \frac{1}{\mu_\mathrm{t}} = l_\mathrm{s} \frac{1}{1-g} \,. \tag{5.16}$$

μ_t has the meaning of a scattering coefficient in which the scattering asymmetry is compensated for, while the transport mean free path is the mean distance after a photon’s inital direction has been randomized.

We will later see that the transport mean free path is a very important value for the description of turbid media as it decisively influences whether a medium can be characterized as *diffusive* or not.

5.3 Radiometric quantities

I will now briefly introduce the most important radiometric quantities needed for the discussion of energy transport by light. The basic quantity used for the description of energy propagation in transport theory is the *radiance*

$$L(\vec{r}, \hat{s}, t) \,, \qquad [L] = \mathrm{W\,m^{-2}\,sr^{-1}} \,. \tag{5.17}$$

It is defined as the average power that at position $\vec{r}$ and time t flows through the unit area oriented along the unit vector $\hat{s}$, created by photons moving within the unit solid angle around $\hat{s}$.[2]

---

[2] A similar quantity is the *spectral radiance* $L_\mathrm{s}(\vec{r}, \hat{s}, t, \nu)$, which is the radiance due to photons within the frequency interval $(\nu, \nu + \mathrm{d}\nu)$. As we will only deal with monochromatic light in all theoretical considerations, the frequency dependence is omitted here for the sake of brevity.

Integrating the radiance over the entire solid angle yields the *irradiance* or *fluence rate*:

$$\Phi(\vec{r},t) = \int_{4\pi} L(\vec{r},\hat{s},t)\,\mathrm{d}\Omega\,, \qquad [\Phi] = \mathrm{W\,m^{-2}}\,. \tag{5.18}$$

The fluence rate expresses the amount of power flowing from any direction through the surface of the unit volume at position $\vec{r}$ and time t. Closely connected to the fluence rate are the energy density u and the photon density n_p:

$$u(\vec{r},t) = \frac{\Phi(\vec{r},t)}{v}\,, \qquad [u] = \mathrm{J\,m^{-3}} \tag{5.19}$$

and

$$n_\mathrm{p}(\vec{r},t) = \frac{u(\vec{r},t)}{h\nu}\,, \qquad [n_\mathrm{p}] = \mathrm{m^{-3}}\,, \tag{5.20}$$

with the speed of light in the medium $v = c_0/n$ and the medium refractive index n.

Finally, it is useful to define the *energy flux vector* $\vec{J}_\mathrm{e}$, which is representing the amount and direction of the net flux of power, as

$$\vec{J}_\mathrm{e}(\vec{r},t) = \int_{4\pi} L(\vec{r},\hat{s},t)\,\hat{s}\,\mathrm{d}\Omega\,, \qquad [\vec{J}_\mathrm{e}] = \mathrm{W\,m^{-2}}\,. \tag{5.21}$$

5.4 The radiative-transfer equation

The radiative-transfer equation [88] (RTE) describes the transport of energy through a medium exhibiting scattering and absorption. In contrast to the multiple-scattering theory based on Maxwell's equations [89], the RTE is a phenomenological equation that lacks a rigorous mathematical formulation accounting for all effects involved in light propagation. Still, it provides a good model for many practical problems and will be the starting point of the derivation of the light-diffusion equation

The RTE describes the mechanisms how the radiance L in a certain volume of a turbid medium is decreased or increased over time. For time-dependent sources, it reads

$$\underbrace{\frac{\partial}{\partial t}\frac{L(\vec{r},\hat{s},t)}{v}}_{1} + \underbrace{\vec{\nabla}\cdot(\hat{s}L(\vec{r},\hat{s},t))}_{2} + \underbrace{\mu_\mathrm{ex}L(\vec{r},\hat{s},t)}_{3} = \underbrace{\mu_\mathrm{s}\int_{4\pi} p(\hat{s},\hat{s}')L(\vec{r},\hat{s},t)\,\mathrm{d}\Omega'}_{4} + \underbrace{q(\vec{r},\hat{s},t)}_{5} \tag{5.22}$$

with the medium speed of light $v = c_0/n$.

The first term represents the total temporal change of the energy flowing through the volume element $\mathrm{d}V$ at the position $\vec{r}$ in the direction of $\hat{s}$. This energy is *decreased* by terms 2 and 3 and *increased* by terms 4 and 5:

- Term 2 describes the net flux of energy that propagates away from $\vec{r}$ along the direction of $\hat{s}$,
- term 3 stands for energy that is scattered away from or absorbed in the volume element $\mathrm{d}V$,
- term 4 is energy coming from an arbitrary direction $\hat{s}'$ that is scattered inside $\mathrm{d}V$ into the direction $\hat{s}$,
- and term 5 represents light that is generated by sources inside the considered volume element.

DEPENDENCE ON ABSORPTION For media with homogeneous absorption ($\mu_\mathrm{a}(\vec{r}) = \text{const.}$), if $L(\vec{r}, \hat{s}, t, \mu_\mathrm{a}\!=\!0)$ is a solution of the RTE for a non-absorbing medium and the source being a temporal Dirac delta function $q(\vec{r}, \hat{s}, t) = q'(\vec{r}, \hat{s})\delta(t)$, then

$$L(\vec{r}, \hat{s}, t, \mu_\mathrm{a}) = L(\vec{r}, \hat{s}, t, \mu_\mathrm{a}\!=\!0) \exp\left(-\mu_\mathrm{a} v t\right) \tag{5.23}$$

is the solution of the RTE when the absorption coefficient of the medium is μ_a. This can easily be seen by inserting Equation 5.23 into the RTE given above. It is also intuitively clear that for homogeneous absorption, if all light is emitted at $t = 0$, then at a time $t > 0$, all light has traveled the same path $l = vt$ and is thus attenuated by the same factor $\exp\left(-\mu_\mathrm{a} v t\right)$, regardless of the detection point. This finding is an important property of the RTE which we will later use again when deriving the light-diffusion equation.

The factor $1/(\mu_\mathrm{a} v)$ has the meaning of the average lifetime of a photon, which we accordingly define as

$$\tau = \frac{1}{\mu_\mathrm{a} v}\,, \qquad [\tau] = \mathrm{s}\,. \tag{5.24}$$

Both expressions are equivalent, although sometimes one or the other can provide a more intuitive feeling for the absorption.

5.5 The light-diffusion equation

The radiative-transfer equation is an integro-differential equation (it contains both differential and integral operators), to which no general analytical solution exists [90]. Instead, the RTE is usually solved numerically, for example with finite-element methods or Monte-Carlo simulations. Unfortunately, such procedures are costly in terms of computation time and thus a simplified but analytically solvable equation is of great worth. When propagation is dominated by multiple scattering, the light-diffusion equation provides exactly such a simplified description. In the following, I will elaborate on the conditions that have to be fulfilled for light propagation to be *diffusive* and subsequently derive the light-diffusion equation.

The diffusion approximation consists of two simplifying assumptions about the transport of light in turbid media [90]. The first one assumes that the radiance L is almost isotropic and can be written as

$$L(\vec{r}, \hat{s}, t) = \frac{1}{4\pi} \Phi(\vec{r}, t) + \frac{3}{4\pi} \vec{J}_{\mathrm{e}}(\vec{r}, t) \cdot \hat{s} \,, \tag{5.25}$$

which are the first two terms of a series expansion in spherical harmonics.

The second assumption states that the time variation of the energy flux vector $\vec{J}_{\mathrm{e}}$ over the time range $\Delta t = l_{\mathrm{t}}/v$ is small compared to the vector itself, which can be written as

$$\frac{l_{\mathrm{t}}}{v} \left| \frac{\partial \vec{J}_{\mathrm{e}}(\vec{r}, t)}{\partial t} \right| \ll \left| \vec{J}_{\mathrm{e}}(\vec{r}, t) \right| \,. \tag{5.26}$$

Both these assumptions are generally justified when scattering dominates over absorption. In this case, every photon undergoes many scattering events and its propagation direction tends to be randomized. Then, also the radiance tends to be isotropic, as required by Equation 5.25. For strongly absorbing media, however, it is intuitively clear that the photon lifetime might be just too small for the propagation directions to be randomized. It is also clear that to support diffusive light propagation, the turbid medium needs to be sufficiently large in every direction, such that photons may indeed scatter many times before exiting through the medium boundaries.

While equations 5.25 and 5.26 are necessary for the derivation of the light-diffusion equation, they are also quite abstract and hard to put into numbers that can be compared with real-world media. By comparing solutions of the diffusion equation with results of Monte-Carlo-based simulations, Ref. 85 translates the diffusion approximation into quantitative constraints on the properties of a turbid medium that need to be fulfilled for diffusive light propagation:

1. Scattering dominates over absorption: $\mu_\mathrm{a}/\mu_\mathrm{t} \leq 0.1$,
2. the medium size is at least 10 transport mean free path lengths in every direction: $V \geq (10\, l_\mathrm{t})^3$,
3. and the photons have traveled paths longer than $4\, l_\mathrm{t}$ before detection.

These conditions are very important for the experimental realization of designs based on the light-diffusion equation. Later, we will see that they impose a rather small window of material parameters usable for the construction of invisibility cloaks.

DERIVATION OF THE LIGHT-DIFFUSION EQUATION With the above assumptions made, the diffusion equation for light can be derived from the RTE. First, we obtain the continuity equation by integrating the absorption-free RTE (that is, with $\mu_\mathrm{a} = 0$) over the complete solid angle and get

$$\frac{\partial}{\partial t}\frac{\Phi(\vec{r},t)}{v} + \vec{\nabla}\cdot\vec{J}_\mathrm{e}(\vec{r},t) = \int\limits_{4\pi} q(\vec{r},\hat{s},t)\,\mathrm{d}\Omega\,. \tag{5.27}$$

Here, no simplifying assumptions needed to be made. Besides, a corresponding equation could be obtained also with absorption included.

To obtain the diffusion equation, the flux vector $\vec{J}_\mathrm{e}$ in Equation 5.27 has to be expressed in terms of the fluence rate Φ. This can be done by multiplying the RTE with $\hat{s}$ and integrating over the whole solid angle. The derivation uses the two assumptions of the diffusion approximation and results in Fick's first law of diffusion [91] (details can be found in Ref. [85]):

$$\vec{J}_\mathrm{e}(\vec{r},t) = -\frac{l_\mathrm{t}}{3}\left(\vec{\nabla}\Phi(\vec{r},t) - 3\int\limits_{4\pi} q(\vec{r},\hat{s},t)\hat{s}\,\mathrm{d}\Omega\right)\,, \tag{5.28}$$

which connects the energy flux to the gradient of the fluence rate. At this point, it is instructive to define the *photon flux vector* $\vec{J}$ as

$$\vec{J}(\vec{r},t) = \frac{\vec{J}_\mathrm{e}(\vec{r},t)}{h\nu}\,, \qquad [\vec{J}] = \mathrm{m}^{-2}\,\mathrm{s}^{-1}\,, \tag{5.29}$$

which describes the amount and direction of photons flowing at the position $\vec{r}$ and time t. If we now divide equations 5.27 and 5.28 by the photon energy $h\nu$ and identify $\Phi = v n_\mathrm{p} h\nu$, we obtain the continuity equation and Fick's law for the photon density n_p:

$$\boxed{\frac{\partial n_\mathrm{p}(\vec{r},t)}{\partial t} + \vec{\nabla} \cdot \vec{J}(\vec{r},t) = \int_{4\pi} \tilde{q}(\vec{r},\hat{s},t)\,\mathrm{d}\Omega} \tag{5.30}$$

and

$$\boxed{\vec{J}(\vec{r},t) = -D\left(\vec{\nabla} n_\mathrm{p}(\vec{r},t) - 3\int_{4\pi} \tilde{q}(\vec{r},\hat{s},t)\hat{s}\,\mathrm{d}\Omega\right)}\,. \tag{5.31}$$

Here, we introduced the *photon diffusivity* D, which depends only on the refractive index n of the medium and the transport mean free path l_t:

$$\boxed{D = \frac{1}{3}\frac{c_0}{n} l_\mathrm{t}}\,, \qquad [D] = \mathrm{m^2\,s^{-1}}\,. \tag{5.32}$$

Plugging Equation 5.31 into Equation 5.30, we obtain the diffusion equation for the photon density

$$\boxed{\vec{\nabla} \cdot \left(D\vec{\nabla} n_\mathrm{p}(\vec{r},t)\right) - \frac{\partial n_\mathrm{p}(\vec{r},t)}{\partial t} = q_0(\vec{r},\hat{s},t)}\,, \tag{5.33}$$

where $q_0 = \int_{4\pi} \tilde{q}\,\mathrm{d}\Omega + 3\,D\int_{4\pi} \tilde{q}\hat{s}\,\mathrm{d}\Omega$ is the photon source term.

In accordance with the radiative-transfer equation and its dependence on absorption given in Equation 5.23, we assume that the diffusion equation and its solutions are modified in an identical way for non-zero absorption, which is thus included simply by adding the term $\mu_\mathrm{a} v\, n_\mathrm{p}(\vec{r},t)$:

$$\vec{\nabla} \cdot \left(D\vec{\nabla} n_\mathrm{p}(\vec{r},t)\right) - \frac{\partial n_\mathrm{p}(\vec{r},t)}{\partial t} = \mu_\mathrm{a} v\, n_\mathrm{p}(\vec{r},t) + q_0(\vec{r},\hat{s},t)\,. \tag{5.34}$$

According, a solution of the diffusion equation for a homogeneous and absorption-free medium can be translated to a solution for a medium with absorption coefficient μ_a by multiplying it with the factor $\exp(-\mu_\mathrm{a} v t)$. With these assumptions, the diffusion equation behaves exactly like the RTE in terms of absorption.[3] Also here, the photon lifetime τ can be used to replace the factor $1/(\mu_\mathrm{a} v)$, according to what is more convenient in the specific situation.

The time-dependent light-diffusion equation (5.33) is mathematically identical to the time-dependent heat-conduction equation as given in its source-free form by Equation 3.1 (with the exception that there is no parameter equivalent to the product $c\rho$ of density and heat capacity). This equality means that under the right conditions (a multiply-scattering medium of the right dimensions with low absorption), light behaves identical to heat in a stationary medium or particles suspended in a solution. This is a remarkable similarity between seemingly completely different physical systems. Consequently, many phenomena originating from the wave nature of light such as interference, reflection, sharp, geometric shadows or polarization effects are absent in light diffusion. As I have argued in chapter 4, it is this diffusive nature of photons in turbid media and a resulting effectively reduced speed of energy transport that helps us overcome the relativity problem of optical invisibility cloaking.

I like to point out that light diffusion, just like any other diffusive process, is a purely statistical phenomenon. More specifically, Fick's law—describing a macroscopic flux of photons along the gradient of the photon density—does not mean that the photons experience any kind of force due to spatial differences in the photon density or that they can "sense" this gradient in any other way. On the contrary, all photons are completely independent from each other and perform individual and undisturbed random walks. Only the entirety of those random walks leads to the macroscopic effects of light diffusion. Thus, studying a single photon's trajectory through a turbid medium in order to learn something about the diffusive properties of this medium is a meaningless endeavour. On the other hand, looking at many such photon trajectories at the same time is indeed a proper tool to study light diffusion. The Monte-Carlo method introduced in chapter 6 takes exactly this approach. While computationally very costly, it comes with the big advantage that also scenarios not adequately described by the diffusion

---

[3] When the diffusion equation is derived from the RTE with absorption included from the beginning on, nothing changes except that the diffusivity D will then depend also on absorption. Even though they lead to different results, both approaches are in principle valid, as absorption may only be a small correction in any way for the diffusion approximation to be valid. It has been shown, though, that for media with rather strong absorption, a diffusivity D that does not depend on absorption leads to results fitting better to experiments [92, 93].

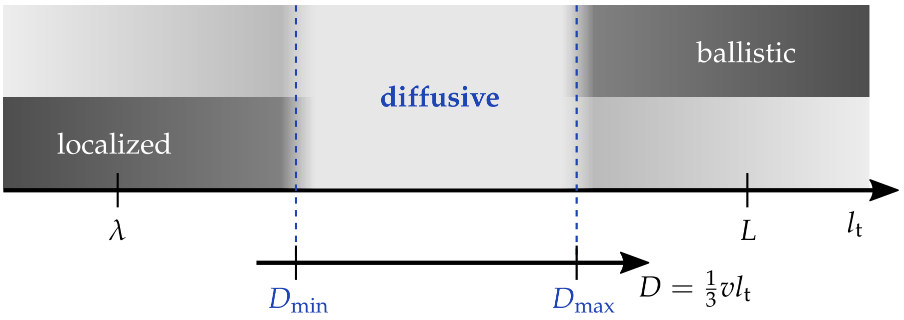

Figure 5.1: Regimes of light propagation depending on the transport mean free path length. The diffusive regime is framed by ballistic propagation for $l_t \approx L$ and localization for $l_t \approx \lambda$, leading to an accessible range of diffusivities between $D_{\min}$ and $D_{\max}$.

equation (see below) are covered without problems.

LIGHT PROPAGATION OUTSIDE THE DIFFUSIVE LIMIT Via the transport mean free path l_t (and assuming that absorption is always significantly weaker than scattering, $\mu_a \ll \mu_t$), it is possible to define different regimes of light propagation, as illustrated in Figure 5.1. For a transport mean free path that is much bigger than the medium thickness L, the photons experience hardly any change of direction due to scattering and thus propagate more or less ballistically. Another extreme case is when l_t is comparable to the light wavelength λ. Then, interference between multiple-scattering paths becomes significant and light can be completely confined in the turbid medium,[4] an effect known as Anderson localization [94], which also today evokes great interest in the scientific community [95, 96]. In between those two extremes lies the regime where light can be described with the diffusion equation.

5.6 SOLUTIONS OF THE DIFFUSION EQUATION

Before we make use of the diffusive nature of photons in turbid media to design an invisibility cloak in section 8.1, I will now present a selection of analytical solutions of the light-diffusion equation. (I won't explicitly

---

[4] In all theoretical considerations presented here, interference effects are simply not considered. Consequently, Anderson localization cannot be a result of the theory derived in this chapter.

derive any solutions here for the sake of brevity. Extensive literature on the derivations can be found in Ref. 85, chapter 4.) The solutions for finite media and the corresponding boundary conditions will play an important role later in the experimental characterization of diffusive media (chapter 7).

SOLUTION FOR AN INFINITE MEDIUM Consider an infinitely extended, homogeneous diffusive medium characterized by its diffusivity D and photon lifetime $\tau = 1/(\mu_{\mathrm{a}} v)$. For an isotropic source q_0 that is a Dirac delta function in time and space,

$$q_0(\vec{r}, t) = \delta^3(\vec{r})\delta(t)\ , \tag{5.35}$$

the solution of the time-dependent diffusion equation (5.34) for $t > 0$ is given by

$$n_{\mathrm{p}}(\vec{r}, t) = \frac{1}{(4\pi D t)^{3/2}} \exp\left(-\frac{r^2}{4Dt} - \frac{t}{\tau}\right)\ , \tag{5.36}$$

with $r = |\vec{r}|$ being the distance from the source. Equation 5.36 is (apart from its absorptive part) equivalent to the so-called *heat kernel*, the fundamental solution of the time-dependent heat-conduction equation. It is the Green's function of the diffusion equation and can thus be used via the superposition principle to obtain solutions for other source types. It represents a Gaussian with a width $\sigma = \sqrt{2Dt}$ that is increasing with time while its height decreases with time, scaled by an exponential decay factor $\exp(-t/\tau)$ due to absorption. This means that sharp features in the photon density tend to soften and "smear out" over time, just as it is the case for the temperature in heat conduction.

BOUNDARY CONDITIONS If we want to obtain solutions of the diffusion equation for finite media, we have to ask ourselves what the boundary condition between a diffusive medium and a non-diffusive medium is.[5] This boundary condition can be derived from the requirement that no diffusive light should enter the medium from the external, non-scattering region. Diffusive light flow directed into the medium can thus only originate from reflections at the boundary Σ. The resulting condition is called *Partial Current Boundary Condition* or PCBC. It connects the photon flux $\vec{J}$ in the direction $\hat{q}$

---

[5] The only boundary condition for an infinite medium is simply that the photon density has to vanish at infinity.

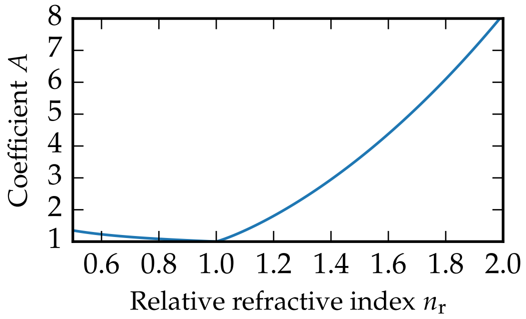

Figure 5.2: PCBC coefficient A versus the relative refractive index $n_\mathrm{r} = n_\mathrm{i}/n_\mathrm{e}$. The higher A is, the more confined the photons are inside the diffusive medium due to total internal reflection.

normal to the interface with the photon density at the interface:

$$\vec{J}(\vec{r},t)\cdot\hat{q}\Big|_{\vec{r}\in\Sigma} = \frac{v}{2A(n_\mathrm{r})} n_\mathrm{p}(\vec{r},t)\Big|_{\vec{r}\in\Sigma} . \tag{5.37}$$

The coefficient $A(n_\mathrm{r})$ depends on the relative refractive index $n_\mathrm{r} = n_\mathrm{i}/n_\mathrm{e}$ between the diffusive medium (n_i) and the surrounding (n_e) and is given by

$$A(n_\mathrm{r}) = \frac{1 + 3\int_0^{\pi/2} R_\mathrm{F}(n_\mathrm{r},\cos\theta)\cos^2\theta\sin\theta\,\mathrm{d}\theta}{1 - 2\int_0^{\pi/2} R_\mathrm{F}(n_\mathrm{r},\cos\theta)\cos\theta\sin\theta\,\mathrm{d}\theta} \tag{5.38}$$

with the Fresnel reflectivity $R_\mathrm{F}(n_\mathrm{r},\cos\theta)$ for unpolarized light. $A(n_\mathrm{r})$ is plotted in Figure 5.2. It has a minimum value of $A(n_\mathrm{r} = 1) = 1$ and is greater than 1 for $n_\mathrm{r} \neq 1$. This means that the photons are more and more confined inside the diffusive medium due to the increasing probability of total internal reflection when the refractive index mismatch to the surrounding increases. Then, fewer photons can escape the diffusive medium. As the proportionality factor between the photon density and the outgoing boundary flux has the unit of a velocity, we define the *photon loss velocity* K as the single coefficient characterizing a diffusive-non-diffusive medium interface:

$$K(v, n_\mathrm{r}) = \frac{v}{2A(n_\mathrm{r})} . \tag{5.39}$$

Using Fick's law (Equation 5.31), the PCBC can also be expressed with the photon density only:

$$\left[n_\mathrm{p}(\vec{r},t) + \frac{D}{K}\frac{\partial}{\partial q} n_\mathrm{p}(\vec{r},t) \right]\Bigg|_{\vec{r}\in\Sigma} = 0 . \tag{5.40}$$

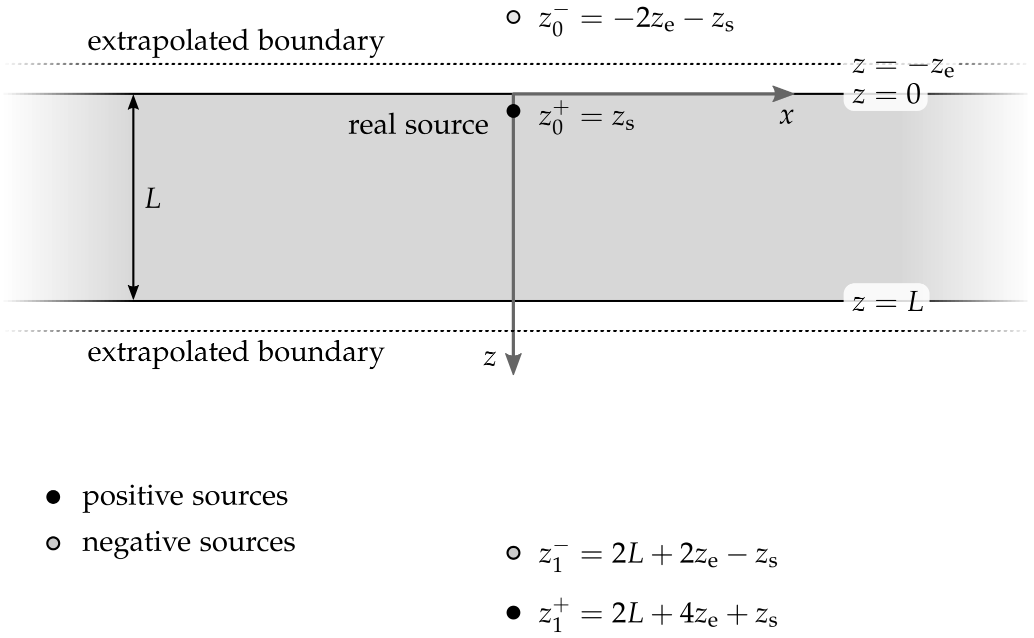

Figure 5.3: Illustration of the method of image sources for solving the diffusion equation for an infinitely extended slab of thickness L. With a point source located at $z_0^+ = z_s$ inside the medium, positive and negative mirror sources are placed along the z-axis. The mirror planes are the extrapolated boundaries (see above) on either side of the slab, where the photon density is assumed to reach a value of zero. Adapted from Ref. 85, Fig. 4.3.

If one assumes that outside of the diffusive medium the derivative of n_p remains constant and equal to the value on the boundary, the photon density itself becomes zero at an *extrapolated distance* z_e from the physical boundary:

$$z_e = \frac{D}{K} \, . \tag{5.41}$$

This assumption of $n_p = 0$ on the surface at the extrapolated distance z_e is called *extrapolated boundary condition* or EBC.

The PCBC and EBC are not the only possible boundary conditions for a diffusive-ballistic medium interface. More choices are outlined in Ref. 85. In many situations, however, all available options lead to results that are almost indistinguishable.

SOLUTIONS OF THE DIFFUSION EQUATION FOR A SLAB of thickness L along z that is infinitely extended along x and y can be obtained from the superposition of solutions for an infinite medium with the method of mirror images [97]. Figure 5.3 illustrates the positions of positive and negative image sources (or rather photon sources and photon "sinks") outside a slab with a single real spatial and temporal delta source located at $(0, 0, z_\mathrm{s})$. The positions of the mth positive and negative mirror sources are constructed from the slab thickness L, the source position z_s, and the extrapolated distance z_e from the EBC condition and are given by

$$\begin{aligned} z_m^+ &= 2m(L+2z_\mathrm{e}) + z_\mathrm{s} \\ \text{and} \quad z_m^- &= 2m(L+2z_\mathrm{e}) - 2z_\mathrm{e} - z_\mathrm{s} \end{aligned} \tag{5.42}$$

with m running from $-\infty$ to ∞. The time-dependent photon density inside the slab is then

$$\begin{aligned} n_\mathrm{p}(\vec{r}, t) = {} & \frac{1}{(4\pi Dt)^{3/2}} \exp\left(-\frac{\rho^2}{4Dt} - \frac{t}{\tau}\right) \\ & \times \sum_{m=-\infty}^{m=\infty} \left\{ \exp\left(-\frac{(z-z_m^+)^2}{4Dt}\right) - \exp\left(-\frac{(z-z_m^-)^2}{4Dt}\right) \right\} , \end{aligned} \tag{5.43}$$

with $\rho = \sqrt{x^2+y^2}$ being the distance from the z-axis and $0 \le z \le L$. The infinite sum of image source terms poses no problem in practice since the summation converges quickly and can usually be truncated after only very few elements.

Integrating Equation 5.43 over x and y from $-\infty$ to ∞ leads to the *homogeneous* photon density for the slab geometry. According to the reciprocity principle, this integration is equivalent to a homogeneous light source that is infinitely extended in the x and y direction. The homogeneous photon density is

$$\begin{aligned} n_\mathrm{p,hom}(z, t) = \int_0^\infty n_\mathrm{p}(\rho, z, t)\, 2\pi\rho \,\mathrm{d}\rho = {} & \frac{1}{(4\pi Dt)^{1/2}} \exp\left(-\frac{t}{\tau}\right) \\ & \times \sum_{m=-\infty}^{m=\infty} \left\{ \exp\left(-\frac{(z-z_m^+)^2}{4Dt}\right) - \exp\left(-\frac{(z-z_m^-)^2}{4Dt}\right) \right\} . \end{aligned} \tag{5.44}$$

If we furthermore integrate Equations 5.43 and 5.44 over all times, we obtain steady-state solutions, equivalent to having continuous-wave (cw) sources:

$$n_{\mathrm{p,cw}}(\vec{r}) = \frac{1}{4\pi D} \sum_{m=-\infty}^{m=\infty} \left\{ \frac{\exp\left(-\mu_{\mathrm{eff}}\sqrt{\rho^2 + (z - z_m^+)^2}\right)}{\sqrt{\rho^2 + (z - z_m^+)^2}} - \frac{\exp\left(-\mu_{\mathrm{eff}}\sqrt{\rho^2 + (z - z_m^-)^2}\right)}{\sqrt{\rho^2 + (z - z_m^-)^2}} \right\} \tag{5.45}$$

and equivalently for homogeneous illumination:

$$n_{\mathrm{p,hom,cw}}(z) = \frac{1}{2\sqrt{\mu_{\mathrm{a}} D}} \times \sum_{m=-\infty}^{m=\infty} \left\{ \exp\left(-\mu_{\mathrm{eff}}|z - z_m^+|\right) - \exp\left(-\mu_{\mathrm{eff}}|z - z_m^-|\right) \right\} . \tag{5.46}$$

Here, μ_{eff} is the effective attenuation coefficient defined as

$$\mu_{\mathrm{eff}} = \sqrt{\frac{\mu_{\mathrm{a}} v}{D}} = \sqrt{\frac{1}{D\tau}} = \sqrt{3\mu_{\mathrm{a}}\mu_{\mathrm{t}}} . \tag{5.47}$$

Note that Equation 5.46 becomes undefined (in the sense of a $0/0$ division) for the non-absorbing case of $\mu_{\mathrm{a}} = 0$. In this case, however, the one-dimensional diffusion equation is solved by a simple linear equation $n_{\mathrm{p}}(z) = az + b$, with the parameters a and b determined by the boundary conditions.

REALISTIC SOURCES The solutions given above assume an isotropic point source embedded inside the diffusive medium at a distance z_{s} from its boundary. Such a situation is not very realistic, as most of the time a diffusive medium will be illuminated from the outside, for example by homogeneous light such as sunlight, or by a so-called pencil beam coming from a laser. A pencil beam impinging under normal incidence can be modeled (using the superposition principle) by a line of isotropic point sources inside the diffusive medium with decreasing intensity according to the Lambert-Beer law. Alternatively (and less costly in terms of calculations), the real source can be substituted by a single point source located at z_{s} as before, with z_{s} being derived from the request that the line of isotropic sources and the single source should have the same first moment. This results in

$$z_{\mathrm{s}} = \frac{1}{\mu_{\mathrm{t}}} = l_{\mathrm{t}} . \tag{5.48}$$

As the transport mean free path l_t is the distance after which a photon's initial direction has been randomized, the relation above also makes sense in an intuitive way.

SOLUTIONS FOR A CUBOID The method of image sources can be adapted to a cuboid diffusive medium with dimensions $L_x \times L_y \times L_z$. Here, a three-dimensional infinite lattice of sources is used. The time-dependent Green's function for a cuboid with a point source located at $(x_\mathrm{s}, y_\mathrm{s}, z_\mathrm{s})$ is then

$$\begin{aligned} n_\mathrm{p}(\vec{r},t) = \frac{1}{(4\pi D t)^{3/2}} \exp\left(-\frac{t}{\tau}\right) \times \sum_{l=-\infty}^{l=\infty} \sum_{m=-\infty}^{m=\infty} \sum_{n=-\infty}^{n=\infty} \\ \Bigg\{ + \exp\left(-\frac{(x-x_{1l})^2+(y-y_{1m})^2+(z-z_{1n})^2}{4Dt}\right) \\ - \exp\left(-\frac{(x-x_{1l})^2+(y-y_{1m})^2+(z-z_{2n})^2}{4Dt}\right) \\ - \exp\left(-\frac{(x-x_{1l})^2+(y-y_{2m})^2+(z-z_{1n})^2}{4Dt}\right) \\ + \exp\left(-\frac{(x-x_{1l})^2+(y-y_{2m})^2+(z-z_{2n})^2}{4Dt}\right) \\ - \exp\left(-\frac{(x-x_{2l})^2+(y-y_{1m})^2+(z-z_{1n})^2}{4Dt}\right) \\ + \exp\left(-\frac{(x-x_{2l})^2+(y-y_{1m})^2+(z-z_{2n})^2}{4Dt}\right) \\ + \exp\left(-\frac{(x-x_{2l})^2+(y-y_{2m})^2+(z-z_{1n})^2}{4Dt}\right) \\ - \exp\left(-\frac{(x-x_{2l})^2+(y-y_{2m})^2+(z-z_{2n})^2}{4Dt}\right) \Bigg\}, \end{aligned} \tag{5.49}$$

with the source positions in all three directions defined as

$$\begin{aligned} x_{1l} &= 2lL_x + 4lz_\mathrm{e} + x_\mathrm{s} \\ x_{2l} &= 2lL_x + (4l-2)z_\mathrm{e} - x_\mathrm{s} \\ y_{1m} &= 2mL_y + 4mz_\mathrm{e} + y_\mathrm{s} \\ y_{2m} &= 2mL_y + (4m-2)z_\mathrm{e} - y_\mathrm{s} \\ z_{1n} &= 2nL_z + 4nz_\mathrm{e} + z_\mathrm{s} \\ z_{2n} &= 2nL_z + (4n-2)z_\mathrm{e} - z_\mathrm{s}\ . \end{aligned} \tag{5.50}$$

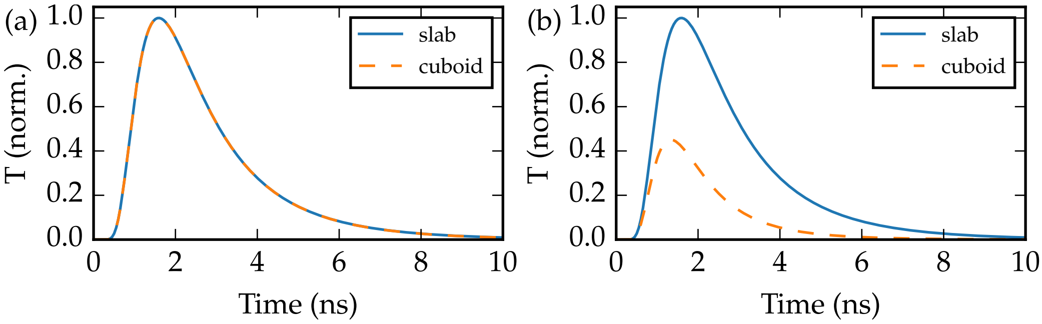

Figure 5.4: Comparison of the time-resolved transmission through a slab of thickness 30 mm and a cuboid of dimensions 150 mm × 80 mm × 30 mm calculated with equations 5.49 and 5.43 ($\mu_\mathrm{t} = 1.6\,\mathrm{mm}^{-1}$, $\mu_\mathrm{a} = 0$, $n_\mathrm{i} = 1.4$, $z_\mathrm{s} = 1/\mu_\mathrm{t}$). (a) Source and detection are at $x = 0$, $y = 0$ (centered with respect to the cuboid surface) and the results for slab and cuboid are indistinguishable. (b) With both source and detection close to the cuboid edge ($x = 70\,\mathrm{mm}$), differences due to the finiteness of the cuboid become pronounced.

Although a bit unpleasant to handle, Equation 5.49 is a straightforward extension of the slab solution given in Equation 5.43.

Figure 5.4 compares the calculated transmission through a slab and a cuboid with equal thickness and optical properties comparable to some of the experiments shown in a later chapter (the transmission is simply proportional to the photon density, see next paragraph). The solutions for slab and cuboid are almost identical when the source and the location of detection are well separated from the cuboid's lateral boundaries. For a source close to these boundaries, however, they act as additional photon loss channels and pronounced differences between slab and cuboid become visible.

CALCULATION OF REFLECTANCE AND TRANSMITTANCE All solutions presented so far represent the photon density n_p inside a diffusive medium. In experiments with finite-sized media, however, the photon density is often not accessible as it would require isotropic measurements of the light intensity inside the medium. The much more convenient quantities with respect to experiments are thus the reflected and transmitted photon flux J_r and J_t. They are easily obtained using the PCBC (Equation 5.37). For the slab, they are given by

$$J_\mathrm{r,slab} = K\, n_\mathrm{p}(z = 0) \quad \text{and} \quad J_\mathrm{t,slab} = K\, n_\mathrm{p}(z = L)\ . \tag{5.51}$$

Equivalently, the outgoing photon flux through the boundary Σ of a cuboid medium is

$$J_{\mathrm{cub}} = K\, n_{\mathrm{p}}(\vec{r} \in \Sigma) \; . \tag{5.52}$$

For the simple case of a non-absorbing, infinitely extended slab of thickness L that is illuminated homogeneously with an incident flux J_{i} from outside, the reflectance R and the transmittance T can be derived simply by connecting the reflected and transmitted flux $J_{\mathrm{r,slab}}$ and $J_{\mathrm{t,slab}}$ from above with a linear equation for the photon density inside the slab: $n_{\mathrm{p}} = az + b$. The resulting diffuse transmittance is

$$T = \frac{J_{\mathrm{t,slab}}}{J_{\mathrm{i}}} = \frac{1}{2 + \frac{KL}{D}} \; . \tag{5.53}$$

This equation represents two important properties of finite diffusive media. First, a maximum of 50 % of the incident light can be transmitted, even for a hypothetically infinitely high diffusivity or an infinitely thin medium. This is simply because diffusion is a non-directional process and any preferred direction of propagation is lost. Second, if the diffusivity is small compared to KL, the diffusive transmission becomes Ohmic: $T(KL \gg D) \propto 1/L$.

An equivalent formula can be derived for a finite photon lifetime τ (or absorption coefficient $\mu_{\mathrm{a}} = 1/(\tau v)$, equivalently):

$$T_{\mathrm{a}} = \frac{2K\sqrt{D/\tau}}{\left(\sqrt{D/\tau} + K\right)^2 \exp\left(+L/\sqrt{D\tau}\right) - \left(\sqrt{D/\tau} - K\right)^2 \exp\left(-L/\sqrt{D\tau}\right)} \; . \tag{5.54}$$

Chapter 6

6 NUMERICAL METHODS FOR DIFFUSIVE LIGHT TRANSPORT

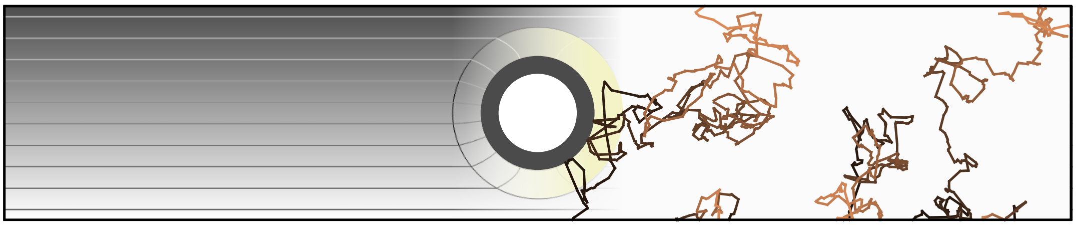

Sample results of the finite-element method (left) and Monte-Carlo photon raytracing (right) for diffuse light

For the design of invisibility cloaks for diffuse light, but also for the interpretation of experimental results, numerical tools that can adequately calculate light transport through the investigated structures are very helpful. In this chapter, I will briefly introduce two such methods: the finite-element method for solving the diffusion equation and Monte-Carlo-based raytracing of individual photons which leads to solutions of the radiative-transfer equation.

6.1 Finite-element method with COMSOL Multiphysics

The light-diffusion equation derived in the preceding chapter is a linear partial differential equation that can be solved analytically for a number of scenarios. However, for more complex problems such as the core-shell geometry to be introduced in section 8.1, analytical solutions are not available and numerical tools need to be employed. One commonly used option is the *finite-element method* [98] which is based on the subdivsion of the complete problem domain into many small parts via the so-called *mesh*, where the equation in question can be solved analytically. Together with the boundary conditions of the complete problem and transition conditions between the mesh elements, a set of linear equations is obtained and solved numerically. The accuracy but also the computation time of the calculation is increased with a finer discretization of the computational domain, that is, with a finer mesh.

The commercial software package COMSOL Multiphysics provides a fully integrated environment for finite-element calculations with tools to model the geometry, define physical boundary conditions, create a mesh, perform calculations, and display or export the results. In this work, the *heat-transfer module* was used to simulate diffusive light transport, making use of the mathematical similarity of the heat-conduction equation and the light-diffusion equation.[1] Therefore, the heat conductivity κ was exchanged by the diffusivity D while both density ρ and specific heat capacity c were set to 1. Boundary conditions at the outer domain surfaces were set according to Equation 5.37.

The big advantage of the finite-element method is its rather low computational cost even for three-dimensional geometries.[2] Hence, results obtained with COMSOL Multiphysics can even be used for optimization routines, as we will see in section 8.2.

The biggest drawback, on the other side, is that by solving the diffuson equation, all media are inherently assumed to be perfectly diffusive, even if this assumption is unphysical. For example, one can easily construct a layer of thickness d with an assumed diffusivity D that leads to a transport mean free path $l_t = 3D/v$ much bigger than d. This by construction violates the

---

[1] The heat-transfer module was also used to obtain the numerical results for the thermal cloak presented in chapter 3.

[2] Compared to other physical systems like electromagnetism or solid mechanics, the cost of computation is particularly low for light diffusion as there is only one scalar variable (the photon density) that is solved for.

diffusion approximation but would still be considered diffusive by COMSOL Multiphysics and thus lead to incorrect results. Similarly, situations where a medium might be just on the border to being diffusive (with respect to the criteria given in section 5.5) might not be modeled correctly anymore with the diffusion equation but still prove useful in experiments. We will see later that the high-diffusivity shell which is part of our diffusive-light core-shell cloaks is *not* a proper diffusive medium in some of our experimental realizations, which leads to discrepancies between the experiment and numerical results obtained from the diffusion equation. Still, such a shell can lead to almost perfect cloaking of diffuse light.

To be able to tackle also such mixtures of diffusive and ballistic light transport, I will now introduce Monte-Carlo-based raytracing of individual photons as the second numerical method of our choice.

6.2 MONTE-CARLO-BASED PHOTON RAYTRACING

In section 5.2, we learned that the scattering and absorption properties of turbid media lead to the probability functions f_θ, f_φ, and f_z for the scattering angles θ and φ and the traveled path length z. Using these functions, a simple scheme can be devised to simulate the path a photon takes through a turbid medium:

1. Choose a starting position $\vec{r}_\mathrm{p}$ and direction $\vec{v}_\mathrm{p}$ according to the light source.[3]
2. Randomly choose a step length l satisfying the probability function f_z.
3. Propagate the photon to $\vec{r}\,'_\mathrm{p} = \vec{r}_\mathrm{p} + l\vec{v}_\mathrm{p}$.
4. Randomly choose scattering angles θ and φ that satisfy the probability functions f_θ and f_φ and update $\vec{v}_\mathrm{p}$ accordingly.
5. Iterate steps 2–4 until the photon exits the medium, is absorbed or exceeds a maximum propagation time. If the photon exits, record its exit position and the overall path length it traveled. The image shown on page 67 displays a few examples of such calculated photon paths.

---

[3] Note that most available raytracers for photorealistic rendering start rays from the detector (the camera) instead of from the light source. This greatly reduces the computation times as no unnecessary light rays that start at the light source but never reach the detector are traced. However, the statistical nature of diffusive light transport prohibits us from doing the same in our Monte-Carlo simulations.

Repeating this scheme for a huge number of photons will (ideally) reproduce the mentioned probability functions for each possible photon path. The distribution of exited photons will then be a solution of the radiative-transfer equation (even though the equation itself is not known to the simulation routine). Photon absorption as well as time-resolved information can easily be accounted for via the total optical path length traveled by each photon. The Monte-Carlo method for photon transport is a tool that is today commonly used in biomedical optics [99].

6.2.1 *Sampling of the probability functions*

In general, random numbers that satisfy the desired probability functions are not directly available. Instead, uniformly distributed random numbers between 0 and 1 are mapped onto the desired distributions via *inverse transform sampling* [100]. The essence of this method is that given a uniformly distributed random variable $u \in [0, 1]$ and an invertible cumulative distribution function (CDF) F, the variable $x(u) = F^{-1}(u)$ is distributed according to F. The CDF is obtained from a probability function f via

$$F(x) = \int_0^x f(x')\,\mathrm{d}x' \,, \tag{6.1}$$

and since $f(x)$ is normalized to 1, $F(x)$ assumes all values between 0 and 1.

As absorption is accounted for via the total path length traveled by a detected photon, the photon step length is based on the scattering coefficient alone:

$$f_l(l) = \mu_\mathrm{s} \exp\left(-\mu_\mathrm{s} l\right) \quad \rightarrow \quad F_l(l) = \int_0^l f_l(l')\,\mathrm{d}l' = 1 - \exp\left(-\mu_\mathrm{s} l\right) . \tag{6.2}$$

Introducing the uniformly distributed random number u, this is easily inverted according to the scheme above to

$$l(u) = F_l^{-1}(u) = -\frac{\ln\left(1-u\right)}{\mu_\mathrm{s}} = -\ln\left(1-u\right) l_\mathrm{s} \,, \tag{6.3}$$

which is the recipe to calculate a random step length l from a uniform random number u.

For a photon step that covers the interface between two diffusive media with the same refractive index but different scattering coefficients $\mu_{s,1}$ and $\mu_{s,2}$, the CDF from above is modified to

$$F_l(l) = 1 - \exp\left(-\mu_{s,1} l_1 - \mu_{s,2} l_2\right) , \tag{6.4}$$

with the partial step lengths l_1 and l_2 in the two media. In an implementation, a total step size l is usually computed according to Equation 6.3 *before* knowing that an interface will be passed after $l_1 < l$. In this case, the remaining step size $\tilde{l}_2 = l - l_1$ has to be rescaled according to the second medium's scattering properties such that the CDF is still fulfilled:

$$l_2 = \tilde{l}_2 \frac{\mu_{s,2}}{\mu_{s,1}} . \tag{6.5}$$

In the same fashion as above, the rule to calculate the scattering angle φ is obtained:

$$\varphi(u) = 2\pi u . \tag{6.6}$$

Obviously, u has to be a *different* random number than before.

However, the CDF for the scattering angle θ is likely to be more complicated:

$$F_\theta(\theta(u)) = 2\pi \int\limits_0^{\theta(u)} p(\theta') \sin\theta' \, \mathrm{d}\theta' , \tag{6.7}$$

and can only be inverted when a simplified analytical model for the scattering phase function $p(\theta)$ is used. This is fulfilled for the *Henyey-Greenstein* phase function [101], which is not only invertible but also depends only on the asymmetry factor g and thus fits well to our previous description of turbid media. The Henyey-Greenstein scattering phase function is defined as

$$p(\theta) = \frac{1}{4\pi} \frac{1 - g^2}{(1 + g^2 - 2g\cos\theta)^{3/2}} . \tag{6.8}$$

It was devised in 1941 to describe scattering of light in interstellar dust clouds and approximates the shape of an actual phase function, yielding full isotropy for $g = 0$ and forward scattering for $g > 0$. Example plots of the Henyey-Greenstein phase function are given in Figure 6.1. Calculating and

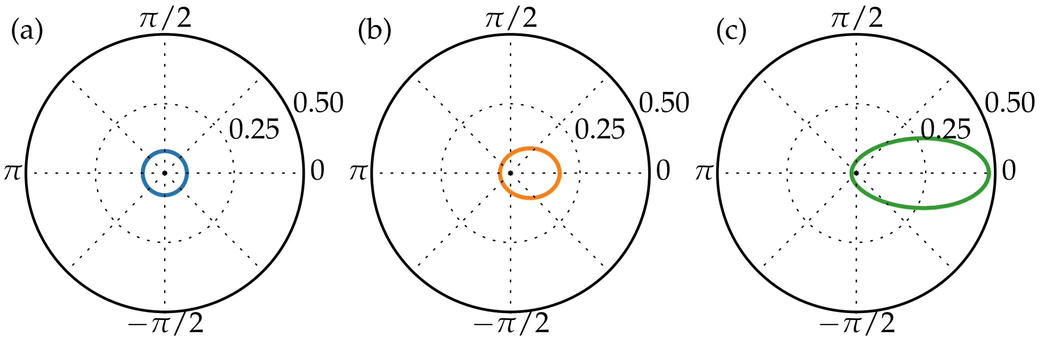

Figure 6.1: Polar plots of the Henyey-Greenstein scattering phase function for three different values of the asymmetry factor g: (a) $g = 0$, (b) $g = 0.25$, (c) $g = 0.5$.

inverting the CDF of the formula above, the sampling rule for the cosine of the scattering angle is then obtained as

$$(\cos\theta)(u) = \begin{cases} \dfrac{1}{2g}\left(1 + g^2 - \left(\dfrac{1-g^2}{1-g+2gu}\right)^2\right) & \text{if } g \neq 0 \\ 1 - 2u & \text{if } g = 0\,. \end{cases} \tag{6.9}$$

(For choosing new propagation directions, only the cosine of θ is needed in any way.)

6.2.2 *Implementation of a photon raytracer*

With the three sampling rules $l(u)$, $(\cos\theta)(u)$, and $\varphi(u)$, a photon raytracer for radiative transport can be implemented. Although some implementations are freely available [102–104], their intended scope and thus also their features vary a lot. Most of them are intended for biomedical applications, making them not easy to adapt to the scenario of diffusive-light cloaking.

Frederik Mayer, who contributed to this project within the scope of his Master's thesis, and I therefore implemented a photon raytracer (called Fast Raytracer fOr Diffusive Optics or FRODO) tailored to our needs.[4] I will briefly list its most important features here.

Since every photon inside a turbid medium is completely independent and because the mathematical operations involved in the tracing process are

---

[4] We also used a programm called MMC (Mesh-based Monte Carlo) by Q. Fang [103], which proved to be too unflexible for our specific needs. I will refrain from showing results obtained with MMC in this thesis.

rather simple, Monte-Carlo raytracing is ideally suited for massive parallelization using graphics processors. We hence implemented FRODO using C++ and Nvidia CUDA in such a way that each photon is traced in a single, independent graphics processor thread. Depending on the available hardware, this enables simultaneous tracing of up to a few thousand photons (compared to 4–16 parallel tracing threads on a current consumer CPU).

We implemented a simple library of *constructive solid geometry* [105] primitives (cuboid, sphere, cylinder, and prism) that can be combined using Boolean operations. Geometries such as the core-shell cloak used in this work are simple to implement with these tools.

Turbid media are specified in FRODO via their absorption coefficient μ_a, scattering coefficient μ_s, asymmetry factor g, and refractive index n. Refractive index mismatches between two adjacent media or to the surrounding are taken into account via the Fresnel coefficients for unpolarized light. Besides turbid media, completely opaque media with a certain reflectance R (and corresponding absorbance $1 - R$) can be defined. Reflection off of such media can be set to be specular or Lambertian, or an arbitrary mixture of the two.

An arbitrary number of point, plane or disc sources can be defined with directional, isotropic, or Lambertian emission patterns. To reduce the amount of data to be saved, planar detectors can be defined that already sort incoming photons into spatial and temporal bins. Thus, the result data that is eventually saved is one image per detector per time bin, reducing the amount of necessary post-processing a lot. The weight of detected photons is scaled according to the Lambert-Beer law using the path lengths traveled in each medium and the corresponding absorption coefficients.

All simulation parameters are controlled via a simple plain-text configuration file, making it easy to call FRODO from other software, for example from MATLAB in combination with an optimization algorithm. As the runtime of a simulation depends heavily on the scattering parameters as well as on the size and complexity of the geometry, giving performance indicators here is not meaningful. I will instead include the computation time whenever results obtained with FRODO are shown in the following chapters.

7

Chapter 7

REALIZATION AND CHARACTERIZATION OF DIFFUSIVE MEDIA

Ingredients and examples of PDMS-based (left) and water-based (right) diffusive media

So far, diffusive media have been the rather abstract concept of scattering particles suspended in a dielectric background medium. In this chapter, I will describe how we realized the different diffusive media used in this work and present methods to characterize them in terms of their scattering coefficient, asymmetry factor, and absorption coefficient.

7.1 Realization of diffusive media

Realizing diffusive media is as simple as homogeneously mixing scattering particles into a non-absorbing background medium. In principle, this background can be gaseous, liquid, or solid (consider clouds, milk, and bone as examples). In this work, we created both liquid and solid diffusive media which I shall describe here shortly. More details on each specific medium will be given later whenever its application is described.

Liquid background media have the big advantage of being very flexible regarding the concentration of scattering particles. A higher concentration can easily be achieved by adding particles, a lower concentration by diluting the medium. We used de-ionized water as the background medium for our early experiments where such flexibility was crucial, with the scatterers ranging from fat droplets in milk to silica (SiO_2) or titania (TiO_2) nanoparticles. The greatest disadvantage of a liquid background medium is the potential sedimentation of suspended particles, which might lead to a change in the diffusivity over time. Futhermore, liquid media are obviously less pleasant to handle and might pose a danger to other lab equipment. One also needs a container that holds the liquid, which might result in less-well-defined boundary conditions of the diffusive medium.

Solid background media come with the obvious advantage of inherent long-term stability and very easy handling. Furthermore, it is straightforward to have different solid diffusive media next to each other, while they would immediately intermix if they were liquid-based. We used the transparent silicone polydimethylsiloxane (PDMS) for all solid diffusive media. Solid PDMS[1] is obtained by mixing a high-viscosity base with a low-viscosity curing agent (in a volume ratio of 10:1), followed by a polymerization over about 24 hours, which can be sped up by a higher ambient temperature. Depending on the type of scattering particles, the viscosity of the constituents of PDMS makes homogeneous mixing of the particles therein difficult. We obtained the best results by stirring the low-viscosity curing agent mixed with the particles for a time of at least 12 hours before mixing it with the high-viscosity base. With this procedure, we couldn't find indications of particle agglomerations.

---

[1] We used the Sylgard® 184 elastomer kit supplied by Dow Corning, USA.

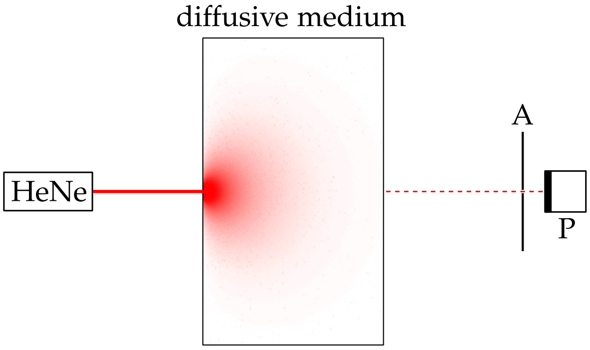

Figure 7.1: Setup for measuring the power that is ballistically transmitted through a diffusive medium. An aperture (A) in front of the photodiode detector (P) aligned with the beam axis of the laser illumination selects only photons that passed the medium without significantly changing their direction and thus without any scattering.

SCATTERING PARTICLES should be low-absorbing dielectric particles with a refractive index that is significantly different from that of the background medium. Furthermore, they should mix well with the backround medium and be chemically stable over a long time.

Over the course of this project, titanium dioxide (TiO_2) nanoparticles[2] proved to be suited best for the controlled realization of diffusive media. TiO_2 is widely used as a white pigment due to its high refractive index of more than 2.5 throughout the visible [106]. The TiO_2 particles we used furthermore had a thin coating of $Al(OH)_3$ and SiO_2 to increase their dispersibility.

Other choices that have eventually been neglected in favor of the TiO_2 nanoparticles were

- fat droplets in milk (which have a rather high absorption and are not long-term stable),
- silica (SiO_2) microparticles (which were also rather absorptive),
- polystyrene and melamine-resin microparticles (which are expensive and have a rather low refractive-index contrast with water or PDMS),
- and TiO_2 particles in white wall paint (which tended to sediment in water and were not well defined due to unknown additives in the paint).

7.2 STATIC CHARACTERIZATION

We have seen in section 5.1 that the ballistic portion (the part that is neither scattered nor absorbed) of a light beam with initial power P_0 traveling through a turbid medium decays with the distance z via the Lambert-Beer law (see Equation 5.8). Thus, by measuring the ballistic transmission $T_{\text{ball}} = P(L)/P_0$ of light through a diffusive medium of thickness L, we can directly obtain the extinction coefficient μ_{ex}:

$$\mu_{\text{ex}} = -\frac{\ln\left(P(L)/P_0\right)}{L} \,. \tag{7.1}$$

Usually, the scattering coefficient is much bigger than the absorption coefficient, which is why for low absorption, the relation above directly yields $\mu_{\text{s}} \approx \mu_{\text{ex}}$, from which also the scattering mean free path can be calculated ($l_{\text{s}} = 1/\mu_{\text{s}}$).

Figure 7.1 shows a scheme of the experimental setup to measure the power ballistically transmitted through a diffusive medium. A collimated laser beam is shone onto the sample. Behind the sample, a small aperture aligned with the laser beam axis selects a small fraction of the solid angle and thus transmits only light that has not significantly scattered on its way through the sample.

Figure 7.2 shows the measured ballistic transmission through PDMS samples with varying amounts of TiO_2 nanoparticles. As the ballistic transmission gets very small for thick samples that are well in the diffusive limit, the test samples used were thinner ($L = 1\,\text{cm}$) than the cloaks we later built ($L = 3\,\text{cm}$).[3] P_0 was measured not for air but for an undoped PDMS sample to correctly account for reflection losses at the medium boundaries. The transmitted power is given on a logarithmic scale and nicely confirms the proportionality of scattering coefficient and scatterer concentration (see Equation 5.1). With this proportionality experimentally confirmed, one can already roughly estimate the diffusivity from a medium's scattering coefficient. (The refractive index n is usually known up front for the background medium and can be assumed not to change significantly with the addition

---

[2] R700 and R706 particles provided from DuPont, USA

[3] For water-based media, the same principle applies. We thus used a cuvette with a thickness of only a few mm to obtain appreciable ballistic transmission for the relevant concentrations of scattering particles.

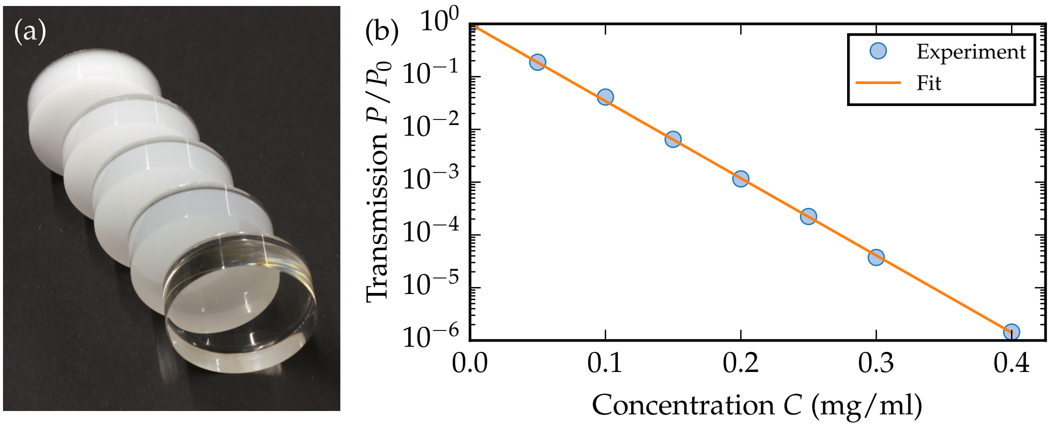

Figure 7.2: (a) Photograph of a few PDMS-based test samples with different concentrations C of TiO_2 nanoparticles. (b) Measured ballistic transmission versus the scattering particle concentration (circles). The exponential fit (solid line) yields the scattering coefficient $\mu_s = 3.37\,\mathrm{ml}/(\mathrm{mg\,mm}) \times C$.

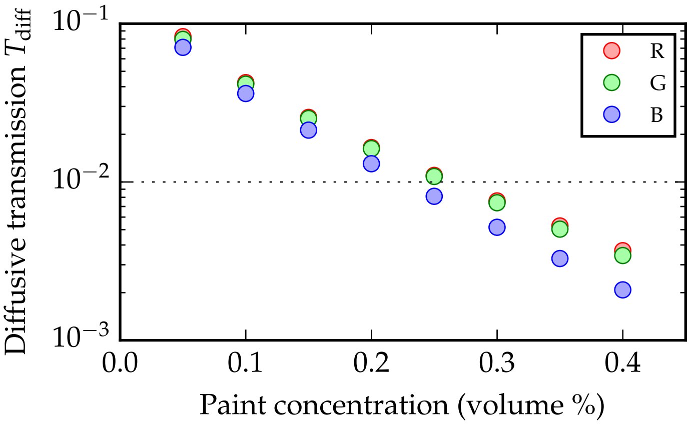

Figure 7.3: Measured diffusive transmission through a homogeneously illuminated water-paint slab with thickness $L = 60\,\mathrm{mm}$ (divided into the red, green, and blue color channel). According to Equation 5.54, the diffusive transmission decreases with an increasing amount of scattering particles.

of scattering particles.) However, for a full characterization, the asymmetry factor g and also the absorption coefficient μ_a are still needed.

One approach to statically determine diffusivity D and absorption coefficient μ_a is to homogeneously illuminate samples with different scatterer concentrations, measure the portion T_{diff} of the light that is transmitted diffusively (in the diffusive limit, the ballistic portion of the transmitted light is negligibly small in any way), and then fit Equation 5.54 to the data with D and μ_a as fit parameters. Figure 7.3 shows results of such a measurement for a water-paint mixture contained in a Plexiglas tank with an inner thickness of $L = 60\,\mathrm{mm}$, illuminated with white light emitted from a computer monitor. The water-paint mixture was continuously stirred to avoid sedimentation and ensure good mixing whenever the paint concentration was changed. The results are given separately for the three color channels of the camera we used for the measurement. Obviously, either the absorption or the scattering coefficient (or both) is wavelength-dependent, resulting in a reddish color tint.[4] The process of fitting Equation 5.54 to the data proved to be unrealiable, however. First, the photon-loss velocity K has to be known for the fit (otherwise, there are just too many free parameters), which was not the case for water-based media where the Plexiglas tank windows prevented a reliable calculation of K. Second, even the results for only two free parameters were not unique with respect to slight variations of both of them at the same time.

In summary, static measurements provide easy experimental access to the scattering coefficient of a diffusive medium, but are not sufficient for a full characterization of the medium's optical properties.

7.3 DYNAMIC CHARACTERIZATION

The main problem in the determination of a medium's diffusivity with static measurements is that in the results, the effects of diffusivity and absorption cannot be distinguished easily from another: the effective absorption coefficient is $\mu_{\mathrm{eff}} = 1/\sqrt{(D\tau)}$, meaning that when the diffusivity decreases, less light is transmitted diffusively but also more light is absorbed due to a longer average time the photons spend inside the medium.

With dynamic, time-resolved measurements, however, distinguishing between diffusion and absorption becomes easy. Consider a diffusive medium that is illuminated at $t = 0$ by a point-like source with a light pulse that is very short compared to the medium's diffusive time constant $\tau_{\mathrm{diff}} = L^2/(6D)$.[5] Then, all light detected at a point in time $t > 0$ anywhere in the medium

---

[4] For the case of DuPont R700 TiO_2 particles in PDMS, more properties of the particles were known and we could identify a wavelength-dependent scattering cross section via Mie theory. (See section 8.4 for details.)

[5] In 3D, the diffusive time constant τ_{diff} is obtained by calculating the mean distance r_{m} a photon has traveled from the origin at time t via the Green's function $n_{\mathrm{p}}(\vec{r}, t)$ for an inifinitely extended absorption-free medium (Equation 5.36): $r_{\mathrm{m}} = \int_0^\infty r^2 n_{\mathrm{p}}(\vec{r}, t)\,\mathrm{d}V = 6Dt$. Setting $r_{\mathrm{m}} = L$ yields $\tau_{\mathrm{diff}} = L^2/(6D)$ [77, 107].

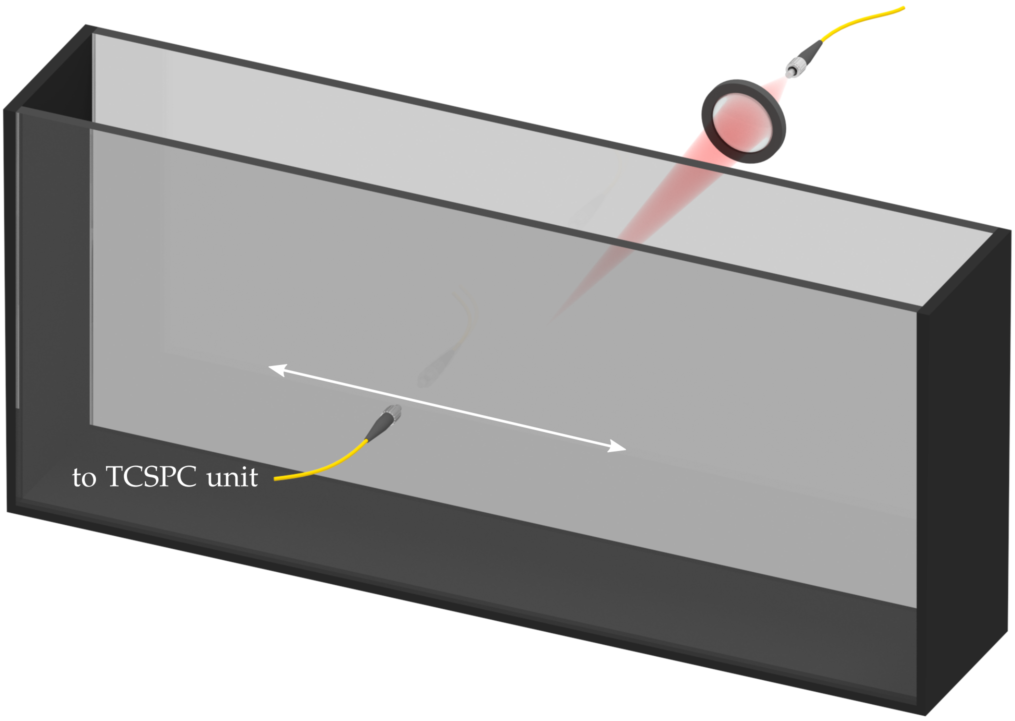

Figure 7.4: Setup for temporally and spatially resolved measurement of diffusive light transmission. The sample (for illustration here an empty tank for water-based media) is illuminated by a focused laser beam. The transmitted light is collected with a multimode fiber and fed into a time-correlated single-photon counting (TCSPC) unit. The detection fiber position can be scanned horizontally to obtain spatial resolution.

or at its boundaries has travelled exactly the same distance and thus experienced exactly the same absorption. In other words, for a given point in time, absorption does not influence the distribution of photons (the "shape" of the photon density), but only their amount.

Looking at the formula for the photon density inside an infinitely extended slab of thickness L again (Equation 5.43),

$$\begin{aligned} n_{\mathrm{p}}(\vec{r},t) = {} & \frac{1}{(4\pi D t)^{3/2}} \exp\left(-\frac{\rho^2}{4Dt} - \frac{t}{\tau}\right) \\ & \times \sum_{m=-\infty}^{m=\infty} \exp\left(-\frac{(z-z_m^+)^2}{4Dt}\right) - \exp\left(-\frac{(z-z_m^-)^2}{4Dt}\right), \end{aligned}$$

it becomes clear that at either side of the slab ($z = 0$ or $z = L$, with ρ being the lateral distance from the z-axis), the photon density is a Gaussian distribution with a squared width σ^2 that is linearly increasing in time without being influenced by absorption [108]:

$$\sigma^2 = 2Dt \, . \tag{7.2}$$

Thus, by temporally and spatially measuring the light transmitted through a slab illuminated with a short and focused light pulse and plotting $\sigma^2/2$ versus t, one immediately gets the diffusivity D from the slope of the plot.[6]

Figure 7.4 shows the setup we used for such temporally and spatially resolved measurements. We illuminated the sample with laser pulses of 50–500 ps duration with a repetition rate of 10 MHz and a wavelength of about 640 nm. The laser[7] was coupled to an optical fiber and then focused onto the sample center behind the far end of the fiber to obtain a small illumination spot. The diffusively transmitted light was then collected with a multimode fiber[8] directly behind the sample and fed to a single-photon counting module[9] which was connected to a time-correlated single-photon counting unit.[10] For single-photon counting, only a maximum of 5 % of the incident photon rate should reach the detector for reliable time resolution. For larger detected photon count rates, the result is biased towards early times because of a too small probability for the detection of late photons [109]. Thus, the generally low light transmission through diffusive media posed no problem for dynamic characterization.

The detection fiber was scanned horizontally via a motorized linear stage to obtain spatial resolution. As the result is rotationally invariant with respect to the laser beam axis (assuming that edge effects due to the finite-sized samples are negligible), spatial resolution along one axis sufficed for a full characterization.

The results of a corresponding measurement for a water-paint mixture inside a Plexiglas tank is shown in Figure 7.5. Panel (a) shows the spatially resolved photon counts for three selected time bins, from each of which the squared Gaussian width σ^2 can be extracted. In panel (b), $\sigma^2/2$ is plotted

---

[6] In the attempt to realize Anderson localization of visible light in three dimensions, deviations from this linear behavior can be used as an indicator for light confinement. [96]

[7] LDH-D-C-640 from PicoQuant, Germany

[8] Core diameter 200 nm, NA = 0.12

[9] SPCM-AQR-14 from PerkinElmer, USA

[10] PicoHarp 300 from PicoQuant, Germany

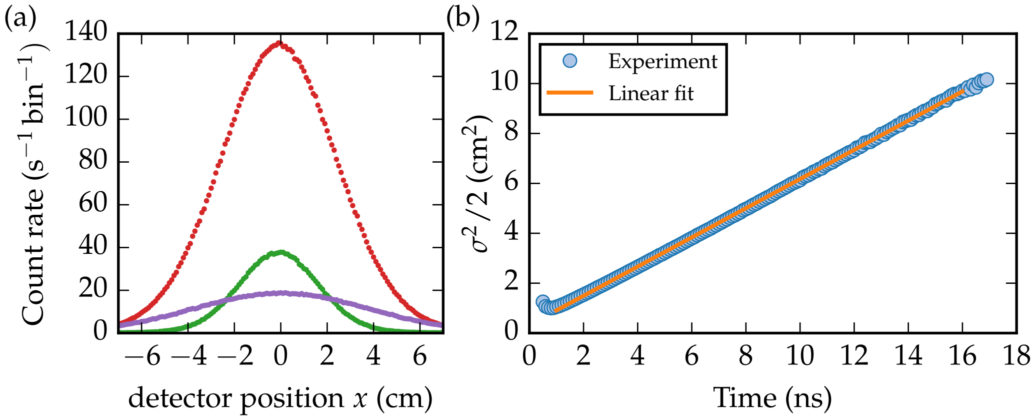

Figure 7.5: (a) Spatially resolved light intensity transmitted through a water-paint mixture with a thickness of $L = 60$ mm and a paint concentration of 0.35 % for 64 ps long time bins at $t = 2$ ns (green dots), $t = 5$ ns (red dots), and $t = 12$ ns (purple dots) after a short laser pulse hits the medium. (b) Squared spatial width $\sigma^2/2$ extracted from the curves as shown in (a) versus time. The slope of the linear fit is the medium diffusivity of $D = 5.27 \times 10^8\,\mathrm{cm^2/s}$

versus the time t, which confirms the expected linear relation between σ^2 and t and directly yields the diffusivity of the medium. The asymmetry factor g can then be calculated from the diffusivity D, the refractive index n, and the scattering coefficient μ_s (determined via static ballistic transmission measurements, see above).

DETERMINING ABSORPTION Absorption is the last missing piece in the puzzle of full characterization of diffusive media. But problems can also occur in the determination of the diffusivity (with the method described above) when the diffusive time constant becomes comparable to the length of the instrument response function of the measurement setup (as it was the case for our PDMS-based samples). Then, the temporal measurement result is a convolution of the temporal response of the setup and the actual sample's response that we are interested in. In this case, the assumption that all light detected at a certain time t has traveled the same distance and thus experienced the same absorption is not valid anymore.

Both these hurdles can be taken with the same temporally and spatially resolved measurement as described before, but with a slightly more complex analysis of the measured data. For known photon-loss velocity K and

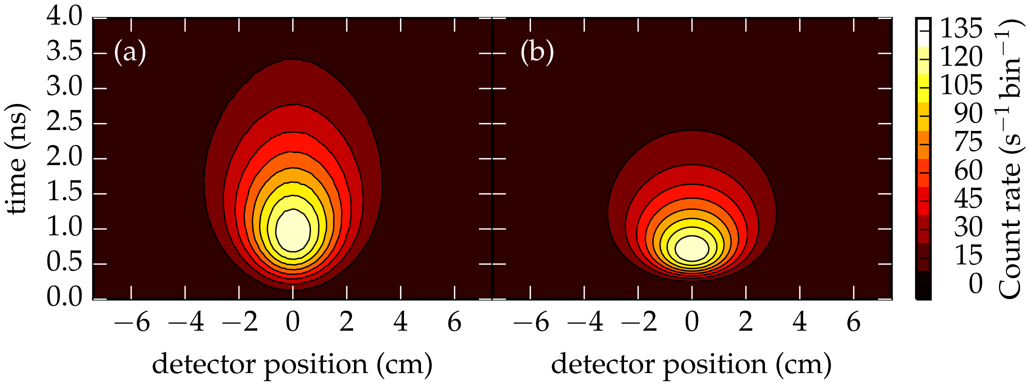

Figure 7.6: (a) Measured temporally and spatially resolved photon count rate transmitted through a PDMS-based diffusive sample with dimensions $15 \times 8 \times 3\,\mathrm{cm}^3$ and a $\mathrm{TiO_2}$ nanoparticle concentration of 0.39 mg/ml, displayed on a false-color scale. The bin width is 64 ps. (b) Deconvoluted data using Equation 5.49 as the fitting model. The deconvolution yields a diffusivity of $D = 11.9 \times 10^8\,\mathrm{cm}^2/\mathrm{s}$ and a photon lifetime of $\tau = 10.5\,\mathrm{ns}$.

medium dimensions, the diffusivity D and the photon lifetime τ are the only free parameters in the equations describing the time-dependent transmission through a diffusive slab or cuboid (equations 5.43 and 5.49 together with equation 5.51). By fitting these equations to the measurement results, we thus can access diffusivity and absorption at the same time.

To obtain the pure temporal response of the diffusive medium, we further need to deconvolute the raw data we measure. To do this, we unfortunately cannot simply take the fourier transform of the measurement and the instrument response, divide the two and fourier-transform back, as such an *inverse filtering* gives bad results once noise is present [109, 110]. Therefore, we start with a guess for the parameters D and τ in the numerical model and convolve this model with the instrument response function (that is, with the measurement result obtained without any sample). We can then use an optimization algorithm that minimizes the error between the measured data and the numerical model, using D and τ as optimization parameters. Figure 7.6 illustrates this deconvolution process for the example of a homogeneous PDMS-based diffusive sample.

The deconvolution method described above can only work if two requirements are met: First, the medium investigated has to be well in the diffusive regime, as otherwise using solutions of the diffusion equation for the data analysis makes no sense. (This is also true when determining a medium's diffusivity via the time-dependent width of the transmitted Gaussian intensity pattern described at the beginning of this section.) Second, the photon-loss velocity K has to be known to reduce the number of free parameters in the numerical model. This condition effectively excludes all water-based media from full characterization, as any container wall (in our case about 5 mm thick Plexiglas) prevents a straightforward calculation of K. For solid samples such as the ones based on PDMS, however, the methods described in this chapter provide a complete toolset for the characterization of diffusive media.

As we will see in the next two chapters, the knowledge gained from the full characterization of diffusive media is crucial for understanding some of the intricacies of diffusive-light cloaking. The four quantities that can be determined (absorption coefficient μ_a, scattering coefficient μ_s, asymmetry factor g, and refractive index n) are also the only parameters needed as input for Monte-Carlo simulations according to section 6.2.

8 Chapter 8

STATIC DIFFUSIVE-LIGHT CLOAKING

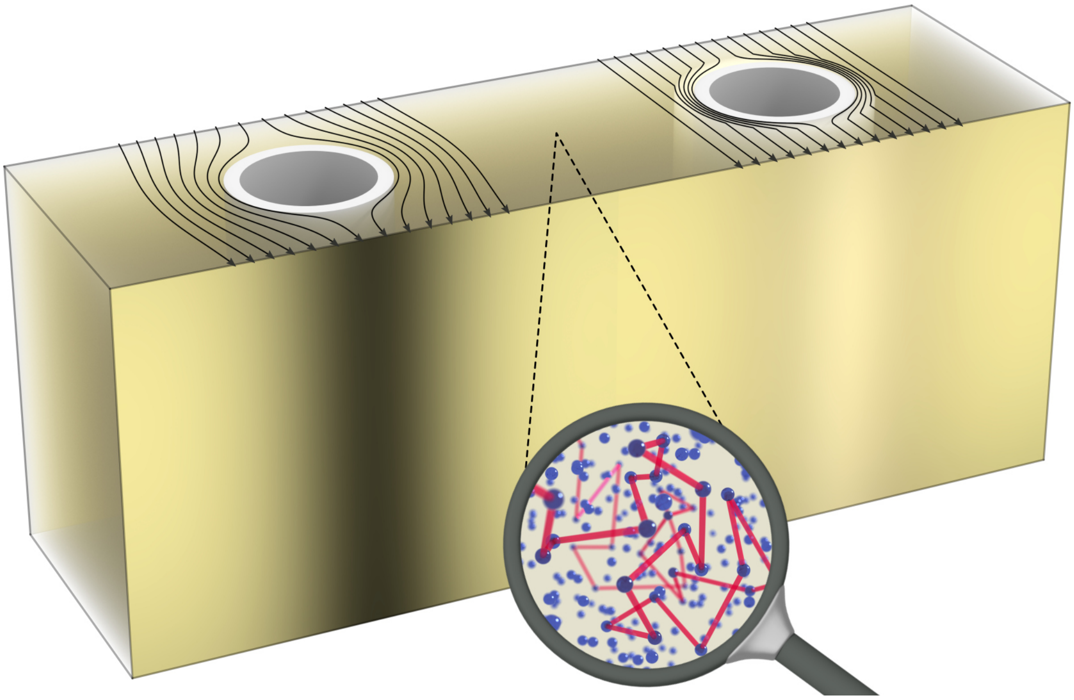

Concept of core-shell cloaking illustrated by photon-flux lines and resulting transmission images

With all necessary theoretical and experimental tools concerning light diffusion ready, I will now show how the concept of neutral inclusions can be used to build macroscopic and broadband static core-shell cloaks for diffuse light. I will present experimental and numerical results for liquid-based as well as solid-based cloaks under several illumination conditions and extend the concept of core-shell cloaking to multi-shell designs for optimized cloaking under inhomogeneous illumination.

8.1 The concept of core-shell cloaking

Since the light-diffusion equation is mathematically very similar—and in the static limit even identical—to the heat-conduction equation introduced in chapter 3, we could in principle simply adapt the design of the thermal cloak to create an invisibility cloak for *static* light diffusion. (We will see in chapter 9 why things are not so easy for *dynamic* diffusive-light cloaking.) We would end up with a multilayer structure consisting of shells with alternatingly high and low diffusivity—and would most probably fail in the attempt to realize it experimentally. As outlined in section 5.5, very thin media with very high diffusivities (as needed in such a multilayered design) don't fulfill the requirements for diffusive light transport. In practice, such layers would contain so few scatterers that most light could pass them without being scattered at all. One could force every layer to be in the diffusive regime by increasing the scatterer concentration everywhere while leaving the contrasts between the rings untouched. Then, however, the resulting structure would have an overall effective diffusivity so low that hardly any light would be transmitted, rendering the cloak effectively lightproof.

Fortunately, a different approach fitting much better to the constraints of light diffusion has been devised already 50 years before the first publications on transformation optics: In 1956, E. H. Kerner published two papers on the elastic and electric properties of composite media [31, 32] and introduced the notion of *neutral inclusions*, which are composite regions with properties that make them appear exactly as their homogeneous surrounding medium.

The idea behind such neutral inclusions is very simple and—translated to the nomenclature of light diffusion—goes like this: Consider a cylindrical (or spherical) region with radius R_1 and a diffusivity D_1 that is lower than the diffusivity D_0 of the homogeneous surrounding medium. When illuminated homogeneously from one side, this low-diffusivity inclusion will disturb the photon flux in the surrounding. As illustrated in Figure 8.1 (a), the flux streamlines in this arrangement will be bent away from the inclusion. This disturbance results in a lower photon density or, in other words, a diffusive shadow, behind the inclusion, illustrated by a lower density of streamlines in Figure 8.1 (a). Similarly, an inclusion with radius $R_2 > R_1$ and a diffusivity D_2 that is *higher* than that of the surrounding will result in flux lines bent *towards* the inclusion (Figure 8.1 (b)) as well as in a brighter region (with a higher photon density) behind. One can now intuitively assume that the disturbance of the photon flux might vanish for the combination of both inclusions, if only the right set of radii R_1 and R_2 and diffusivities D_0, D_1, and D_2 is found. As it turns out, this assumption is correct (see the straight streamlines in Figure 8.1 (c)) and even leads to an analytical formula connecting radii and diffusivities that is also known as the *Hashin-Shtrikman formula* [33, 39]. Its derivation is not very instructive for the understanding of core-shell cloaking and shall be omitted here. (A concise derivation can be found in chapter 7 of Ref. 39.) Under the prerequisite of a constant gradient of the photon density ($\vec{\nabla} n_\mathrm{p} = \mathrm{const.}$), which translates directly to a *homogeneous illumination*, one finds

$$\frac{R_2}{R_1} = \sqrt{\frac{(D_2 + D_0)(D_2 - D_1)}{(D_2 - D_0)(D_2 + D_1)}} \tag{8.1}$$

for cylindrical symmetry, and

$$\frac{R_2}{R_1} = \sqrt[3]{\frac{(2D_2 + D_0)(D_2 - D_1)}{(D_2 - D_0)(2D_2 + D_1)}} \tag{8.2}$$

for spherical symmetry. In the following, I will usually call the inner, low-diffusivity part of such an inclusion *core*, and the outer, high-diffusivity part *shell*.

The neutral inclusion described by equation 8.1 or 8.2 is not a cloak yet. It is an invisible object, but once we try to hide something inside the core, the photon flux will again be disturbed by whatever we try to hide and the invisibility will collapse. As we already learned in chapter 3 on thermodynamic cloaking, a good isolation of the cloaked region is crucial. Here, we can achieve this by setting the diffusivity D_1 of the core to exactly zero. As can be seen in Figure 8.1 (d), the streamlines of the photon flux are then completely "pushed out" of the core,[1] which is compensated for by the high-diffusivity shell around it. A medium with $D = 0$ is a perfect diffuse reflector, meaning that not a single photon can enter it. We can thus realize the same behavior with a hollow instead of a solid core, carving out a region (shown in white in Figure 8.1 (d)) where arbitrary objects can be hidden. For

---

[1] An analog to a medium with $D = 0$ is a type-1 superconductor with $\mu = 0$ that entirely expulses the magnetic field from itself when below the critical temperature. This expulsion was also used for static magnetic cloaking [27, 28].

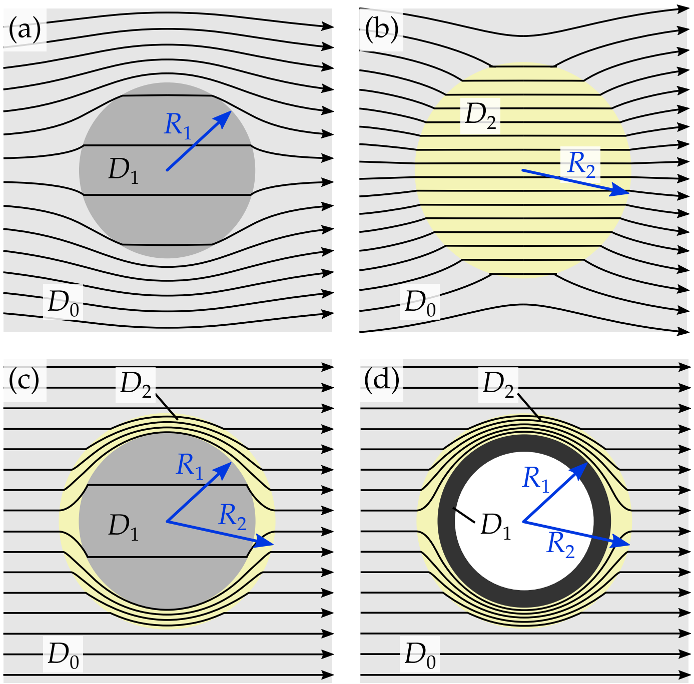

Figure 8.1: Illustration of core-shell cloaking inside a homogeneous background medium with diffusivity D_0 that is homogeneously illuminated from the left. (a) An inclusion with radius R_1 and diffusivity $D_1 < D_0$ disturbs the light flow and leads to convex streamlines (black arrows) bent away from the inclusion. (b) An inclusion with radius R_2 and diffusivity $D_2 > D_0$ has the opposite effect and leads to streamlines bent towards the inclusion. (c) Combining (a) and (b) with the right diffusivities leads to a neutral core-shell inclusion that does not disturb the overall light flux anymore and thus becomes invisible. (d) For $D_1 = 0$, the core expulses all light and thus can be made hollow. Together with the high-diffusivity shell, it forms a core-shell cloak inside which arbitrary objects can be hidden, while the light flow remains as if there was only the homogeneous surrounding. All streamlines were calculated using COMSOL Multiphysics with the boundaries far away to mimick an infinite diffusive medium.

$D_1 = 0$, equations 8.1 and 8.2 simplify to

$$\frac{R_2}{R_1} = \sqrt{\frac{D_2 + D_0}{D_2 - D_0}} \quad \Leftrightarrow \quad \frac{D_2}{D_0} = \frac{R_2^2 + R_1^2}{R_2^2 - R_1^2} \tag{8.3}$$

for cylindrical symmetry and

$$\frac{R_2}{R_1} = \sqrt[3]{\frac{D_2 + D_0/2}{D_2 - D_0}} \quad \Leftrightarrow \quad \frac{D_2}{D_0} = \frac{R_2^3 + R_1^3/2}{R_2^3 - R_1^3} \tag{8.4}$$

for spherical symmetry, respectively. Once the radii R_1 and R_2 are chosen and the diffusivity D_0 of the background medium is known, the shell's diffusivity D_2 is automatically determined.

So how is this concept of core-shell cloaking connected with transformation physics? For the design of the thermodynamic cloak for heat propagation in section 3.2, we used a laminate structure with layers of alternatingly high and low heat conductivity to realize an effectively anisotropic heat conductivity that would guide heat around the cloak's center. A core-shell cloak as presented here can be seen as an extreme simplification of such a structure down to only two layers: the zero-diffusivity core isolates the cloaked region from any incident light, while the high-diffusivity shell guides light around the core with an effectively higher speed than in the surrounding and thus compensates for the detour the light has to take. In this sense, the core-shell cloak is just another example of an anisotropic layered metamaterial structure like the one used before, but simplified to the extreme.

The working principle of core-shell cloaking can be understood on yet another level if one thinks of the diffusivity as a "conductivity for light", in analogy to the electric conductiviy σ. As the underlying equations are identical, this notion is perfectly valid. In this picture, a bad conductor (the core) and a good conductor (the shell) are connected in parallel to recreate the overall conductivity of the surrounding.

8.2 A MULTI-SHELL DESIGN FOR OPTIMIZED CLOAKING UNDER INHOMOGENEOUS ILLUMINATION

In the previous section, I explained how core-shell cloaks can be seen as a brute simplification of multilayer structures based on transformation physics. But as a core-shell cloak is so much simpler (conceptually and practically) than multilayer laminates with alternatingly high and low diffusivities, one might ask why anyone would ever want to use such structures for diffusive-light cloaking. The simple answer is that while transformation-physics-based structures work for any illumination condition by design, core-shell cloaks require *homogeneous* illumination to work. For inhomogeneous illumination, the cloaking performance will inevitably suffer.

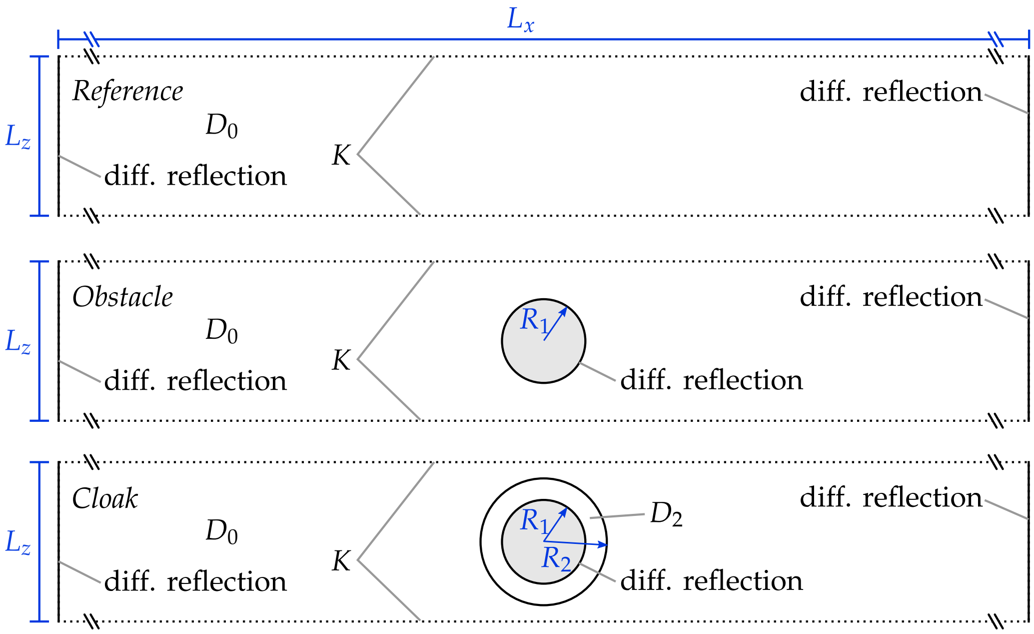

Figure 8.2: Sketch of the two-dimensional models implemented in COMSOL Multiphysics for the numerical investigation of core-shell cloaking under inhomogeneous illumination. The *reference* is a bare homogeneous rectangular medium with a diffusivity D_0. For the *obstacle*, a diffusely reflecting circle with radius R_1 (that is, the core with $D_1 = 0$) is "cut out" of the background medium. For the *cloak*, a circular shell with outer radius R_2 is added. Parameters are $R_1 = 0.8\,\mathrm{cm}$, $R_2 = 1.5\,R_1$, $L_x = 30\,R_2$, $L_z = 2.5\,R_2$, $K = 3.63 \times 10^8\,\mathrm{cm}^2/\mathrm{s}$, .

In the following, I will show with numerical studies how the error of core-shell cloaks under inhomogeneous illumination can be quantified. I will then demonstrate how by simply using two shells with different diffusivities instead of just one, this error can greatly be reduced to an almost perfect level.

8.2.1 Numerical model

All calculations were performed with COMSOL Multiphysics, solving the light-diffusion equation for two-dimensional models in the x-z plane. The restriction to two dimensions is identical to a three-dimensional geometry that is infinitely extended and translationally invariant along the y direction

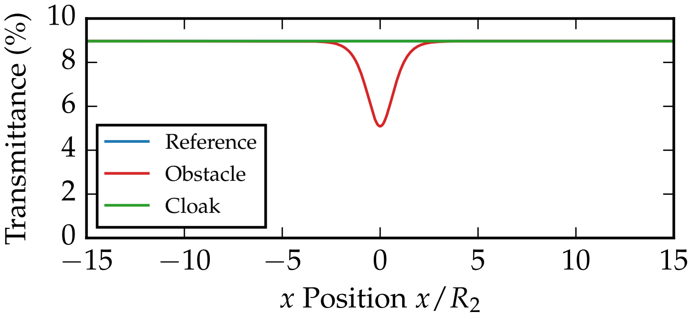

Figure 8.3: Calculated transmittance through reference, cloak, and obstacle modeled according to Figure 8.2 with homogeneous illumination. In the vicinity of the obstacle, the transmittance drops by roughly 50 %. The cloak appears exactly identical to the reference. Diffusivities are $D_0 = 11.9 \times 10^8\,\text{cm}^2/\text{s}$ and $D_2 = 2.6\,D_0$.

and drastically reduces the computation times. Figure 8.2 illustrates the three models we implemented in COMSOL Multiphysics. The homogeneous surrounding (the *reference*) is modeled as a rectangular domain with length L_x, depth L_z, and diffusivity D_0. The horizontal boundaries are open according to the partial-current boundary condition explained in section 5.5, with a photon-loss velocity of $K = 3.63 \times 10^8\,\text{m}^2/\text{s}$ (corresponding to a refractive index mismatch of $n_\text{i}/n_\text{o} = 1.4$). The vertical boundaries are isolated, translating to diffusive reflection there. In principle, one could also assume a homogeneous background medium that is infinitely extended in both x and z. However, as all diffusive media in our experiments were finite, we chose a geometry here that is similar to the experimental conditions.[2] The *obstacle* is an identical rectangular domain with an isolating circle “cut out”. The isolation results in perfect diffusive reflection and thus is identical to a diffusivity of $D_1 = 0$. Finally, a shell with diffusivity D_2 is added around the core in the *cloak* model. For all calculations presented in this section, an incident light flux was defined at the geometry’s bottom boundary and the transmitted flux was obtained at the top boundary.

8.2.2 *Error definition and results for an unmodified cloak*

Figure 8.3 shows the calculated transmittances for the reference, obstacle, and cloak model under homogeneous illumination. As to be expected (also

---

[2] As the multi-shell study was actually performed after most of the experiments, the parameters used here fit roughly to the latest PDMS-based cloaks presented in subsection 8.4.3.

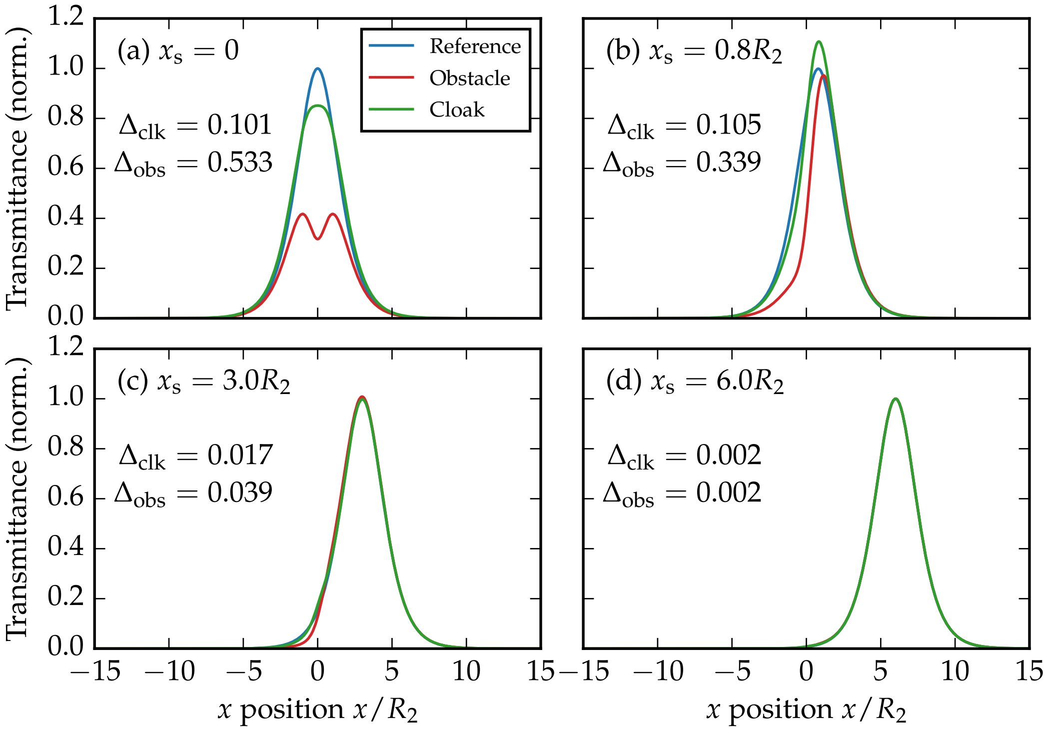

Figure 8.4: Calculated normalized transmittance curves as shown in Figure 8.3, but for inhomogeneous illumination with a Gaussian intensity pattern (full width at half-maximum of $w_s = 0.5\,\text{mm}$) centered at different positions x_s. In contrast to homogeneous illumination, this line-like illumination leads to deviations from the reference also for the cloak structure. For large distances of the source from the core or core-shell structure, the transmittances of both obstacle and cloak approach that of the reference. The normalized standard deviations Δ_{obs} and Δ_{clk} of obstacle and cloak, respectively, are given according to Equation 8.5.

compare Figure 8.1), cloak and reference are impossible to distinguish, while the zero-diffusivity core in the obstacle disturbs the light flow, resulting in a dip in the transmitted intensity.

Things changed significantly when inhomogeneous illumination was introduced. Figure 8.4 shows identical transmittance profiles[3] as Figure 8.3,

---

[3] In contrast to Figure 8.3, the curves in Figure 8.4 are normalized to the reference transmittance. Since the illuminated area (a thin line) and the detection area (the whole domain boundary) are different, absolute transmittance values for inhomogeneous illumination don't allow for an intuitive interpretation as for homogeneous illumination.

but for a spatially Gaussian illumination pattern with a full width at half maximum of $w_\mathrm{s} = 0.5\,\mathrm{mm}$ (translated to three dimensions, this corresponds to illumination with a thin line-like source). From panel (a) to panel (d), the source position x_s (that is, the median of the Gaussian) was varied with respect to the center ($x = 0$) of the illuminated boundary. For source positions close to this center, the cloak transmits light differently than the reference, leading to a modified transmittance profile. For $x_\mathrm{s} = 0$, the cloak's transmittance is a bit flattened and thus lower than the reference curve. In contrast, the cloak's transmittance is even higher than that of the reference when the source is placed just a bit off-center. For sources far away from the core or core with shell, the transmittance profiles of both cloak and obstacle converge to that of the reference. This is an expected and trivial outcome, as any structure that disturbs the light flow has no effect if one just goes sufficiently far away.

To quantify the error introduced by the obstacle or cloak, we have defined the normalized standard deviation

$$\Delta = \frac{\sqrt{\Sigma_i (I_i - I_i^0)^2}}{\sqrt{\Sigma_i (I_i^0)^2}}\,, \tag{8.5}$$

where I_i is the ith data point of the transmittance curve of interest and I_i^0 is the corresponding reference value. The sum runs over all data points, but could in principle also be truncated to the region where the transmittance is significantly bigger than zero. For centered illumination ($x_\mathrm{s} = 0$), we found a deviation Δ_obs for the obstacle of more than 50 %, and about 10 % for the cloak's deviation Δ_clk.

Since the light-diffusion equation (5.33) is linear, any arbitrary illumination pattern can be synthesized by a superposition of point sources (or line sources in a two-dimensional model). In the context of cloaking performance, each of these point sources is connected to a different value of the deviation Δ. To be able to give a single error value that represents not only one but all possible illumination patterns at the same time, we averaged Δ over all relevant source positions, that is, over all source positions with a significantly non-zero value of Δ. Figure 8.5 depicts Δ_obs and Δ_clk versus the source position interval of $[0, 6R_2]$, discretized with a spacing of $0.1R_2$. Since the problem is symmetric, only positive source positions were considered. Averaging over all points led to $\overline{\Delta}_\mathrm{obs} = 0.121$ and $\overline{\Delta}_\mathrm{clk} = 0.036$.

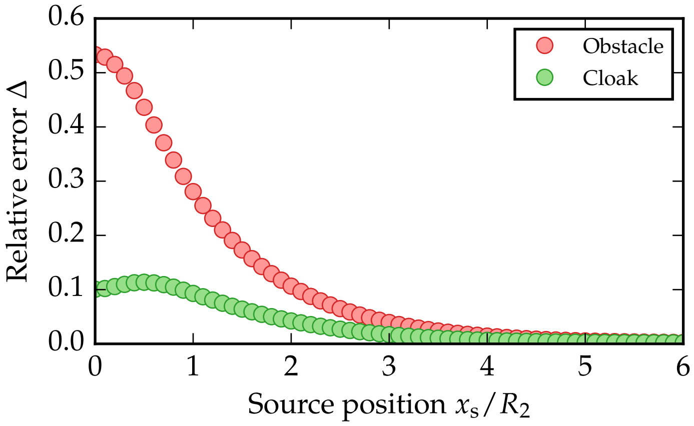

Figure 8.5: Normalized standard deviation Δ according to Equation 8.5 versus the source position x_s for the obstacle and the unmodified cloak. (Each pair of data points corresponds to one set of transmittance curves as shown in Figure 8.4.) For an appropriate discretization and range of the source position, the average errors $\overline{\Delta}_{\text{obs}} = 0.121$ and $\overline{\Delta}_{\text{clk}} = 0.036$ are obtained for obstacle and cloak, respectively.

8.2.3 *Optimized cloak with one and two shells*

The average normalized standard deviation $\overline{\Delta}$ introduced above is a single scalar that characterizes the cloaking performance of a structure for all possible lighting conditions and can thus be used easily for optimization procedures.

MINIMIZING THE DEVIATION FOR A SINGLE SHELL Utilizing remote control of COMSOL Multiphysics via the MATLAB LiveLink$^{\text{TM}}$, we minimized the cloak's average deviation $\overline{\Delta}_{\text{clk}}$ with a simple optimization algorithm[4] and the shell diffusivity D_2 as the free parameter. This optimization did not yield a substantial improvement, reducing $\overline{\Delta}_{\text{clk}}$ from 0.036 to 0.034 only. The corresponding diffusivity was $D_{2,\text{opt}} \approx 33.4 \times 10^8\,\text{cm}^2/\text{s} = 1.08 \times D_2$. Thus, a slightly higher shell diffusivity leads to improved cloaking performance under inhomogeneous illumination. However, modifying D_2 of course introduces an error for homogeneous illumination (see Figure 8.7), making this approach somewhat questionable.

---

[4] Nelder-Mead simplex algorithm [111] with tolerances $\delta D_2 = 0.005 D_{2,\text{start}}$ and $\delta\overline{\Delta} = 0.001$

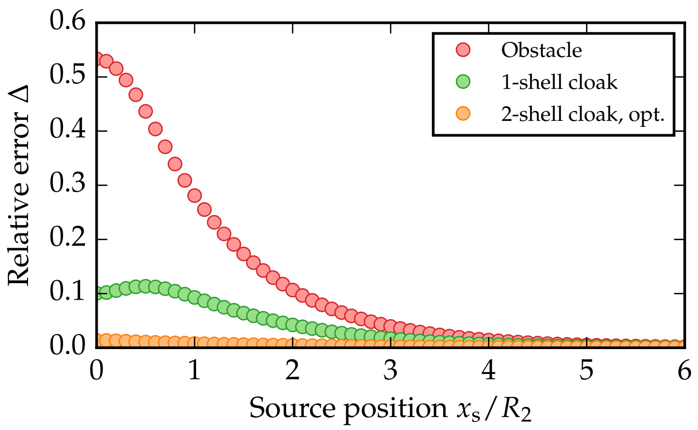

Figure 8.6: Normalized standard deviation Δ as in Figure 8.5, but including results for an optimized 2-shell cloak with $D_{s,1} = 6.84 \times D_0$ and $D_{s,2} = 0.458 \times D_0$. For this cloak, the average deviation is significantly reduced by about one order of magnitude to $\overline{\Delta}_{clk,2} = 0.00355$.

MINIMIZING THE DEVIATION WITH TWO SHELLS To increase the cloaking performance under inhomogeneous illumination without compromises for homogeneous illumination, we apparently needed more parameters to adjust. We therefore divided the single cloaking shell into two equally thick shells with independent diffusivities $D_{s,1}$ and $D_{s,2}$. We then performed the same optimization routine as before, with both shell diffusivities as free parameters, initialized both with the ideal single-shell diffusivity $D_2 = 2.6\,D_0$ obtained from Kerner's formula (Equation 8.3).

With two shell diffusivities to tune, the results are much more convincing, as shown in Figure 8.6. On average, the deviation Δ_{clk} was reduced by

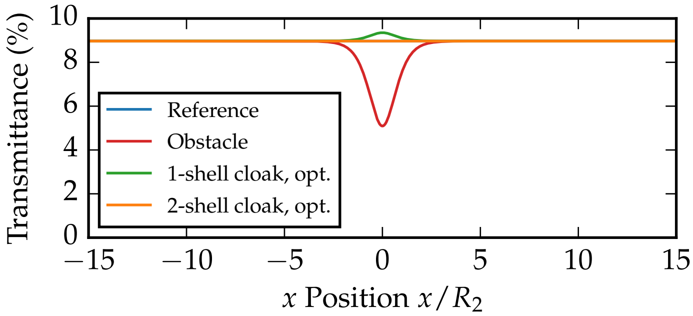

Figure 8.7: Transmittance profiles for homogeneous illumination as in Figure 8.3, but for an optimized version of the single-shell cloak and an optimized 2-shell cloak. While optimization of the single-shell cloak for inhomogeneous illumination introduces an error for inhomogeneous illumination, the optimized 2-shell cloak performs surprisingly well under both conditions and cannot be distinguished from the reference.

Figure 8.8: Dependence of the average deviation $\overline{\Delta}_{\mathrm{clk}}$ under inhomogeneous illumination on the shell thickness of a single-shell cloak. Parameters other than R_1 and R_2 are as described in Figure 8.2. (a) For a fixed core radius $R_1 = 0.267\,L_z$, thin shells lead to better cloaking performance due to an overall smaller cloak. (b) In contrast, cloaks with thick shells perform better when the overall cloak size $2R_2 = 0.8\,L_z$ is held constant.

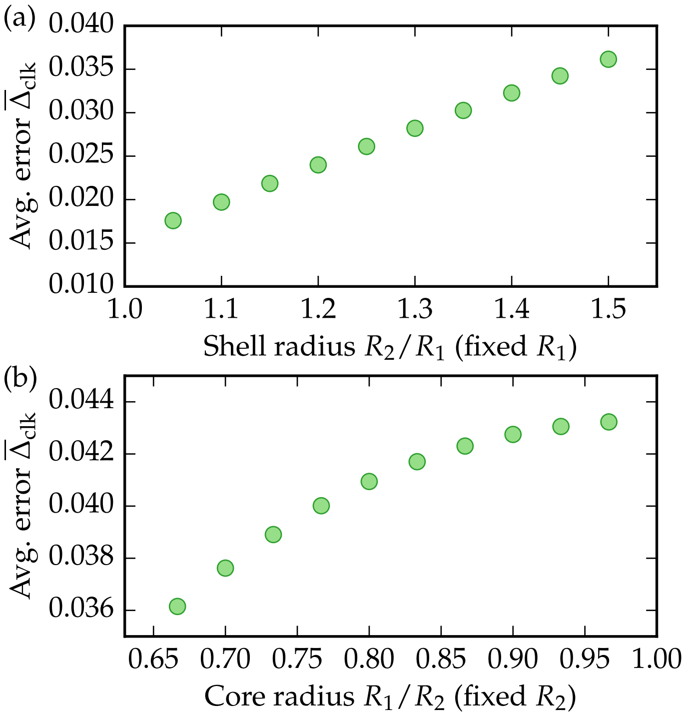

slightly more than one order of magnitude, with an optimized average deviation of $\overline{\Delta}_{\mathrm{clk},2} = 0.00355$ (compared to a non-optimized value of 0.036). The resulting shell diffusivities are $D_{\mathrm{s},1} = 81.4 \times 10^8\,\mathrm{cm}^2/\mathrm{s} = 6.84 \times D_0$ for the inner shell and $D_{\mathrm{s},2} = 5.45 \times 10^8\,\mathrm{cm}^2/\mathrm{s} = 0.458 \times D_0$ for the outer shell.

As illustrated in Figure 8.7, the optimized 2-shell cloak also performs well under homogeneous illumination, where no deviation from the horizontal straight reference line can be detected.

8.2.4 Influence of the shell thickness

It has been claimed in the literature on core-shell cloaks for static magnetic fields [27] as well as for static heat conduction [68] that thin shells lead to better cloaking performance under inhomogenous excitation than thick shells. As the underlying differential equations for magnetostatics, static heat conduction, and static light diffusion are mathematically identical, this dependence on the shell thickness should be the same in light diffusion. We therefore calculated the average standard deviation $\overline{\Delta}_{\mathrm{clk}}$ as defined above for a geometry as in Figure 8.2 and varied the shell thickness (and also the shell diffusivity such that it always satisfied Equation 8.3). Results are shown in Figure 8.8.

Indeed, for a fixed core radius $R_1 \approx 0.267\,L_z$, the deviation $\overline{\Delta}_{\mathrm{clk}}$ is increasing with increasing shell radius R_2, as illustrated in Figure 8.8 (a). However, increasing R_2 means that also the overall size of the cloak is increased. Figure 8.8 (b) shows results for $\overline{\Delta}_{\mathrm{clk}}$ where we fixed the shell radius $R_2 = 0.4\,L_z$ and instead varied the core radius R_1. In this case, contradictory to the statement made in Ref. 27, a thinner shell leads to a bigger value of $\overline{\Delta}_{\mathrm{clk}}$ and thus to a worse cloaking performance.

Obviously, care must be taken for statements about how the shell thickness influences the cloaking performance under inhomogeneous illumination. For a fixed core size, a thin shell indeed leads to better cloaking because the overall size of the cloak is reduced. For a fixed overall cloak size, however, cloaks with thick shells (and thus smaller cores) perform better.

8.2.5 Discussion

The numerical studies presented in this section show that simple core-shell cloaks that work perfectly under homogeneous illumination can be revealed by inhomogeneous illumination conditions. This is not surprising, since homogeneous illumination is explicity required for the derivation of these cloak designs. Much more surprising is that by simply dividing the cloaking shell into two shells and adjusting their diffusivities individually, one obtains a cloak that is only slightly more complex but performs amazingly well under both homogeneous and inhomogeneous illumination. Compared to a single-shell cloak, its cloaking performance improves by about one order of magnitude.

Conceptually, adding a second shell is a step towards transformation physics, where anisotropic material parameters are often realized by layered materials with alternatingly low and high parameters. In our case, the inner shell adjacent to the zero-diffusivity core has a high diffusivity $D_{\mathrm{s},1} > D_0$, while the outer shell has a low diffusivity $D_{\mathrm{s},2} < D_0$. Adding yet more shells would probably further increase the cloaking performance but seems a bit superfluous considering how small the remaining deviation is already for two shells.

When I introduced the concept of core-shell cloaking in section 8.2, I predicted that transformation-physics-based designs for diffusive-light cloaking comprising many layers with high diffusivity contrasts would probably fall victim to the restrictions that the diffusion approximation imposes for the combination of diffusivity and medium size. It remains to be seen whether the simplest of such multilayer approaches—a two-shell design as presented here—will in the end be realizable experimentally. See subsection 8.4.7 for a further discussion of this aspect based on experimental results.

8.3 LIQUID-BASED DIFFUSIVE-LIGHT CLOAKS

We tried first attempts at diffusive-light cloaking for a water-based surrounding. As outlined before, this provides great flexibility in the ratio of diffusivities between shell and surrounding, which was crucial for those early experiments. The main findings of this section have been published in Ref. 112.

8.3.1 Sample fabrication and experimental setup

Figure 8.9 shows a photograph of the experimental setup. We used a custom-made Plexiglas tank[5] as a container for the water-based background medium. Its inner dimensions were $35.5 \times 16 \times 6\,\mathrm{cm}^3$, resulting in a total volume of about 3.4 l. All except the front and back walls were made from smooth black Plexiglas to avoid any light entering or escaping through these walls. In order to create a "free" diffusive medium, we also tested an entirely transparent tank. However, the Plexiglas walls then acted as waveguides for the incident light, creating a "bypass" around the diffusive medium inside. This bypass disturbed measurements, especially for high scatterer concentrations and thus a low diffusive transmission through the tank. The tank rested on two motorized magnetic stirrers[6] with one stir bar each lying on the tank floor. By continuous stirring during the experiments, sedimentation of the scattering particles was avoided and newly added particles were mixed quickly with the contained solution.

We mixed de-ionized water with ordinary white wall paint[7] to obtain a diffusive medium. Compared to milk and silica particles, this water-paint mixture showed the lowest color dependence in diffusive transmission measurements identical to the one shown in Figure 7.3. See figures A.1, A.2,

---

[5] supplied by GLASSCHMID®, Germany

[6] MR Hei-Standard from Heidolph Instruments GmbH, Germany

[7] Schöner Wohnen Polarweiss from J. D. Flügger, Germany

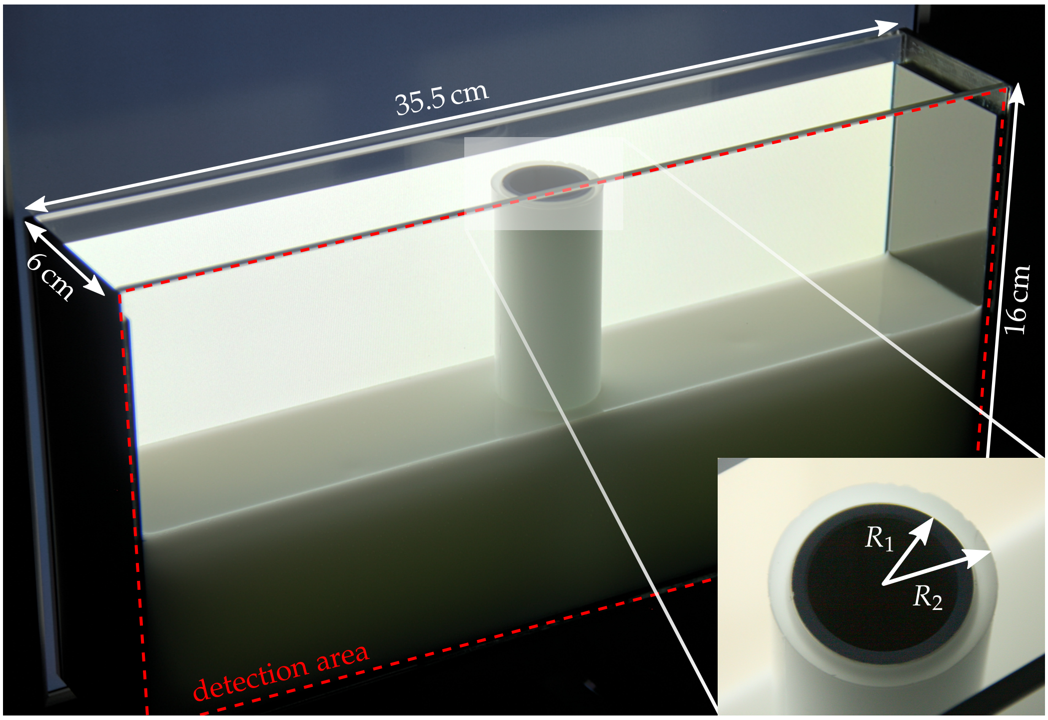

Figure 8.9: Photograph of the experimental setup. A Plexiglas tank containing the water-based surrounding (half-filled only for illustration) stands in front of a computer monitor acting as a white-light source. Centered inside the tank is the aluminum core coated with a 4 mm thick layer of microparticle-doped PDMS. The red dashed line indicates the field of view of the camera used to take photographs of the light emerging from the tank. Adapted from Ref. 112, Fig. 1B.

and A.3 in Appendix A for corresponding characterization measurements.

Ballistic transmission measurements (see Figure A.4) through a 1 cm thick glass cuvette filled with the water-paint mixture yielded a scattering mean free path of

$$l_s = \frac{1\,\text{mm}}{11.33 \times C} \tag{8.6}$$

with the paint volume concentration C given in %.

An ideal core has a diffusivity of exactly zero: it is a perfect diffusive reflector, neither transmitting nor absorbing any incident light. In order to come close to this ideal, we used a hollow aluminum cylinder and a hollow stainless-steel sphere for the core in two and three dimensions, respectively. To achieve a diffuse rather than a specular reflection, we furthermore coated

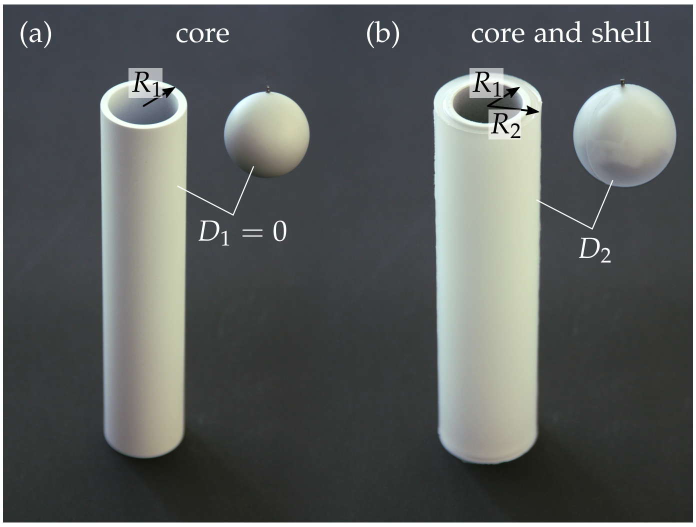

Figure 8.10: Photographs of fabricated core and core-shell structures. (a) Cores made of metal coated with white paint. (b) Identical structures with an additional shell of microparticle-doped PDMS (doping concentration: 1 mg/ml. Dimensions are: $2R_1 = 32.1$ mm, $2R_2 = 39.8$ mm (cylinders); and $2R_1 = 33.2$ mm and $2R_2 = 39.9$ mm (spheres).

the core with a thin layer of a white acrylic spray paint.[8] The white paint layer also reduced absorption of light at the core surface, which otherwise prevented successful cloaking altogether. Photographs of the two- and three-dimensional cores are shown in Figure 8.10 (a).

For the shell, we coated identical painted metal structures with a 4 mm thick layer of PDMS mixed with melamine-resin microparticles[9] at a concentration of 1.0 mg/ml as scatterers.[10] After mixing the particles with the liquid PDMS constituents, the mixture was poured into demountable metal molds (see Figure B.1) with the aluminum cylinder or steel sphere inside. The mold walls were coated with a thin layer of polytetrafluoroethylene (PTFE or Teflon®) to avoid adhesion of the PDMS to the molds and thus aid removal of the samples after polymerization. Figure 8.10 (b) shows the finished core-shell structures.

For the experiments, the core or core-shell structures were placed centered into the tank containing the water-paint mixture (see Figure 8.9). The tank was placed in front of a computer monitor used as a flexible and configurable light source. For the spherical samples, the structures were suspended in the tank with a thin wire fastened to the tank lid.

---

[8] Dupli-Color Acryl Deco Matt weiß from Motip Dupli GmbH, Germany

[9] MF-F-10.2 (monodisperse, 10 µm diameter), Charge: MF-F-1960-1 from microParticles GmbH, Germany

[10] At this point, the particle concentration was somewhat arbitrary. We chose this initial concentration of 1.0 mg/ml based on how small test samples appeared to the eye.

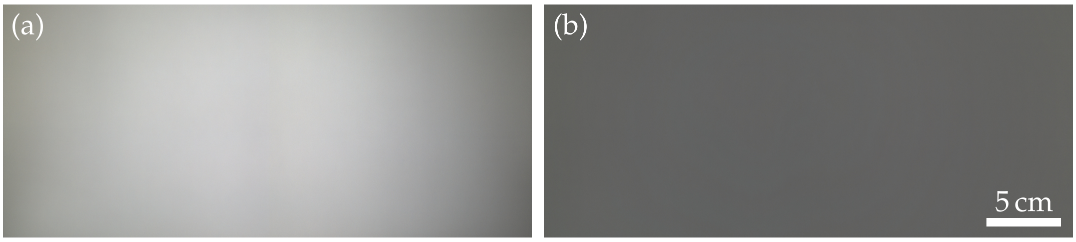

Figure 8.11: Photographs of the computer monitor surface used for illuminating the samples (cropped to only the illumination area). (a) By default, the monitor emits inhomogeneously. (b) The corrected intensity distribution is darker but homogeneous up to a remaining variation of less than 5 %.

We took photographs of the light emerging the tank with an optical CCD camera[11] centered with respect to the tank surface. The red dashed line in Figure 8.9 illustrates the field of view of the camera. To reduce noise, we usually averaged over 20 consecutive exposure.

8.3.2 *Experimental results*

To guarantee that any features visible in the photographs are due to the diffusive samples and not due to the setup, it was important to ensure homogeneous illumination of the tank. Figure 8.11 (a) shows a photograph of the bare computer monitor surface when a white rectangle the size of the tank was displayed. Obviously, the monitor brightness was not homogeneous at all by default. On the contrary, intensity differences of up to 30 % were measured. To compensate for this intrinsic inhomogeneity, we modified the picture displayed on the monitor by adding to it the inverse of the (inhomogeneous) intensity distribution measured in Figure 8.11 (a), followed by a re-scaling to the usual RGB color space. Figure 8.11 (b) shows a photograph of the monitor surface after this brightness correction. The result is a somewhat dimmer but homogeneous illumination area (with a remaining variation of less than 5 %).

We furthermore set the camera white balance such that the bare illumination pattern (without any sample) was perceived as white. Any color variation in the diffusively transmitted light was then due to the sample itself.

---

[11] XCR-5005 CR from Sony, Japan

Figure 8.12: Example photograph of the homogeneously illuminated tank with 0.175 % paint in the water. To avoid edge effects from light absorption at the tank boundaries, result images were cropped to the size of the dashed box.

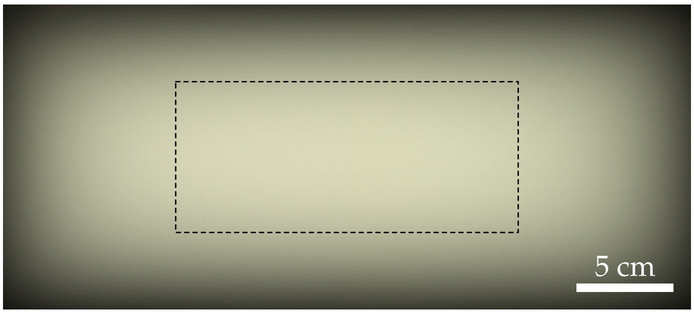

Sample nomenclature After homogenizing the illumination area, we examined the light transmission through three different samples:

1. *Reference*: just the homogeneous surrounding with diffusivity D_0, that is, the tank filled only with the water-paint mixture,
2. *Obstacle*: the painted aluminum core (with $D_1 = 0$) placed in the tank containing the water-paint mixture, and
3. *Cloak*: the painted core coated with the high-diffusivity shell (D_2) placed in the tank.

These three types of samples appeared already in the numerical study on inhomogeneous illumination (see Figure 8.2). They will be used repeatedly in this work and will consistently be named reference, obstacle, and cloak (together with a sample ID that appears again in Appendix C, where every sample and its fabrication parameters are listed). While the obstacle sample will lead to a disturbance of the light flux (it is "the object to hide"), the cloak should ideally appear exactly like the homogeneous reference.

Finding the right paint concentration With the core and shell radii R_1 and R_2 as given in the caption of Figure 8.10 ($R_2/R_1 = 1.24$), the necessary diffusivity contrast between shell and surrounding is $D_2/D_0 = 4.72$ for the cylindrical samples according to the two-dimensional Hashin-Shtrikman formula (Equation 8.1). But since the two diffusive media of surrounding and shell were based on different material systems that could not be characterized completely, the shell's diffusivity was unknown and we could not determine the necessary concentration of paint in the tank

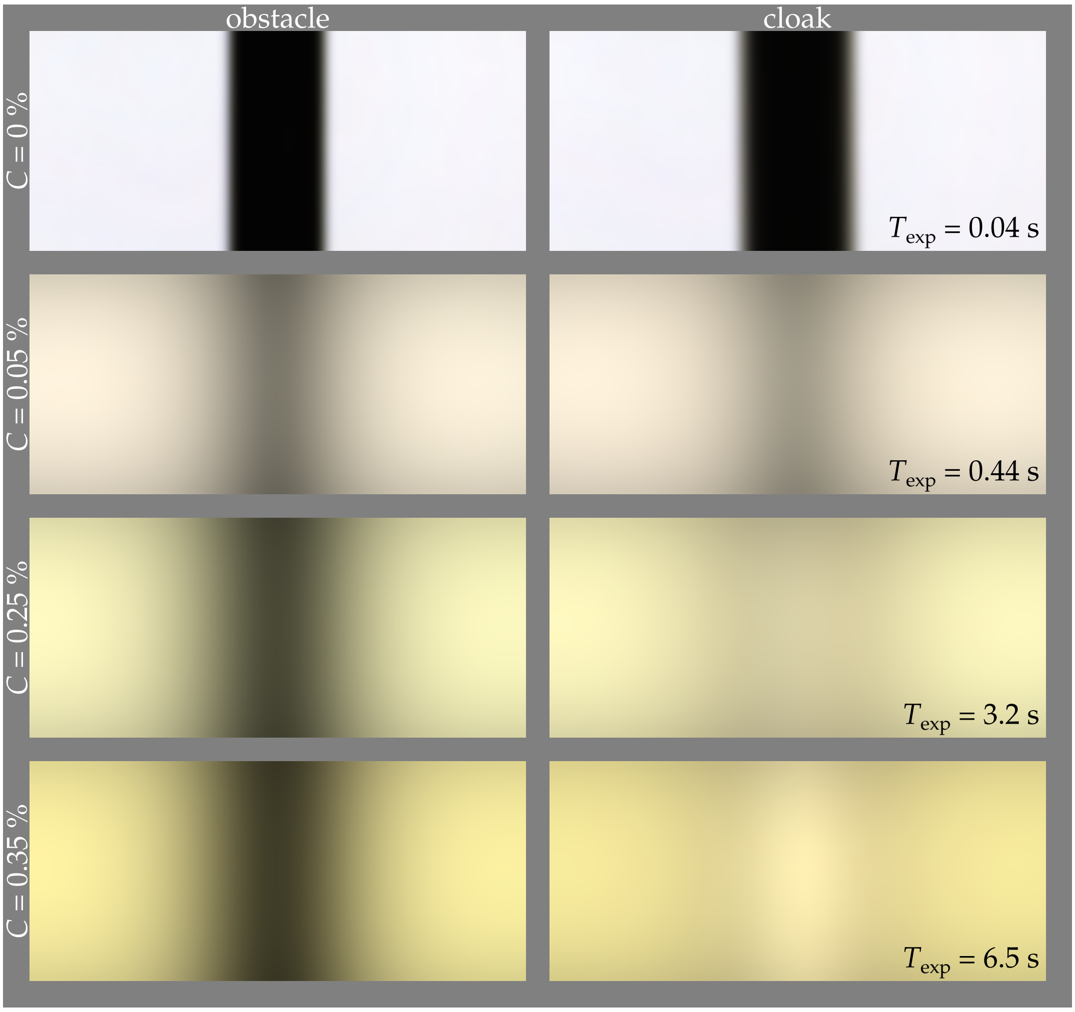

Figure 8.13: Photographs of the light transmitted through obstacle and cloak for different paint concentrations in the surrounding (cropped to the dashed rectangle shown in Figure 8.12). Without any paint (first row), obstacle and cloak cast ballistic shadows. The silhouettes appear a bit blurred because the camera was focused onto the tank's exit window during the entire measurement. With increasing paint concentration, this shadow becomes diffuse and vanishes (except for small intensity variations) for the cloak at a concentration of 0.35 %. Images within each row are shown on the same normalized intensity scale. The resulting effective exposure times T_{exp} are given for each row.

up front. Thus, we chose an experimental optimization, starting with pure water inside the tank, that is, with a paint concentration of $C = 0\,\%$. We then successively increased the paint concentration until we found good cloaking performance, taking photographs of reference, obstacle, and cloak for each step. With this method, any effects of absorption are automatically compensated for (with the disadvantage that one might thus not even notice such effects). Figure 8.12 shows one of these photographs for the reference sample. Obviously, significant edge effects are caused by light absorption at the black tank walls. To avoid these edge effects in the evaluation of the results, we cropped 25 % of the pictures from all four edges as indicated by the dashed rectangle.

Figure 8.13 displays such photographs taken for different paint concentrations C for the cylindrical obstacle and cloak samples. When there is no paint at all in the water inside the tank, light propagation is purely ballistic. As neither obstacle nor cloak are transparent, they will both block a significant portion of the incident light, casting sharp shadows behind them (see first row of Figure 8.13). Due to its larger overall dimensions, the cloak's shadow is even bigger than that of the obstacle. This nicely illustrates that any cloak can only work in the surrounding it has been designed for.

The remaining rows in Figure 8.13 show the same tank surface photographs, but with different finite amounts of white paint mixed into the water. Both photographs within each row are shown on the same scale, whereas each row is normalized such that the full RGB intensity range is used (with increasing paint concentration, less light is transmitted by the samples). The corresponding effective exposure times are given for each row. While the obstacle casts a pronounced (albeit now diffuse) shadow regardless of the paint concentration, the shadow cast by the cloak becomes less and less pronounced and finally vanishes for a paint concentration of $C = 0.35\,\%$ (last row of Figure 8.13). It is obvious though that the cloak is not entirely perfect, as some remaining color and intensity variations are still visible for this paint concentration. Changing the paint concentration further did not reduce these variations.

With increasing paint concentration and thus increasing scattering coefficient μ_s, the transmitted light also showed an increasingly pronounced yellowish tint. I will investigate this tint quantitatively in subsection 8.4.4.

A more quantitative analysis of the cloaking performance can be performed with the help of Figure 8.14, where we added plots of the intensity along a horizontal cut through the result images. Panels (a)–(c) show results for only

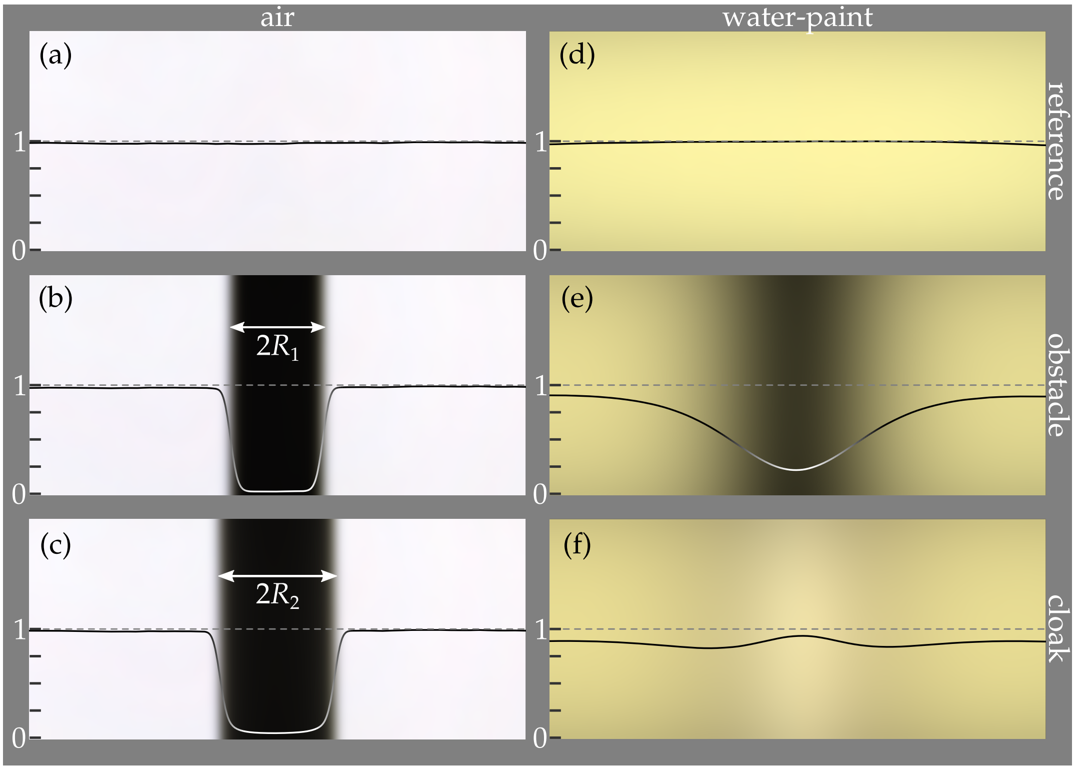

Figure 8.14: Photographs of light exiting the Plexiglas tank illuminated homogeneously with white light. In (a)–(c), the surrounding is the empty tank, while in (d)–(f), the tank is filled with de-ionized water mixed with 0.35 % white paint. The solid curves are horizontal intensity cuts along the gray dashed lines. Images and cuts within each column are shown on the same normalized intensity scale. Effective exposure times are 38 ms for (a)–(c) and 6140 ms for (d)–(f), illustrating the decrease in transmittance for the diffusive case. The obstacle casts a pronounced shadow in air (b) as well as in the diffusive surrounding (e). In contrast, the cloak (f) appears like the homogeneous reference except for small intensity variations of about ±10 %. Sample IDs are WR1, WO1, and WC1 for reference, obstacle, and cloak, respectively. Reproduced from Ref. 112, Fig. 2.

air inside the tank (a situation almost identical to the first row of Figure 8.13 with only water), while panels (d)–(f) show results for a water-paint mixture with the optimal paint concentration of 0.35 %. All intensity cuts are given by solid lines and are normalized to the reference for air or the water-paint mixture, respectively. In panel (b), we again see the geometrical shadow cast by the obstacle, which turns into a diffuse shadow in panel (e) with the

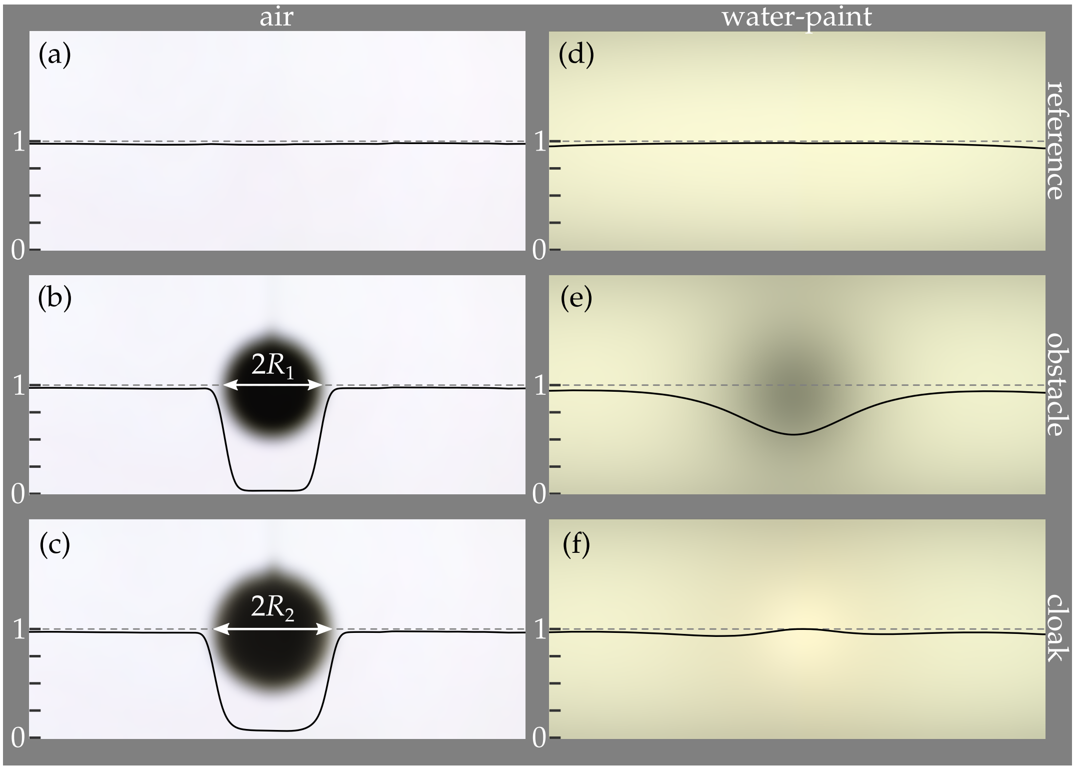

Figure 8.15: Measured results as in Figure 8.14, but for spherical samples and a paint concentration of 0.175 %. Effective exposure times are 38 ms for (a)–(c) and 1610 ms for (d)–(f). All significant features are qualitatively similar to the cylindrical case but less pronounced. Sample IDs are WR2, WO2, and WC2 for reference, obstacle, and cloak, respectively. Reproduced from Ref. 112, Fig. 3.

water-paint mixture in the tank. Directly behind the obstacle, the intensity drops by about 70 % with respect to the reference. The cloak in panel (f) almost completely restores the homogeneous intensity distribution of the reference, with remaining variations of about ±10 %. (Without absorption or boundary effects, we would expect both reference and cloak to be perfectly homogeneous, compare Figure 8.4.) Furthermore, the yellowish tint is a bit less pronounced directly behind the cylindrical cloak. This difference is not surprising as shell and surrounding are based on different material systems which don't necessarily possess the same color dependence in their optical properties.

Figure 8.15 shows the same results as exhibited in Figure 8.14, but for the spherical obstacle and cloak samples. In three dimensions, the necessary diffusivity contrast between cloaking shell and surrounding is lower than for cylindrical symmetry. The three-dimensional Hashin-Shtrikman formula (Equation 8.2) yields $D_2/D_0 = 3.06$ for $R_2/R_1 = 1.20$. Consequently, we found the best cloaking performance at a lower paint concentration of $C = 0.175\,\%$, resulting in a higher net transmission and a less pronounced yellowish tint. Apart from that, the results are very similar. The bare samples (without any water in the tank) cast geometric black shadows while with the water-paint mixture present, the cloak almost perfectly restores the homogeneous intensity distribution of the reference. All significant features are qualitatively similar to Figure 8.14 but less pronounced for the spherical samples. This fact combined with the higher fabricational complexity of spherical samples made us choose cylindrical geometries in later experiments.

SAMPLE BRIGHTNESS As already indicated by the effective exposure times given in figures 8.14 and 8.15, the diffusive transmission of the water-based samples was very small. Precisely (measured in the center of the surrounding without obstacle or cloak), it was $T_{\text{diff}} = 2.3\,\%$ for a paint concentration of $C = 0.175\,\%$ and $T_{\text{diff}} = 0.5\,\%$ for $C = 0.35\,\%$. In the experiments, this required a suppression of all possible stray light, which would otherwise have appeared in the photographs taken. At this time, we did not know exactly whether the low transmission was caused by absorption or merely a low diffusivity (or both). However, as the diffusive transmission decreased by a factor of almost 5 when the paint concentration was increased by a factor of 2, we suspected that absorption did play an appreciable role (see Equation 5.53).

In the context of PDMS-based diffusive-light cloaking, we managed to increase the transmission by more than one order of magnitude, enabling us to examine the samples even under daylight conditions (see section 8.4 for details).

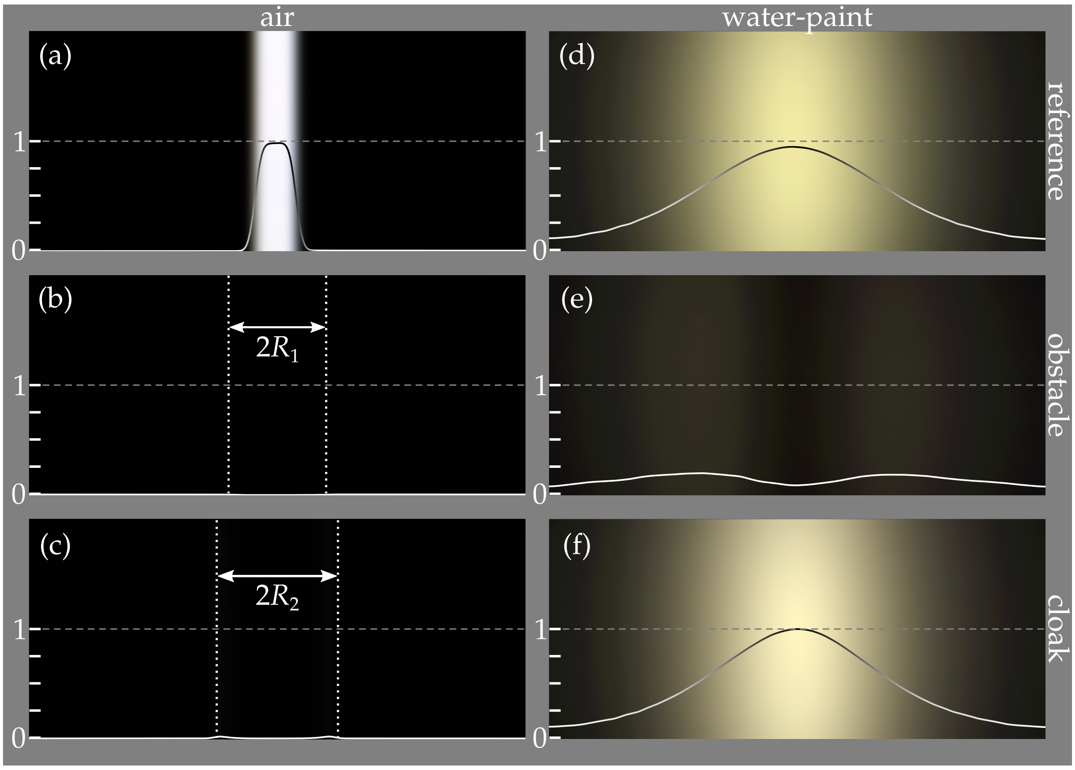

Figure 8.16: Measurement results for cylindrical samples as in Figure 8.14, but for an inhomogeneous, line-like illumination pattern visible in panel (a). The cloak works fairly well also for this excitation, irregardless of the homogeneous illumination formally required by core-shell theory. Reproduced from Ref. 112, Fig. 2.

INHOMOGENEOUS ILLUMINATION In section 8.2, we saw how, conceptually, core-shell cloaks can be optimized for inhomogeneous illumination by dividing the shell in two. However, also cloaks with a single shell perform not too bad under inhomogeneous illumination. We tested this experimentally already for the water-based samples using line-like and point-like illumination patterns for cylindrical and spherical geometry, respectively. Results are presented in figures 8.16 and 8.17 in the same way as before for homogeneous illumination. In both cases, the obstacle blocks virtually all light from the line-like or point-like source behind. In contrast, the cloak reproduces the reference intensity profile quite well in both cases. It should be noted that the intensity profiles of the cylindrical cloak and the reference differ qualitatively from those obtained numerically in section 8.2 (see Fig-

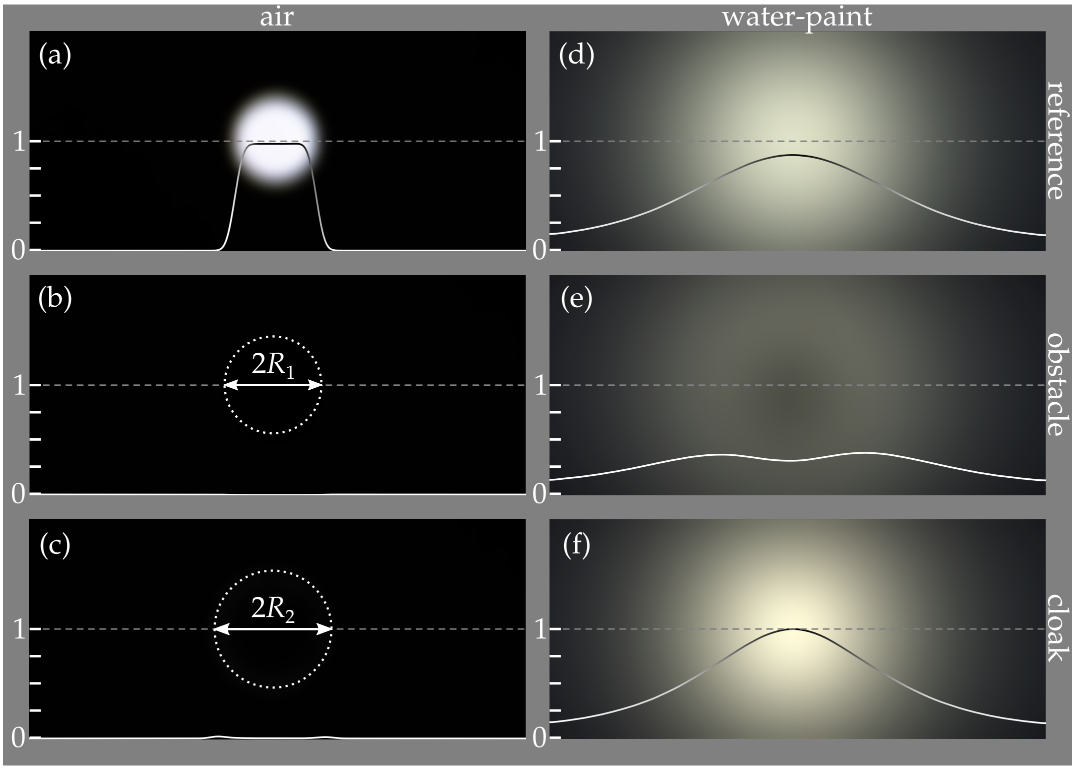

Figure 8.17: Measurement results for spherical samples as in Figure 8.15, but for an inhomogeneous, point-like illumination pattern visible in panel (a). Also here, the cloak reproduces the reference intensity profile rather well. Reproduced from Ref. 112, Fig. 3.

ure 8.4 (a)). There, the cloak has a slightly lower, flattened transmittance curve than the reference. In our experimental results (Figure 8.16 (d) and (f)), however, the cloak's overall transmittance is higher and a bit "sharper" than that of the reference. Considering that the numerical study in section 8.2 was based on an idealized, absorption-free model and used a much narrower illumination linewidth, these slight differences are not too surprising. Besides, we could reproduce the experimentals results numerically, as I will present in the following.

8.3.3 Numerical results

In Ref. 112, we also reproduced the experimental results of figures 8.14 to 8.17 numerically via COMSOL calculations solving the diffusion equation. At this time, however, we had not yet characterized the surrounding diffusivity by time-resolved transmission measurements as described in section 7.3. Instead, we (crudely) assumed the scattering mean free path to be equal to the transport mean free path, ignoring the effect of the asymmetry factor g. This led to an assumed diffusivity that was lower than in reality. Furthermore, the shell diffusivity was not known, and both the photon lifetime τ_0 in the surrounding and the photon-loss velocity K of the tank windows had been determined by static diffusive transmission measurements, a method which later proved not to be very robust (see section 7.2). Even though the numerical results reported in Ref. 112 fit rather well to the experiments, I choose to show new calculations here based on updated parameters we determined in the course of dynamic diffusive-light cloaking.

Figure 8.18 illustrates the model with all parameters we implemented in COMSOL Multiphysics. Besides the parameters already known from the previous chapters (diffusivities D_0, $D_1 = 0$, and D_2 of surrounding, core, and shell, respectively; surrounding photon lifetime τ_0; and photon-loss velocity K), we introduced another photon lifetime τ_{12} accounting for absorption at the interface between core and shell. The shell itself was assumed to be absorption-free due to its low concentration of scatters compared to the surrounding. The most notable simplification compared to the experiment is the assumption of diffusively reflecting surfaces for the non-transparent tank walls. Under homogeneous illumination and with core and shell far away, this assumption translates to an infinitely extended medium normal to these walls, whereas the black tank walls in the experiment absorbed a significant portion of the incident light.

With the time-resolved characterization techniques described in the last chapter, we found a diffusivity of $D_0 = 5.27 \times 10^8\,\mathrm{cm}^2/\mathrm{s}$ for a paint concentration of $0.35\,\%$. (This results in $D_0 = 10.54 \times 10^8\,\mathrm{cm}^2/\mathrm{s}$ for $C = 0.175\,\%$.) The four remaining parameters D_2, τ_0, τ_{12}, and K, however, were not directly accessible via experimental characterization. Only by comparing both static and time-resolved numerical results to corresponding experiments, we were able to obtain trustworthy values for all of them (see chapter 9 for details).

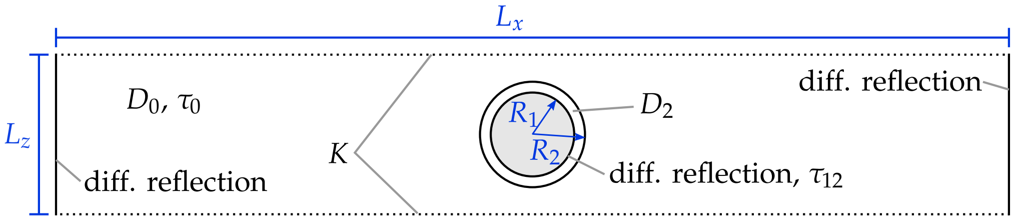

Figure 8.18: Two-dimensional sketch of the three-dimensional model for COMSOL Multiphysics corresponding to the water-based experiments. Geometric parameters (shown in blue) are: $L_x = 35.5\,\text{cm}$, $L_y = 16\,\text{cm}$, $L_z = 6\,\text{cm}$, R_1 and R_2 as given in Figure 8.10. The dotted black lines indicate the transparent tank walls where transmittive boundary conditions with the photon-loss velocity K are set. All other outer boundaries are set to be perfectly reflecting.

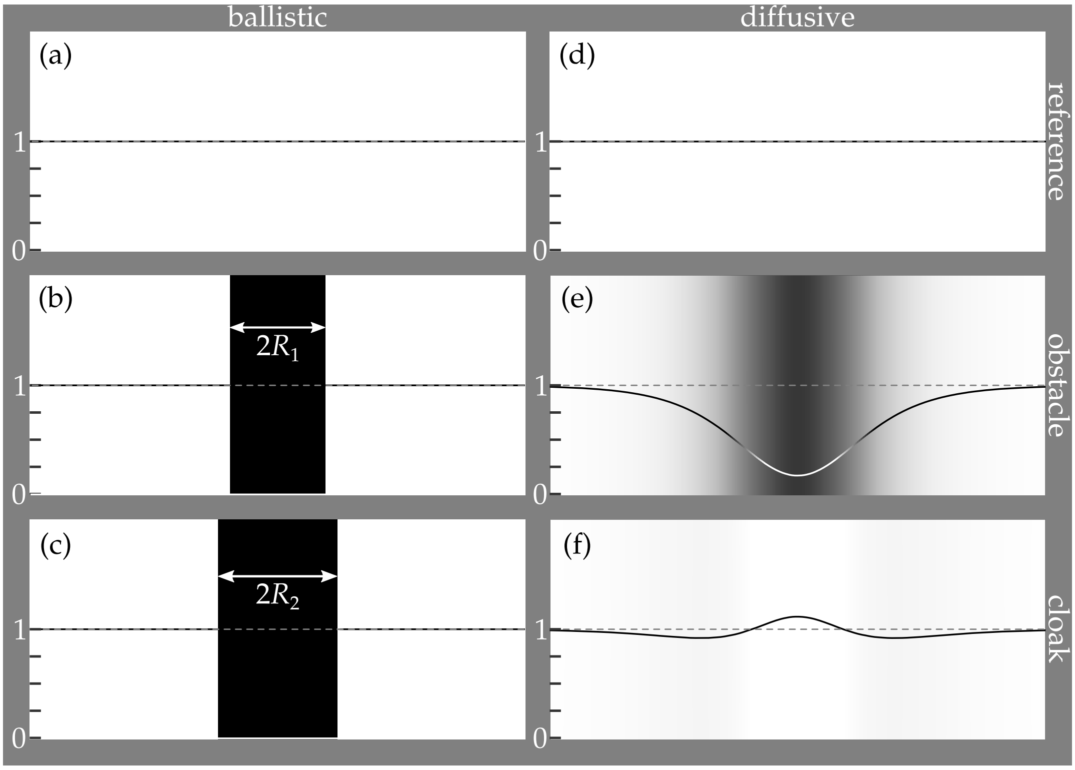

Figure 8.19: Calculated photon densities $n_\text{p}(x, y, z = L)$ corresponding to the experimental results shown in Figure 8.14. (a)–(c) are just schemes following geometric optics. Parameters are $L = 6\,\text{cm}$, $2R_1 = 32.1\,\text{mm}$, $2R_2 = 39.8\,\text{mm}$, $D_0 = 5.27 \times 10^8\,\text{cm}^2/\text{s}$, $D_2 = 72.1 \times 10^8\,\text{cm}^2/\text{s}$, $\tau_0 = 10\,\text{ns}$, $\tau_{12} = 0.245\,\mu\text{s}$, and $K = 0.1\,c_0$.

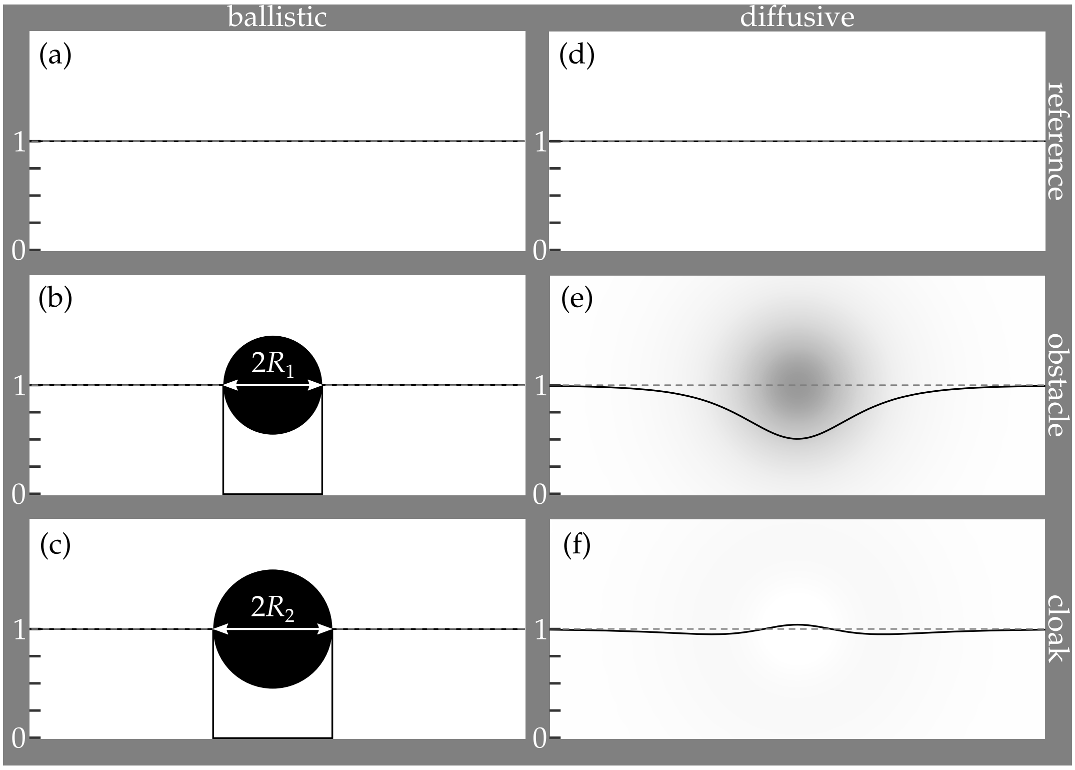

Figure 8.20: As Figure 8.19, but for spherical geometry. Parameters are $L = 6\,\text{cm}$, $2R_1 = 33.2\,\text{mm}$, $2R_2 = 39.9\,\text{mm}$, $D_0 = 10.54 \times 10^8\,\text{cm}^2/\text{s}$, $D_2 = 72.1 \times 10^8\,\text{cm}^2/\text{s}$, $\tau_0 = 10\,\text{ns}$, $\tau_{12} = 0.245\,\mu\text{s}$, and $K = 0.1\,c_0$.

This situation improved a lot for the all-solid-state structures presented in the next section.

Figures 8.19 and 8.20 exhibit the calculated photon densities corresponding to the experiments shown in figures 8.14 and 8.15. (The images corresponding to an empty tank are just schemes following geometric optics.) All significant features of the experimental results are well reproduced by the numerical model, with the exception of any tint or color variations (color dependence is not accounted for by the diffusion equation).

It is important to note that the intensity "wiggles" we saw in the experimental results for both cloak samples could only be reproduced numerically by introducing significant absorption on the core's surface (via the photon lifetime $\tau_{12} = 0.245\,\mu\text{s}$), while at the same time increasing the ratio of shell and surrounding diffusivity to a value of $D_2/D_0 = 13.68$ (6.84) for cylindrical (spherical) geometry. This ratio is 2.9 (2.2) times larger than the one

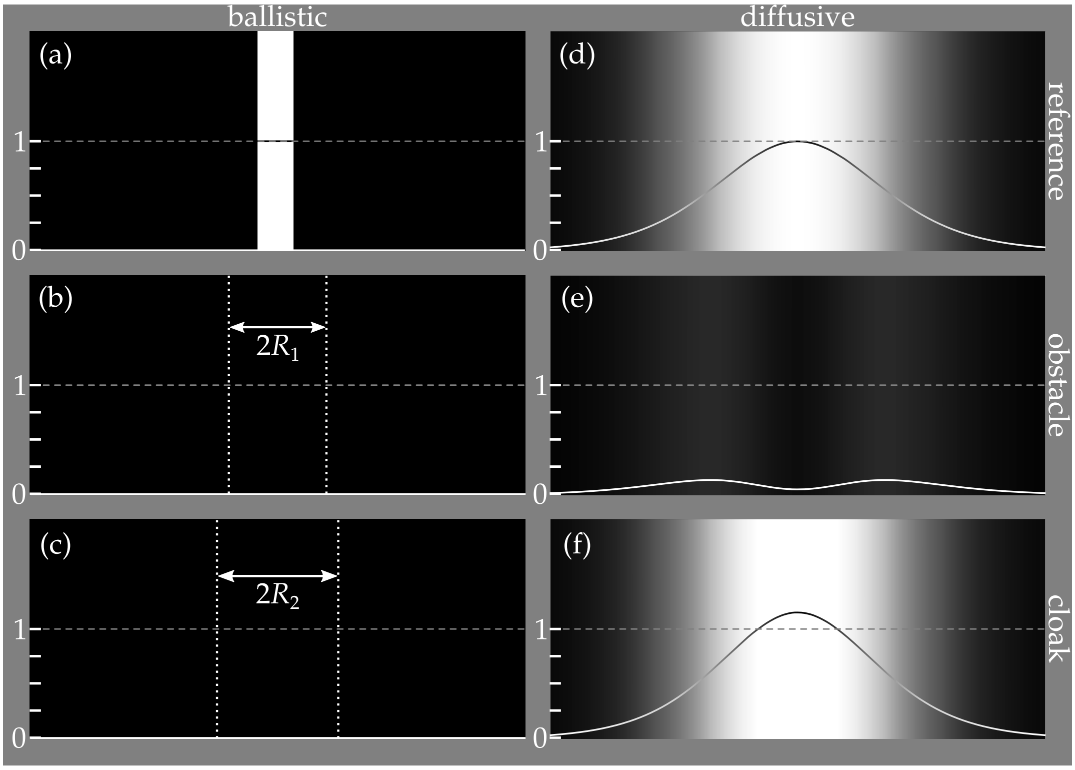

Figure 8.21: Numerical results as in Figure 8.19, but for inhomogeneous, line-like illumination. (a)–(c) are sketches following geometric optics. (d)–(f) nicely reproduce the experimental results presented in Figure 8.16. Parameters are $L = 6\,\text{cm}$, $2R_1 = 32.1\,\text{mm}$, $2R_2 = 39.8\,\text{mm}$, $D_0 = 5.27 \times 10^8\,\text{cm}^2/\text{s}$, $D_2 = 72.1 \times 10^8\,\text{cm}^2/\text{s}$, $\tau_0 = 10\,\text{ns}$, $\tau_{12} = 0.245\,\mu\text{s}$, and $K = 0.1\,c_0$.

the Hashin-Shtrikman formula returns for the idealized, absorption-free case. In other words, the most significant absorption seems to happen at the core surface, and has to be compensated for by increasing the shell's diffusivity. This conclusion is strengthened by the fact that with a polished aluminum cylinder as the core, we could not achieve cloaking at all (up to a surrounding paint concentration so high that the samples transmitted virtually no light anymore).

Figures 8.21 and 8.22 show calculated photon densities for inhomogeneous line-like or point-like illumination, corresponding to the experimental conditions shown in figures 8.16 and 8.17, respectively. Also here, theory and experiment agree very well in all significant features.

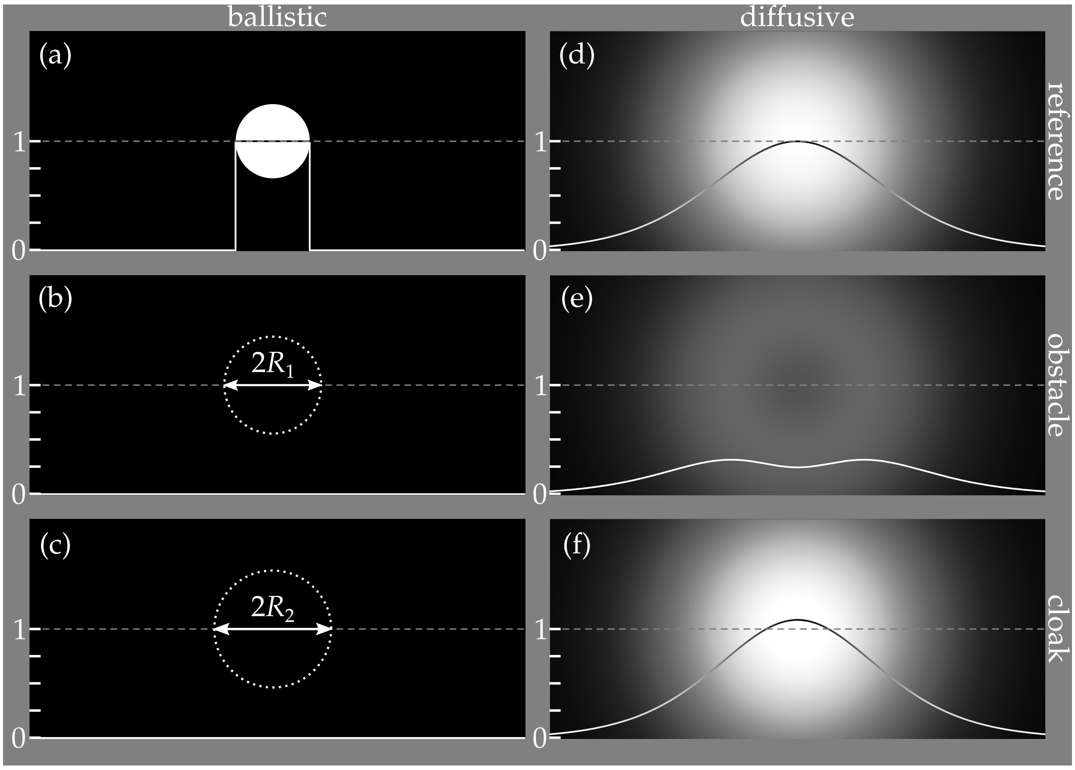

Figure 8.22: Numerical results as in Figure 8.20, but for inhomogeneous, point-like illumination. (a)–(c) are sketches following geometric optics. (d)–(f) nicely reproduce the experimental results presented in Figure 8.17. Parameters are $L = 6\,\mathrm{cm}$, $2R_1 = 33.2\,\mathrm{mm}$, $2R_2 = 39.9\,\mathrm{mm}$, $D_0 = 10.54 \times 10^8\,\mathrm{cm}^2/\mathrm{s}$, $D_2 = 72.1 \times 10^8\,\mathrm{cm}^2/\mathrm{s}$, $\tau_0 = 10\,\mathrm{ns}$, $\tau_{12} = 0.245\,\mu\mathrm{s}$, and $K = 0.1\,c_0$.

8.3.4 *Discussion*

So far, I presented water-based core-shell cloaks (one cylindrical and one spherical) that are about five orders of magnitude larger than the operation wavelength (qualifying them as *macroscopic*) and work throughout the entire visible spectrum (qualifying them as *broadband*). As explained in chapter 2, this combination is impossible for “ordinary” optics described by Maxwell’s equations for continua.

The results are not perfect, however, and mainly three aspects called for improvement: First, the absolute overall transmittance of the samples was very low (only about 0.5 % for the cylindrical geometry). Second, the water-based surrounding was not easy to handle and not long-term stable. Both these points make the cloaks not very convincing in the context of real-world applications outside a lab environment. Third, absorption at the core surface seemed to compromise the cloaking performance by leading to well-visible variations in the perceived brightness of the cloak surface.

All these aspects triggered us to devise solid instead of liquid structures with higher transmittance and optimized cloaking performance, which I will describe in the next section.

8.4 ALL-SOLID-STATE CLOAKS MADE OF PDMS

As explained above, the shortcomings of the water-based cloaks for diffuse light made us look for a different material system that would allow for compact, all-solid-state samples with high transmission and low absorption. From here on, we only considered cylindrical structures for easier fabrication and a more pronounced obstacle shadow to be cloaked.

8.4.1 Cloak design and sample fabrication

We chose to reduce all sample dimensions compared to the rather large water-based experiments, ending up with cuboids with dimensions $L_x = 15\,\mathrm{cm}$, $L_y = 8\,\mathrm{cm}$, and $L_z = 3\,\mathrm{cm}$ (compared to $35.5 \times 16 \times 6\,\mathrm{cm}^3$ before). This reduction in size led to samples that were easier to handle, store, and transport, as well as to a potentially higher diffusive transmittance according to Equation 5.53. To further facilitate a higher overall transmission through the samples, we decided to change the radii to $R_2/R_1 = 1.5$ (formerly 1.25), which reduces the necessary contrast in diffusivities to $D_2/D_0 = 2.6$ for cylindrical geometries (formerly 4.56).[12]

As PDMS doped with scattering particles proved to be a good solution for the cloaking shell in the previous experiments, we decided to use this material for both shell and surrounding of the all-solid-state cloaks. This required a two-step molding process to first fabricate the shell around the core and then incorporate both together in the homogeneous surrounding (see Figure B.2 for photographs of the molds). This increased complexity in fabrication was outweighed, however, by the big advantage that with identical materials used for shell and surrounding, the contrast in their scattering particle concentrations was known. Consequently, also the contrast in their diffusivities was known (assuming being in the diffusive regime),

---

[12] Besides that, initial tests with $R_2/R_1 = 1.25$ didn't lead to successful cloaking.

which removed one of the big unknowns of the water-based experiments.

Furthermore, reference samples made entirely of particle-doped PDMS could be used to fully characterize the diffusivity D_0, the absorption coefficient μ_a, and the photon-loss velocity K (see section 7.3 for details), leaving the core surface photon lifetime τ_{12} as the only remaining unknown parameter.

CORE MATERIAL AND SCATTERING PARTICLES For the core, we again chose a hollow aluminum cylinder coated with a thin layer of white spray paint, with a radius of $R_1 = 8\,\text{mm}$. The shell radius then was $R_2 = 1.2\,\text{cm}$, leaving a gap of only 3 mm between shell and sample boundary.

We tested different scattering particles for doping of the PDMS, among them polystyrene microparticles[13] and the same white wall paint used before for the surrounding. We ruled out the white paint for not knowing its exact ingredients and a suspected high absorption. The polystyrene particles showed a saturation of their scattering mean free path with increasing particle concentration and were thus ruled out as well. We finally settled on titanium dioxide nanoparticles in powder form[14] with a mean diameter of 245 nm. See figures A.5, A.6, and A.7 for ballistic transmission measurements on test samples of these three types of scattering media.

8.4.2 Results for aluminum cores

As written above, the ratio $R_2/R_1 = 1.5$ leads to a required diffusivity ratio of $D_2/D_0 = 2.6$. However, cloak samples with a shell that had 2.6 times fewer TiO_2 particles than the surrounding did not show successful cloaking. In contrast, they still showed a diffuse shadow similar to the one we encountered for the water-based obstacle previously. Figure 8.23 shows the result of such a cloak with particle concentrations in the surrounding and the shell of $C_0 = 0.13\,\text{mg/ml}$ and $C_2 = 0.05\,\text{mg/ml}$, translating into scattering mean free paths of $l_{s,0} = 2.28\,\text{mm}$ and $l_{s,2} = 5.94\,\text{mm}$, respectively.

We thus again optimized the needed ratio of particle concentrations experimentally. We found the best cloaking performance for a surrounding particle

---

[13] PS particles 1–20 μm from microparticles GmbH, Germany

[14] R700 from DuPont, USA

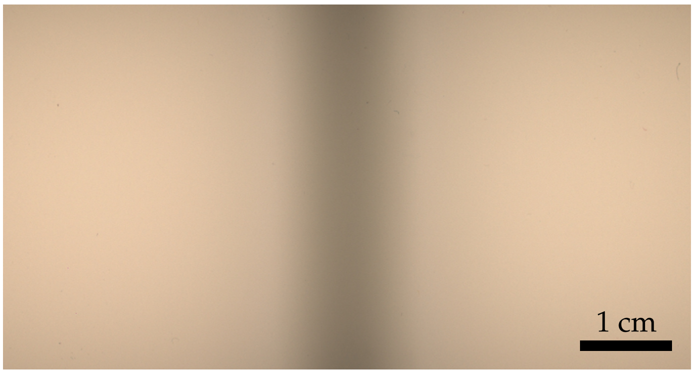

Figure 8.23: Photograph of a homogeneously illuminated PDMS-based cloak (cropped by 25 % from all sides) with particle concentrations in surrounding and shell of $C_0 = 0.13\,\mathrm{mg/ml}$ and $C_1 = 0.05\,\mathrm{mg/ml}$, respectively, corresponding to the required diffusivity contrast of $D_2/D_0 = 2.6$ for absorption-free media. The shell does not cloak the aluminum core successfully, as evident from the pronounced shadow visible in the center. Sample ID: TC1.

concentration of $0.49\,\mathrm{mg/ml}$ (a scattering mean free path of $0.606\,\mathrm{mm}$) and a ratio of concentrations of $C_2/C_0 = 6.5$, that is, 2.5 times larger than the theoretical value given by the Hashin-Shtrikman formula. Note that the surrounding scattering mean free path was significantly smaller than in our initial attempt, while the scattering mean free path of the shell ($l_{s,2} = 3.96\,\mathrm{mm}$) didn't change too much. For yet smaller particle concentrations in the shell, we observed the onset of pronounced ballistic transmission through the cloak sample, which is why we had to adjust the surrounding concentration instead, sacrificing overall transmittance. We then fabricated the reference and the obstacle sample with the same surrounding particle concentration C_0.

Figure 8.24 shows photographs of these three samples when illuminated homogeneously with white light. The superimposed intensity cuts are normalized to the light transmitted by a transparent, undoped block of PDMS. The samples show a maximum transmittance of about 5 %. Otherwise, the results look very similar to those obtained for a water-paint-based surrounding (see Figure 8.14). In particular, the cloak still showed the same intensity and color variations as before. This was discouraging as it meant that even with a larger shell and thus with a relaxed required diffusivity contrast between shell and surrounding, we did not obtain better cloaking than for the water-based cloaks.

It has to be stressed though that the scattering mean free path $l_{s,2} =$

Figure 8.24: Photographs of PDMS samples as shown in Figure 8.23, but for an experimentally optimized contrast in particle concentrations for the cloak sample, leading to reasonable cloaking performance. The solid curves are horizontal intensity cuts along the gray dashed lines, normalized to the transmittance of an undoped PDMS cuboid. Despite a larger shell radius and thus a relaxed required diffusivity contrast, there is no significant improvement of the cloaking performance compared to the water-paint-based results presented in Figure 8.14. Particle concentrations (scattering mean free paths) are $C_0 = 0.49\,\mathrm{mg/ml}$ in the surrounding ($l_{s,0} = 0.606\,\mathrm{mm}$) and $C_2 = 0.075\,\mathrm{mg/ml}$ in the shell ($l_{s,2} = 3.96\,\mathrm{mm}$).

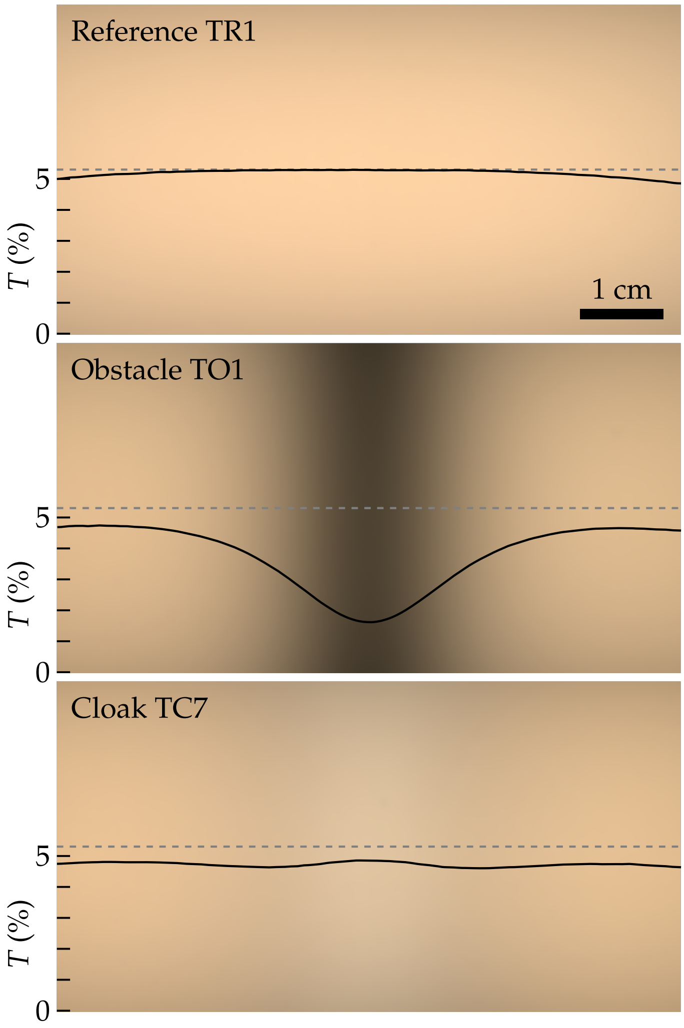

3.96 mm in the shell is almost identical to the shell thickness of 4 mm. This equality is quite drastically violating the diffusion approximation outlined in section 5.5. With this in mind, it is astounding that we observe successful cloaking at all.

NUMERICAL RESULTS In order to understand the origin of the remaining imperfections better, we again tried to fit numerical calculations to our experimental results. This time, however, we could reduce the number of unknown parameters in the numerical model to just one by first characterizing the homogeneous reference sample with the time-resolved

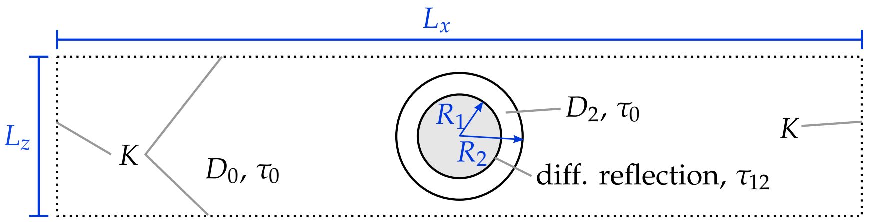

Figure 8.25: Two-dimensional sketch of the three-dimensional numerical model for COMSOL Multiphysics, corresponding to the PDMS-based samples. Geometric parameters (shown in blue) are: $L_x = 15\,\text{cm}$, $L_y = 8\,\text{cm}$, $L_z = 3\,\text{cm}$, $R_1 = 0.8\,\text{cm}$, and $R_2 = 1.2\,\text{cm}$. All outer boundaries are defined as in Equation 5.37 with the photon-loss velocity $K = 3.63 \times 10^9\,\text{cm/s}$ calculated according to Equation 5.39.

transmission measurement described in section 7.3. With a calculated photon-loss velocity of $K = 3.63 \times 10^7\,\text{m/s}$ (obtained from Equation 5.39 with the refractive index $n_{\text{PDMS}} = 1.4$), the characterization yielded a diffusivity of $D_0 = 9.0 \times 10^8\,\text{cm}^2/\text{s}$ and a photon lifetime of $\tau_0 = 10.3\,\text{ns}$. Figure 8.25 illustrates the slightly modified numerical model used in COMSOL Multiphysics (compare with Figure 8.18), where we accounted for the finiteness of the sample in all dimensions and assumed the photon lifetime τ_0 to be valid for both shell and surrounding. The shell diffusivity D_2 was obtained by scaling the surrounding diffusivity D_0 with the particle concentration ratio $C_2/C_0 = 6.5$. The only parameter in this model that could not be determined in advance was the photon lifetime τ_{12}, determining the absorption of light at the core surface.

Numerical results for the photon density $n_{\text{p}}(x, y, z = L)$ roughly matching the experiments were found for a core photon lifetime of $\tau_{12} = 0.12\,\mu\text{s}$ and are shown in Figure 8.26. Zero absorption at the core (that is, an infinitely long photon lifetime $\tau \to \infty$) led to a significant increase in the cloak's transmittance in the central region behind the shell, heavily overcompensating the shadow cast by the obstacle.

This finding again suggests that the biggest factor detrimental to the cloak's performance was absorption at the surface of the spray-painted aluminum core, just as it was for the water-paint-based samples. This similarity is not particularly surprising, as the core was identical in both configurations. However, with the more extensive experimental characterization possible with PDMS-based samples and identical material systems used for shell and surrounding, this assumption of an absorptive core could be strengthened.

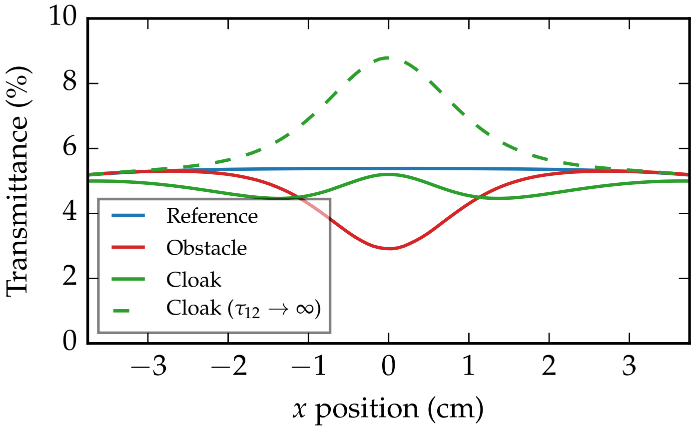

Figure 8.26: Numerically calculated photon transmittance through PDMS-based samples corresponding to Figure 8.24. Geometric parameters as given in Figure 8.25. The remaining parameters are $D_0 = 9.0 \times 10^8\,\mathrm{cm}^2/\mathrm{s}$, $D_2 = 6.5\,D_0$, $\tau_0 = 10.3\,\mathrm{ns}$, $\tau_{12} = 0.12\,\mu\mathrm{s}$ (solid green line), $\tau_{12} \to \infty$ (dashed green line). Without absorption at the core, the cloak heavily overcompensates the shadow cast by the obstacle.

8.4.3 Results for high-reflectivity oxide ceramic cores

With the results of the preceding paragraphs in mind, the logical step to further improve the cloaking performance of PDMS-based cloaks was to replace the coated aluminum that we had used for the core since the start of our work on diffusive-light cloaking by a different material with the highest possible diffuse reflectivity. Since there is no easy way of directly measuring this reflectivity (one would need a reference material with a reflectivity of exactly 1, which does not exist in this world, or—for a known source—collect all light reflected into all directions), we could only compare different materials among each other to evaluate their reflectivity.[15]

There are easily available ceramic materials such as MACOR or Corian (by DuPont, USA), which in our tests were however not surpassing the reflectivity of the painted aluminum (see Figure A.9). We also tested a sample of an alumina ceramic called Sintox AL, supplied by Morgan Advanced Ceramics, USA, which had a higher reflectivity than painted aluminum throughout the whole visible part of the spectrum (see Figure A.9).

---

[15] This limitation bore the slight risk of choosing a material that is more reflective than aluminum coated with white spray paint, but still not reflective enough for a significant

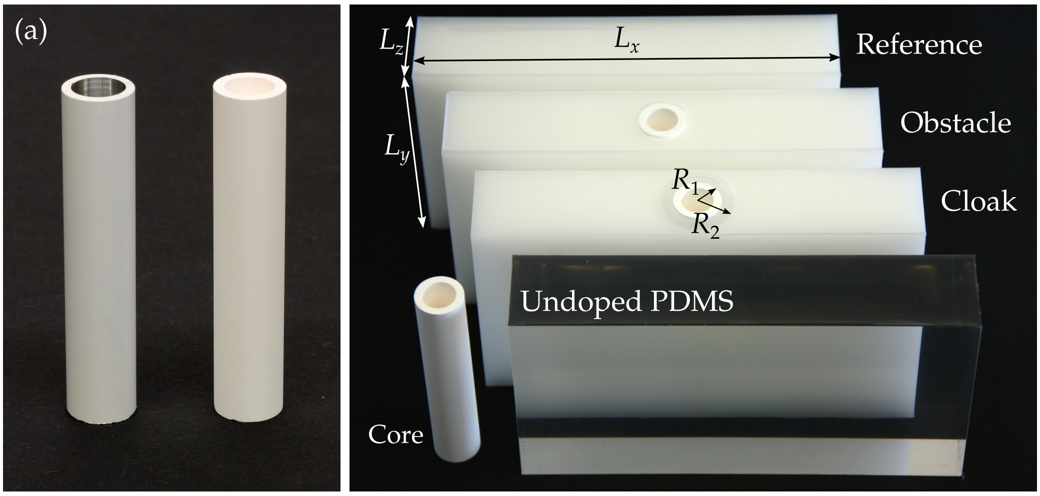

Figure 8.27: (a) Photograph of an aluminum cylinder coated with white acrylic paint (left-hand side) and an oxide ceramic cylinder (Accuflect® B6, right-hand side) under homogeneous diffuse illumination. The Accuflect® B6 cylinder shows a reflectivity that is 9 % (5 %) higher than that of the aluminum cylinder for the camera's red (blue) color channel. (b) Photograph of the fabricated reference, obstacle, and cloak sample next to a cuboid of undoped PDMS and an isolated Accuflect® B6 core for comparison. Dimensions are $L_x = 15\,\mathrm{cm}$, $L_y = 8\,\mathrm{cm}$, $L_z = 3\,\mathrm{cm}$, $R_1 = 0.8\,\mathrm{cm}$, and $R_2 = 1.2\,\mathrm{cm}$. Panel (b) taken from Ref. 113, Fig. 1.

We finally settled on another oxide ceramic called *Accuflect® B6* (Accuratus Corporation, USA), which was easier available and comparable to Sintox AL in its specifications. The specified Lambertian reflectivity of bulk Accuflect® B6 material is greater than 96 % throughout the whole visible spectrum and reaches values of 99 % for wavelengths greater than 650 nm. The specified specular reflectance is smaller than 0.5 % for all visible light. We obtained hollow Accuflect® B6 cylinders with an outer diameter of 16 mm (identical to the aluminum cylinders we used previously) and an inner diameter of 13.5 mm. Figure 8.27 (a) shows a photograph of both types of cylinders side by side under homogeneous diffuse illumination. The reflectivity of the Accuflect® B6 cylinder is up to 9 % higher than that of the painted aluminum core and furthermore appears to have a lower angular variation (which fits to the specified Lambertian reflection pattern).

---

improvement of the cloaking performance when used for the cloak's core.

THE SAMPLE FABRICATION worked just as for the aluminum cores, with the difference that when molding the shell, we used a Teflon-coated aluminum cylinder that was replaced by the oxide-ceramic cylinder after polymerization of the PDMS. This way, we prevented the intrusion of liquid PDMS into the highly porous ceramic cylinder, which would have otherwise compromised its reflecting properties. We could not identify any significant effect of the inevitable extra PDMS-air interface resulting from this fabrication procedure. The fabricated reference, obstacle, and cloak samples can be seen in Figure 8.27 (b).

EXPERIMENTAL RESULTS Just as for the cloaks with aluminum cores, we optimized the scattering particle concentrations of shell and surrounding experimentally. For a shell particle concentration of $C_0 = 0.1\,\mathrm{mg/ml}$, we found an optimized cloaking performance for a surrounding particle concentration of $C_2 = 0.39\,\mathrm{mg/ml}$, which means that the ratio of concentrations was still 1.5 times larger than what theory had predicted (namely $D_2/D_0 = 2.6$), but at the same time considerably smaller than the value we found previously for aluminum cores. Furthermore, the absolute concentration of particles the surrounding decreased (from formerly $0.49\,\mathrm{mg/ml}$), which resulted in a higher overall transmittance. The slight increase in the shell particle concentration (formerly $0.075\,\mathrm{mg/ml}$) also helped in optimizing the cloaking performance, supposedly by reducing the ballistic portion of light propagation in the shell. But also in this case, the shell (with a scattering mean free path of $l_{s,2} = 2.97\,\mathrm{mm}$ compared to a shell thickness of $4\,\mathrm{mm}$) was still violating the conditions given for the diffusion approximation (see section 5.5).

Nevertheless, the cloaking performance turned out to be excellent with the new ceramic cores, surpassing that of all cloaks we had built previously. See Figure 8.28 for photographs of reference, obstacle, and cloak under homogeneous illumination. The clearly visible shadow cast by the obstacle is almost perfectly suppressed by the cloak, with hardly any intensity or color variations visible.

Figure 8.29 (a) exhibits the absolute transmittance for horizontal cuts along the center of reference, obstacle, and cloak under homogeneous illumination, again normalized to the light transmitted through a clear, undoped PDMS cuboid as shown in Figure 8.27 (b). Apart from a slight overall difference in transmittance, reference and cloak are almost indistinguishable. The shadow cast by the obstacle is less pronounced than in earlier experiments

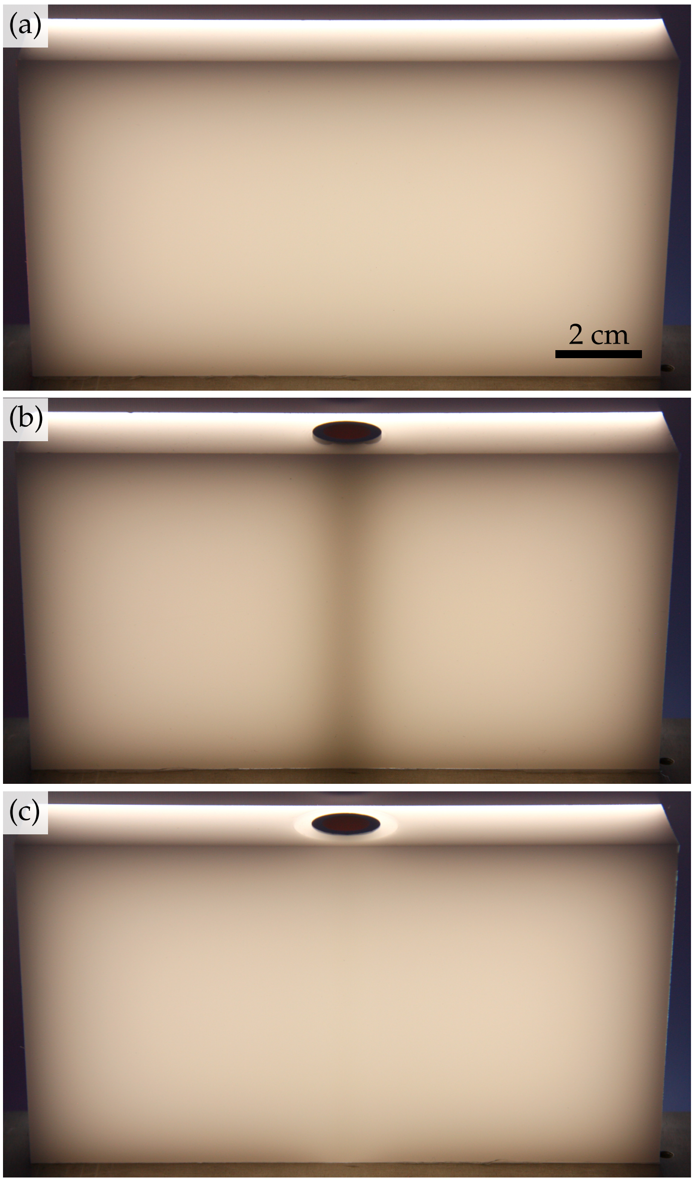

Figure 8.28: Photographs of PDMS-based samples with hollow high-reflectivity Accuflect® B6 cylinders used as the core under homogeneous illumination. (a) Homogeneous reference medium (AR1) with a TiO_2 particle concentration of $C_0 = 0.39\,\mathrm{mg/ml}$ ($l_{s,0} = 0.76\,\mathrm{mm}$). (b) Obstacle (AO1) with an Accuflect® B6 core inside the otherwise homogeneous surrounding. (c) Cloak (AC4) with an additional high-diffusivity shell with a particle concentration of $C_2 = 0.1\,\mathrm{mg/ml}$ ($l_{s,2} = 2.97\,\mathrm{mm}$). To the bare eye, the cloak works without any intensity or color variations as observed for cloaks with aluminum cores (compare figures 8.14 and 8.24). The sample shown in panel (c) is a nearly perfect macroscopic cloak for diffuse visible light. Reproduced from Ref. 113.

(compare figures 8.14 and 8.24), which is another indication for the significantly reduced core absorption. With an absolute transmittance of about 7 %, inspecting the cloaking performance is possible in daylight conditions, for example by holding the samples against the sun or the room light.

To demonstrate how crucial the right ratio of the particle concentrations in shell and surrounding is, we fabricated two more cloaks with a shell particle concentration 10 % higher and 10 % lower than that of the optimized cloak,

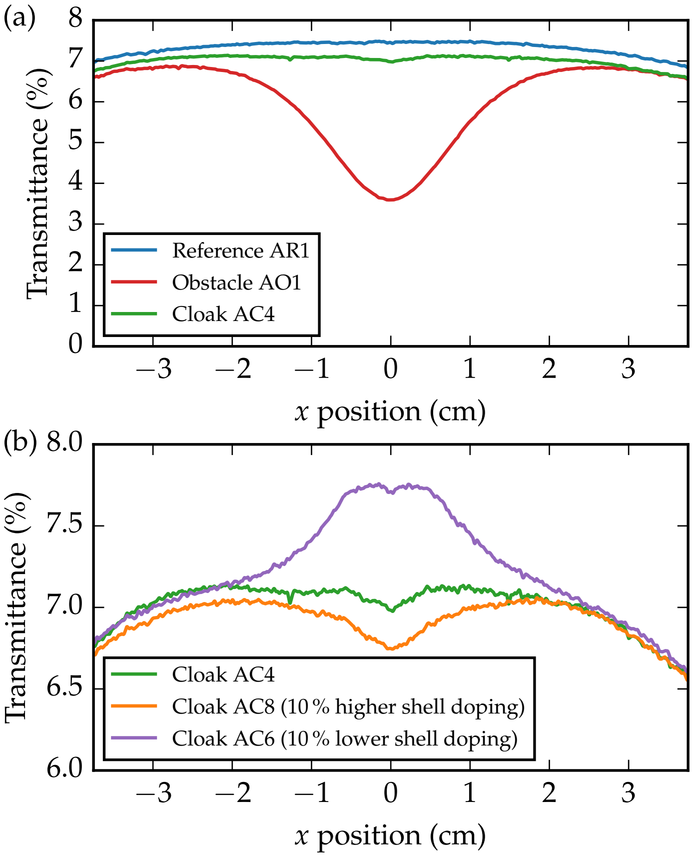

Figure 8.29: Measured transmittance of PDMS-based samples under homogeneous illumination, normalized to the light transmitted through an undoped block of clear PDMS. (a) Comparison of reference, obstacle, and cloak as shown in Figure 8.28. (b) Comparison of the optimized cloak with one version with a 10 % higher shell doping concentration ($l_{s,2} = 2.70\,\mathrm{mm}$ and $D_2/D_0 = 3.55$, orange curve) and one with a 10 % lower shell doping concentration ($l_{s,2} = 3.30\,\mathrm{mm}$ and $D_2/D_0 = 4.33$, purple curve). Both do not show optimal cloaking. Reproduced from Ref. 113, Fig. 3.

respectively. Both of them did not show optimal cloaking. Corresponding transmittance results are shown in Figure 8.29 (b).

FOR A QUANTITATIVE EVALUATION of the fabricated samples, we first inspected the maximum deviations of both obstacle and cloak from the reference, analyzing the transmittance profiles showed in Figure 8.29. We found a maximum deviation of 5.2 % for the cloak, which is 10 times smaller than the maximum deviation of 52 % for the obstacle.

To include not only a single point (namely, the center of the sample) but a wider region in the quantitative analysis, we again (see Equation 8.5) make use of the normalized standard deviation

$$\Delta = \frac{\sqrt{\Sigma_i (I_i - I_i^0)^2}}{\sqrt{\Sigma_i (I_i^0)^2}}\,, \tag{8.7}$$

which had already been used for the evaluation of mechanical cloaks in Ref. 76.[16] I_i is the ith data point of the quantity to be evaluated (in our case, the transmittance of cloak or obstacle) and I_i^0 is the corresponding reference value. The sum runs over all data points of a selected region. Naturally, this region has to be chosen with care and most importantly identical for all samples that should be compared with each other. For a spatial region identical to the one used for the intensity cuts in Figure 8.29, we obtain $\Delta_{\text{obs}} = 24.2\,\%$ for the obstacle and $\Delta_{\text{clk}} = 4.35\,\%$ for the cloak, translating to an improvement by a factor of 5. This value is actually not so large, which stems mainly from the constant global offset between the reference transmittance curve and the corresponding curves for obstacle and cloak. While this leads to an appreciable deviation of the cloak that is "only" a factor of 5 smaller than that for the cloak, this deviation is virtually invisible for the detector which is most natural when comparing optical cloaks: our eyes (see Figure 8.28). This seeming discrepancy is due to the fact that our eyes are very good at detecting steep gradients (as for the obstacle's shadow), but not so good in comparing absolute brightnesses.

We also re-evaluated the measurement results for water-paint-based cloaking as depicted in Figure 8.14 with the method above. We obtained $\Delta_{\text{obs}} = 40.1\,\%$ for the obstacle and $\Delta_{\text{clk}} = 11.3\,\%$ for the cloak. This result again demonstrates the significant improvement of the cloaking performance with the introduction PDMS-based cloaks with highly reflective cores.

SAMPLE REPRODUCABILITY To investigate the origin (rather than debate the significance) of the constant offset of the reference transmittance curve from those of cloak and obstacle seen in Figure 8.29, we compared the measured transmittance profiles of samples that were nominally identical in all their fabrication parameters. Figure 8.30 (a) shows such profiles for two nominally identical cloak samples, Figure 8.30 (b) for two nominally identical reference samples. To facilitate the evaluation, the vertical axis is stretched with respect to Figure 8.29 (a). While both cloak samples indeed show hardly any deviation from each other in their transmittance, the curves corresponding to the two reference samples do have a constant offset of roughly 0.25 %, which is comparable to the mentioned offset between reference and cloak in Figure 8.29 (a). Another cloak sample (not shown)

---

[16] In general, the quantitative analysis of cloaks is not yet common practice in the scientific community. Notable exceptions are references 20, 76, 114, and 115

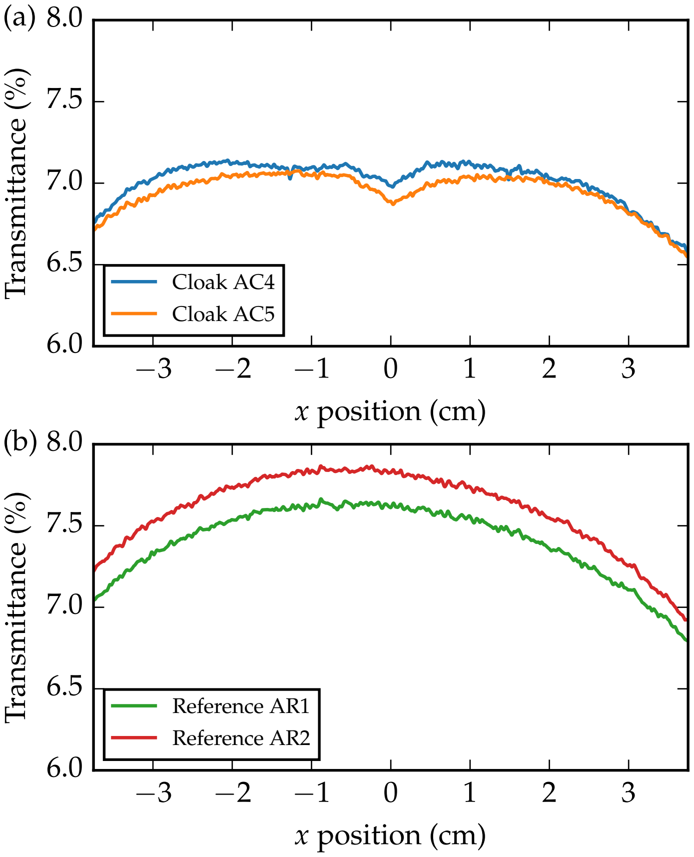

Figure 8.30: Measured transmittance profiles of nominally identical samples to investigate the sample reproducability (note the stretched vertical scale). (a) Two nominally identical cloak samples show hardly any deviation. (b) Significant deviation of about 0.25 % between two nominally identical reference samples. This deviation is comparable to the one seen in Figure 8.29 (a). The most likely origin are errors in measuring the amount of the liquid PDMS base during the fabrication of the PDMS-nanoparticle mixture for the homogeneous surrounding.

also exhibited a constant transmittance offset with respect to other cloak samples. The most likely origin of these deviations are measuring errors in the fabrication of the PDMS-nanoparticle mixture for the homogeneous surrounding, where measuring the amount of the liquid PDMS base was done via the measuring lines of conventional beakers. Instead of measuring the volume, precise weighing could potentially improve the accuracy of the fabrication process.

ASYMMETRY IN THE TRANSMITTANCE CURVES All measured intensity and transmittance profiles presented so far exhibit a slight asymmetry, with the right half of the curve being a bit lower than the left half. Uneven lighting or inhomogeneous samples could be ruled out (for example, rotating the samples by 180° did not change the measured asymmetry). Instead, the asymmetry was most likely caused by the camera CCD chip used, the two halves of which were read out in parallel using separate analog-to-digital

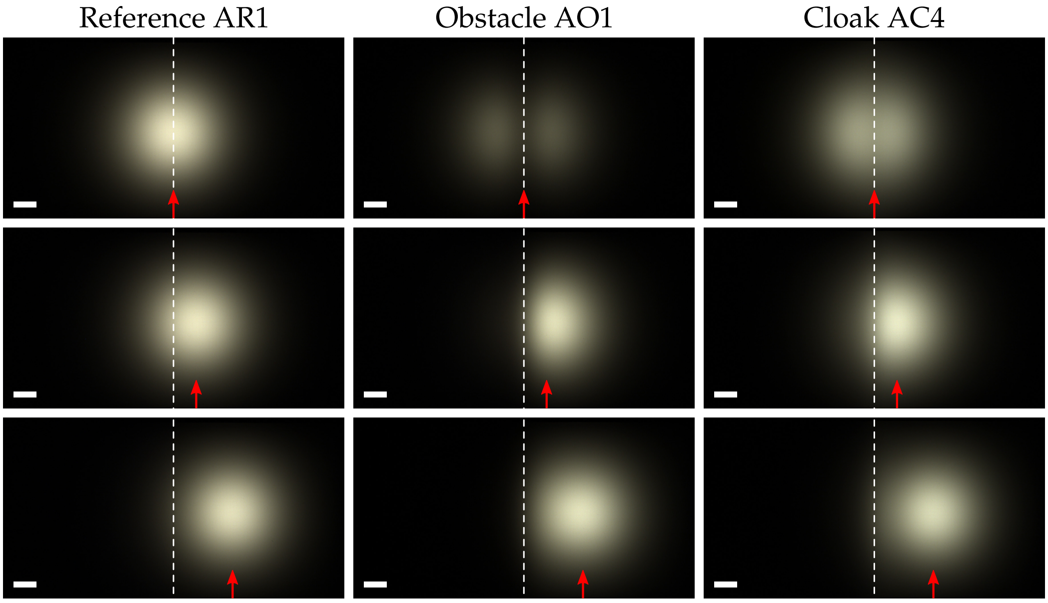

Figure 8.31: Photographs (uncropped) of PDMS-based samples with Accuflect® B6 cores illuminated by a point-like white light spot emerging from a mutlimode fiber. The white dashed lines indicate the sample center, the red arrows mark the position x_s of the illumination spot. Cloaking works reasonably well, with the strongest deviations visible for centered illumination (first row). For off-center illumination (third row), all three samples appear similar. Length of the white scale bar: 1 cm.

converters. Under certain lighting conditions (for example when focusing the camera directly onto the monitor screen), huge differences arose in the brightness and color of the right and left half of the captured images, a phenomenon also called *tap inbalance*. While no obvious inbalance was visible when capturing the diffusive media discussed, the consistent asymmetry in the measurement results suggests that a slight inbalance persisted. A single-tap camera (where the whole chip is read out via a single analog-to-digital converter) could be used to verify and probably eliminate this problem.

INHOMOGENEOUS ILLUMINATION We also examined the cloak's performance under inhomogeneous illumination. Therefore, we used a setup similar to the one displayed in Figure 7.4. We coupled white light into the horizontally scannable multimode fiber we previously used for detection and thus illuminated the samples with a point-like light spot. Of course,

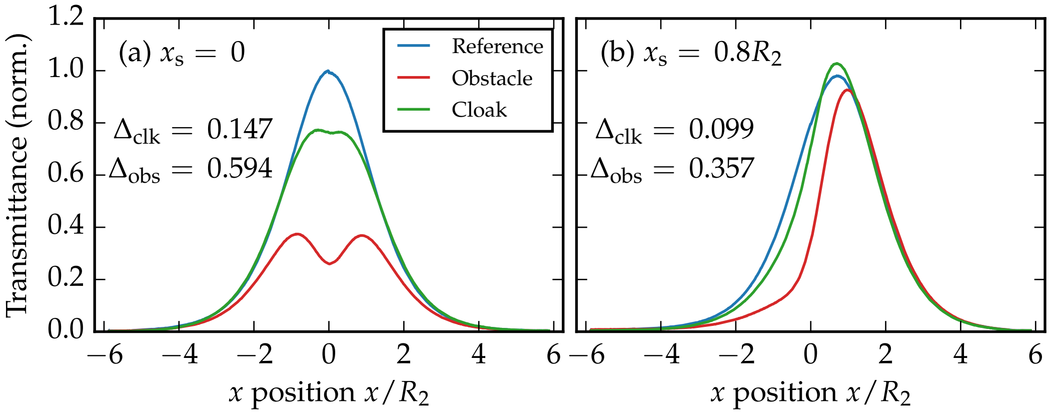

Figure 8.32: Normalized transmittance profiles obtained by integrating the photographs shown in the first two rows of Figure 8.31 vertically and averaging over the three RGB color channels. The normalized standard deviation Δ with respect to the reference (Equation 8.7) is given for obstacle and cloak.

the point-like illumination of the cylindrical samples breaks the vertical translational invariance. However, the computer monitor (which we tried to use for a line-like illumination as in Figure 8.16) proved to be too unstable in its white-light output over the rather long measurement times needed for scanning the complete width of the sample. As previously, we took photographs of the light transmitted through the samples. We scanned the excitation fiber over the whole sample width in steps of 1 mm, leading to 149 photographs per measurement.

Figure 8.31 shows such photographs of the reference, obstacle, and cloak sample for three different positions of the illumination spot (marked by the red arrows). For centered illumination (first row in Figure 8.31), the obstacle very obviously casts a pronounced shadow, while the cloak looks fairly close to the reference, albeit a bit darker. For an illumination position far away from the sample center, all three samples show similar transmission patterns.

To calculate the normalized standard deviation Δ (as defined in Equation 8.7) with respect to the reference, we vertically integrated each photograph (and averaged over the three RGB color channels). With this integration, we effectively mimic an infinitely extended medium under line-like illumination and thus obtain transmittance profiles comparable to those shown earlier for homogeneous illumination. As the transmitted intensity is practically zero at the top and bottom sample boundaries in Figure 8.31, the finiteness of the samples introduces only a small error. Figure 8.32

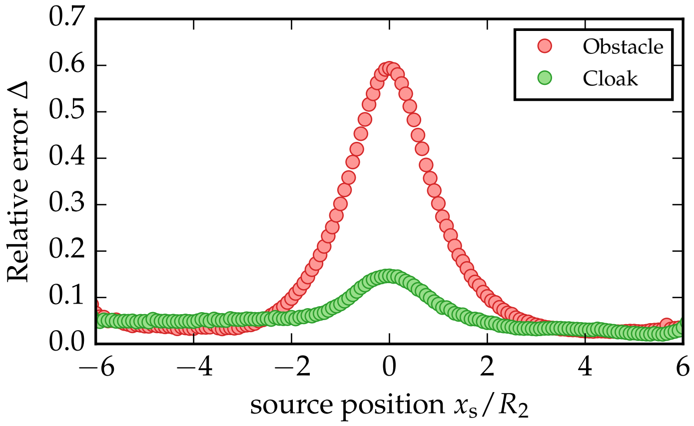

Figure 8.33: Normalized standard deviation of obstacle and cloak with respect to the reference versus the source position x_s. (Each data point corresponds to one transmittance profile as shown in Figure 8.32.) The cloak outperforms the obstacle for nearly all source positions.

shows these transmittance profiles for the first two source positions shown in Figure 8.31. Qualitatively, the profiles are similar to the ones obtained from an idealized numerical calculation presented in section 8.2 (compare Figure 8.4 (a) and (b)). One should keep in mind though that the numerical calculations did not account for any absorption in the samples and thus inherently differ from the experiments.

Finally, Figure 8.33 displays the deviations of obstacle and cloak versus the source position. Obviously, the cloak performs significantly better than the obstacle for almost all source positions. One would expect both deviations Δ_{obs} and Δ_{clk} to converge to zero for source positions far away from the sample center. This convergence does not occur here because of the constant offset the reference transmittance showed with respect to obstacle and cloak due to fabrication imperfections (see Figure 8.29 (a)).

All in all, also this latest generation of core-shell cloaks for diffuse light performs not too bad under inhomogeneous illumination conditions. We did not look further into optimizing this performance with a two-shell design as presented in section 8.2 since the shell in the current design turned out to be operating beyond the diffusion description, rendering approaches solely based on the diffusion equation inappropriate for further experiments. Further details of this discrepancy are found in subsections 8.4.6 and 8.4.7.

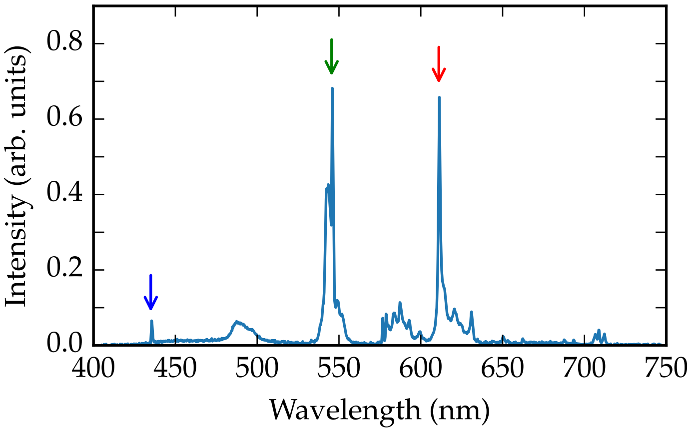

Figure 8.34: Measured spectrum of the white light emitted from the computer monitor we used for the sample illumination. The three main spectral peak wavelengths corresponding to the three RGB colors are: $\lambda_\mathrm{R} = 611\,\mathrm{nm}$, $\lambda_\mathrm{G} = 545\,\mathrm{nm}$, and $\lambda_\mathrm{B} = 435\,\mathrm{nm}$ (see colored arrows).

8.4.4 *Color tint examination with Mie theory*

As noted before, all the samples we illuminated with white light showed a certain color tint in their transmission. This tint was yellowish for the water-paint-based experiments and rather reddish for the PDMS-based samples, and furthermore increased with increasing scatterer concentration. It consistently resulted in a diffuse transmission that was highest for red light and lowest for blue light (also see figures A.1 to A.3).

In principle, such a color tint can originate from a wavelength-dependent absorption coefficient $\mu_\mathrm{a}(\lambda)$ as well as from a wavelength-dependent scattering coefficient $\mu_\mathrm{s}(\lambda)$, which would directly translate into a wavelength-dependent diffusivity $D(\lambda)$. However, the absorption coefficient $\mu_\mathrm{a} = 1/(\tau v)$ turned out to be several orders of magnitude smaller than the scattering coefficient for all analyses we performed: Typical values for the photon lifetime were $\tau \approx 10\,\mathrm{ns}$, which translates into $\mu_\mathrm{a} \approx 0.0005\,\mathrm{mm}^{-1}$ for a PDMS-based medium with $n = 1.4$. In contrast, typical scattering coefficients for the surrounding medium were $\mu_\mathrm{s} = 1/l_\mathrm{s} \approx 1\,\mathrm{mm}^{-1}$, which is 2000 times larger than the quoted absorption coefficient. Thus, absorption can most likely be ruled out as the origin of tinted diffuse transmission of light.

To explore the effect of a wavelength-dependent scattering coefficient, we carried out Mie scattering calculations using a freely available web-based calculator [116]. We measured the three main spectral intensity peak wavelengths $\lambda_\mathrm{R} = 611\,\mathrm{nm}$, $\lambda_\mathrm{G} = 545\,\mathrm{nm}$, and $\lambda_\mathrm{B} = 435\,\mathrm{nm}$ of the light emitted from the computer monitor we used for white-light illumination of our samples (see Figure 8.34) and used them as the input wavelengths for

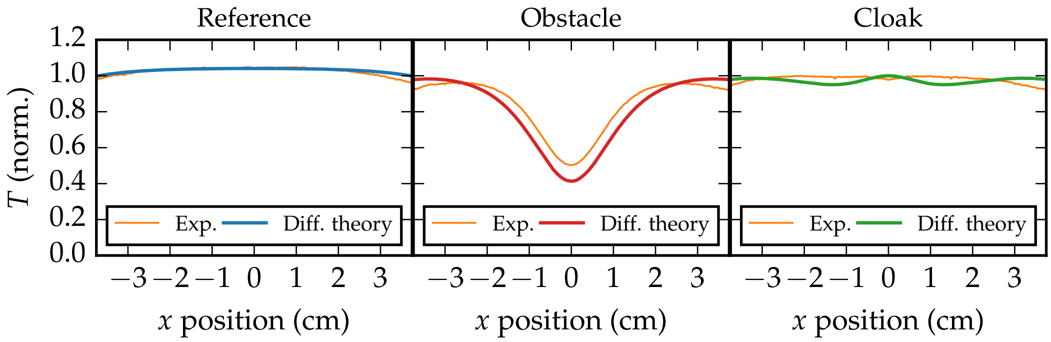

Figure 8.35: Normalized transmittance profiles calculated with diffusion theory for reference, obstacle, and cloak with corresponding experimental results from Figure 8.29 (a) shown for comparison (thin orange lines). Parameters are $D_0 = 11.9 \times 10^8\,\mathrm{cm}^2/\mathrm{s}$, $D_2 = 3.9D_0$, $\tau_0 = 10.5\,\mathrm{ns}$, $\tau_{12} = 0.23\,\mu\mathrm{s}$, and $K = 3.63 \times 10^9\,\mathrm{cm}/s$. Experiment and theory do not agree well, suggesting that the shell cannot be described with diffusion theory anymore.

the Mie scattering calculator.

The TiO_2 nanoparticles have a mean diameter of $d = 245\,\mathrm{nm}$ with a polydispersity of 45 %, and a refractive index of about 2.7. Feeding the Mie calculator with the above parameters and the host refractive index of $n_{\mathrm{PDMS}} = 1.4$, we obtained a scattering cross section (which is inversely proportional to the diffusivity) that varied by about 20 % between the red and blue measured monitor wavelengths. The reddish tint visible in the photographs shown in Figure 8.28 translates into a relative deviation between the red and blue color channel of about 30 %. Given the mentioned polydispersity of the scattering particles and the fact that the diffusive transmittance is only approximately proportional to the diffusivity (see Equation 5.53), the numerical and experimental results agree fairly well.

8.4.5 *Limits of the diffusion description*

Via the time-resolved measurement of the diffusive transmission through the reference sample (with a particle concentration of 0.39 mg/ml corresponding to a scattering mean free path of $l_{s,0} = 0.76\,\mathrm{mm}$) as described in section 7.3, we obtained a surrounding diffusivity of $D_0 = 11.9 \times 10^8\,\mathrm{cm}^2/\mathrm{s}$ and a photon lifetime of $\tau_0 = 10.5\,\mathrm{ns}$. For numerical calculations corresponding to the experiments shown before, we scaled D_0 with the mean free path ratio $l_{s,2}/l_{s,0} = 3.9$ between shell and surrounding to obtain a shell diffusivity of $D_2 = 46.41 \times 10^8\,\mathrm{cm^2/s}$. We then performed calculations with COMSOL Multiphysics with the same numerical model we used before (see Figure 8.25), again with only the core surface photon lifetime τ_{12} as a free parameter. Figure 8.35 shows (for an optimized core photon lifetime of $\tau_{12} = 0.23\,\mu\mathrm{s}$) the calculated transmittance curves of reference, obstacle, and cloak (solid lines) superimposed onto the experimental results (thin orange lines) as shown in Figure 8.29. To reduce the significance of the sample preparation imperfections which led to a constant offset in the experimental reference curve, all curves are normalized to the maximum of the corresponding cloak curve. Except for the reference, numerical and experimental results do not fit well. Specifically, the numerical results for the cloak still contain intensity variations like we have seen them for previous experiments (compare figures 8.14 and 8.24), but which are absent in the present experimental results. Furthermore, the shadow cast by the obstacle is significantly more pronounced in the numerical results.

This discrepancy suggests that with the current concentrations of scattering particles (which were chosen as small as possible to enhance the diffusive transmittance), light propagation in the shell cannot be adequately described by the diffusion equation anymore. In other words, simply extrapolating the shell diffusivity from the surrounding diffusivity via the contrast in scatterer concentrations is not justified here. As noted before, this aspect is not really surprising when one considers the constraints imposed by the diffusion approximation (see section 5.5), which demand a medium to be at least 10 times the transport mean free path l_t in size to qualify as fully diffusive. For our parameters, already the scattering mean free path $l_{s,2} = 2.97\,\mathrm{mm}$ (which is generally smaller than l_t) is comparable to the shell thickness.

A careful comparison of figures 8.24 and 8.26 reveals that also for the cloaks with painted aluminum cores, the calculated transmittance variations were larger than the ones observed experimentally, suggesting that also there, the diffusion description was not entirely valid.

In conclusion, it is not only absorption at the core surface that requires a ratio of particle concentrations in shell and surrounding larger than what theory predicts, but also the mere fact that the shell is not a strictly diffusive medium anymore. More importantly, we have to appreciate that the diffusion equation and its numerical solutions are not necessarily appropriate tools for the description and design of diffusive-light structures aiming at high absolute light transmittances. Consequently, Kerner's formula—which strictly assumes pure diffusion of light—can still serve as the starting point but not as a holistic recipe for designing high-transmittance diffusive-light cloaks.

8.4.6 Monte-Carlo-based raytracing results

In light of the findings above, we performed Monte-Carlo-based (MC) photon raytracing simulations with FRODO (see section 6.2 for details on the implementation), corresponding to the transmission measurements on PDMS-based cloaks with ceramic cores shown in Figure 8.28. The geometry of the model was identical to the sample geometry, with surrounding and shell assumed to be turbid media. The core cylinder was assumed to have a Lambertian reflection pattern with a reflectivity R (and an absorptivity $1 - R$, such that no light could enter the core). Apart from the core reflectivity, all necessary simulation parameters (see section 6.2) were determined experimentally earlier. The scattering coefficient followed directly from the scattering mean free path ($\mu_s = 1/l_s$), which was determined via ballistic transmission measurements and could be extrapolated to any given TiO_2 nanoparticle concentration (compare Figure A.7). As the diffusivity D_0 of the surrounding medium had been determined by time-resolved diffusive transmission measurements (which also yield the absorption coefficient μ_a) and as the host refractive index n_{PDMS} was known, the asymmetry factor $g = 0.544$ followed directly from the definition of the diffusivity (Equation 5.32). Table 8.1 summarizes the parameters used for surrounding and shell.

We assumed a Lambertian plane source with the same size as the illuminated sample area ($15 \times 8\,\text{cm}^2$) at a position of $z_s = -1.4999\,\text{cm}$, that is, lying $1\,\mu\text{m}$ deep inside the sample geometry. A plane detector of the same size and with a resolution of $1500 \times 800\,\text{px}$ was assumed right behind the geometry at a position of $z_d = 1.5001\,\text{cm}$. A total number of 1 billion photons was traced in each simulation, with a cutoff propagation time of

Table 8.1: Monte-Carlo raytracing parameters for simulations corresponding to the transmission experiments shown in Figure 8.28: absorption coefficient μ_a, scattering coefficient μ_s, asymmetry factor g, and refractive index n.

Medium	μ_a (mm^{-1})	μ_s (mm^{-1})	g	n
Surrounding	0.000445	1.314	0.544	1.4
Shell	0.000445	0.337	0.544	1.4

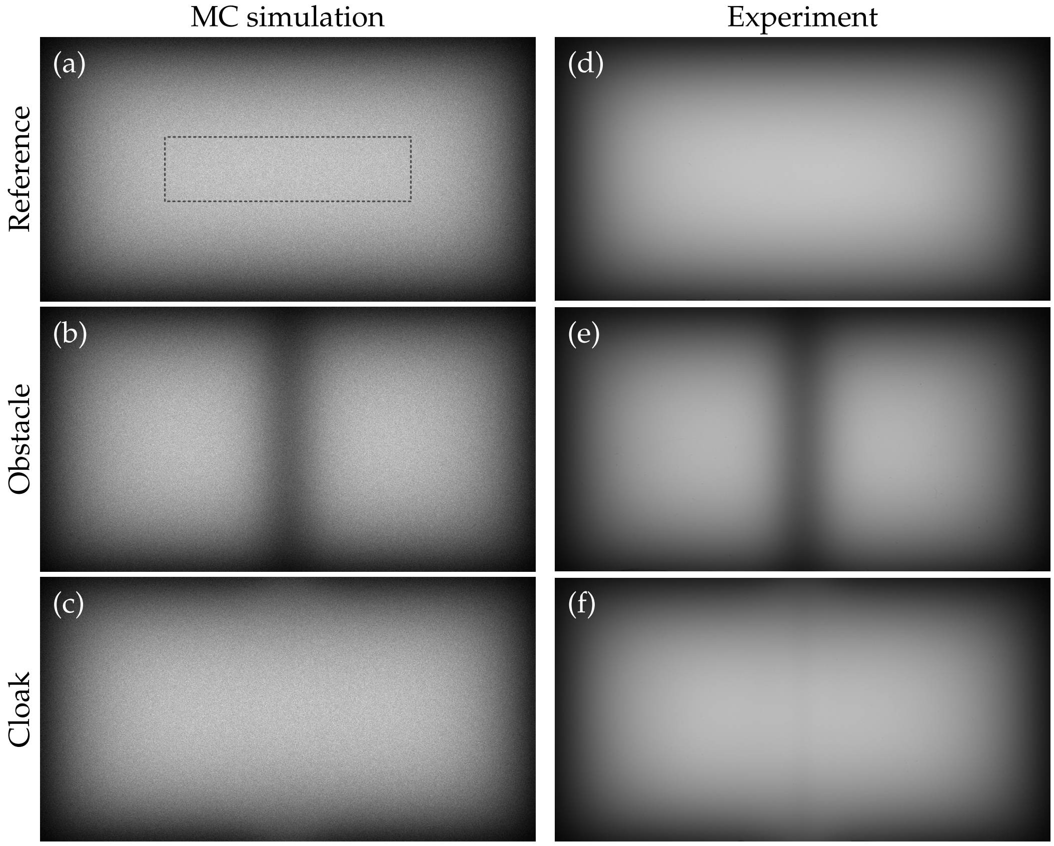

Figure 8.36: Comparison of Monte-Carlo-based raytracing images with experimental results. (a) to (c): Transmission images calculated via Monte-Carlo raytracing of individual photons, assuming a core reflectivity of $R = 0.98$. Geometry as in Figure 8.25, optical parameters are given in Table 8.1. (d) to (f): Grayscale versions of the photographs shown in Figure 8.28. In contrast to diffusion theory (compare Figure 8.35), MC raytracing reproduces the experimental results very well. The dotted line in (a) marks the region used for obtaining the transmittance profiles shown in Figure 8.37. Computation times were (a) 1 h 5 min, (b) 1 h 30 min, (c) 1 h 32 min.

$t_{\max} = 7.5\,\text{ns}$ (on average, this cutoff time was reached by about 0.005 % of the traced photons).

Figure 8.36 shows raytraced transmission images (panel (a) to (c)) corresponding to the parameters given above and a core reflectivity of $R = 0.98$ (which is in agreement with the reflectivity the manufacturer specifies for the Accuflect® B6 material). For comparison, grayscale versions of the ex-

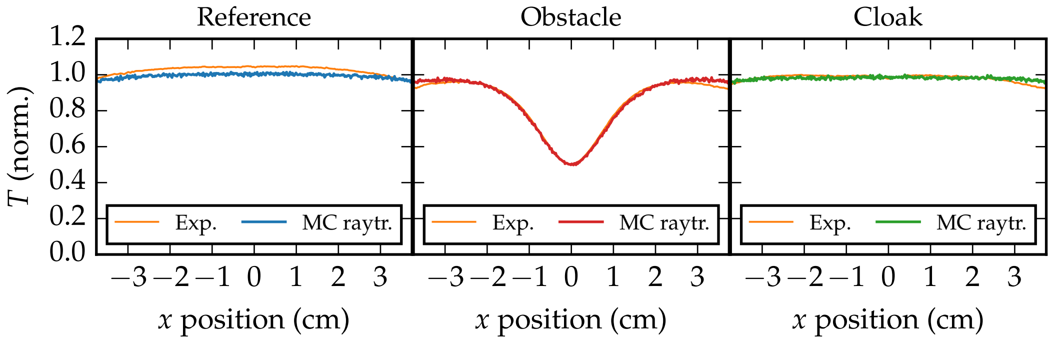

Figure 8.37: Normalized transmittance profiles of the images shown in Figure 8.36 (a)–(c), vertically averaged over the region marked in Fig. 8.36 (a). The thin orange curves are the experimental data shown in Figure 8.29 (a). Experiments and MC raytracing results are in excellent agreement.

perimental results from Figure 8.28 are shown in panels (d) to (f). Both sets of images are scaled to the maximum intensity of the reference image. Experimental and numerical results agree very well.

A more detailed comparison is shown in Figure 8.37, which displays intensity cuts of the MC results superimposed onto the experimental data in the same way as Figure 8.35 does for the numerical results obtained with diffusion theory. To obtain intensity profiles with an appreciable signal-to-noise ratio, the region marked by the dotted line in Figure 8.36 (a) was vertically averaged for reference, obstacle, and cloak. Care was taken to define this region well separated from the image borders, where edge effects might affect the result. Again, the experimental as well as the numerical data were normalized to the maximum of the cloak's intensity profile to lower the significance of the constant offset in the experimental reference curve caused by sample preparation imperfections (see subsection 8.4.3). Apart from slight deviations towards the sample edges where the experimental data show a more pronounced drop in intensity, the MC simulations reproduce the experimental results excellently.

ABSOLUTE CALCULATED TRANSMITTANCE VALUES In principle, the MC simulations should yield transmittance results that are also quantitatively right—given that all experimental conditions are translated properly to the simulation parameters and boundary conditions. The simulations presented in figures 8.36 and 8.37 yield a transmittance of $T \approx 9.5\,\%$ for the reference (evaluated by averaging over a 200 by 300 pixel big area in the center of

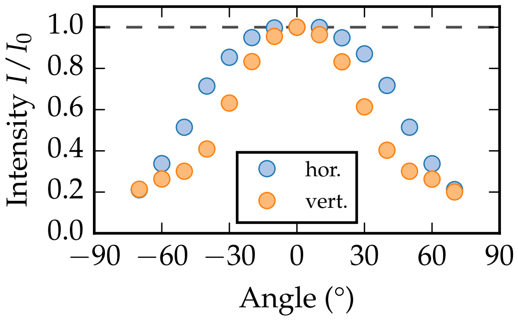

Figure 8.38: Measured horizontal and vertical angular emission pattern of the computer monitor we used for homogeneous illumination of our samples. The emission pattern is neither Lambertian (dashed line) nor purely directional, and is thus difficult to properly translate to the MC simulation conditions.

the calculated image), which differs significantly from the corresponding measured transmittance of about 7.5 %. Several aspects may lead to this difference, all of which are examples of the difficulty of translating an experiment accurately to simulation parameters.

First, our experiments resulted in a transmittance that is conceptually a bit unusual. Remember that to obtain the transmittance, we divided the brightness of light detected after propagation through a diffusive sample by the brightness of a transparent cuboid of undoped PDMS under identical illumination. However, the introduction of scattering particles not only changes the amount of light that exits the sample, but also significantly modifies the distribution of the light's exit angle. As the camera has an aperture smaller than the sample, this modification results in the detection of a different portion of the actually transmitted light. In our case, this portion *decreased* with the introduction of the diffusive sample since the computer monitor we used is biased towards a directional emission pattern (see Figure 8.38), while the emission pattern of a diffusive medium is very roughly Lambertian [85]. As we assumed a detector right behind the sample (and just as large as the sample surface), virtually all (that is, systematically more) light was detected in our MC simulations. Introducing a "real" camera with a finite aperture and distance from the sample geometry identical to the experiment could improve this aspect, albeit with the cost of losing all photons that do not hit the camera aperture. To obtain a similar signal-to-noise ratio as before, a much larger number of photons would then need to be traced, resulting in drastically increased computation times.

Second, the measured angular emission pattern of our light source (shown in Figure 8.38) is beyond what can currently be implemented in our ray-tracing software, which restricts planar sources to either a Lambertian or a purely directional emission pattern. Compared to Lambertian sources, directional sources lead to slightly higher overall transmittance values.

Third, the sandblasted aluminum molds used for the sample fabrication led to roughened rather than smooth outer sample surfaces. This likely changed the amount and quality of reflections that photons experienced when they hit a sample edge. This roughness cannot be accounted for in the MC simulations, which assume perfectly smooth outer sample boundaries that only lead to Fresnel-type reflections.

In conclusion, these differences between the experimental conditions and what can be modeled numerically make it not really meaningful to compare the MC results with the experiments in a quantitative manner.

TOWARDS GENUINELY DIFFUSIVE OR BALLISTIC LIGHT PROPAGATION We have seen that Monte-Carlo-based raytracing provides an excellent tool to bridge the gap between diffusive and ballistic light propagation which we have hit with the latest generation of all-solid-state cloaks for diffuse light. By further increasing or decreasing the scattering coefficients in both shell and surrounding, the MC results should eventually converge to a solution obtained from the diffusion equation or from ballistic optics, respectively.

To test these expected convergences, we performed MC simulations for an idealized model with a geometry as used before, but without any absorption (surrounding and shell absorption coefficient $\mu_a = 0$ and core reflectivity $R = 1$) and with perfectly reflecting lateral geometry boundaries, mimicking a structure that is infinitely extended in the illumination plane. We furthermore used a directional rather than Lambertian source. A detector virtually in contact with the sample would otherwise have resulted in a blurry image even without any scattering. For such a model, the reference transmittance is the same everywhere (that is, a straight line in the transmittance profiles). We kept the ratio of scattering coefficients $\mu_{s,2}/\mu_{s,0}$ equal to the ideal diffusivity ratio $D_2/D_0 = 2.6$, but multiplied both with different factors f to move between the ballistic and the diffusive regime. A factor $f = 1$ corresponds to a scattering coefficient of $\mu_{s,0} = 1.314\,\mathrm{mm}^{-1}$ for the surrounding identical to the one in the experiments and corresponding MC simulations.

Figure 8.39 shows calculated transmission images for different factors f together with horizontal transmittance profiles. The images (Figure 8.39 (a) to (e)) are individually normalized to keep all features visible, while the transmittance cuts (panels (f) to (j)) show how the amount of transmitted light decreases with increased scattering. Panels (c) and (h) of Figure 8.39 clearly show that for a surrounding scattering coefficient as we had used it in our latest experiments, a shell scattering coefficient according to theory

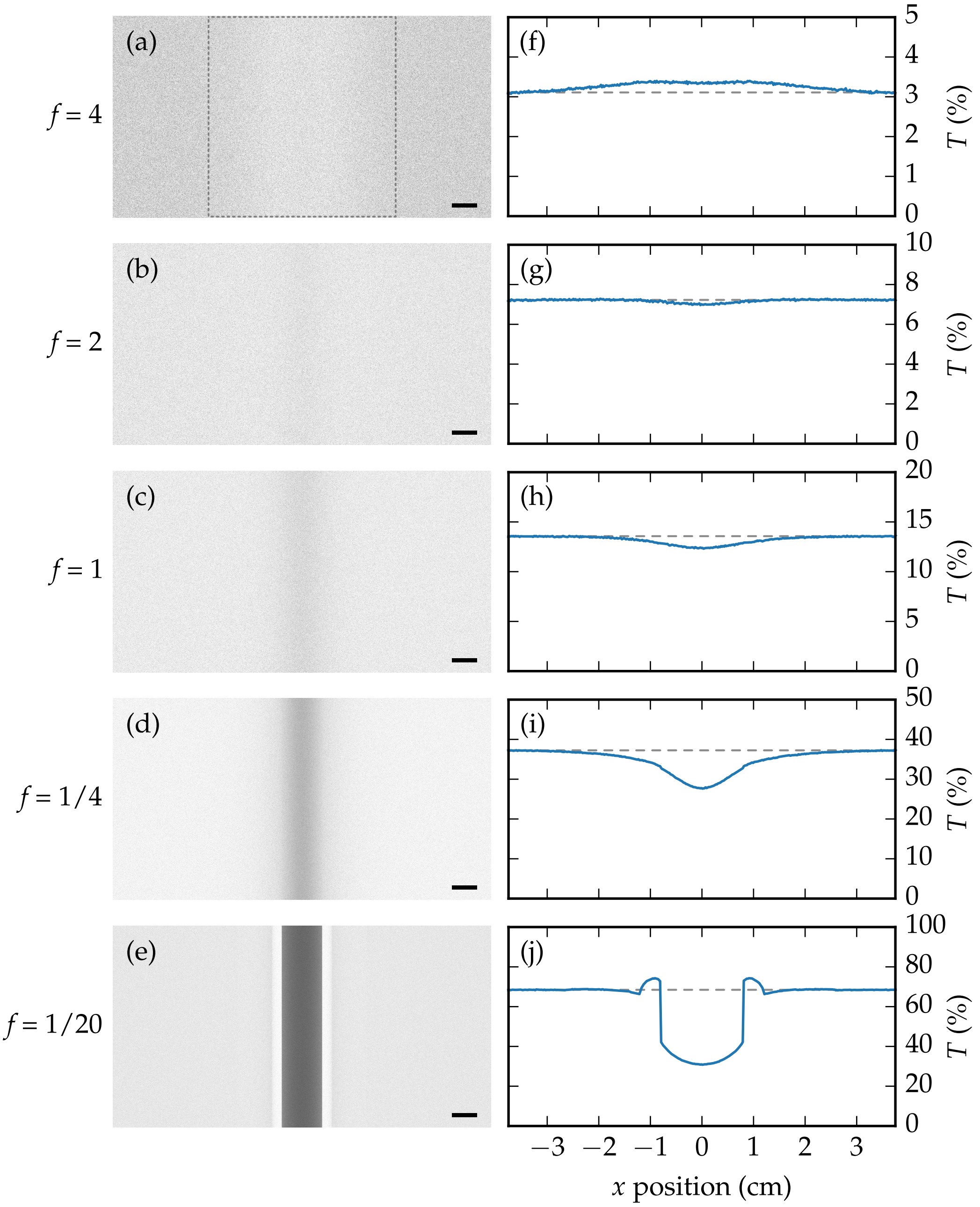

Figure 8.39: Transition between the diffusive and the ballistic regime. (a)–(e) Transmission images of a lossless core-shell cloak (geometrical parameters as before) obtained by MC raytracing of 1 billion photons. The scattering coefficients of surrounding and shell vary with the scaling factor f: $\mu_{s,0} = f \times 1.314\,\mathrm{mm}^{-1}$, $\mu_{s,2} = \mu_{s,0}/2.6$. Length of the black scale bar: 1 cm. (f)–(j) Transmittance profiles were obtained by averaging over the area marked by the dashed rectangle in (a). Dashed horizontal lines are guides to the eye.

does not lead to successful cloaking, even for lossless media under perfectly homogeneous illumination (that is, without any edge effects caused by the finiteness of the sample). Decreasing both scatterer concentrations by the same factor f worsens the deviations from the diffusion description, with the results for $f = 1/20$ already looking very close to ballistic light propagation. In this case, the shell is clearly visible as two bright stripes next to the core. On the other hand, increasing the scatterer concentration in both shell and surrounding at first brings the results closer to what diffusion theory predicts, albeit with the cost of a significantly decreased absolute transmittance (panels (b) and (g)). For yet stronger scattering, however, the cloak seems to overcompensate the shadow cast by the core (panels (a) and (f) for $f = 4$), contrary to our expectations. Further increasing the global factor f such that the transport mean free path satisfies the diffusion approximation in both surrounding and shell led to an even stronger overcompensation. Currently, we do not understand this behavior. To the best of our knowledge, errors in the raytracing implementation can be excluded, which leaves us with either a modeling mistake or a physical reason that leads to the observed overcompensation. It remains to be seen which is the case.

8.4.7 Discussion

At the end of section 8.3, I identified three major shortcomings of the otherwise impressive water-paint-based cloaks for diffuse light: low overall light transmission through the samples, uncomfortable handling of the inherently unstable liquid-based cloaks, and a core absorption that compromised the cloaking performance. With the all-solid-state samples and highly reflective ceramic cores presented in this section, all three shortcomings have been resolved. The new PDMS-based samples are compact, easy to handle and have an overall transmittance increased by more than one order of magnitude, allowing the assessment of the cloaking performance in daylight. The new core material allowed to reduce the necessary contrast in scatterer concentrations between shell and surrounding and further enhanced the cloaking performance to an almost perfect level. I'd like to point out that this makes the cloaks "classroom-ready", and at the time of writing, a new experiment on light diffusion and cloaking is being devised for the student labs at the physics faculty of the Karlsruhe Institute of Technology.

Furthermore, numerical calculations showed that to achieve this level of cloaking with large overall light transmission, one actually needs to push the design out of the purely diffusive regime and slightly towards ballistic light transport. Our self-written Monte-Carlo-based photon raytracer FRODO proved to be an excellent tool for investigations within this intermediate regime.

However, the fact that the latest cloaks operate at least partly in this intermediate regime between diffusive and ballistic light propagation also has consequences for the further improvement of those cloaks. Specifically, it means that the two-shell approach for optimized cloaking performance under inhomogeneous illumination presented in section 8.2 cannot simply be used as a design recipe for upcoming experiments: While in this design, the diffusivity of the second, outer shell is smaller than that of the surrounding and thus might be realizable, the first, inner shell requires a diffusivity yet much larger than that of the single shell used in our experiments so far. Since both shells would also be thinner, the diffusion equation will most certainly not be adequate for describing this shell, which compromises the entire two-shell design. One could of course increase the amount of scattering particles in all media equally and thus push also the shells back to diffusive light transport. However, this would come at the cost of a significantly reduced overall light transmission, re-introducing one of the shortcomings we have solved with the PDMS-based cloaks. Still, studying the two-shell design might not have entirely been in vain. It remains to be seen whether the introduction of two shells with scatterer concentrations that are only slightly different from the optimized one-shell concentration (and thus don't stress the diffusive model too much) would result in an improved performance under inhomogeneous excitation after all.

9 Chapter 9

TRANSIENT BEHAVIOR OF CLOAKS FOR DIFFUSE LIGHT

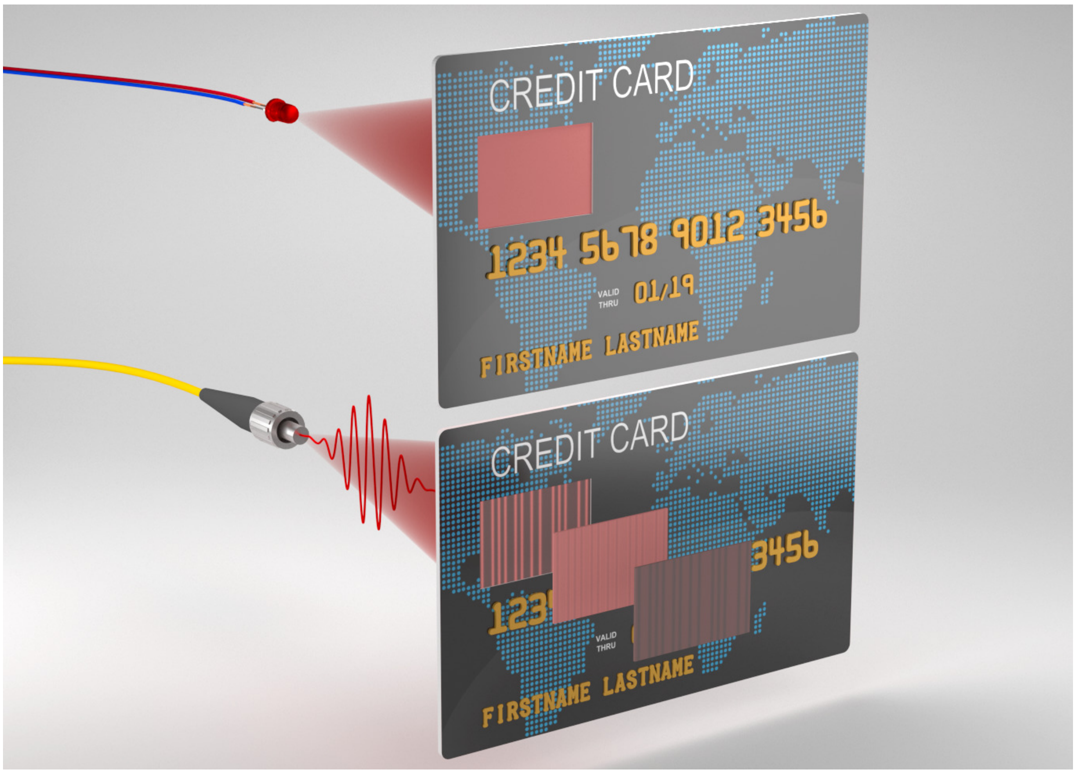

Artistic view of a high-end security device based on core-shell cloaks, visible only under pulsed illumination

Core-shell cloaks work amazingly well in the static case even for inhomogeneous illumination. But how do they behave once the illumination becomes dynamic? In this chapter, I will show that not only a core-shell cloak but cloaks for diffuse light in general fail under truly transient conditions. This chapter is based on the master's thesis of Andreas Niemeyer. Its main findings have been published in Ref. 117.

So far, all our experiments (with the exception of some characterization measurements) on core-shell cloaks for diffuse light have been performed in the quasi-static regime, that is, for illumination conditions that vary slowly with respect to the diffusive and absorptive time constants. In this chapter, I will investigate how such cloaks behave under truly transient conditions. This question is not only significant in terms of transformation physics and cloaking, but also for practical applications in time-resolved diffuse optical tomography where human tissue is illuminated with short optical pulses and the detected scattered light is used to reconstruct the tissue distribution [118, 119].

For the combinations of diffusivities D and medium lengths L used so far,

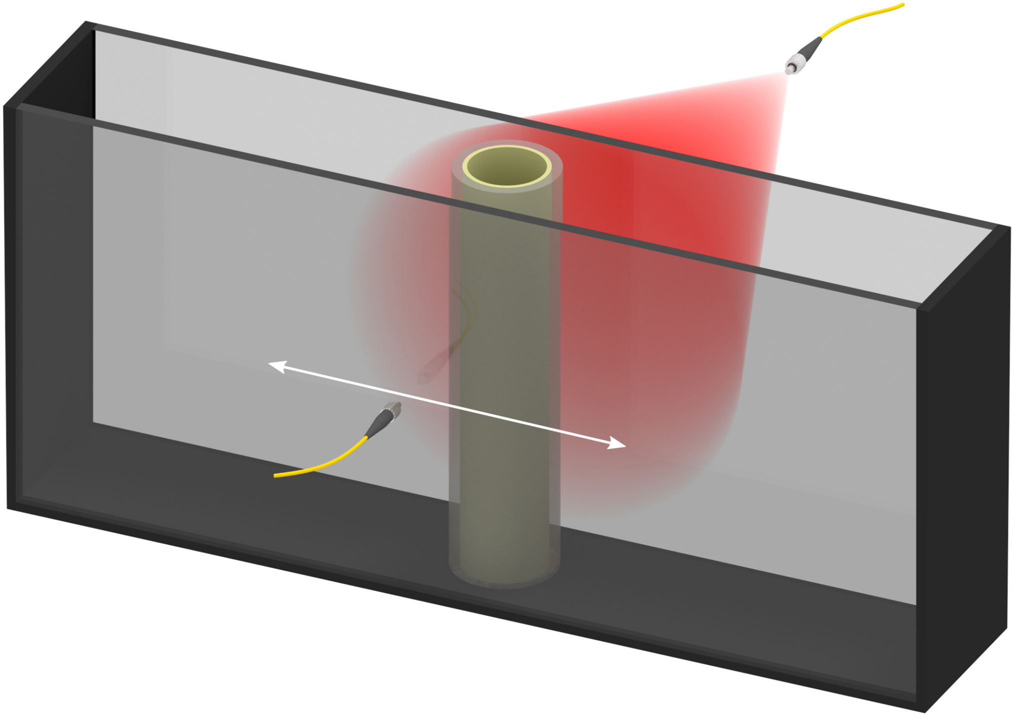

Figure 9.1: Setup for measuring the transient behavior of diffusive-light cloaks. The sample (here, the tank used for water-based experiments with the cloak structure inside) is illuminated with picosecond laser pulses emerging divergently from a fiber. The transmitted light is collected with a multimode fiber and fed into a time-correlated single-photon counting unit. Scanning the fiber horizontally yields spatial resolution.

both time constants mentioned above were on the order of 10^{-8} s. Thus, to resolve the temporal response of the samples, both excitation and detection needed to work on timescales significantly below 10^{-8} s, which is way out of range with conventional and also with most high-speed cameras. As for the dynamic characterization of diffusive media (see section 7.3), we thus again utilized a pulsed picosecond laser source and time-correlated single-photon counting detection.

9.1 Experimental setup

The experimental setup was very similar to the one we already used for the dynamic characterization of diffusive media and is illustrated for the example of water-based experiments in Figure 9.1. Instead of focusing the excitation laser spot onto the sample surface, we used the unmodified divergent beam emerging from the excitation fiber, leading to a spot size on the sample surface with a full width at half-maximum (FWHM) of about 3.2 cm. We used the same laser source as described before (pulses with 50–500 ps duration and a repetition rate of 10 MHz) and again scanned the detection fiber horizontally to obtain spatial resolution. See section 7.3 for further details on the measurement setup.

9.2 Results for water-based media

Figure 9.2 exhibits the measurement results for the water-paint-based cylindrical reference (a), obstacle (b), and cloak (c) sample (0.35 % paint concentration in the water) with parameters as described in section 8.3. We scanned the detection fiber in 1 mm steps from −70 mm to 70 mm (that is, over roughly half of the tank width) and integrated for 30 s at each detection position. On the right-hand side of Figure 9.2, we plot the spatially and temporally resolved photon count rate as a color-coded contour plot with $t = 0$ corresponding to the time when the laser pulse maximum reached the tank surface. We furthermore plot one vertical cut for a centered detection fiber (dashed line in the contour plots) together with the laser pulse for reference (black and gray data points on the left-hand side of each panel). As seen before in corresponding static experiments, the obstacle blocks most of the incoming light and is clearly distinguishable from the reference. However, also the cloak's results differ significantly from those of the reference. Specif-

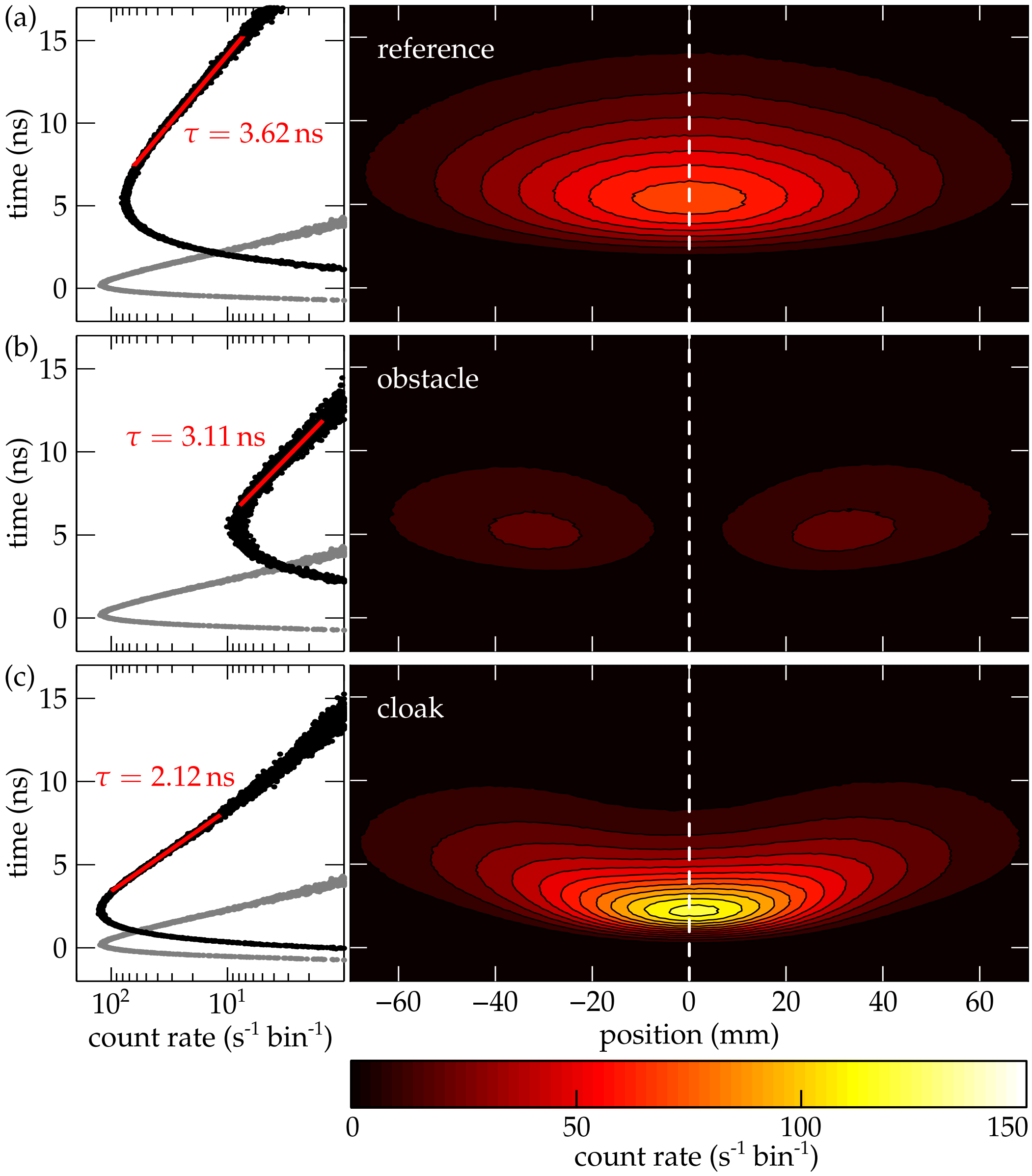

Figure 9.2: Measured spatially and temporally resolved diffusive transmission of light through the water-paint-based samples reference (a), obstacle (b), and cloak (c) as described in section 8.3. In each panel, we plot the spatially and temporally resolved photon count rate in a color-coded contour plot next to a vertical cut (black data points) for a centered detection position. The gray data points correspond to ballistic transmission through an empy tank. The contour plots reveal the failure of the cloak under transient conditions: It transmits light too quickly through the cloaking shell, leading to an overshooting of the light intensity for early times and a shadow for later times. Reproduced from Ref. 117, Fig. 2.

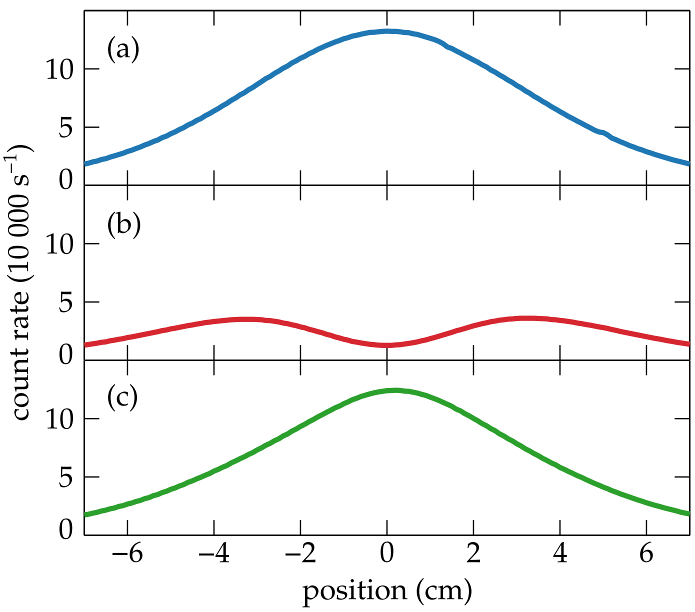

Figure 9.3: Measured photon count rate as shown in Figure 9.2, but integrated over time, corresponding to static illumination. For the reference (blue curve), a bell-shaped curve similar to the one for static, line-like illumination as shown in Figure 8.16 is obtained. The obstacle blocks most of the incidident light (red curve) while the cloak reasonably reproduces the transmission profile of the reference (green curve).

ically, the maximum photon count rate is higher for the cloak and occurs earlier in time, leading to a steeper rising edge of the count rate distribution. In contrast, the count rates for later times are significantly smaller than for the reference. In short, the cloak fails its purpose of appearing exactly identical to the homogeneous reference. Intuitively, the high-diffusivity shell transports light too quickly and thus leads to an overshooting of the transmitted intensity for early times. It is this light which then misses for later times, leading to a shadow with respect to the reference. This aspect is also illustrated by the decay time constant given in Figure 9.2 (c), which is much smaller for the cloak than for the reference. Integrating the results over all time steps corresponds to static illumination and leads to bell-shaped curves as depicted in Figure 9.3. These curves are very similar to those shown in Figure 8.16, with reasonable agreement between reference and cloak.

We performed similar experiments also on the PDMS-based samples with smaller overall dimensions and higher diffusivities with respect to the water-based cloaks. The results were qualitatively very similar to the ones just described and did not result in any new conclusions, which is why I will not dwell on them here.

Figure 9.4 depicts corresponding results obtained from calculations with COMSOL Multiphysics, using a numerical model as illustrated in Figure 8.18,

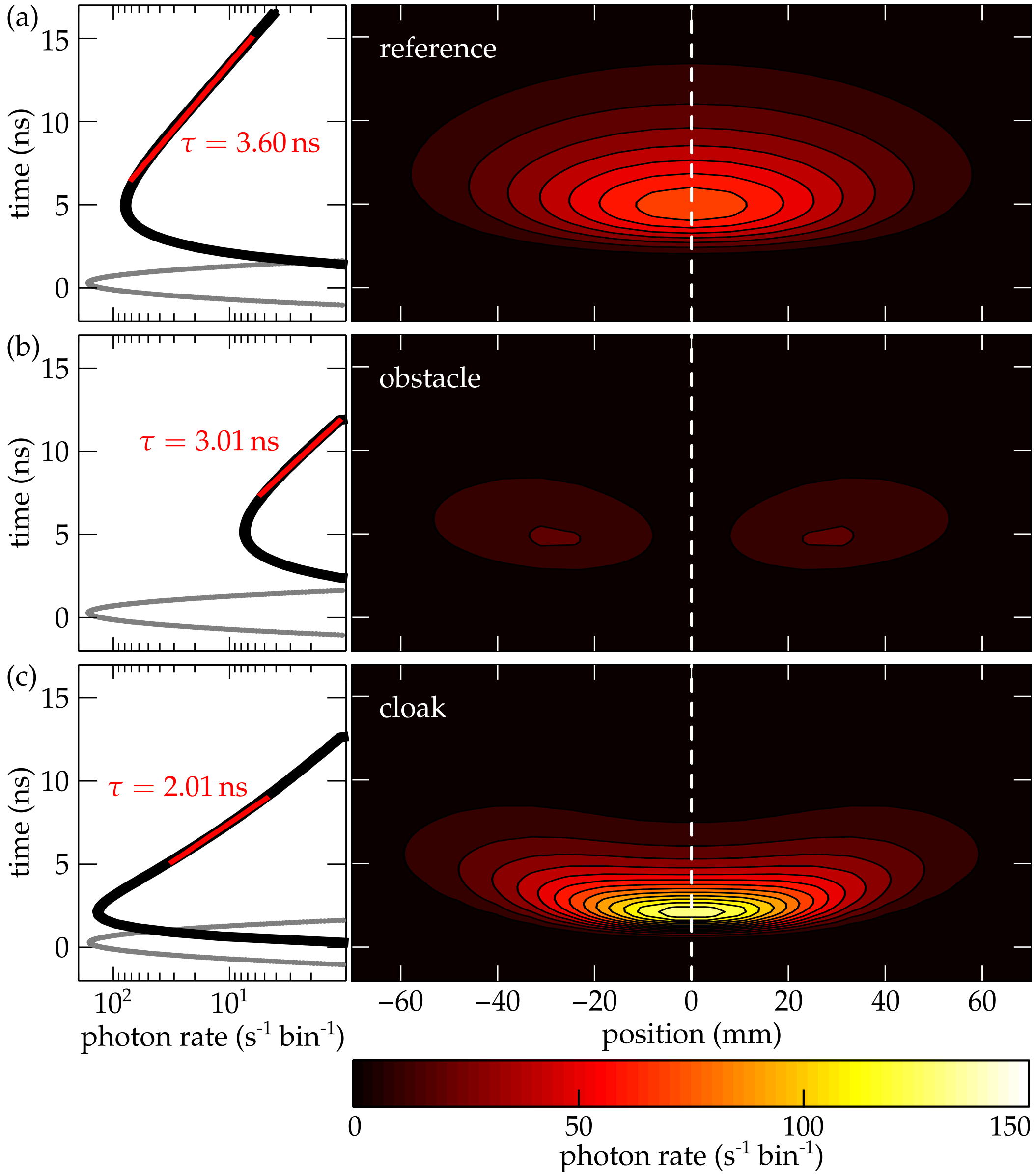

Figure 9.4: Numerically calculated diffusive transmission corresponding to Figure 9.2. Numerical model as in Figure 8.18, adapted for time-resolved calculations. Parameters are $L = 6\,\mathrm{cm}$, $2R_1 = 32.1\,\mathrm{mm}$, $2R_2 = 39.8\,\mathrm{mm}$, $D_0 = 5.27 \times 10^8\,\mathrm{cm}^2/\mathrm{s}$, $D_2 = 72.1 \times 10^8\,\mathrm{cm}^2/\mathrm{s}$, $\tau_0 = 10\,\mathrm{ns}$, $\tau_{12} = 0.245\,\mu\mathrm{s}$, and $K = 0.1\,c_0$.

adapted for time-resolved calculations and a Gaussian illumination pattern with a FWHM of 3.2 cm as in the experiments. As described already in section 8.3 in the context of static numerical calculations, of the necessary calculation parameters only the surrounding diffusivity $D_0 = 5.27 \times 10^8\,\mathrm{cm^2/s}$ could be determined experimentally (see Figure 7.5). Still, with both static and time-resolved experimental results to compare with, appropriate parameters for the numerical model (given in Figure 9.4) could be obtained in a straightforward way. The numerical results shown agree very well with the experiments.

9.3 Why all diffuse-light cloaks fail transiently

We just saw that the core-shell cloaks that work so well in the static regime fail under truly transient conditions. But do they fail merely because of inevitable imperfections such as absorption, inhomogeneous illumination or finite samples? Or do they fail because of a more fundamental reason?

Figure 9.5 shows calculated images of the light transmitted through a lossless core-shell cloak with a surrounding that is conceptually infinitely extended in the lateral direction (via isolated boundaries) and illuminated

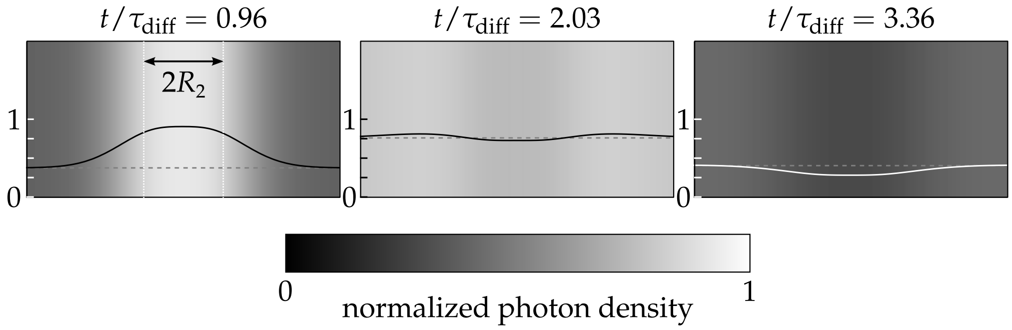

Figure 9.5: Calculated images of light transmitted through a lossless diffusive core-shell cloak with radii $R_2/R_1 = 1.25$, $L = 3R_2$, and $D_2/D_0 = 4.56$. The images are snapshots for different times after a spatially homogeneous illumination pulse at t_0. All times are normalized to the diffusive time constant $\tau_{\mathrm{diff}} = L^2/(6D_0)$. The solid curves are horizontal intensity cuts, while the horizontal dashed line depicts the transmitted intensity of a homogeneous sample for comparison. Similarly to the experiments shown in Figure 9.2, the cloak transmits too much light for early times (bright spot in the first image), the lack of which later leads to a distinct shadow. Adapted from Ref. 117, Fig. 4.

with a homogeneous short light pulse. It is thus an "ideal" core-shell cloak that cloaks perfectly for static illumination, leading to a completely homogeneous transmission distribution (not depicted here). For the transient case, however, also this ideal cloak fails and exhibits the same behavior we saw in our experiments: It transmits light through its shell too quickly, leading to an early overshooting of the transmitted intensity (first column in Figure 9.5), followed by a lack of photons and thus a visible shadow for later times (third column in Figure 9.5).

As it turns out, not only core-shell cloaks, but cloaks for diffuse light propagation in general inevitably fail under truly transient conditions. This is simply because the time-dependent—in contrast to the time-independent—light-diffusion equation is *not* form-invarient under spatial transformations. To clarify this point, I will compare light diffusion to heat conduction. In section 3.1, we have seen that the time-dependent heat-conduction equation

$$\vec{\nabla} \cdot \left(\kappa \vec{\nabla} T(\vec{r}, t) \right) - c\rho \frac{\partial T(\vec{r}, t)}{\partial t} = 0 \tag{9.1}$$

turns into the following equation upon a spatial transformation $\vec{r} \rightarrow \vec{r}\,'$ characterized by its Jacobian $J_{ij} = \partial r_i' / \partial r_j$:

$$\vec{\nabla}' \cdot \left(\kappa \overleftrightarrow{J}(\vec{r}) \overleftrightarrow{J}^{\mathrm{T}}(\vec{r}) \frac{1}{\det \overleftrightarrow{J}(\vec{r})} \vec{\nabla}' T(\vec{r}, t) \right) - \frac{c\rho}{\det \overleftrightarrow{J}(\vec{r})} \frac{\partial T(\vec{r}, t)}{\partial t} = 0 \, . \tag{9.2}$$

In this equation, all effects of the transformation (that is, all terms with $\overleftrightarrow{J}(\vec{r})$) can be absorbed into the material parameters, precisely into the heat conductivity κ and into the product of density and specific heat capacity $c\rho$. If we, however, transform the time-dependent light-diffusion equation (Equation 5.33) in the same way, we end up with the following equation:

$$\vec{\nabla}' \cdot \left(D \overleftrightarrow{J}(\vec{r}) \overleftrightarrow{J}^{\mathrm{T}}(\vec{r}) \frac{1}{\det \overleftrightarrow{J}(\vec{r})} \vec{\nabla}' n_{\mathrm{p}}(\vec{r}, t) \right) - \frac{1}{\det \overleftrightarrow{J}(\vec{r})} \frac{\partial n_{\mathrm{p}}(\vec{r}, t)}{\partial t} = 0 \, . \tag{9.3}$$

This equation is identical to Equation 9.2 (upon exchanging D and $n_{\mathrm{p}}(\vec{r}, t)$ by κ and $T(\vec{r}, t)$, respectively), with the crucial exception that now there is no material parameter in front of the time-derivative into which the term $1/\det \overleftrightarrow{J}(\vec{r})$ could be absorbed: there is no light-diffusive counterpart to $c\rho$ from heat conduction. Consequently, the equation above is generally

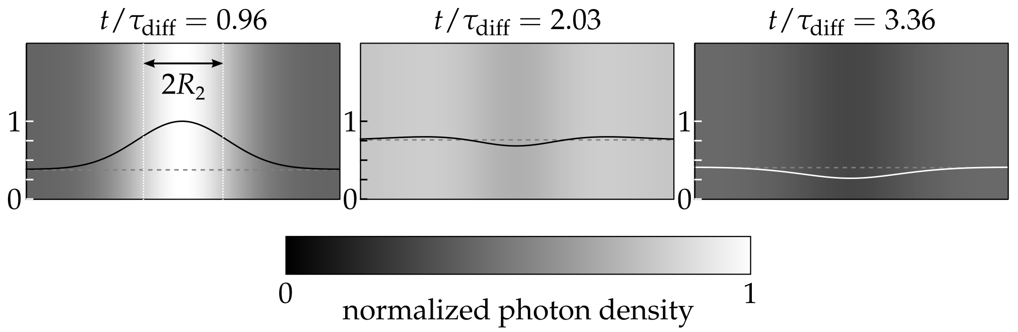

Figure 9.6: Numerical results as in Figure 9.5, but for a cloak designed via transformation physics according to Equation 9.3 (ignoring the term $1/\det(\overset{\leftrightarrow}{J}(\vec{r}))$ in front of the time-derivative). This more complex cloak fails as well in the transient case, exhibiting a similar behavior as the core-shell cloak shown in Figure 9.5. Adapted from Ref. 117, Fig. 4.

not form-invariant under arbitrary spatial transformations. Only for a transformation for which the Jacobian determinant is spatially constant, $\det \overset{\leftrightarrow}{J}(\vec{r})$ could be pulled into to the spatial derivate on the left-hand side of the equation and be absorbed in the diffusivity as well. This, however, is generally not the case, even though different types of transformations and their effects have already been investigated for acoustic cloaking [120, 121].

We tested what happens if one naively ignores the stray term $1/\det \overset{\leftrightarrow}{J}(\vec{r})$ in Figure 9.6 and implements just the spatial part of the transformation in COMSOL Multiphysics. As depicted in Figure 9.6, the resulting transmission images look very similar to those for the lossless core-shell cloak shown in Figure 9.5. This demonstrates that at least with the straightforward Pendry-type spatial transformation (Equation 2.1), transformation physics fails for transient diffusive-light cloaking.

9.4 EXPLOITING THE FAILURE FOR HIGH-END SECURITY ITEMS

The inherent failure of diffusive-light cloaks under transient illumination conditions is not necessarily bad news. It is of course bad news from the perspective of transformation physics and cloaking, but as I hinted at in the introduction of this chapter, some medical diagnostics methods [118, 119] rely on exactly this failure. If diffusive-light cloaks (and especially simple core-shell cloaks) worked as well under transient conditions, those diagnostics methods would not be unique and thus much less useful in practical applications.

We came up with another idea of how the transient failure of core-shell cloaks could be put to use to create high-end security devices. As illustrated artistically in Figure 9.7, one could create a pattern such as a barcode with miniaturized cylindrical core-shell cloaks that would be invisible under static, everyday illumination. Only with pulsed illumination and time-resolved detection, transmission contrast would increase and reveal the pattern and the information encoded in it.

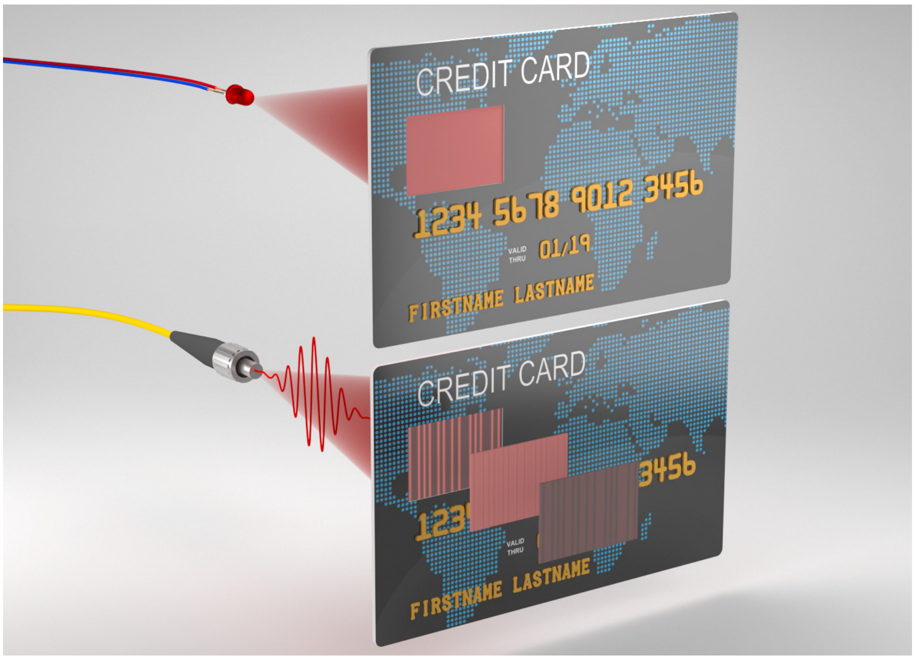

Figure 9.7: Artistic view of high-end security devices consisting of miniaturized cylindrical core-shell cloaks for diffuse light. Under normal, static illumination conditions, an observer would only see a diffusively transmitting area. Only with pulsed illumination and time-resolved detection (illustrated by the three stacked illuminated areas in the lower half of the image), the cloaks would fail and hidden features would become visible.

Chapter 10

10

INVERTED NEUTRAL INCLUSIONS FOR ENHANCED REFLECTION CONTRAST

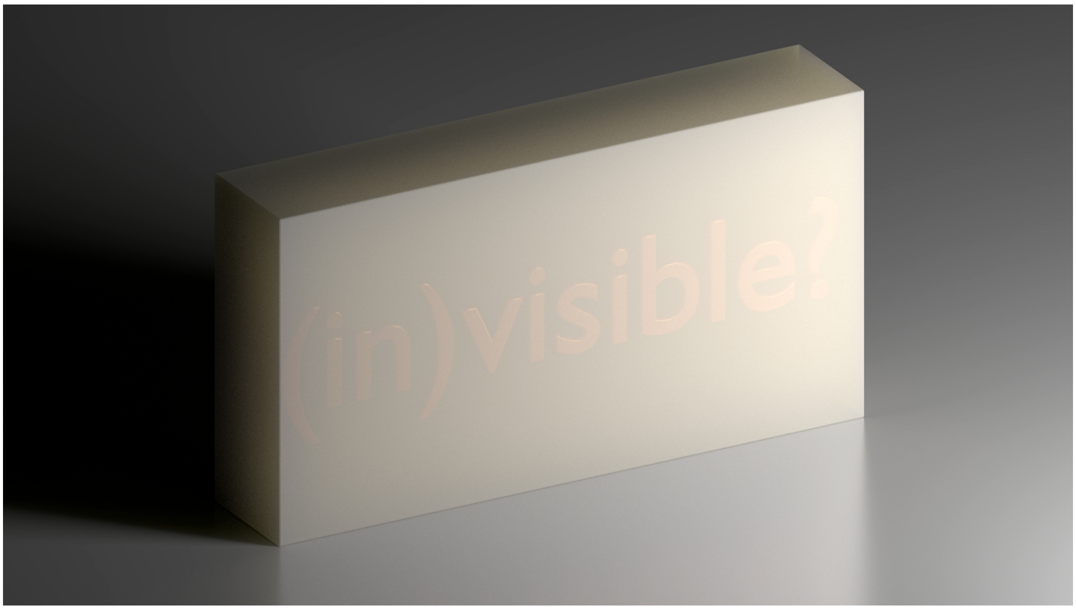

Illustration of an uncloaked structure inside a diffuse medium, which creates almost no contrast in reflection

So far, I have presented and assessed diffusive-light cloaks only with respect to the light they transmit. In this chapter, I will show that in reflection, there is not much to hide in the first place, because the large overall reflectance of diffusive media diminishes the relative contrast of the disturbance caused by the obstacle. I will then investigate whether inverting the core-shell cloak design to an approach with a high-diffusivity core and a low-diffusivity shell can help to overcome this contrast problem. This chapter is based on the bachelor's thesis of Carlos Jamarillo.

10.1 Reflectance of pdms-based core-shell cloaks

In principle, the core-shell cloaks presented so far should work in reflection just as well as in transmission. At least for the idealized case of absorption-free and laterally infinitely extended media, all light that is not transmitted should instead be reflected. Thus, all reflectance patterns should just be the inverse of the transmittance patterns we observed before. The obstacle should result in a highlight instead of a shadow, while reference and cloak should again be ideally indistinguishable.

The experimental setup for measuring the (static) reflectance pattern of our diffuse samples needed to be modified with respect to the one for transmission measurements and is shown in Figure 10.1. The sample was illuminated by a two-dimensional white-LED grid behind a Plexiglas diffusor, both aligned with respect to the sample center. The illumination area was significantly bigger than the sample cross section to create a diffuse rather than a directional illumination. The camera was inserted into holes in both the LED grid and the diffusor plate to allow for a normal viewing direction with respect to the sample surface. To get rid of remaining illumination inhomogeneities, we spray-painted an aluminum plate with lateral dimensions

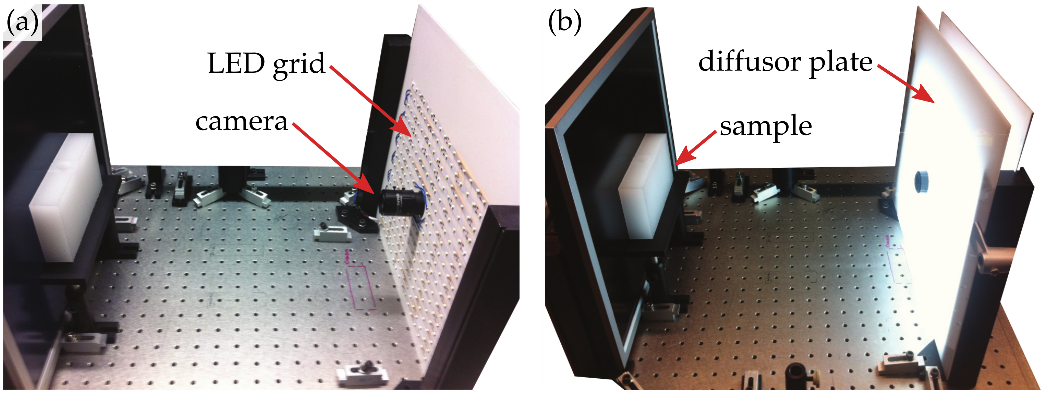

Figure 10.1: Experimental setup for measuring the reflectance of core-shell cloaks under homogeneous illumination. The sample is illuminated by a grid of white LEDs placed behind a Plexiglas diffusor plate. The reflected light is collected by the camera which is peeking through holes in the illumination plates. The photographs taken are then normalized to a reference photograph of an aluminum plate coated with white paint.

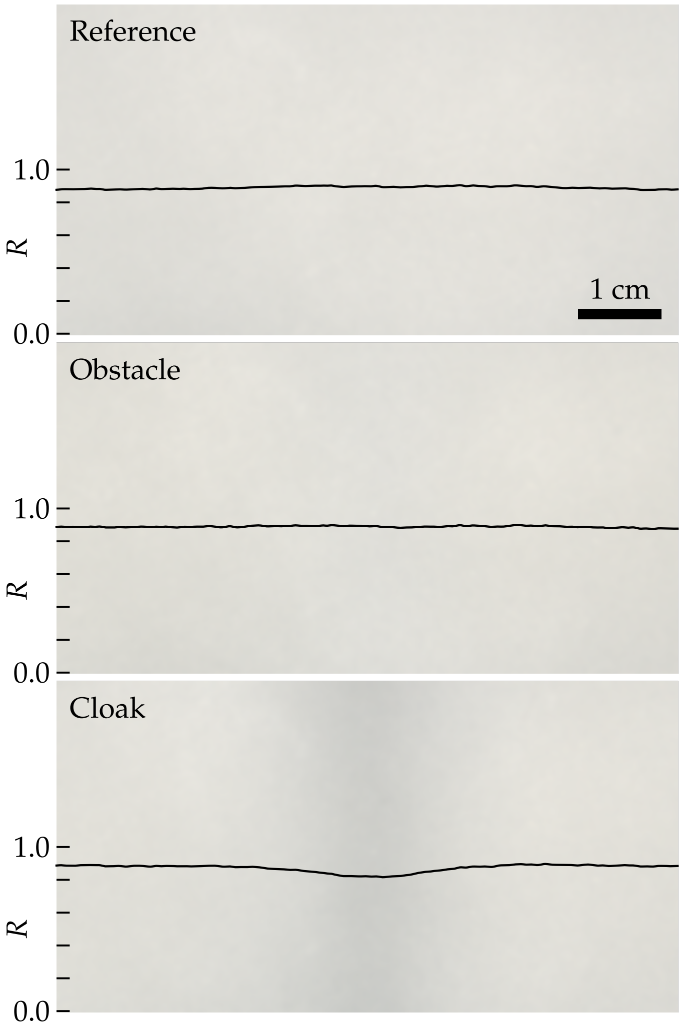

Figure 10.2: Photographs of the light reflected by PDMS-based samples with aluminum cores in obstacle and cloak under homogeneous illumination (corresponding transmission measurements are shown in Figure 8.24). The images are normalized to the reflectance of a painted aluminum plate and cropped by 25 % from all sides. The obstacle has no visible effect on the reflectance pattern. In contrast, the cloak does not succeed in reconstructing the reference pattern and shows a small but visible drop in its reflectance in the sample center. Most likely, the high ratio of scatterer concentrations in surrounding and shell needed for absorption compensation in transmission (see subsection 8.4.2) causes this failure in reflection.

identical to our samples with white paint and used it as a reference object. All photographs taken of the diffuse samples were divided by a photograph of this reference plate taken under identical illumination and then cropped by 25 % from all sides as previously. The computer monitor used as the light source in most of the previous (static) transmission measurements merely acted as a dark background.

Results for cloaks with aluminum core Figure 10.2 shows such normalized photographs of the first generation of PDMS-based samples, namely those with spray-painted aluminum cores inside of the obstacle and

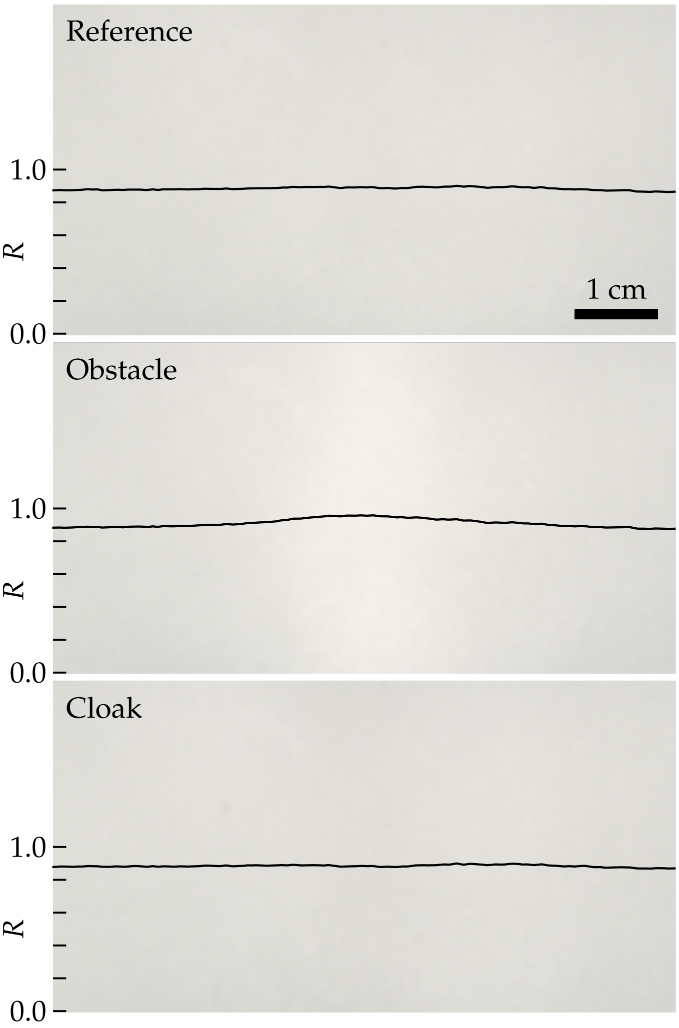

Figure 10.3: Photographs as in Figure 10.2, but for samples with Accuflect® B6 cores in obstacle and cloak (see figures 8.28 and 8.29 for corresponding transmission measurements). The obstacle results in an increase in reflectance, as expected from inverting the corresponding transmission pattern. The relative contrast, however, is much smaller in reflection than in transmission due to the high overall reflectance of diffusive media. In contrast to Figure 10.2, the cloak appears exactly as the reference. As there was not much to cloak in reflection in the first place, inverted core-shell inclusions were studied in an attempt to create a larger obstacle contrast.

the cloak structures. At first sight, all three images look pretty similar, with an average reflectance of 89 % for the reference (with respect to the painted aluminum plate). Specifically, the obstacle seems to have no effect on the reflectance pattern, which appears just like the one obtained for the reference. The cloak, however, fails in this configuration and shows a slight decrease in reflectance near the sample center. Most likely, compensating the core absorption for transmission cloaking performance by increasing the ratio of scatterer concentrations in surrounding and shell was detrimental to the cloaking performance in reflection.

Results for cloaks with Accuflect® B6 core Equivalent photographs for the latest versions of PDMS-based samples with Accuflect® B6 ceramic cores are shown in Figure 10.3. Here, results closer to the expectations raised in the beginning of this chapter were obtained. The obstacle indeed shows a slight reflectance peak in the center, while the cloak very well resembles the homogeneous reflectance pattern of the reference sample.

The reflectance contrast for the obstacle shown in Figure 10.3 is very small—so small actually, that one might question whether it is worth the effort to hide this contrast with a complex cloak structure. This problem of low reflection contrast stems from the generally very large absolute reflectance of diffusive media. As I pointed out in section 5.5, the theoretical minimum for the diffusive reflectance is 50 percent: In a diffusive medium, light loses any preferred propagation direction, such that for an infinite diffusivity or infinitesimally small medium thickness, exactly half of the light is transmitted and half is reflected. In practice, the diffusive reflectance is much higher. In section 8.4, we managed to push the diffusive transmittance of our samples to about 7 %, which still results in more than 90 % reflection (ignoring light that is escaping from the lateral sample boundaries). If for those samples the obstacle casts a shadow in transmission that is 50 % as bright as the homogeneous reference (and excluding any absorption), this *absolute* transmittance contrast of 3.5 % translates into a *relative* reflectance contrast of only $3.5/93 \approx 4\,\%$, a value smaller than the deviations our cloaks showed in transmission up to the latest, optimized generation.

In order to create an obstacle structure that was “cloakable” also in reflection, we came up with inverted versions of the core-shell cloaks used copiously in the last chapters.

10.2 DESIGN OF INVERTED NEUTRAL INCLUSIONS

The most straightforward way to generate a higher reflectance contrast for the obstacle would be to significantly increase the surrounding diffusivity D_0. Then, the overall reflectance would decrease, increasing the contrast a disturbance such as the zero-diffusivity core creates. However, this would also imply pushing the high-diffusivity shell (which already could not fully be described with diffusion theory anymore, see subsection 8.4.5) even further towards the ballistic regime of light propagation, which would in turn at one point harm the cloaking performance. So even though the surrounding's dimensions in principle allow for a much larger diffusivity

D_0, the shell's dimensions prevent us from utilizing it.

However, the design approach of a zero-diffusivity core and a high-diffusivity shell is not the only possible combination that yields a neutral inclusion according to the Hashin-Shtrikman formula. A high-diffusivity core combined with a low-diffusivity shell is valid just as well and indeed fits better to the restrictions the dimensions of the design impose on the different diffusivities. In the limit of a very large core diffusivity D_1 (as opposed to $D_1 = 0$), the right-hand side of Equation 8.1 becomes

$$\lim_{D_1 \to \infty} \sqrt{\frac{(D_2 + D_0)(D_2 - D_1)}{(D_2 - D_0)(D_2 + D_1)}} \approx \sqrt{\frac{D_0 + D_2}{D_0 - D_2}} = \frac{R_2}{R_1} \, . \tag{10.1}$$

Solving for D_2/D_0 results in

$$\frac{D_2}{D_0} = \frac{R_2^2 - R_1^2}{R_2^2 + R_1^2} < 0 \, , \tag{10.2}$$

which is exactly the inverse of the corresponding Equation 8.3 for a zero-diffusivity core. For the usual values of $R_1 = 0.8\,\mathrm{cm}$ and $R_2 = 1.2\,\mathrm{cm}$, a diffusivity contrast of $D_2/D_0 = 0.38$ is obtained (compared to $D_2/D_0 = 2.6$ for a zero-diffusivity core). This inversion indeed allows for a higher absolute surrounding diffusivity and will thus hopefully lead to an increased obstacle contrast in reflectance.

Two important constrictions of the above approach should be noted. First, since the core diffusivity is non-zero, the option of carving out a hiding place inside of it ceases to exist. Consequently, such an "inverted" core-shell structure is not a cloak but merely an invisible object.

Second, the limit of $D_1 \to \infty$ is obviously not realizable, since also the high-diffusivity core has to adhere to the limits of light-diffusion theory as described in chapter 5. Should the core violate these limits, the core-shell structure will most likely be revealed both in transmission and in reflection. For smaller diffusivities D_1, though, the contrast between D_2 and D_0 decreases, leading to a less favorable configuration in the context of enhancing the reflectance contrast of the uncloaked core.

In order to maximize the amount of light transported through the core, we decided not to include any scattering particles at all in this region. Out of practical reasons, we furthermore decided to leave away the PDMS host medium altogether, resulting in a hollow core or *void*. Without any scatterers, such a void transmits light entirely ballistically and thus of course heavily violates the assumption of diffusive media. However, we expected to be able to compensate for this violation by adjusting the ratio of diffusivities of shell and surrounding, just as we had been able to compensate for the significant core absorption in our early experiments on core-shell cloaking for diffuse light.

10.3 Sample fabrication

Two types of samples were produced for investigating inverted neutral inclusions:

- A *void* sample, comprising the homogeneous surrounding with the same dimensions as before ($15 \times 8 \times 3\,\mathrm{cm}^3$) and a cylindrical hole instead of the solid core with radius $R_1 = 0.8\,\mathrm{cm}$.
- A *void-shell* sample, where a shell identical to the cloaking shell used before (radius $R_2 = 1.2\,\mathrm{cm}$) surrounds the cylindrical void.

The fabrication procedure for the structures was essentially identical to that of the all-solid-state core-shell cloaks described in section 8.4, using the same materials and molds. As scatterers, we used slightly different TiO_2 nanoparticles,[1] albeit with scattering properties virtually identical to those of the particles used before (compare figures A.7 and A.8).

After polymerization of both shell and surrounding, the Teflon-coated aluminum core was removed to leave a ballistically transmitting void. For the outer surfaces of the surrounding medium, the sandblasted walls of the aluminum molds helped to reduce unwanted specular reflections when inspecting the reflectance pattern of the samples.

10.4 Experimental results

Despite expecting significant deviations from the predictions of diffusion theory due to sacrificing diffusive transport in the core in favor of maximum photon transport, we first fabricated a sample with the theoretically calculated diffusivity ratio of $D_2/D_0 = 0.38$ between surrounding and shell. We chose a TiO_2 nanoparticle concentration of $C_0 = 0.1\,\mathrm{mg/ml}$ for the surrounding, corresponding to a transport mean free path of $l_{t,0} \approx 6\,\mathrm{mm} = L_z/5$. A

---

[1] R706 from DuPont, USA

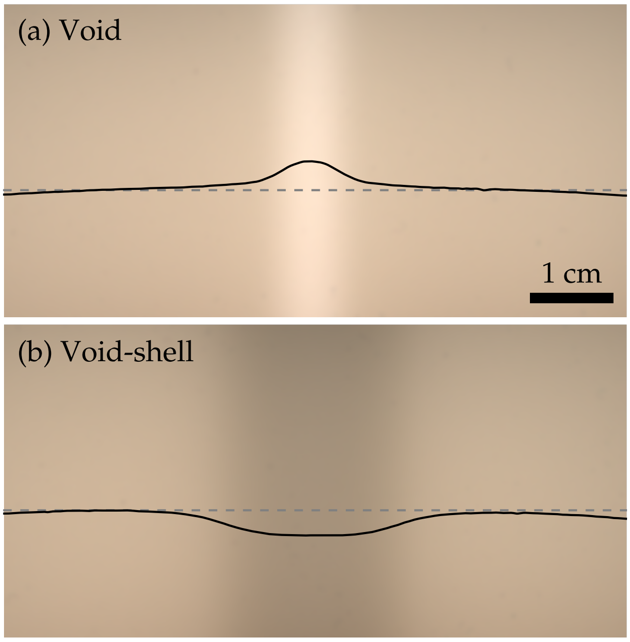

Figure 10.4: Photographs of the light transmitted through TiO_2-doped PDMS samples with a scatterer-free void under homogeneous illumination. The solid black lines are horizontal intensity cuts. (a) The void sample with a surrounding particle concentration of $C_0 = 0.1\,\mathrm{mg/ml}$ features a distinct intensity peak due to higher light transmission through its center. (b) A void-shell structure with $C_2 = 2.6\,C_0$ of surrounding and shell corresponding to diffusion theory does not result in an invisible neutral inclusion since the particle-free void cannot be described by diffusion.

yet lower particle concentration would have brought light propagation in the surrounding too close to ballistic transport. Following Equation 10.2, we obtained $C_2 = 0.26\,\mathrm{mg/ml}$ for the shell.

Figure 10.4 shows transmission measurements for a corresponding void as well as for a void-shell sample. As expected, the ballistically transmitting void leads to an increase in the transmitted light intensity, visible as a bright vertical stripe in the sample's transmission pattern (Figure 10.4 (a)). With a relative increase of about 20 %, this effect is significant but less pronounced than the shadow we observed previously for core-shell cloaking. The void-shell sample shown in Figure 10.4 (b) should ideally exhibit a perfectly homogeneous transmittance pattern. Instead, it shows a broad dark stripe in the center, indicating (as expected) that the non-diffusive void makes alterations to the diffusivity contrast between shell and surrounding necessary.

We thus experimentally optimized the shell's concentration C_2 of scattering particles with respect to the deviations from a homogeneous transmittance pattern, while fixing the surrounding particle concentration C_0. We obtained the best results for $C_2 = 1.5\,C_0$, corresponding to a diffusivity contrast of $D_2/D_0 = 0.67$ (as opposed to the theoretical value for perfectly diffusive

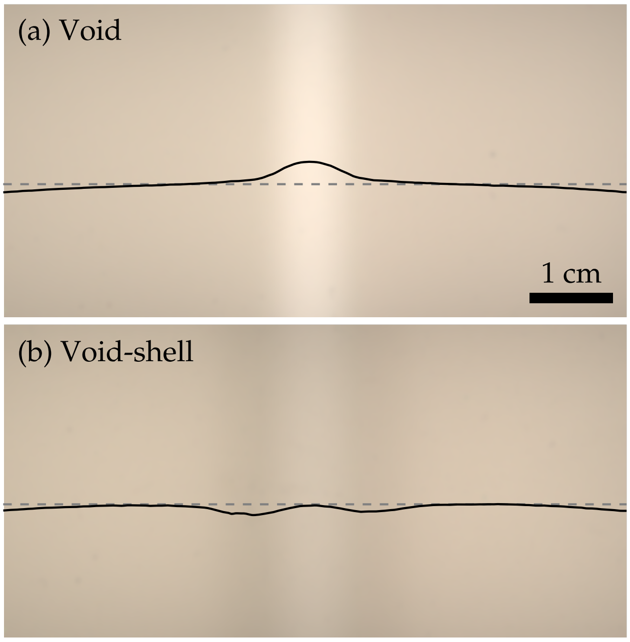

Figure 10.5: Photographs as in Figure 10.4, but for an optimized particle concentration ratio of $C_2/C_0 = 1.5$. In contrast to the void alone (panel (a)), the optimized void-shell structure (panel (b)) features a reasonably homogeneous transmittance pattern with remaining intensity variations of about 5 %. Compared to the excellent results for similar core-shell cloaks (section 8.4), these variations indicate that the scatterer-free void violates diffusion theory in a way that cannot be completely compensated for by adjusting the shell diffusivity.

media of $D_2/D_0 = 0.38$).

Figure 10.5 shows the transmittance pattern of the optimized void-shell sample, again in comparison with a void-only sample. Due to the decreased concentration of scattering particles in the shell, the combination of void and shell comes reasonably close to imitating a homogeneous sample, with remaining variations in the transmitted intensity of about 5 %. The results are, however, not nearly as convincing as the latest results of core-shell cloaking as shown in section 8.4. This indicates that stripping the core of all scattering particles is a more severe violation of the diffusive description of core-shell-based neutral inclusions than pushing a high-diffusivity shell slightly towards the ballistic regime of light propagation.

Reflectance measurements With the ratio of scattering particle concentrations C_2/C_0 optimized for invisibility in transmission, we also measured the samples' behavior in reflection, analogously to the measurements described in section 10.1. The resulting reflectance patterns are shown in Figure 10.6. The void-shell sample appears reasonably homogeneous and doesn't show any traces of either the void's or the shell's influence on the photon flux inside the sample (Figure 10.6 (b)). Unfortunately, the dip in the

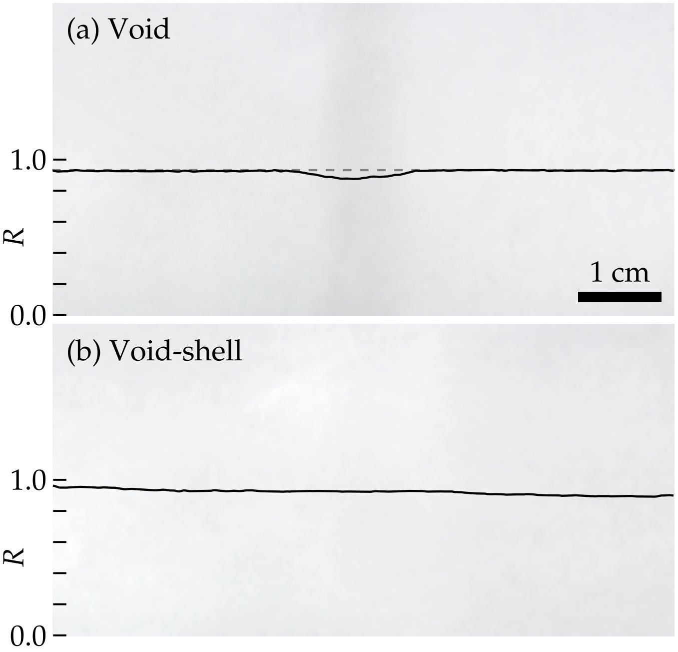

Figure 10.6: Photographs of the light reflected by the samples investigated in Figure 10.5. (See Figure 10.2 for measurement details.) Despite a maximized surrounding diffusivity, the reflectance contrast created by the void (panel (a)) is negligible. This contrast is concealed well by the optimized void-shell structure exhibiting a nearly perfectly homogeneous reflectance pattern (panel (b)), but its magnitude makes it questionable whether this concealment is necessary altogether.

light intensity reflected by the void sample shown in Figure 10.6 (a) is no more pronounced than the slight intensity peak observed in Figure 10.3 for an "obstacle" sample. The relative drop in intensity is roughly 4 %, which yet again raises the question whether it is meaningful to try to hide such a small effect in the first place.

10.5 Maximum transmission and reflection contrast for high- and low-diffusivity cores

Why was the reflectance decrease caused by the scatterer-free void so minute even for a maximized surrounding diffusivity? And what could be the means to further optimize this decrease? To answer these questions, we have numerically calculated the transmittance and reflectance contrast of both a zero-diffusivity core ($D_1 = 0$) and a high-diffusivity core ($D_1 \to \infty$) embedded in a homogeneous surrounding with diffusivity D_0. We used an idealized model (corresponding to the obstacle case illustrated in Figure 8.2) without any absorption, isolating lateral boundaries, and dimensions as in the experiments. For different values of the surrounding diffusivity D_0, we obtained both the reflectance and the transmittance curves and calculated the

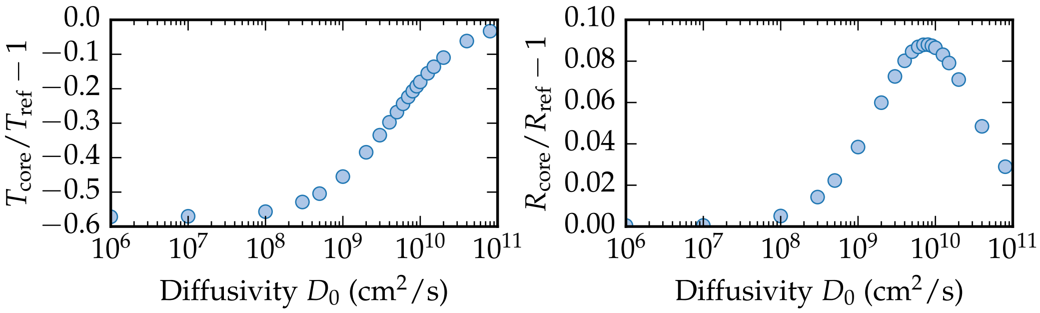

Figure 10.7: Calculated relative transmittance and reflectance contrasts for a core with diffusivity $D_1 = 0$, embedded in a homogeneous surrounding with diffusivity D_0. (Numerical model as described in Figure 8.2.) Unlike the transmittance contrast, the reflectance contrast is limited to a maximum of roughly 9 % even for assumed arbitrarily large diffusivities that violate diffusion theory.

maximal relative deviation $T_{\mathrm{core}}/T_{\mathrm{ref}} - 1$ in transmission (or $R_{\mathrm{core}}/R_{\mathrm{ref}} - 1$ in reflection) of the dip or peak caused by the core with respect to the corresponding curve of a homogeneous reference.

Figure 10.7 depicts the resulting transmittance and reflectance contrasts for a core with diffusivity $D_1 = 0$ and a surrounding diffusivity ranging from $D_0 = 10^6\,\mathrm{cm}^2/\mathrm{s}$ to $D_0 = 10^{11}\,\mathrm{cm}^2/\mathrm{s}$. It has to be noted though that assumed diffusivities $D_0 > 20 \times 10^8\,\mathrm{cm}^2/\mathrm{s}$ start to violate the diffusion approximation for the chosen sample thickness of $L_z = 3\,\mathrm{cm}$ and the results for such diffusivities need to be taken with a grain of salt. Nevertheless, the data clearly show that the contrast in reflectance never surpasses a value of about 9 % even for unrealistic surrounding diffusivities, while the reflectance contrast ranges between −60 % and zero.

A very similar result is obtained for a core with a very large assumed diffusivity of $D_1 = 10^5 \times D_0$. As noted earlier in this chapter, the notion of a core diffusivity approaching infinity is not compatible with diffusion theory, and neither is the above assumption for most values of D_0. The corresponding transmittance and reflectance contrasts depicted in Figure 10.8 thus have to be seen as hypothetical rather than realistic. They do, however, provide an upper boundary for the values attainable with more realistic choices of the diffusivities. Just as for a zero-diffusivity core, the reflectance contrast reaches a maximum (absolute) value of about 9 %, while the transmittance

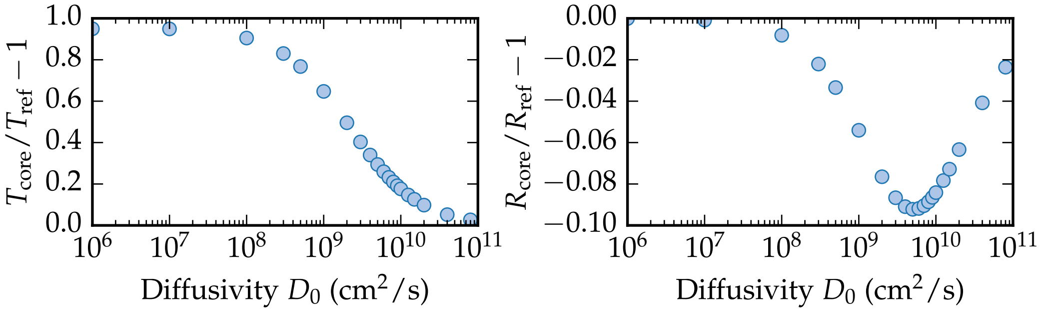

Figure 10.8: Calculated transmittance and reflectance contrasts as in Figure 10.7, but for a high-diffusivity core with $D_1 = 10^5 \times D_0$. Also in this configuration, the reflectance contrast stays below 10 % while the transmittance contrast does not display such a limitation.

contrast takes on the full range of values between 0 and 100 % for the given surrounding diffusivities.

In summary, investigating inverted neutral inclusions for diffuse light seems to have been of no great avail. The goal of increasing the reflectance contrast of a core-only sample to a “cloakable” level could not be reached, with no significant improvement with respect to the obstacle sample fabricated in terms of core-shell cloaking. Furthermore, the core diffusivities necessary for appreciable contrasts are so high that a proper diffusive realization seems out of reach. This limitation was visible especially in transmission, where the performance of the core-shell cloaks with a zero-diffusivity core could not be reproduced with a clearly non-diffusive, scatterer-free void used as the core. It finally turned out that even for the hypothetical option of arbitrarily large diffusivities, the contrast in reflectance would always fall short of that in transmittance by a big margin.

Chapter 11

11 CONCLUSIONS AND OUTLOOK

In this thesis, I presented experiments as well as analytical and numerical calculations on cloaking in heat conduction and light diffusion. Here, I will briefly summarize the main results of this work and re-iterate its most relevant arguments. In doing so, I shall also try to take a look beyond what has been done and discuss future prospects, challenges, and possible applications.

PART I OF THIS WORK DEALT WITH the experimental extension of the concepts of transformation physics to the realm of transient heat conduction. Using the notion of cars driving on a regular grid of streets inside a city as a metaphor for an arbitrary physical energy flux, I explained the fundamentals of transformation physics in chapter 2: A (purely virtual) deformation of space with a mathematical (coordinate) transformation leads to a (again virtual) specific desired behavior of an energy flux such as invisibility cloaking or field concentration. Transformation physics teaches us how to map the effects of such a virtual transformation onto a real-world material distribution.

Based on theoretical work on the form-invariance of the heat-conduction equation, I then presented the design, fabrication, and characterization of an "invisibility" cloak for transient heat flux (chapter 3). By drilling holes into a thin copper plate and filling them with the transparent silicone polydimethylsiloxane (PDMS), the heat conductivity of the plate was made inhomogeneous and anisotropic in such a way that incident heat was smoothly guided around an isolated ring in the plate's center. Viewed with an infrared heat camera, the plate's transient temperature distribution appeared exactly as that of a homogeneous plate. A numerical study of the relevant time scales showed how demanding it is to generate truly transient heat flux over the rather large dimensions of the samples, and indeed, only the beginning phase of our experiments qualified as actually transient.

Practical real-world applications of transformation thermodynamics are yet to be conceived of. Applications in heat management such as protection of integrated circuits on computer chips have been proposed in the literature. However, the specific feature of a thermal cloak as opposed to a mere thermal isolation—namely not disturbing the downstream heat flux behind the cloaked object—seems to be less important to this end than the isolation itself (which did not improve for the cloak structure). This is especially significant as any sharp features and steep gradients in a temperature distribution are "smeared out" over time due to the diffusive nature of heat conduction. Nevertheless, thermal cloaking and transformation thermodynamics developed into a currently very active field in the scientific churning, with new publications appearing on a more or less monthly basis.

PART II OF THIS WORK JUMPED BACK to the historical and scientific corner stone of transformation physics and cloaking: optical invisibility. I began with an explanation of the so-called relativity problem in chapter 4: As light inevitably takes a detour in space around the hidden region inside an invisibility cloak, it must travel there with a higher velocity in order to make up for the detour and emerge behind the cloak as if nothing was there. In vacuum or air, these velocities would exceed the vacuum speed of light. While such superluminal speeds are fine for very narrow wavelength ranges, relativity strictly forbids broadband, dispersion-free optical cloaking where the transport of energy would become superluminal. I furthermore argued how the effective speed of optical energy transport is tremendously decreased in media where multiple scattering dominates light propagation, causing every photon to propagate on zig-zag-like random paths. This slowness is controlled by the concentration of scattering centers in such diffusive media and opens up a window for ideal invisibility cloaking, rendering the relativity problem irrelevant.

In chapter 5, I presented a theoretical description of turbid media where light is assumed to interact with matter solely by scattering and absorption. Starting from four simple optical properties—namely the absorption coefficient, the scattering coefficient, the average scattering asymmetry, and the refractive index—I showed under which conditions light transport in such media can be described by a diffusion equation for light, completely equivalent to electrons diffusing in a metal or solid particles in a liquid. These conditions mainly require scattering that is dominant over absorption and sufficiently large media such that initial photon directions can be randomized. In chapter 6, I briefly introduced two numerical methods for the description of such diffusive light transport. The finite-element method implemented in COMSOL Multiphysics directly solves the diffusion equation while Monte-Carlo-based raytracing of individual photons provides a more microscopic approach that also covers the intermediate regime between diffusive and ballistic transport. In the context of this thesis, a fast and flexible Monte-Carlo raytracer for diffusive optics was implemented. As a last prelude to diffusive-light cloaking itself, chapter 7 dealt with the fabrication and characterization of diffusive media, introducing liquid- as well as solid-based media with different kinds of scatterings particles. A toolbox of static as well as dynamic techniques was presented which allow for the complete characterization of turbid media via the four optical properties named above.

In chapter 8, I first introduced the concept core-shell cloaks for static light diffusion, which—consisting of only two homogeneous isotropic domains—provide a huge simplification over the inhomogeneous and anisotropic structures based on transformation physics. I furthermore extended the concept of core-shell cloaking to a two-layer approach for optimized performance under inhomogeneous illumination. The latter violates the prerequisite for the derivation of the core-shell design and thus inevitably leads to deviations from good cloaking. Numerical optimization showed, however, that by dividing the shell into just two shells with independent diffusivities, these deviations can almost completely be eliminated. In practice, however, it remains to be seen whether the large necessary contrast in diffusivities together with the small shell thicknesses will prevent an experimental realization. I then proceeded to describe the successful realization of single-shell cloaks, first with a diffusive surrounding based on a mixture of water and white wall paint, followed by all-solid-state versions consisting of titania-nanoparticle-doped PDMS. By virtue of reduced absorption of the hollow, diffusively reflecting core, the latest version of the PDMS-based structures featured close to perfect cloaking performance and a high overall transmittance such that cloaking could be inspected in daylight conditions instead of only in a dark optical lab. Since the experimental results for these structures could not be confirmed with finite-element calculations solving the diffusion equation, we suspected that the high-diffusivity shell could not be described solely by diffusion anymore but was featuring a mixture of diffusive and ballistic light transport due to its low concentration of scattering particles. Corresponding simulations with our Monte-Carlo photon raytracer excellently confirmed this assumption.

In chapter 9, I proceeded to investigate the behavior of our cloaks under transient instead of static conditions. Therefore, the samples were illuminated with picosecond laser pulses and the transmitted light was temporally resolved via a single-photon counting unit. Surprisingly, the cloaks do not work at all under truly transient conditions. The high-diffusivity shell transports light too quickly and leads to an early overshooting of the transmitted intensity, which in turn results in a lack of photons for later times. As it turned out, this failure is not caused by fabricational imperfections or finite absorption and is not even limited to core-shell cloaks. Since the dynamic light-diffusion equation is not form-invariant under spatial transformations, it is rather an inherent limitation for any diffusive-light cloak. Only for the unlikely but not yet deeply investigated case of a transformation that leads to a spatially constant Jacobian determinant, dynamic diffusive-light cloaking would become possible. In any way, the cloaking failure is good news for biomedical diagnostics relying on the uniqueness of time-of-flight measurements of photons diffusively transmitted through biological tissues. Furthermore, structures that are visible only under pulsed illumination and time-resolved detection might find application in high-end security devices.

I finally presented the investigation of inverted core-shell structures for enhancing back-reflection contrast in chapter 10. While diffusive-light cloaking should work in reflection just as well as in transmission, the reflectance contrast of the to-be-cloaked disturbance caused by the zero-diffusivity core is so small that it evokes doubts whether a cloak has any meaning in the first place. By inverting the core-shell cloak to an invisible structure with a high-diffusivity core and a low-diffusivity shell, we hoped to be able to access a greater surrounding diffusivity, resulting in a lower absolute reflectance and thus in higher relative reflectance contrasts. Corresponding samples were fabricated where the core was implemented as a scatterer-less void to allow for maximal light throughput and thus a maximal disturbance of the light flow. Unfortunately, we could not achieve reflectance contrasts larger than the one already observed for the latest version of PDMS-based samples with a zero-diffusivity core. Numerical calculations even suggest that the reflectance contrast is inherently much smaller than the transmittance contrast. Furthermore, invisibility in transmission suffered considerably from the complete lack of scattering particles in the void, which pushed the core all the way to ballistic instead of diffusive transport.

One could wonder whether cloaking in diffuse light is meaningful at all and argue that in a diffusive setting, one does not see much in any way. On the other hand, diffuse light is literally all around us, whether coming from natural objects such as clouds or man-made objects such as a white wallpaper. Thinking a bit broader about diffusive-light cloaking can very well result in potential applications. The active area of large-scale organic light-emitting diodes (OLEDs), for example, is partially shadowed by metal wires that help reduce the Ohmic resistance of the emission-side electrode. Furthermore, scattering layers are already used in practice to enhance the outcoupling efficiency of the thin-film structure of such OLEDs. Connecting these two aspects, the concepts of diffusive-light cloaking could be used create structured scattering layers that not only increase the outcoupling efficiency but also cloak the metal wires and thus homogenize the perceived OLED brightness. To this end (and also for the design of multi-shell structures as described earlier), having tools such as our photon raytracer at hand to describe also light transport that is neither completely diffuse nor completely ballistic is extremely important. Besides lighting homogenization, utilizing the transient failure inherent to even more complex cloaks for diffuse light for high-end security features is not out of reach, especially if one thinks about miniaturized versions of the cloaks presented in this thesis.

In a more general view, these potential applications demonstrate that research in transformation physics is actually not so much about creating a seemingly magical, Harry-Potter-style invisibility cloak to don and disappear from the perception of others. As stressed already in chapter 2, the real goal of transformation physics and invisibility cloaking is to gain full control over physical energy flows, with cloaking being one popular (and particularly demanding) benchmark example. When looked upon and thought about from this more holistic perspective, unprecedented applications will eventually arise not only in heat conduction and light diffusion.

Appendix A

A CHARACTERIZATION OF DIFFUSIVE MEDIA

This appendix chapter contains the results of the characterization measurements for various diffusive media used throughout this thesis.

A.1 DIFFUSIVE TRANSMISSION MEASUREMENTS FOR WATER-BASED MEDIA

This subsection contains results of diffusive transmission measurements for water-based diffusive media as described in section 7.2. The results are mainly useful for assessing how wavelength-dependent the different media's scattering properties are.

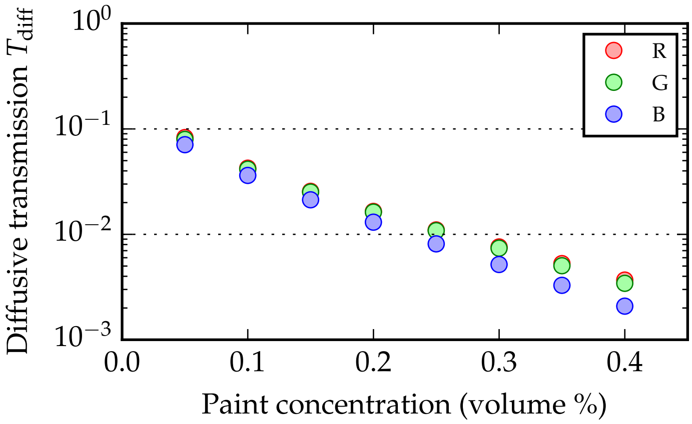

Figure A.1: Diffusive transmittance of water mixed with varying amounts of white wall paint, separated into the camera's three color channels.

Figure A.2: Diffusive transmittance of water mixed with varying amounts of milk, separated into the camera's three color channels. Note the strong separation of the blue channel, indicating strong absorption for small wavelengths.

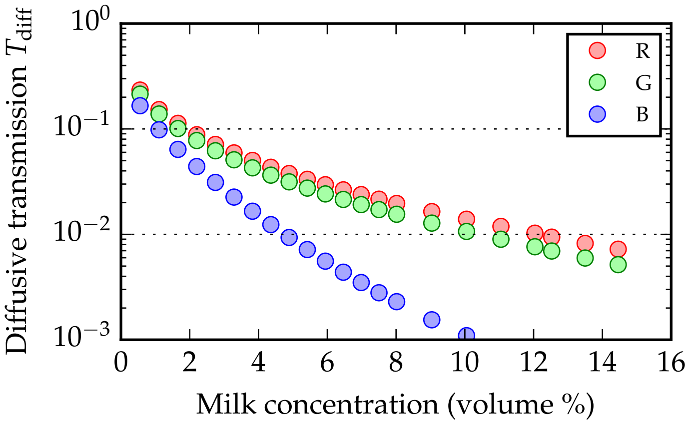

Figure A.3: Diffusive transmittance of water mixed with varying amounts of silica particles, separated into the camera's three color channels. The separation of the color channels and thus the amount of absorption lies between that for a water-paint mixture and that for a water-milk mixture.

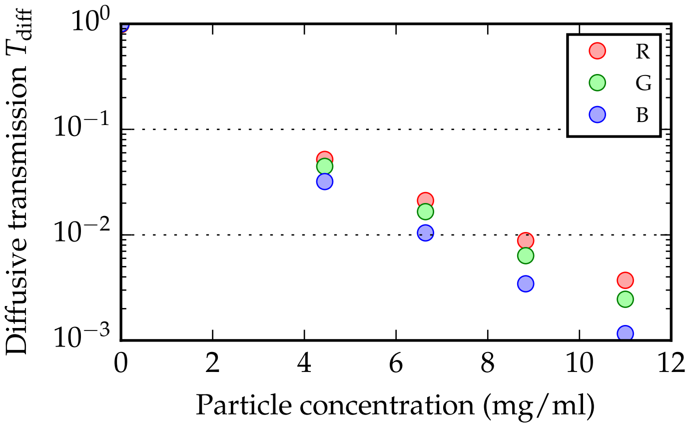

A.2 Ballistic transmission measurements

This subsection contains the results of several ballistic transmission measurements as described in section 7.2, both for water-based and for PDMS-based diffusive media. The measurements give direct access to the scattering mean free path l_s of these media.

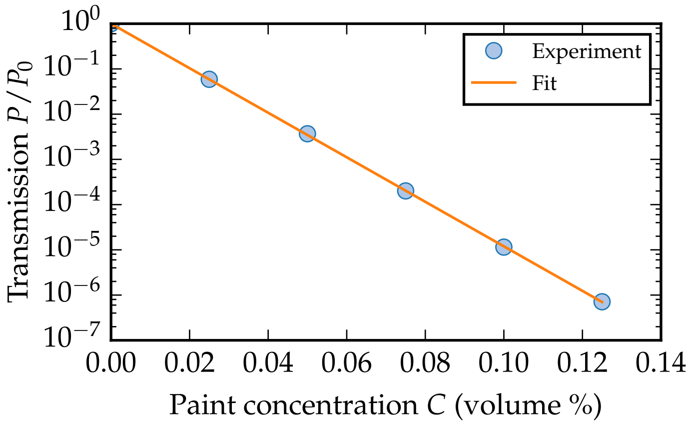

Figure A.4: Ballistic transmission of red light ($\lambda = 632.8\,\mathrm{nm}$) through a 1 cm thick cuvette filled with water mixed with white wall paint. The fit yields a scattering mean free path of $l_s = 88.5\,(\mu\mathrm{m}\,\%)/C$.

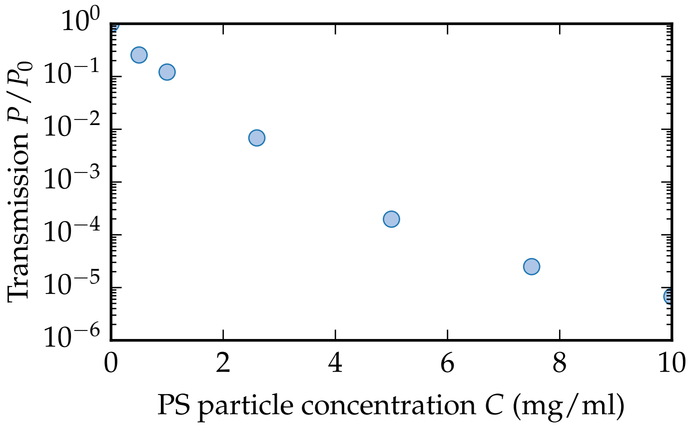

Figure A.5: Ballistic transmission of red light ($\lambda = 632.8\,\mathrm{nm}$) through 1 cm thick PDMS test samples doped with polystyrene microparticles. The saturation of the transmission for high particle concentrations indicates clustering of the particles, rendering them unfit for the creation of diffusive media.

Figure A.6: Ballistic transmission of red light ($\lambda = 632.8\,\mathrm{nm}$) through 1 cm thick PDMS test samples doped with white wall paint. The fit yields a scattering mean free path of $l_s = 503\,(\mu\mathrm{m}\,\%)/C$.

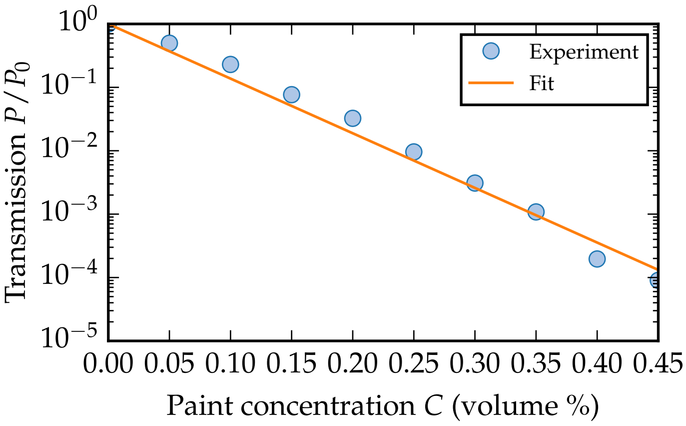

Figure A.7: Ballistic transmission of red light ($\lambda = 632.8\,\mathrm{nm}$) through 1 cm thick PDMS test samples doped with TiO_2 nanoparticles (DuPont R700). The fit yields a scattering mean free path of $l_s = 297\,(\mu\mathrm{m}\,\mathrm{mg/ml})/C$.

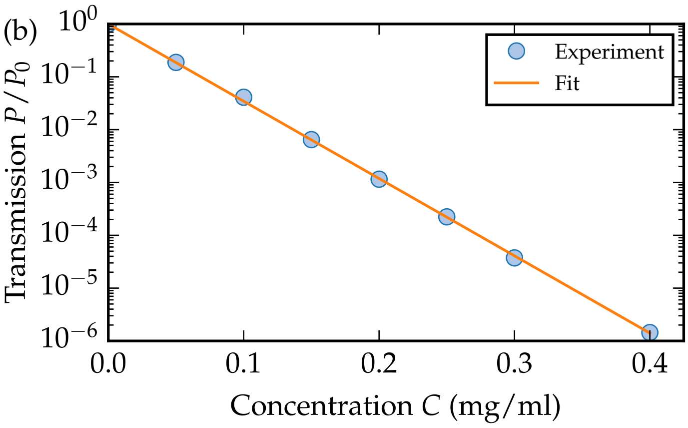

Figure A.8: Ballistic transmission of red light ($\lambda = 632.8\,\mathrm{nm}$) through 1 cm thick PDMS test samples doped with TiO_2 nanoparticles (DuPont R706). The fit yields a scattering mean free path of $l_s = 287\,(\mu\mathrm{m}\,\mathrm{mg/ml})/C$.

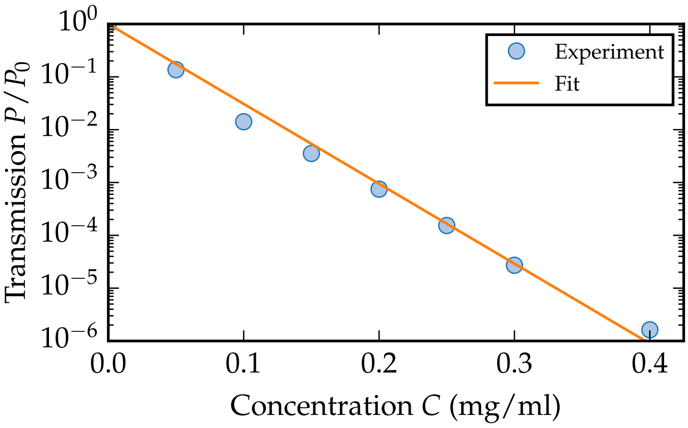

A.3 COMPARISON OF POTENTIAL CORE MATERIALS

In our search of a material with the highest possible diffusive reflectivity to be used for the cylindrical core of our cloak samples, we compared the reflective qualities of a number of materials. Of the materials tested (see Figure A.9), only the alumina ceramic *Sintox AL* from Morgan Advanced Ceramics, USA, showed a higher reflectivity than aluminum coated with a white paint layer, but was not available in the cylindrical shape we needed. We finally opted for another alumina ceramic called *Accuflect*, supplied by Accuratus, USA.

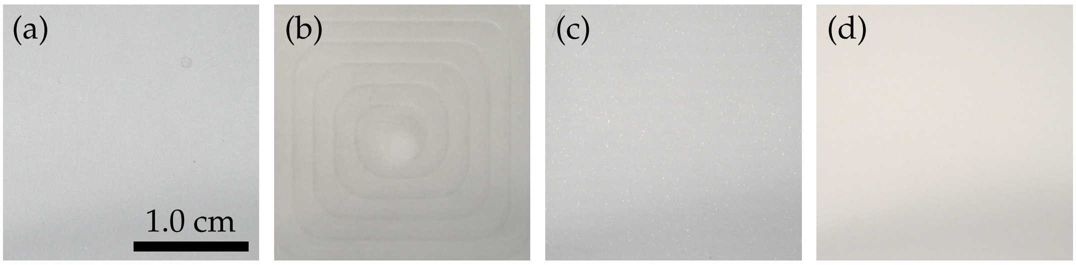

Figure A.9: Photographs of different diffusively reflecting materials under identical homogeneous illumination. The colors are normalized to (a) aluminum coated with white spray-paint (relative intensity of $(1.0, 1.0, 1.0)$ for the red, green, and blue camera color channel). (b) Corian, relative intensity $(0.93, 0.91, 0.88)$ (c) MACOR, relative intensity $(1.01, 1.00, 0.99)$ (d) Sintox AL, relative intensity $(1.12, 1.08, 1.05)$

Appendix B

B PDMS CASTING MOLDS

Figures B.1 and B.2 show photographs of the PDMS casting molds used for fabricating the water-based and PDMS-based samples, respectively.

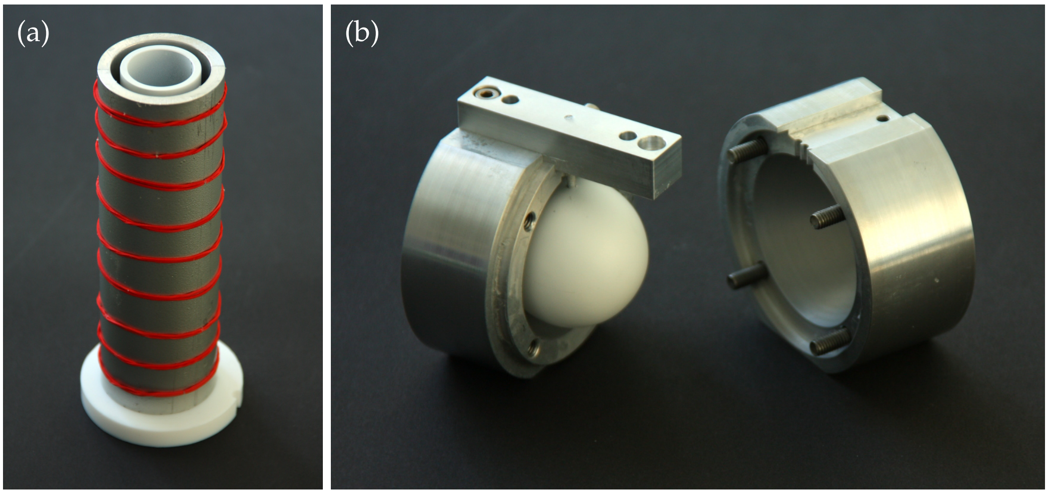

Figure B.1: Molds for casting the PDMS shells used for water-based diffusive-light cloaking. (a) Mold for cylindrical shells, cylinder height is 16 cm. (b) Mold for spherical shells.

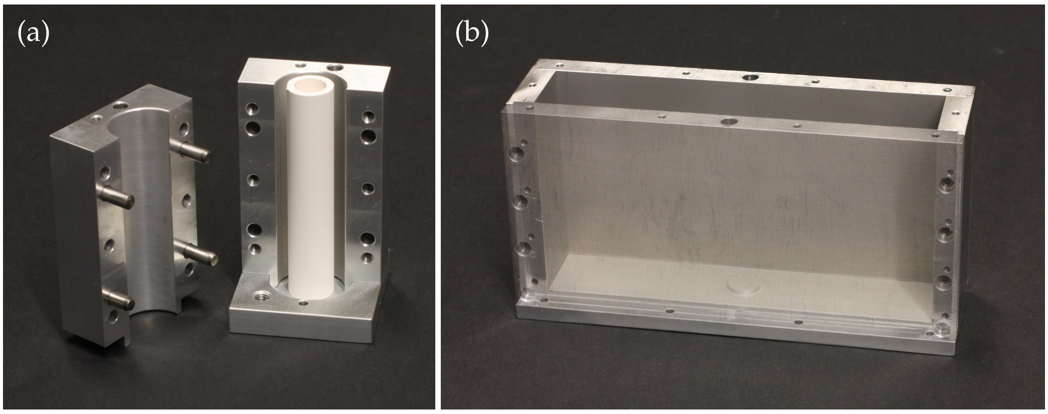

Figure B.2: Molds for fabrication of all-solid-state core-shell cloaks. (a) Mold for casting the PDMS shell around a near-zero diffusivity core (Accuflect® B6 core inside the mold for illustration). Cylinder height is 8 cm (b) Mold for casting the solid PDMS surrounding. Inner dimensions are $15 \times 8 \times 3\,\mathrm{cm}^3$.

C

Appendix C

DIRECTORY OF DIFFUSIVE SAMPLES

The following table lists all reference, obstacle, and cloak samples used in the experiments on diffusive-light cloaking.

Table C.1: List of the diffusive samples presented in this thesis and their parameters.

Name	Host	Dimensions cm^3	R_1 cm	R_2 cm	Surr. dopant	C_0	Shell dopant	C_2 mg/ml	Core
WR1	water	$35.5 \times 16 \times 6$	–	–	paint	0.35 %	–	–	–
WR2	water	$35.5 \times 16 \times 6$	–	–	paint	0.175 %	–	–	–
WO1	water	$35.5 \times 16 \times 6$	1.6	–	paint	0.35 %	–	–	painted Al
WO2 (sph.)	water	$35.5 \times 16 \times 6$	1.6	–	paint	0.175 %	–	–	painted Al
WC1	water	$35.5 \times 16 \times 6$	1.6	2.0	paint	0.35 %	MF	1	painted Al
WC2 (sph.)	water	$35.5 \times 16 \times 6$	1.6	2.0	paint	0.175 %	MF	1	painted Al
TR1	PDMS	$15 \times 8 \times 3$	–	–	TiO_2	0.49 mg/ml	–	–	–
TO2	PDMS	$15 \times 8 \times 3$	0.8	–	TiO_2	0.49 mg/ml	–	–	painted Al
TC1	PDMS	$15 \times 8 \times 3$	0.8	1.2	TiO_2	0.13 mg/ml	TiO_2	0.05	painted Al
TC7	PDMS	$15 \times 8 \times 3$	0.8	1.2	TiO_2	0.49 mg/ml	TiO_2	0.075	painted Al
AR1	PDMS	$15 \times 8 \times 3$	–	–	TiO_2	0.39 mg/ml	–	–	–
AR2	PDMS	$15 \times 8 \times 3$	–	–	TiO_2	0.39 mg/ml	–	–	–
AO1	PDMS	$15 \times 8 \times 3$	0.8	–	TiO_2	0.39 mg/ml	–	–	Accuflect® B6
AC4	PDMS	$15 \times 8 \times 3$	0.8	1.2	TiO_2	0.39 mg/ml	TiO_2	0.1	Accuflect® B6
AC5	PDMS	$15 \times 8 \times 3$	0.8	1.2	TiO_2	0.39 mg/ml	TiO_2	0.1	Accuflect® B6
AC6	PDMS	$15 \times 8 \times 3$	0.8	1.2	TiO_2	0.39 mg/ml	TiO_2	0.09	Accuflect® B6
AC8	PDMS	$15 \times 8 \times 3$	0.8	1.2	TiO_2	0.39 mg/ml	TiO_2	0.11	Accuflect® B6

BIBLIOGRAPHY

[1] J. B. Pendry, D. Schurig, and D. R. Smith, "Controlling Electromagnetic Fields", Science **312**, 1780–1782 (2006) (cited on pages 5, 6, 12, 13, 16).

[2] A. J. Ward and J. B. Pendry, "Refraction and geometry in Maxwell's equations", J. Mod. Opt. **43**, 773–793 (1996) (cited on page 6).

[3] H. Hashemi, B. Zhang, J. D. Joannopoulos, and S. G. Johnson, "Delay-Bandwidth and Delay-Loss Limitations for Cloaking of Large Objects", Phys. Rev. Lett. **104**, 253903 (2010) (cited on pages 6, 17, 43).

[4] U. Leonhardt, "Optical Conformal Mapping", Science **312**, 1777–1780 (2006) (cited on pages 6, 12).

[5] D. Schurig, J. J. Mock, B. J. Justice, S. A. Cummer, J. B. Pendry, A. F. Starr, and D. R. Smith, "Metamaterial Electromagnetic Cloak at Microwave Frequencies", Science **314**, 977–980 (2006) (cited on pages 6, 17, 31, 42).

[6] V. M. Shalaev, "Transforming Light", Science **322**, 384–386 (2008) (cited on pages 6, 17).

[7] L. H. Gabrielli, J. Cardenas, C. B. Poitras, and M. Lipson, "Silicon nanostructure cloak operating at optical frequencies", Nat. Photon. **3**, 461–463 (2009) (cited on page 6).

[8] M. Wegener and S. Linden, "Shaping optical space with metamaterials", Phys. Today **63**, 32–36 (2010) (cited on page 6).

[9] X. Chen, Y. Luo, J. Zhang, K. Jiang, J. B. Pendry, and S. Zhang, "Macroscopic invisibility cloaking of visible light", Nat. Commun. **2**, 176 (2011) (cited on page 6).

[10] N. Landy and D. R. Smith, "A full-parameter unidirectional metamaterial cloak for microwaves", Nat. Mater. **12**, 25–28 (2012) (cited on pages 6, 17).

[11] J. Li and J. B. Pendry, "Hiding under the Carpet: A New Strategy for Cloaking", Phys. Rev. Lett. **101**, 203901 (2008) (cited on pages 6, 18).

[12] J. Valentine, J. Li, T. Zentgraf, G. Bartal, and X. Zhang, “An optical cloak made of dielectrics”, Nat. Mater. **8**, 568–571 (2009) (cited on pages 6, 19).

[13] T. Ergin, N. Stenger, P. Brenner, J. B. Pendry, and M. Wegener, “Three-Dimensional Invisibility Cloak at Optical Wavelengths”, Science **328**, 337–339 (2010) (cited on pages 6, 19).

[14] H. Chen and C. T. Chan, “Acoustic cloaking in three dimensions using acoustic metamaterials”, Appl. Phys. Lett. **91**, 183518 (2007) (cited on pages 6, 17).

[15] A. N. Norris, “Acoustic cloaking theory”, Proc. R. Soc. A **464**, 2411–2434 (2008) (cited on pages 6, 17).

[16] B.-I. Popa, L. Zigoneanu, and S. A. Cummer, “Experimental Acoustic Ground Cloak in Air”, Phys. Rev. Lett. **106**, 253901 (2011) (cited on pages 6, 19).

[17] G. W. Milton, M. Briane, and J. R. Willis, “On cloaking for elasticity and physical equations with a transformation invariant form”, New J. Phys. **8**, 248 (2006) (cited on pages 6, 17).

[18] M. Brun, S. Guenneau, and A. B. Movchan, “Achieving control of in-plane elastic waves”, Appl. Phys. Lett. **94**, 061903 (2009) (cited on pages 6, 17).

[19] M. Farhat, S. Guenneau, and S. Enoch, “Ultrabroadband Elastic Cloaking in Thin Plates”, Phys. Rev. Lett. **103**, 024301 (2009) (cited on pages 6, 17).

[20] N. Stenger, M. Wilhelm, and M. Wegener, “Experiments on Elastic Cloaking in Thin Plates”, Phys. Rev. Lett. **108**, 014301 (2012) (cited on pages 6, 17, 31, 127).

[21] A. V. Amirkhizi, A. Tehranian, and S. Nemat-Nasser, “Stress-wave energy management through material anisotropy”, Wave Motion **47**, 519–536 (2010) (cited on pages 6, 17).

[22] A. Norris and A. Shuvalov, “Elastic cloaking theory”, Wave Motion **48**, 525–538 (2011) (cited on pages 6, 17).

[23] W. J. Parnell and T. Shearer, “Antiplane elastic wave cloaking using metamaterials, homogenization and hyperelasticity”, Wave Motion **50**, 1140–1152 (2013) (cited on page 6).

[24] F. Yang, Z. L. Mei, T. Y. Jin, and T. J. Cui, “dc Electric Invisibility Cloak”, Phys. Rev. Lett. **109**, 053902 (2012) (cited on pages 6, 17, 20, 22, 37).

[25] W. X. Jiang, C. Y. Luo, Z. L. Mei, and T. J. Cui, “An ultrathin but nearly perfect direct current electric cloak”, Appl. Phys. Lett. **102**, 014102 (2013) (cited on pages 6, 17, 37).

[26] T. Han, H. Ye, Y. Luo, S. P. Yeo, J. Teng, S. Zhang, and C.-W. Qiu, “Manipulating DC Currents with Bilayer Bulk Natural Materials”, Adv. Mater. **26**, 3478–3483 (2014) (cited on pages 6, 20).

[27] F. Gömöry, M. Solovyov, J. Šouc, C. Navau, J. Prat-Camps, and A. Sanchez, “Experimental Realization of a Magnetic Cloak”, Science **335**, 1466–1468 (2012) (cited on pages 6, 20, 89, 98, 99).

[28] M. Solovyov, J. Souc, and F. Gomory, “Magnetic Cloak for Low Frequency AC Magnetic Field”, IEEE T. Appl. Supercon. **25**, 1–5 (2015) (cited on pages 6, 20, 89).

[29] J. Prat-Camps, C. Navau, and A. Sanchez, “A Magnetic Wormhole”, Sci. Rep. **5**, 12488 (2015) (cited on pages 6, 20).

[30] S. Guenneau, C. Amra, and D. Veynante, “Transformation thermodynamics: cloaking and concentrating heat flux”, Opt. Express **20**, 8207–8218 (2012) (cited on pages 7, 16, 22, 24–26, 37).

[31] E. H. Kerner, “The Electrical Conductivity of Composite Media”, Proc. Phys. Soc. B **69**, 802 (1956) (cited on pages 7, 20, 88).

[32] E. H. Kerner, “The Elastic and Thermo-elastic Properties of Composite Media”, Proc. Phys. Soc. B **69**, 808 (1956) (cited on pages 7, 20, 88).

[33] Z. Hashin and S. Shtrikman, “A Variational Approach to the Theory of the Effective Magnetic Permeability of Multiphase Materials”, J. Appl. Phys. **33**, 3125–3131 (1962) (cited on pages 7, 89).

[34] A. Alù and N. Engheta, “Achieving transparency with plasmonic and metamaterial coatings”, Phys. Rev. E **72**, 016623 (2005) (cited on pages 7, 20).

[35] M. Kadic, T. Bückmann, R. Schittny, and M. Wegener, “Experiments on cloaking in optics, thermodynamics and mechanics”, Phil. Trans. R. Soc. A **373**, 20140357 (2015) (cited on pages 12, 16).

[36] R. Schittny and M. Wegener, “Physikalische Tarnkappen”, Spektrum **1**, 80 (2014) (cited on pages 12–14).

[37] A. Greenleaf, Y. Kurylev, M. Lassas, and G. Uhlmann, "Full-Wave Invisibility of Active Devices at All Frequencies", Commun. Math. Phys. **275**, 749–789 (2007) (cited on page 15).

[38] M. Kadic, T. Bückmann, R. Schittny, and M. Wegener, "Metamaterials beyond electromagnetism", Rep. Prog. Phys. **76**, 126501 (2013) (cited on pages 16, 17, 25).

[39] G. W. Milton, *The Theory of Composites* (Cambridge University Press, Cambridge, 2002) (cited on pages 17, 25, 89).

[40] B. Banerjee, *An Introduction to Metamaterials and Waves in Composites* (Taylor & Francis, 2011) (cited on page 17).

[41] R. V. Craster and S. Guenneau, *Acoustic Metamaterials* (Springer Netherlands, 2013) (cited on page 17).

[42] S. A. Cummer and D. Schurig, "One path to acoustic cloaking", New J. Phys. **9**, 45–45 (2007) (cited on page 17).

[43] S. Zhang, C. Xia, and N. Fang, "Broadband Acoustic Cloak for Ultrasound Waves", Phys. Rev. Lett. **106**, 024301 (2011) (cited on page 17).

[44] W. Kan, V. M. García-Chocano, F. Cervera, B. Liang, X.-y. Zou, L.-l. Yin, J. Cheng, and J. Sánchez-Dehesa, "Broadband Acoustic Cloaking within an Arbitrary Hard Cavity", Phys. Rev. Applied **3**, 064019 (2015) (cited on page 17).

[45] S. Brûlé, E. H. Javelaud, S. Enoch, and S. Guenneau, "Experiments on Seismic Metamaterials: Molding Surface Waves", Phys. Rev. Lett. **112**, 133901 (2014) (cited on page 17).

[46] A. Diatta and S. Guenneau, "Controlling solid elastic waves with spherical cloaks", Appl. Phys. Lett. **105**, 021901 (2014) (cited on page 17).

[47] M. Farhat, S. Enoch, S. Guenneau, and A. B. Movchan, "Broadband Cylindrical Acoustic Cloak for Linear Surface Waves in a Fluid", Phys. Rev. Lett. **101**, 134501 (2008) (cited on page 17).

[48] W. X. Jiang, C. Y. Luo, S. Ge, C.-W. Qiu, and T. J. Cui, "An Optically Controllable Transformation-dc Illusion Device", Adv. Mater. **27**, 4628–4633 (2015) (cited on page 17).

[49] R. V. Kohn, H. Shen, M. S. Vogelius, and M. I. Weinstein, "Cloaking via change of variables in electric impedance tomography", Inverse Probl. **24**, 015016 (2008) (cited on page 17).

[50] T. Ergin, J. Fischer, and M. Wegener, “Optical Phase Cloaking of 700 nm Light Waves in the Far Field by a Three-Dimensional Carpet Cloak”, Phys. Rev. Lett. **107**, 173901 (2011) (cited on page 19).

[51] M. Gharghi, C. Gladden, T. Zentgraf, Y. Liu, X. Yin, J. Valentine, and X. Zhang, “A Carpet Cloak for Visible Light”, Nano Lett. **11**, 2825–2828 (2011) (cited on page 19).

[52] L. Zigoneanu, B.-I. Popa, and S. A. Cummer, “Three-dimensional broadband omnidirectional acoustic ground cloak”, Nat. Mater. **13**, 352–355 (2014) (cited on page 19).

[53] M. Rahm, D. Schurig, D. A. Roberts, S. A. Cummer, D. R. Smith, and J. B. Pendry, “Design of electromagnetic cloaks and concentrators using form-invariant coordinate transformations of Maxwell’s equations”, Photonic. Nanostruct. **6**, 87–95 (2008) (cited on page 19).

[54] S. Guenneau, D. Petiteau, M. Zerrad, and C. Amra, “Bicephalous transformed media: concentrator versus rotator and cloak versus superscatterer”, Opt. Express **22**, 23614 (2014) (cited on page 19).

[55] R. S. Kapadia and P. R. Bandaru, “Heat flux concentration through polymeric thermal lenses”, Appl. Phys. Lett. **105**, 233903 (2014) (cited on pages 19, 37).

[56] F. Chen and D. Yuan Lei, “Experimental Realization of Extreme Heat Flux Concentration with Easy-to-Make Thermal Metamaterials”, Sci. Rep. **5**, 11552 (2015) (cited on page 19).

[57] W. X. Jiang, C. Y. Luo, H. F. Ma, Z. L. Mei, and T. J. Cui, “Enhancement of Current Density by dc Electric Concentrator”, Sci. Rep. **2**, 956 (2012) (cited on pages 19, 22).

[58] H. Chen, B. Hou, S. Chen, X. Ao, W. Wen, and C. T. Chan, “Design and Experimental Realization of a Broadband Transformation Media Field Rotator at Microwave Frequencies”, Phys. Rev. Lett. **102**, 183903 (2009) (cited on page 19).

[59] H. Chen, C. T. Chan, and P. Sheng, “Transformation optics and metamaterials”, Nat. Mater. **9**, 387–396 (2010) (cited on page 19).

[60] D. A. Roberts, M. Rahm, J. B. Pendry, and D. R. Smith, “Transformation-optical design of sharp waveguide bends and corners”, Appl. Phys. Lett. **93**, 251111 (2008) (cited on page 19).

[61] L. H. Gabrielli, D. Liu, S. G. Johnson, and M. Lipson, "On-chip transformation optics for multimode waveguide bends", Nat. Commun. **3**, 1217 (2012) (cited on page 19).

[62] L. Sanchis, V. M. García-Chocano, R. Llopis-Pontiveros, A. Climente, J. Martínez-Pastor, F. Cervera, and J. Sánchez-Dehesa, "Three-Dimensional Axisymmetric Cloak Based on the Cancellation of Acoustic Scattering from a Sphere", Phys. Rev. Lett. **110**, 124301 (2013) (cited on page 20).

[63] B. Vial and Y. Hao, "Topology optimized all-dielectric cloak: design, performances and modal picture of the invisibility effect", Opt. Lett. **23**, 23551 (2015) (cited on page 20).

[64] T. Bückmann, M. Thiel, M. Kadic, R. Schittny, and M. Wegener, "An elasto-mechanical unfeelability cloak made of pentamode metamaterials", Nat. Commun. **5**, 4130 (2014) (cited on page 20).

[65] L. Zeng, "Bi-layer steady state current cloak", Phys. Lett. A **378**, 923–926 (2014) (cited on page 20).

[66] X. He and L. Wu, "Thermal transparency with the concept of neutral inclusion", Phys. Rev. E **88**, 033201 (2013) (cited on page 20).

[67] T. Han, X. Bai, D. Gao, J. T. L. Thong, B. Li, and C.-W. Qiu, "Experimental Demonstration of a Bilayer Thermal Cloak", Phys. Rev. Lett. **112**, 054302 (2014) (cited on pages 20, 37).

[68] H. Xu, X. Shi, F. Gao, H. Sun, and B. Zhang, "Ultrathin Three-Dimensional Thermal Cloak", Phys. Rev. Lett. **112**, 054301 (2014) (cited on pages 20, 37, 98).

[69] T. H. Chen, F. Yang, and Z. L. Mei, "A simple and flexible thermal illusion device and its experimental verification: A simple and flexible thermal illusion device", Phys. Status Solidi A **212**, 1746–1750 (2015) (cited on page 20).

[70] R. Fleury, F. Monticone, and A. Alù, "Invisibility and Cloaking: Origins, Present, and Future Perspectives", Phys. Rev. Applied **4**, 037001 (2015) (cited on page 20).

[71] R. Schittny, M. Kadic, S. Guenneau, and M. Wegener, "Experiments on Transformation Thermodynamics: Molding the Flow of Heat", Phys. Rev. Lett. **110**, 195901 (2013) (cited on pages 21, 23, 28–30, 37).

[72] A. P. Calderón, "On an inverse boundary value problem", Comput. Appl. Math **25**, 133–138 (2006) (cited on page 22).

[73] R. Kohn and M. Vogelius, “Determining conductivity by boundary measurements”, Commun. Pure Appl. Math. **37**, 289–298 (1984) (cited on page 22).

[74] A. Greenleaf, M. Lassas, and G. Uhlmann, “On nonuniqueness for Calderón’s inverse problem”, Math. Res. Lett. **10**, 685–693 (2003) (cited on page 22).

[75] S. Narayana and Y. Sato, “Heat Flux Manipulation with Engineered Thermal Materials”, Phys. Rev. Lett. **108**, 214303 (2012) (cited on pages 22, 37).

[76] T. Bückmann, M. Kadic, R. Schittny, and M. Wegener, “Mechanical metamaterials with anisotropic and negative effective mass-density tensor made from one constituent material: Metamaterials with anisotropic and negative effective mass-density tensor”, Phys. Status Solidi B **252**, 1671–1674 (2015) (cited on pages 24, 127).

[77] R. B. Bird, W. Stewart, and E. N. Lightfoot, *Transport phenomena*, 1st ed. (Wiley, New York, 2002) (cited on pages 34, 80).

[78] R. Hu, X. Wei, J. Hu, and X. Luo, “Local heating realization by reverse thermal cloak”, Sci. Rep. **4**, 3600 (2014) (cited on page 37).

[79] Y. Ma, Y. Liu, M. Raza, Y. Wang, and S. He, “Experimental Demonstration of a Multiphysics Cloak: Manipulating Heat Flux and Electric Current Simultaneously”, Phys. Rev. Lett. **113**, 205501 (2014) (cited on page 37).

[80] M. Raza, Y. Liu, and Y. Ma, “A multi-cloak bifunctional device”, J. Appl. Phys. **117**, 024502 (2015) (cited on page 37).

[81] M. Moccia, G. Castaldi, S. Savo, Y. Sato, and V. Galdi, “Independent Manipulation of Heat and Electrical Current via Bifunctional Metamaterials”, Phys. Rev. X **4**, 021025 (2014) (cited on page 37).

[82] T. Han, X. Bai, D. Liu, D. Gao, B. Li, J. T. L. Thong, and C.-W. Qiu, “Manipulating Steady Heat Conduction by Sensu-shaped Thermal Metamaterials”, Sci. Rep. **5**, 10242 (2015) (cited on page 37).

[83] G. Dolling, C. Enkrich, M. Wegener, C. M. Soukoulis, and S. Linden, “Simultaneous Negative Phase and Group Velocity of Light in a Metamaterial”, Science **312**, 892–894 (2006) (cited on page 42).

[84] J. S. Toll, “Causality and the Dispersion Relation: Logical Foundations”, Phys. Rev. **104**, 1760–1770 (1956) (cited on page 42).

[85] F. Martelli, S. D. Bianco, A. Ismaelli, and G. Zaccanti, *Light Propagation Through Biological Tissue and Other Diffusive Media: Theory, Solutions, and Software*, 1st ed. (SPIE Press, Bellingham (Washington), 2010) (cited on pages 45, 54, 58, 60, 138).

[86] A. T. Young, "Rayleigh scattering", Appl. Opt. **20**, 533–535 (1981) (cited on page 47).

[87] G. Mie, "Beiträge zur Optik trüber Medien, speziell kolloidaler Metallösungen", Ann. Phys. **330**, 377–445 (1908) (cited on page 47).

[88] S. Chandrasekhar, *Radiative Transfer* (Oxford University Press, London/Dover, 1960) (cited on page 51).

[89] A. Ishimaru, *Wave propagation and scattering in random media*, Vol. 1 (Academic Press, New York, 1978) (cited on page 51).

[90] J. J. Duderstadt and W. R. Martin, *Transport Theory* (John Wiley & Sons, New York, 1979) (cited on page 53).

[91] A. Fick, "Ueber Diffusion", Ann. Phys. **170**, 59–86 (1855) (cited on page 54).

[92] M. Bassani, F. Martelli, G. Zaccanti, and D. Contini, "Independence of the diffusion coefficient from absorption: experimental and numerical evidence", **22**, 853–855 (1997) (cited on page 56).

[93] R. Aronson and N. Corngold, "Photon diffusion coefficient in an absorbing medium", J. Opt. Soc. Am. A **16**, 1066–1071 (1999) (cited on page 56).

[94] P. W. Anderson, "Absence of Diffusion in Certain Random Lattices", Phys. Rev. **109**, 1492–1505 (1958) (cited on page 57).

[95] H. Hu, A. Strybulevych, J. H. Page, S. E. Skipetrov, and B. A. van Tiggelen, "Localization of ultrasound in a three-dimensional elastic network", Nat. Phys. **4**, 945–948 (2008) (cited on page 57).

[96] T. Sperling, W. Bührer, C. M. Aegerter, and G. Maret, "Direct determination of the transition to localization of light in three dimensions", Nat. Photon. **7**, 48–52 (2013) (cited on pages 57, 82).

[97] D. Contini, F. Martelli, and G. Zaccanti, "Photon migration through a turbid slab described by a model based on diffusion approximation. I. Theory", Appl. Opt. **36**, 4587–4599 (1997) (cited on page 61).

[98] J. N. Reddy, *An introduction to the finite element method*, 3rd ed., McGraw-Hill series in mechanical engineering (McGraw-Hill, Boston, 2006) (cited on page 68).

[99] C. Zhu and Q. Liu, "Review of Monte Carlo modeling of light transport in tissues", J. Biomed. Opt. **18**, 050902 (2013) (cited on page 70).

[100] L. Devroye, *Non-uniform random variate generation* (Springer, New York, 1986) (cited on page 70).

[101] L. C. Henyey and J. L. Greenstein, "Diffuse radiation in the Galaxy", Astrophys. J. **93**, 70–83 (1941) (cited on page 71).

[102] Q. Fang and D. A. Boas, "Monte Carlo simulation of photon migration in 3D turbid media accelerated by graphics processing units", Opt. Express **17**, 20178–20190 (2009) (cited on page 72).

[103] Q. Fang, "Mesh-based Monte Carlo method using fast ray-tracing in Plücker coordinates", Biomed. Opt. Express **1**, 165–175 (2010) (cited on page 72).

[104] A. Doronin and I. Meglinski, "Online object oriented Monte Carlo computational tool for the needs of biomedical optics", Biomed. Opt. Express **2**, 2461–2469 (2011) (cited on page 72).

[105] J. D. Foley, ed., *Computer graphics: principles and practice*, 2nd ed., Addison-Wesley systems programming series (Addison-Wesley, Reading (Massachusetts), 1995) (cited on page 73).

[106] J. R. Devore, "Refractive Indices of Rutile and Sphalerite", J. Opt. Soc. Am. **41**, 416–417 (1951) (cited on page 77).

[107] B. Palsson and S. Bhatia, *Tissue engineering* (Pearson Prentice Hall, Upper Saddle River, NJ, 2004), 407 pp. (cited on page 80).

[108] J. H. Page, H. P. Schriemer, A. E. Bailey, and D. A. Weitz, "Experimental test of the diffusion approximation for multiply scattered sound", Phys. Rev. E **52**, 3106–3114 (1995) (cited on page 82).

[109] D. V. O'Connor and D. Phillips, *Time-correlated single photon counting* (Academic Press, London, 1984) (cited on pages 82, 84).

[110] N. Wiener, *Extrapolation, Interpolation, and Smoothing of Stationary Time Series* (MIT Press, Cambridge, Massachusetts, 1977) (cited on page 84).

[111] J. A. Nelder and R. Mead, "A Simplex Method for Function Minimization", Comput. J. **7**, 308–313 (1965) (cited on page 96).

[112] R. Schittny, M. Kadic, T. Bückmann, and M. Wegener, "Invisibility cloaking in a diffusive light scattering medium", Science **345**, 427–429 (2014) (cited on pages 100, 101, 107, 108, 110–112).

[113] R. Schittny, A. Niemeyer, M. Kadic, T. Bückmann, A. Naber, and M. Wegener, "Diffuse-light all-solid-state invisibility cloak", Opt. Lett. **40**, 4202 (2015) (cited on pages 123, 125, 126).

[114] S. Mühlig, A. Cunningham, J. Dintinger, M. Farhat, S. B. Hasan, T. Scharf, T. Bürgi, F. Lederer, and C. Rockstuhl, "A self-assembled three-dimensional cloak in the visible", Sci. Rep. **3**, 2382 (2013) (cited on page 127).

[115] M. Farhat, P.-Y. Chen, H. Bagci, C. Amra, S. Guenneau, and A. Alù, "Thermal invisibility based on scattering cancellation and mantle cloaking", Sci. Rep. **5**, 9876 (2015) (cited on page 127).

[116] S. Prahl, *Mie Scattering Calculator*, (2012) `http://omlc.org/calc/mie_calc.html` (cited on page 132).

[117] R. Schittny, A. Niemeyer, M. Kadic, T. Bückmann, A. Naber, and M. Wegener, "Transient behavior of invisibility cloaks for diffusive light propagation", Optica **2**, 84–87 (2015) (cited on pages 143, 146, 149, 151).

[118] D. Boas, D. Brooks, E. Miller, C. DiMarzio, M. Kilmer, R. Gaudette, and Q. Zhang, "Imaging the body with diffuse optical tomography", IEEE Signal Proc. Mag. **18**, 57–75 (2001) (cited on pages 144, 151).

[119] T. Durduran, R. Choe, W. B. Baker, and A. G. Yodh, "Diffuse optics for tissue monitoring and tomography", Rep. Prog. Phys. **73**, 076701 (2010) (cited on pages 144, 151).

[120] N. H. Gokhale, J. L. Cipolla, and A. N. Norris, "Special transformations for pentamode acoustic cloaking", J. Acoust. Soc. Am. **132**, 2932–2941 (2012) (cited on page 151).

[121] Y.-L. Tsai and T. Chen, "Transformation Media in Acoustics with Constant Bulk Modulus or Constant Density Tensor", J. Mech. (2015) `10.1017/jmech.2015.65` (cited on page 151).

ACKNOWLEDGMENTS

The research presented in this work has not been a one-man job. There might be just a single name on the title page, but plenty of people contributed to this work in one way or another. Here, I want to express my thanks and gratitude to all of them.

First and most of all, I want to thank my supervisor, Prof. Dr. Martin Wegener, for giving me the opportunity to work in this exciting field of physics. I am truly grateful for his scientific guidance and supervision, which I could not have imagined to be any better. He was always keen to hear from my newest results, provided plenty of stimulating input yet always gave me the freedom to develop my own ideas and trusted me with presenting our results to international audiences. I further want to express my gratitude to Prof. Dr. Carsten Rockstuhl, who generously agreed on co-refereeing this thesis.

Next, I want to especially thank all those who worked closest with me during the last years for all the intense and fruitful discussions and shared lab time. First to mention is Muamer Kadic, who supported the entire spectrum of topics I covered with theoretical knowledge and invaluable COMSOL wizardry. I also thank Tiemo Bückmann for sharing with me the struggle of creating and characterizing mechanical metamaterials (which in the end never made it into this thesis), Andreas Niemeyer for our joint work on time-resolved cloaking which led to a much deeper understanding of light diffusion, and Frederik Mayer for his help in developing a GPU-based photon raytracer from scratch.

I furthermore want to express my deep gratitude to all former and current members of our group for all the generous help I received whenever I asked for it, for countless fruitful discussions, and for loads of stories, fun, and laughter during and after work. It was this pleasant atmosphere which made me enjoy every single day of work in the last years.

I am also especially indebted to Renate Helfen, Ursula Mösle, and Claudia Alaya from the secretariat, to Michael Hippe, Helmuth Lay, and Werner Gilde from the electronics workshop, to Mario Nusche and Frank Landhäusser from the mechanical workshop, and to our technician Johann Westhauser.

Forming the backbone of the institute, they provided invaluable and time-saving services that allowed me to always focus on the essentials of my research.

I further want to thank all those who critically proofread this thesis, namely Andrea Scheiwe, Andreas Niemeyer, Carlos Jamarillo, Frederik Mayer, Johannes Kaschke, Muamer Kadic, Tiemo Bückmann, and Tobias Frenzel.

Finally, I want to express my gratitude and love to my parents Marlis and Thomas, my brother Frank, my sister Luisa, and my lovely girlfriend Kyoungjin. They are the persons dearest to me and I want to thank them for their loving and unconditional support.